Dissertation
submitted to the
Combined Faculties of the Natural Sciences and Mathematics
of the Ruperto-Carola University of Heidelberg, Germany
for the degree of
Doctor of Natural Sciences

Put forward by
Tamasi Rameshchandra Kar
Born in: Mumbai, Maharashtra, India
Oral Examination: 04-11-2020

A Triplet Track Trigger for Future High Rate Collider Experiments

Referees: Prof. Dr André, Schöning

Prof. Dr Silvia, Masciocchi

Dedicated to the superwomen in my life,

Maa, Ahalya Kar
&
Grand-Maa, Sarojini Panigrahi.

Kurzfassung

Mit dem bereits begonnenen Ausbau des Large Hadron Collider (LHC) zum sogenannten High-Luminosity LHC (HL-LHC) soll eine Luminosität erreicht werden, die dem Siebenfachen des Wertes entspricht, für den der LHC einst entworfen wurde ($\mathsf{L} = 10^{34}\,\mathrm{cm}^{-2}\mathrm{s}^{-1}$). Außdem wird der Bau eines neuen 100 km langen Hadronen-Speicherrings erwägt, dessen Betrieb dem des LHC folgen soll. Der sogenannte hadron-hadron Future Circular Collider (FCC-hh) hätte zum Ziel, Protonen mit einer Schwerpunktsenergie von $\sqrt{s} = 100\,\mathrm{TeV}$ und $\mathsf{L} \sim 30 \times 10^{34}\,\mathrm{cm}^{-2}\mathrm{s}^{-1}$ zu kollidieren. Eine hohe Luminosität erlaubt detaillierte Analysen von seltenen Prozessen wie z.B. der Produktion von Higgs-Paaren und ermöglicht damit eine direkte Messung der trilinearen Higgs-Selbstkopplung (λ).

Die vorliegende Arbeit enthält eine Untersuchung des Zerfallskanals $\mathrm{HH} \rightarrow b\bar{b}b\bar{b}$ auf Generatorebene unter Annahme einer triggerlosen Auslese am FCC-hh. Am FCC-hh (HL-LHC) wird eine durchschnittliche Anzahl von Pile-up-Ereignissen von $\langle\mu\rangle \sim 1000$ (200) über eine Länge von ca. 10 cm erwartet, was die Rekonstruktion von Trigger-Objekten zu einer großen Herausforderung macht. Um die Menge an zu speichernden Daten und gleichzeitig die Trigger-Schwellen möglichst niedrig zu halten, sind neue Trigger-Systeme notwendig, die davon profitieren könnten, auf möglichst niedriger Ebene Spurdetektoren einzusetzten. Spurdetektoren verfügen zusätzlich zu einer hohen Impulsauflösung über eine sehr hohe Ortsauflösung (im Gegensatz zu kalorimeterbasierten Triggern). In dieser Arbeit wird daher ein neuartiger sogenannter Triplet Track Trigger (TTT) vorgeschlagen, welcher auf drei bei großem Radius ($\sim 1\,\mathrm{m}$) dicht beieinanderliegenden Lagen von (vorzugsweise monolithischen) Pixelsensoren basiert. Die Anordnung ermöglicht eine simple Spurrekonstruktion, die mit hoher Geschwindigkeit in Hardware durchgeführt werden kann, was den Einsatz auf niedrigster Trigger-Ebene erlaubt. Die vorgestellten TTT-Studien basieren auf vollständigen Geant4-Simulationen und Rekonstruktionen für den ATLAS Inner Tracker (HL-LHC) und den Reference-Tracker des FCC-hh. Hohe Impuls- und z-Vertex-Auflösung erlauben die Gruppierung von TTT-Spuren entlang der Strahlachse, was mit Hilfe von Jet-Cluster-Algorithmen die Rekonstruktion von TTT-Jets ermöglicht. Es kann eine ausgezeichnete Pile-Up-Unterdrückung für die $\mathrm{HH} \rightarrow b\bar{b}b\bar{b}$ Multi-Jet-Topologie unter FCC-hh-Bedingungen ($\langle\mu\rangle$=1000) gezeigt werden. Eine Reduktion der Ereignis-Rate von 40 MHz auf 1 MHz (4 MHz) wird erreicht bei einer Trigger-Effizienz von ca. 60 % (80 %). Eine entsprechende Schätzung für die statistische Signifikanz des Signals ergibt $S/\sqrt{B} \sim 16$ (19) mit vernachlässigbaren systematischen Unsicherheiten und $\int \mathsf{L}\mathrm{dt} = 30\,\mathrm{ab}^{-1}$.

Abstract

The Large Hadron Collider (LHC) will have a major upgrade, called the High Luminosity LHC (HL-LHC), after which the proton beams will collide with around 7 times the design luminosity of the LHC ($\mathsf{L} = 10^{34}\mathrm{cm}^{-2}\mathrm{s}^{-1}$). There are also studies being conducted for a 100 km large circular hadron collider, called the hadron-hadron Future Circular Collider (FCC-hh), for the post LHC era. It aims to collide proton beams with $\sqrt{s} = 100\,\mathrm{TeV}$ and $\mathsf{L} \sim 30 \times 10^{34}\,\mathrm{cm}^{-2}\mathrm{s}^{-1}$. High luminosities allow for a detailed study of elusive processes, for example, Higgs pair production, thus enabling direct measurement of the trilinear Higgs self-coupling (λ).

In this regard, a generator level study is presented in the thesis using the HH $\rightarrow b\bar{b}b\bar{b}$ physics channel assuming trigger-less readout at FCC-hh. An average pile-up of $\langle\mu\rangle \sim 1000$ (200) is expected at the FCC-hh (HL-LHC) within a vertex region of $\sim 10\,\mathrm{cm}$. A vast pile-up complicates object reconstruction and forces trigger systems to increase the thresholds of trigger objects to satisfy bandwidth and storage limitations of an experiment. Hence, there is a need for a trigger that makes a smart selection of hard collision events from a sea of pile-up collisions at the earliest possible stage of a trigger system. Track triggers are attractive candidates for such demanding situations as they have a very good pointing resolution (unlike calorimeter triggers) in addition to a good momentum resolution. A new concept, the Triplet Track Trigger (TTT) is proposed to be used at the very first trigger level. It consists of three closely spaced highly granular pixel (preferably monolithic sensors) detector layers at large radii ($\sim 1\,\mathrm{m}$). It uses a very simple and fast track reconstruction algorithm, that can be easily implemented in hardware. TTT tracking performance studies are presented using full Geant4 simulation and reconstruction for the ATLAS Inner Tracker (at HL-LHC) and reference tracker of the FCC-hh. Very good momentum and z-vertex resolution allow grouping of TTT tracks into several bins along the beam-axis, where jet clustering algorithms run in parallel to form TTT-jets. The TTT allows for excellent pile-up suppression for the HH $\rightarrow b\bar{b}b\bar{b}$ multi-jet signature in $\langle\mu\rangle = 1000$ conditions of FCC-hh. A rate reduction from the 40 MHz bunch collision frequency to 1 MHz (4 MHz) is achieved for a trigger efficiency of $\sim 60\,\%$ ($80\,\%$). A corresponding rough estimate on $S/\sqrt{B} \sim 16$ (19) is obtained with negligible systematic uncertainties and $\int \mathsf{L}\mathrm{dt} = 30\,\mathrm{ab}^{-1}$.

Contents

Introduction and Outline

The quest to understand the universe and its manifestations have intrigued humans since the pre-historic times. Questions such as: "What are we made of?" "What are the very basic constituents of nature and how do they interact?" have led humans to dive deeper into the studies related to the composition of matter. From the *Atomic theory* – that proposed atoms to be indivisible in the 18th century – to the well established *Standard Model (SM) of particle physics* [1–4] formulated in the 1970s – describing the most fundamental particles of matter and their interactions – humans have come very far in addressing some of the very foundational questions.

This thesis is structured into three parts. The first part is the motivation that describes the physics inspiration behind the studies presented here. According to our present understanding, everything in the universe is made from a few basic building blocks (or fundamental particles), governed by the four fundamental forces in nature: the *gravitational*, the *weak*, the *electromagnetic*, and the *strong* force. The SM of particle physics mathematically lays out the building blocks of nature: *quarks*, *leptons*, *force carriers* (photon (γ), W and Z bosons and gluons), and the very special *Higgs boson.* A more detailed account of the SM is given in Section 1.1.

As of today, the SM is known to be incredibly precise and accurate in its theoretical predictions. However, its development so far would not have been possible without a close interplay between theory and experiment. Much of the credit goes to the rapid growth of the particle colliders that accelerate charged particles close to the speed of light, within a vacuum beampipe using electromagnetic fields. The largest particle collider in operation today is the *Large Hadron Collider (LHC)* [5] at the European Organization for Nuclear Research (CERN) in Geneva. It circulates proton (or heavy ion) beams in two concentric 27 km rings in opposite directions before colliding them (every 25 ns) at the interaction points (IP) of its four major experiments, namely, *ATLAS* [6], *CMS* [7], *ALICE* [8] and *LHCb* [9]. It is designed to collide proton-proton (pp) beams with a centre-of-mass energy of 14 TeV and instantaneous luminosities of $10^{34}\,\mathrm{cm^{-2}s^{-1}}$. In the year 2012, the only missing piece of the SM particles, the Higgs boson, was discovered, which led to a noble prize winning discovery and has been the biggest triumphs of the LHC so far [10, 11]. A list of the different Higgs production modes and its decay channels is presented in Section 1.5. However, several experimental findings and observations suggest that the SM is far from complete. For example, the SM does not explain the presence of *gravity*, the *matter anti-matter asymmetry*, and the nature of *dark matter.* In addition to the above limitations of the SM, a few other subtle issues like the *hierarchy problem*, i.e. the vast difference in the mass scales between the SM content ($\sim 10^2$ GeV) and the unification scale or the *Plank scale* ($\sim 10^{19}$ GeV), or the presence of a large number of free parameters, etc. indicate that there must be some *new physics* beyond the standard model *(BSM).*

Few of these mysteries can be answered if we have a deeper understanding of Electroweak Symmetry Breaking (EWSB) and hence the shape of *Higgs potential* (which can be explained by the SM and BSM theories); see Chapter 2. To understand this within the SM of particle physics one has to measure some of the very rare physics processes, for example, *Higgs pair production* will allow measurement of the *trilinear Higgs self-coupling* (λ). Measuring λ is important because it probes the shape of the Higgs potential. A pair of Higgs bosons decay about $\sim 33\,\%$ of the times to $b\bar{b}b\bar{b}$. However, measurement of the $4b$ final sate in di-Higgs production is extremely challenging because of the presence of the overwhelming QCD multi-jet background. Chapter 3 presents a detailed generator level analysis using $\mathrm{HH} \to b\bar{b}b\bar{b}$ channel in the gluon-gluon fusion process for a 100 TeV pp collider. Some BSM theories may modify the Higgs potential resulting in enhanced cross-section of some of the otherwise very rare SM processes. However, predictions from theory models need to be backed by experimental observations. Therefore, many physics analyses that involve BSM searches look for deviations (e.g. excess or deficit in the observed number of events) from the SM predictions. A first estimate on the signal significance of $\mathrm{HH} \to b\bar{b}b\bar{b}$ process and precision of λ measurement for a 100 TeV pp collider with $\mathcal{L} = 30\,\mathrm{ab}^{-1}$ is presented in Sections 3.2 and 3.3 using generator level studies. This concludes the first part.

Majority of the analyses carried out at the LHC experiments involve either measurement of SM processes or searches for new phenomena involving physics BSM. Towards the end of Run2 (2015 - 2018), the LHC managed to collide proton beams at its design centre-of-mass energy of 14 TeV. However, this is not sufficient to explore the extremely rare physics processes. High precision studies require a large amount of physics data covering a wide phase-space region and for this one wants to reach the highest possible collision rate. One way to increase the collision rate is by increasing the beam luminosities. The LHC and its experiments will, therefore, have a major upgrade during the years 2025–2027, after which the proton beams will collide with around 7 times the design luminosity of the LHC (at its maximum possible centre-of-mass energy of 14 TeV). This major upgrade of the LHC is called the *High Luminosity upgrade of the LHC (HL-LHC)* [12], and it will deliver more than ten times the data collected until now in 10 years ($3000\,\mathrm{fb}^{-1}$). Studies are also being conducted for about 4 times larger ($\sim 100\,\mathrm{km}$) circular collider for the post LHC era, i.e. beyond 2040. Three variants of such a *Future Circular Collider (FCC)* [13] are presently being studied with a staged programme, starting with an *electron-positron collider (FCC-ee)*, followed by a *hadron-hadron collider (FCC-hh)* with a possible intermediate stage of an *electron-hadron collider (FCC-eh)*. The hadron-hadron variant of FCC aims to collide proton beams with a centre-of-mass energy of 100 TeV every 25 ns (as baseline) and luminosities of $\sim$ 30 times that of the LHC's designed beam luminosity. A target total integrated luminosity of $\sim 30\,\mathrm{ab}^{-1}$ has been set over $\sim 25-30$ years of its operation. With this, the FCC-hh will not only extend the LHC mass reach for observation of new particles by almost an order of magnitude but also allow for high precision measurements of various observations that would be made at FCC-ee. The ATLAS experiment at the HL-LHC (in Chapter 4), and the baseline experiment at the FCC-hh (in Chapter 5) are described in the second part of this thesis.

On the one hand, increased luminosity (and energy) of the proton beams will allow for collecting more data, thereby, increasing the probability of measuring the elusive physics processes. On the other hand, it poses several challenges to the existing detectors and analyses. One of the main challenges that must be dealt with due to very high beam luminosities is a huge amount of *pile-up*. Around 200 (1000) pile-up collisions are expected along the beam (z)-axis in a length of $\pm 10\,\text{cm}$ for HL-LHC (FCC-hh) experiments. As a result, the final-state objects from the hard collisions get superimposed with hundreds to thousands of soft hadrons from the pile-up. Since pile-up biases the kinematics of the final-state objects from the hard collisions (due to superimposition of soft hadrons), pile-up also has a huge impact on the trigger system of an experiment. A trigger system that satisfies the reduced data rate requirement (from 40 MHz to $\mathcal{O}(10)$ kHz) by making a smart selection of interesting events at the very first stage of a trigger system is needed. Coarse granularity calorimeter information is being used until now for making trigger decisions in experiments like ATLAS and CMS. Although calorimeters have a very good energy resolution and particle identification feature, they generally lack a good pointing resolution to point the calorimeter jets to a particular vertex. The effect of a vast pile-up (~ 1000) in the FCC-hh environment on calorimeter jets (leading to substantial rise in the trigger thresholds) obtained by emulating a calorimeter with specifications similar to the baseline detector design of FCC-hh is presented in Section 5.4. Chapter 6 briefly discusses the various steps involved in the most commonly used track reconstruction algorithms in HEP experiments. Ideally, charged particle tracks that provide excellent momentum and pointing (vertex) resolution can be used to make a very efficient selection of the desired signal events. Track triggers are on the wish-list of many high rate experiments; track reconstruction being the most complex, computationally expensive and time-consuming parts of object reconstruction, cannot be used at the very first trigger level.

This thesis proposes a track trigger for very high rate experiments – called the *Triplet Track Trigger (TTT)* – that can be used at the very first trigger level. The TTT concept uses a very simple and fast track reconstruction algorithm that can be implemented in hardware, for example, an FPGA. Geometrically, it consists of a stack of three closely spaced highly granular pixel detector layers at large radii ($\sim 1\,\text{m}$), called a detector triplet. Typically a TTT gap-size (between the layers of the triplet) of around 20 to 40 mm is chosen. Charged particles traversing such a detector triplet in a uniform magnetic field make a circular trajectory in the transverse plane and a straight line in the longitudinal plane. A detailed description of the TTT concept is given in Chapter 7. Full Geant4 simulations and track reconstruction with the TTT for the ATLAS Inner Tracker at HL-LHC (*ATLAS setup*) and FCC-hh baseline tracker geometry (*FCC setup*) have been performed in this regards and detailed in Section 7.3. Simulation studies using five different TTT gap-sizes are presented for the FCC setup. An optimal gap-size is chosen by comparing the tracking performances.

The third part of the thesis contains three different chapters. In Chapter 8, the results of the TTT tracking performance, i.e. reconstruction efficiency, track purity and track parameter resolution, using the modified ATLAS (in HL-LHC) and FCC-hh tracker geometries are presented. In the ATLAS setup, the TTT tracking performance is also compared with the offline quality tracks obtained with the official ATLAS simulation and track reconstruction framework (*ATHENA*). Chapter 9 gives a detailed description of TTT trigger performance studies and the corresponding results for the FCC setup using an average pile-up of 1000. Very good momentum and z-vertex resolution allow grouping of TTT tracks into several bins along the beam-axis. The TTT tracks can be clustered into 'TTT-jets' – parallelly in several z-bins – and from the TTT-jet momentum, the z-bin containing the hard collision vertex can be identified. The additional z-vertex information (that calorimeters cannot provide), allows for substantial pile-up suppression at a very early stage of event reconstruction. As a result, the TTT can be used to efficiently trigger events involving different kinds of final-state signatures (e.g. isolated tracks, mono-, di- and multi-jets), even in a very high pile-up environment. In particular, the focus is kept on signal events with multi-jet signatures, for example, HH → $b\bar{b}b\bar{b}$ physics channel that can be triggered efficiently using four jets. A rough estimate on the signal significance for HH → $b\bar{b}b\bar{b}$ using the TTT after accounting for trigger inefficiencies is presented in Section 9.5. Finally, Chapter 10 presents a summary of the important results of this thesis.

Part I

Motivation

1

Theory

This chapter discusses some of the underlying theory concepts serving as a basis to understand the following chapters better. It starts by introducing the *Standard Model (SM)* of particle physics in Section 1.1, where a brief description of its particle content, together with a short mathematical formulation on electroweak and strong interactions is given. The SM of particle physics is currently the best description of the subatomic world; however, it does not explain the complete picture. Some fundamental questions that the SM cannot answer and possible physics searches within SM and Beyond Standard Model (BSM) at future hadron colliders are discussed in Chapter 2. The intricacies of *hadron-hadron collisions* at collider experiments – with focus on simulation of proton-proton (pp) collisions – is presented in Section 1.2. Section 1.3 gives an introduction to *jets* (which is one of the most crucial objects in particle physics, both concerning theory and experiment) and their clustering algorithms at hadron colliders. In particular, the importance of jets arising from b quarks and some of their peculiar characteristics that help tag them is also discussed. A few basic parameters concerning hadron colliders, for example, beam *luminosity* and *pile-up* are reviewed in Section 1.4. Finally, Section 1.5 briefs about the different Higgs production mechanisms and its decay channels at hadron colliders.

1.1 The Standard Model of Particle Physics

Formulated in the 1970s, the Standard Model (SM) [1–4] of particle physics is the best theory till-date that describes the most fundamental building blocks of the universe. Based on *Quantum Field Theory (QFT)*, it beautifully explains how the elementary particles of matter interact using a set of mathematical equations. It represents a fundamental step in an attempt to unify the four fundamental forces that govern the laws of nature, namely the *strong*, the *electromagnetic*, the *weak*, and the *gravitational* force (although it explains only the first three of them). The particle content of the SM is composed of two different kinds of particles, namely, the elementary particles of matter, called the *fermions* (particles with a half-integral spin that obey Fermi-Dirac statistics) and the mediators that govern their interactions, called the *bosons* (particles with an integral spin that obey Bose-Einstein statistics).

Quarks and *leptons*, including their anti-particles, constitute the fermionic sector and appear in three different *generations*:

$$\begin{aligned}\text{quarks}: &\begin{pmatrix}u\\d\end{pmatrix}\ \begin{pmatrix}c\\s\end{pmatrix}\ \begin{pmatrix}t\\b\end{pmatrix}\\ \text{leptons}: &\begin{pmatrix}\nu_e\\e^-\end{pmatrix}\begin{pmatrix}\nu_\mu\\\mu^-\end{pmatrix}\begin{pmatrix}\nu_\tau\\\tau^-\end{pmatrix},\end{aligned}$$

where u, d, c, s, t, and b stands for the *up, down, charm, strange, top* and *bottom* quarks, while ν_e, ν_μ, and ν_τ denote the three different flavours of electrically neutral leptons (called neutrinos) for the corresponding charged counterparts, namely, the *electron (e^-), muon (μ^-),* and *tau (τ^-).* The anti-particles are omitted for simplicity. The charged leptons carry an integral electric charge ($-1|e|$), while quarks carry fractions of electric charge, with the up-type quarks (u, c, t) having an electric charge of $+2/3|e|$ and the down-type quarks (d, s, b) having an electric charge of $-1/3|e|$. Here $|e| \approx 1.602 \times 10^{-19}$C represents the elementary electric charge of an electron. The corresponding anti-particles of these fermions possess the same mass, same lifetime but opposite electric charge. Unlike the leptons, quarks do not exist as free particles and always form bound states due to *quark confinement* called *hadrons.* The hadrons are of two different types, namely, the *baryons* that are combinations of three quarks or anti-quarks, and the *mesons* that are combinations of quark anti-quark pairs.

The gauge bosons (having integral spin) and the scalar boson (massive spin 0 particle, i.e. the Higgs boson) together constitute the bosonic sector of SM particles. The gauge bosons consist of the massive: W^+, W^- and Z^0 bosons responsible for weak interactions, and the massless: photons (γ) and the eight gluons (g) that mediate the electromagnetic and the strong interactions, respectively. The Higgs boson [14–16] is an excitation of the Higgs field and plays a unique role in the SM, by explaining why other elementary particles are massive.

The fundamental interactions between the SM particles are based on the theory of *local gauge invariance*, i.e. the assumption that the Lagrangian doesn't change under a set of gauge transformations which are space-time dependent.
The simplest example of an abelian (i.e. commutative) gauge theory, which is invariant under local phase transformations of the group $U(1)$ is *Quantum Electrodynamics (QED).* QED explains the interaction of charged fermions with its gauge field, i.e. the electromagnetic field via the exchange of a massless mediator, the photon (γ). In QED, the gauge principle generates an interaction between the charged fermion and the gauge field. In other words, the local gauge invariance requires the introduction of an additional term to the Lagrangian of the Dirac fermion, which is linear in the gauge field (A_μ).

The *electroweak sector* of the SM is explained by extending the gauge principle to non-abelian (non-commutative) groups $SU(2) \otimes U(1)$. The electroweak theory (discussed in more detail in Section 1.1.1) on its own does not assign masses to the fermions and the bosons. Mass terms can be included via the mechanism of *spontaneous symmetry breaking*, which is introduced in Section 1.1.2. The *Brout-Englert-Higgs (BEH)-mechanism* introduced in Section 1.1.3, spontaneously breaks $SU(2) \otimes U(1)_\mathrm{Y}$ to $U(1)_\mathrm{QED}$ and generates masses for the $W^{\pm}$, and Z^0 bosons.[1] Besides, it makes the inclusion of fermionic mass terms possible and predicts the existence of a massive scalar particle, called the *Higgs boson*.

The fundamental theory of strong interactions, known as *Quantum Chromodynamics (QCD)*, requires the Lagrangian to be invariant under local $SU(3)_{\mathrm{C}}$ transformations. A brief introduction to QCD is presented in Section 1.1.4.

To summarise, the SM is a gauge theory in which the Lagrangian describing it is invariant under the symmetry group $SU(3)_{\mathrm{C}} \otimes SU(2) \otimes U(1)_{\mathrm{Y}}$, which describes the strong, weak and the electromagnetic interactions, via the exchange of spin-1 gauge fields: the eight massless gluons and one massless photon, respectively, for the strong and electromagnetic interactions, and the three massive bosons, $W^{\pm}$, and Z^0, for the weak interaction [17].

1.1.1 Electroweak Theory

The electroweak theory is a gauge-invariant QFT based on the symmetry group $SU(2) \otimes U(1)$, which describes both the electromagnetic and the weak interactions. Unlike the electromagnetic force which acts over large distances (scaling inversely with the square of the distance), the weak force acts over very short distances $\sim \mathcal{O}(10^{-18}\mathrm{m})$ at the electroweak scale ($\gtrsim 100\,\mathrm{GeV}$). It is about 10 million times weaker than the electromagnetic force. All the fundamental fermions (both quarks and leptons) are subject to weak interactions that are mediated by the charged and the neutral weak bosons, namely, $W^{\pm}$, and Z^0 boson. They can be classified by the quantum numbers of the weak isospin I, I_3, and the weak hypercharge Y and are related to the electric charge Q by:

$$Q = I_3 + \frac{\mathrm{Y}}{2}. \tag{1.1}$$

In weak interaction, the *left-handed* fermions appear in *doublets*, while their *right-handed* counterparts appear in *singlets*. The left- and the right-handed fermion chiralities interact differently with the massive gauge bosons, i.e. only left-handed (right-handed) fermions (anti-fermions) couple to the W boson whereas the Z boson couples differently to the left- and the right-handed fermions (depending on the hypercharge). Besides, the Z bosons couplings to the neutrino involve only left-handed chiralities (since Q $=0$ and $I_3 = 0$ for the right-handed neutrino implies Y $= 0$). The left- and the right-handed chiralities can be obtained by applying the corresponding projection operators L and R to the fermion fields:

$$L \equiv \frac{(1-\gamma^5)}{2}, \; R \equiv \frac{(1+\gamma^5)}{2}, \tag{1.2}$$

where $\gamma^5 = i\gamma^0\gamma^1\gamma^2\gamma^3$. [2]

---

[1] Note that the subscripts Y, QED, and C used in this section, correspond to the weak hypercharge, electromagnetic charge and the colour charge, respectively.

[2] Note that in this chapter, the gamma matrices (also known as the Dirac matrices) are often indicated as γ^μ, where μ signifies the space-time components of a four-vector ($\mu = 0, 1, 2, 3$). Besides, few other notations, for example, ∂_μ denotes the partial derivative w.r.t. x^μ, i.e. $\frac{\partial}{\partial x^\mu}$ and D_μ similarly represents the covariant derivative. The product of the Hermitian conjugate of field ψ ($\psi^\dagger$) with γ^0 is denoted by $\overline{\psi}$, i.e. $\overline{\psi} \equiv \psi^\dagger\gamma^0$.

Considering a single family of quarks for simplicity, with fields

$$\psi_1(x) = \begin{pmatrix} u \\ d \end{pmatrix}_L, \quad \psi_2(x) = u_R, \quad \psi_3(x) = d_R, \tag{1.3}$$

the free Lagrangian can be written as:

$$\mathscr{L}_0 = \sum_{j=1}^{3} i\,\overline{\psi}_j(x)\,\gamma^\mu\,\partial_\mu\,\psi_j(x). \tag{1.4}$$

Note that the following discussion also holds for the leptonic fields that can be obtained by replacing u by ν_e and d by e^- in Equation 1.3. $\mathscr{L}_0$ is invariant under the global transformation in flavour space:

$$\begin{aligned} \psi_1(x) &\to \psi_1'(x) \equiv \exp\{iy_1\beta\}U_L\psi_1(x), \\ \psi_2(x) &\to \psi_2'(x) \equiv \exp\{iy_2\beta\}\psi_2(x), \qquad (1.5) \\ \psi_3(x) &\to \psi_3'(x) \equiv \exp\{iy_3\beta\}\psi_3(x), \qquad (1.6) \end{aligned}$$

where U_L denotes the $SU(2)_L$ transformation that acts only of ψ_1:

$$U_L \equiv \exp\left\{i\,\frac{\sigma_i}{2}\,\alpha^i\right\} \qquad (i = 1, 2, 3). \tag{1.7}$$

The parameters y_i, called hypercharges, are analogous to charge in QED and σ_i are the Pauli matrices. Requiring $\mathscr{L}_0$ to be invariant under local $SU(2)_L \otimes U(1)_\mathrm{Y}$ gauge transformation, $\alpha^i \to \alpha^i(x)$ and $\beta \to \beta(x)$, calls for the partial derivatives to be replaced by the covariant derivatives:

$$\mathscr{L} = \sum_{j=1}^{3} i\,\overline{\psi}_j(x)\,\gamma^\mu\,D_\mu\,\psi_j(x), \tag{1.8}$$

$$\text{with} \qquad D_\mu \equiv \partial_\mu + i\,g\,\frac{\sigma_i}{2}\,W_\mu^i + i\,g'\,\frac{\mathrm{Y}}{2}\,B_\mu. \tag{1.9}$$

Four different gauge bosons (W_μ^i associated with the isospin triplet and B_μ associated with Y) are introduced in the covariant derivative – with g and g' being the $SU(2)$ and $U(1)$ coupling constants – since there are four gauge parameters, $\alpha^i(x)$ and $\beta(x)$; see Reference [17] for more details. The physical field responsible for charged current interaction (with $W^\pm$ as mediators) is given by a linear combination of W_μ^1 and W_μ^2:

$$W_\mu^\pm \equiv \frac{W_\mu^1 \mp i\,W_\mu^2}{\sqrt{2}}. \tag{1.10}$$

Similarly, the physical fields for neutral current gauge bosons Z^0 and photon are given by a linear combination of W_μ^3 and the weak hypercharge field B_μ:

$$Z_\mu \equiv W_\mu^3\,\cos\theta_W - B_\mu\,\sin\theta_W, \tag{1.11}$$

$$A_\mu \equiv W_\mu^3\,\sin\theta_W + B_\mu\,\cos\theta_W, \tag{1.12}$$

where θ_W is the Weinberg angle (or weak mixing angle). The Lagrangian also includes higher power of gauge fields implying self-interaction between the gauge fields.

Note that the gauge symmetry forbids the introduction of a mass term for the gauge bosons. Fermionic masses are also not included, as they would communicate the left- and right-handed fields, which have different transformation properties, and therefore would produce an explicit breaking of the gauge symmetry [17].

1.1.2 Spontaneous Symmetry Breaking

Long before the experiments determined the masses of the $W^{\pm}$ and the Z bosons, it was known that they were massive from the fact that weak interactions are of finite range. As mentioned before, the mechanism of spontaneous symmetry breaking introduces mass terms for the gauge bosons and the fermions, while softly breaking the $SU(2) \otimes U(1)_{\mathrm{Y}}$ symmetry. To understand this, let's consider a complex scalar field ϕ with a $U(1)$ symmetry, i.e. $\phi(x) \rightarrow \phi'(x) \equiv e^{i\,\theta}\phi(x)$, where θ is a constant and hence a global parameter, independent of space-time. The Lagrangian of this field is invariant under the above global $U(1)$ transformation and is given by:

$$\mathscr{L} = \partial_\mu \phi^\dagger\, \partial^\mu \phi - V(\phi), \qquad V(\phi) = \mu^2\, \phi^\dagger\, \phi + \lambda\, (\phi^\dagger\, \phi)^2, \tag{1.13}$$

with a mass term μ and a positive quartic coupling λ describing the potential $V(\phi)$.

In QFT, the ground state is the vacuum; thus for $\mu^2 > 0$, a unique vacuum exists that is symmetric under $U(1)$ phase rotations. $V(\phi)$ has the form of a parabola and is sketched in Figure 1.1(a). For $\mu^2 < 0$, the field $\phi = 0$ describes a local maximum (an unstable point), and the (stable) minima are found by evaluating:

$$\frac{\partial^2 V(\phi)}{\partial \phi^2} = \mu^2 + 2\,\lambda\, \phi^\dagger\, \phi = 0. \tag{1.14}$$

This implies, $\phi^\dagger\, \phi = \frac{-\mu^2}{2\lambda}$ and hence degenerate minima exist, i.e. there are multiple states with the same minimum (vacuum) energy:

$$|\phi_0| = \sqrt{\frac{-\mu^2}{2\,\lambda}} \equiv \frac{v}{\sqrt{2}} \implies \phi_0 = \frac{v}{\sqrt{2}}\, e^{i\,\theta}. \tag{1.15}$$

The potential has the shape of a *Mexican hat* in 3D and a sketch of it in 2D is shown in Figure 1.1(b). By choosing a specific solution, for example, $\theta = 0$ as the ground state, the

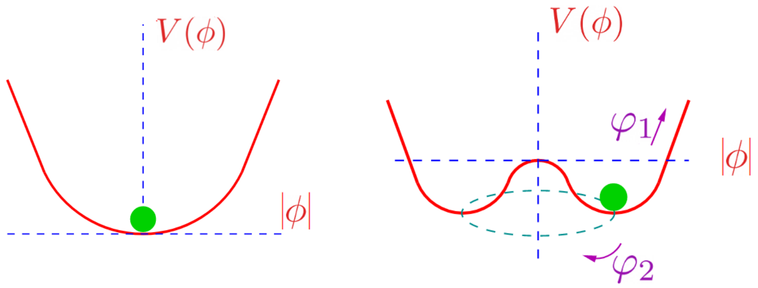

(a) **(b)**

Figure 1.1: Shape of the scalar potential for $\mu^2 > 0$ (a) and $\mu^2 < 0$ (b). A continuous set of degenerate vacua for the later, lying on the ring in the complex plane is indicated by the green dashed circle. It corresponds to the different phases θ connected through a massless field excitation φ_2; Figure adapted from [17].

symmetry gets spontaneously broken. The excitations (other states) can be parametrised with real fields φ_1 and φ_2 around ϕ_0 as:

$$\phi(x) = \frac{1}{\sqrt{2}}\left(v + \varphi_1(x) + i\,\varphi_2(x)\right) \tag{1.16}$$

The Lagrangian in Equation 1.13, thus takes the following form:

$$\mathscr{L} = \frac{1}{2}\partial_\mu(\varphi_1 - i\varphi_2)\partial^\mu(\varphi_1 + i\varphi_2) - \mu^2\phi_0^2 - \lambda\phi_0^4 + \mu^2\varphi_1^2 - \lambda v\varphi_1(\varphi_1^2 + \varphi_2^2) - \frac{\lambda}{4}(\varphi_1^2 + \varphi_2^2)^2, \tag{1.17}$$

with the masses of the fields φ_1 and φ_2 given by:

$$M^2_{\varphi_1} = -\frac{\partial^2\mathscr{L}}{\partial\varphi_1^2}\bigg|_{\varphi_1=\varphi_2=0} = -2\mu^2 \tag{1.18}$$

and

$$M^2_{\varphi_2} = -\frac{\partial^2\mathscr{L}}{\partial\varphi_2^2}\bigg|_{\varphi_1=\varphi_2=0} = 0. \tag{1.19}$$

From Figure 1.1(b), one can see that the excitations with energies same as the ground state energy lie along a flat ring in the potential and costs no energy (which explains the presence of a massless field φ_2). In other words, if a Lagrangian is invariant under a continuous symmetry group G, but the ground state is only invariant under a subgroup $H \subset G$, then there must exist massless spin-0 particle (Goldstone boson) for each generator in G that does not belong to H (also known as the Goldstone theorem).

1.1.3 Higgs Mechanism

The above solution hasn't fixed the mass problem, but at first look, it made it worse by introducing the massless Goldstone bosons. Adding explicit mass terms in the Lagrangian would lead to divergences; hence the problem is solved by introducing an isospin doublet with $SU(2)$ symmetry:

$$\phi(x) \equiv \begin{pmatrix}\phi^+(x)\\ \phi^0(x)\end{pmatrix}. \tag{1.20}$$

and with weak hypercharge Y = 1 chosen so as to give the correct couplings between ϕ and the photon field A_μ. Requiring local gauge invariance under the $SU(2)_L \otimes U(1)_\mathrm{Y}$ group yields a gauged scalar Lagrangian of the Goldstone model similar to Equation 1.13:

$$\mathscr{L}_S = (D_\mu\phi)^\dagger D^\mu\phi - \mu^2\,\phi^\dagger\phi - \lambda\,(\phi^\dagger\phi)^2, \qquad \mu^2 < 0, \quad \lambda > 0, \tag{1.21}$$

with the covariant derivative same as defined in Equation 1.9 for $Y = 1$. As seen in the previous section, requiring $\mu^2 < 0$, and $\lambda > 0$ yields an infinite number of degenerate states with minimum energy given by:

$$|\phi_0| = \frac{1}{\sqrt{2}}\begin{pmatrix}0\\ v\end{pmatrix}, \qquad v = \sqrt{\frac{-\mu^2}{\lambda}}. \tag{1.22}$$

By selecting a particular ground state, the $SU(2)_L \otimes U(1)_\text{Y}$ is spontaneously broken to the electromagnetic subgroup $U(1)_\text{QED}$. The Goldstone theorem then implies, the presence of three massless states.[3] By parametrising the scalar doublet with four fields $\theta^i(x)$ and $h(x)$ as:

$$\phi(x) = \exp\left(i\,\frac{\sigma_i}{2}\,\theta^i(x)\right)\frac{1}{\sqrt{2}}\begin{pmatrix}0\\ \upsilon + h(x)\end{pmatrix}, \tag{1.23}$$

the local gauge freedom can be used to set a unitary gauge, $\theta^i(x) = 0$, which yields:

$$\phi(x) = \frac{1}{\sqrt{2}}\begin{pmatrix}0\\ \upsilon + h(x)\end{pmatrix}. \tag{1.24}$$

Thus, the local invariance of the Lagrangian in $SU(2)_L$ allows getting rid of the three fields $\theta^i(x)$ that would be the massless Goldstone bosons. Inserting this in the kinetic part of $\mathscr{L}$ yields:

$$(D_\mu\phi)^\dagger D^\mu\phi = \frac{1}{2}\partial_\mu h\,\partial^\mu h + (\upsilon+h)^2\left(\frac{g^2}{4}W_\mu^\dagger W^\mu + \frac{g^2}{8\,\cos^2\theta_W}Z_\mu Z^\mu\right). \tag{1.25}$$

The masses of the W and the Z bosons can be obtained similar to Equation 1.18, and are given by:

$$M_Z\,\cos\theta_W = M_W = \frac{1}{2}\upsilon g. \tag{1.26}$$

Thus, spontaneous symmetry breaking that gives rise to the three massless Goldstone bosons, are sort of eaten up by the three real fields which then acquire masses as given by Equation 1.26. Notice that γ remains massless owing to the unbroken $U(1)_\text{QED}$ symmetry. The latest measured values for the masses of W and Z bosons are $M_W \approx 80.379 \pm 0.012$ GeV and $M_Z \approx 91.187 \pm 0.0021$ GeV [18]. M_W and M_Z allow determination of the electroweak mixing angle with $\sin^2\theta_W = 1 - \frac{M_W^2}{M_Z^2} \approx 0.2234$ [18].[4]

From Equation 1.23, one can see that a new scalar filed $h(x)$ corresponding to the Higgs boson (H) has been introduced in $\mathscr{L}_S$. Expanding the Higgs potential $V(\phi)$ to higher order yields:

$$\mathscr{L}_H = \frac{1}{2}\partial_\mu h\,\partial^\mu h - \lambda\,\upsilon^2\,h^2 - \lambda\,\upsilon\,h^3 - \frac{\lambda}{4}h^4, \tag{1.27}$$

and the Higgs mass is then given by:

$$M_H^2 = -\left.\frac{\partial^2\mathscr{L}_H}{\partial h^2}\right|_{h=0} = 2\,\lambda\,\upsilon^2 \implies M_H = \sqrt{2\,\lambda}\,\upsilon. \tag{1.28}$$

---

[3] Note that there are three generators of $SU(2)$, commonly knows as the well known Pauli matrices $\sigma_i,\ i = 1, 2, 3$.

[4] Note that an independent estimate on $\sin^2\theta_W$ can be obtained from the decay of $\mu^- \to e^-\,\overline{\nu}_e\nu_\mu$ via the exchange of W^-. The momentum transfer involved is $q^2 = (p_\mu - p_{\nu_\mu})^2 = (p_e + p_{\nu_e})^2 \ll M_W^2$ and hence the W propagator can be approximated through a local four-fermion interaction which depends on the Fermi coupling constant G_F. The electroweak scale (or υ) is directly determined using G_F and is given by $\upsilon = \left(\sqrt{2}\,G_F\right)^{-1/2} = 246\,\text{GeV}$.

The Higgs mass is experimentally determined to be $M_H = 125.10 \pm 0.14\,\mathrm{GeV}$ [10, 11, 18]. Similarly, a Yukawa coupling between the Higgs boson and the fermions gives the fermion masses:

$$M_f = c_f \frac{\upsilon}{\sqrt{2}}, \tag{1.29}$$

where c_f are independent parameters (known as Yukawa coupling constants) that can be different for different fermions.

1.1.4 Quantum Chromodynamics

Quantum Chromodynamics (QCD) is a gauge theory describing strong interactions. Historically, the origin of strong force lies in nuclear physics, when questions arose about what kept the positively charged protons bound together with the neutrons inside the nucleus of an atom without repulsion. Yukawa proposed the theory of strong, attractive force between the protons and the neutrons that is due to the exchange of a meson (called the pion). Soon afterwards a large number of hadrons were discovered. Gell-Mann introduced a structure based on fundamental particles called quarks and gluons to organise all the discovered particles w.r.t. their mass, electric charge, and strangeness (property of a particle that is conserved in strong interactions but not in weak interactions). This explanation made it clear that a strong force mediated by gluons holds the quarks together.

As mentioned before, hadrons are sub-divided into two different types, namely, mesons that are bound states of a quark and an anti-quark, and baryons that are bound states of three quarks or anti-quarks. An additional quantum number, called the *colour charge* was introduced for quarks to solve the problem of baryons (which is a fermion) composed of three quarks with parallel spin and no relative angular momentum (thereby, violating Pauli's exclusion principle). The quarks exist in three different colour states, and all the observable states are colourless, which implies that free quarks cannot be observed in nature. This is also known as *quark confinement*. However, measurements of the proton structure functions show that at very high energies, the partons (quarks and gluons) behave as free particles but are strongly bound otherwise. This is the so-called *asymptotic freedom* in QCD.

QCD is a gauge theory based on the symmetry group $SU(3)_C$ with colour as the charge associated to it. If q_f^α be the quark field (triplet) of colour α and flavour f, the free Lagrangian that is invariant under the global $SU(3)_C$ transformations in colour space is given by:

$$\mathscr{L}_0 = \sum_f \overline{q}_f \left(i\gamma^\mu \partial_\mu - m_f\right) q_f \tag{1.30}$$

$$\ni q_f^\alpha \to (q_f^\alpha)' \equiv U^\alpha_\beta\, q_f^\beta, \qquad UU^\dagger = U^\dagger U = 1, \qquad \text{and} \qquad \det U = 1 \tag{1.31}$$

with the transformation matrix:

$$U = \exp\left(i\frac{\lambda^a}{2}\theta_a\right). \tag{1.32}$$

There are eight generators associated with $SU(3)_C$ denoted by λ^a (a = 1, 2, ...,8) that are commonly known as the Gell-Mann matrices, and θ_a are arbitrary parameters. The Gell-Mann matrices are 3×3 traceless matrices and satisfy the commutation relation: $[\lambda^a, \lambda^b] = 2i\, f^{abc}\, \lambda^c$, where f^{abc} are the $SU(3)_C$ structure constants. Requiring local gauge invariance of the Lagrangian such that $\theta \to \theta(x)$, calls the need for additional gauge fields (i.e. eight different gluons $G^\mu_a(x)$) to be added to the regular derivative to obtain the covariant derivative:

$$D^\mu \equiv \partial^\mu - i\, g_s \frac{\lambda^a}{2} G^\mu_a(x) \equiv \partial^\mu - i\, g_s G^\mu(x) \tag{1.33}$$

The field-strength tensor for the gluon fields can be written as:

$$G^{\mu\nu} = \partial^\mu G^\nu - \partial^\nu G^\mu - i\, g_s\, [G^\mu, G^\nu], \tag{1.34}$$

and the QCD Lagrangian reads as follows:

$$\mathscr{L}_{\text{QCD}} \equiv -\frac{1}{4}\text{Tr}[G^{\mu\nu}G_{\mu\nu}] + \sum_f (i\, \bar{q}_f\, \gamma^\mu\, \partial_\mu q_f + g_s\, \bar{q}_f\, \gamma^\mu\, G_\mu\, q_f - m_f\, \bar{q}_f\, q_f). \tag{1.35}$$

The QCD Lagrangian explains the colour interaction between the quarks and the gluons and that quarks can emit gluons. Besides, it also contains a term for the cubic and quartic interaction between the gauge fields (*gauge self-interaction*) with a unique coupling g_s (called the strong coupling constant) due to the non-commutative nature of the $SU(3)$ group. However, the presence of asymptotic freedom at high energies and quark confinement at low energies suggests that we cannot understand both the energy regimes with a single universal constant g_s. At high energies (or small length scales), the QCD coupling becomes relatively small, and thus the asymptotic behaviour allows for a perturbative calculation of strong interactions. The computation of perturbative corrections, however, involves divergent loop integrals. Examples of Feynman diagrams showing contributions from higher order loops that may lead to infinities at high energy are shown in Figure 1.2. Like in electroweak theory, these divergences must be dealt with by a redefinition of fields and couplings, which is known as *renormalisation.* A dynamic coupling known as the QCD *running coupling* α_s is introduced with a scale parameter μ that allow for loop corrections from gluon self-interactions leading to vanishing coupling strength at high energies. In other words, the gauge self-interactions of the gluons spread out the QCD charge, thereby, generating an *anti-screening* effect.[5] The asymptotic freedom is weakened linearly with the number of flavours due to fermion loops (shown in the gluon self-energy diagram to the right in Figure 1.2).

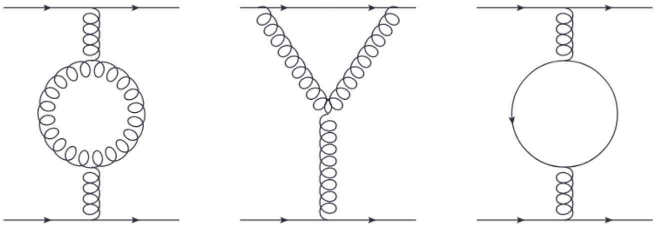

Figure 1.2: Feynman diagrams contributing to the renormalisation of the strong coupling.

---

[5] Note that, such an effect does not take place in QED as the photons do not carry any electric charge unlike gluons that carry a colour charge.

1.2 Hadron-Hadron Collision

Smashing particles at high energies, like those available at various particle colliders, greatly help scientists to unravel the mysteries of the universe and in particular to test the SM of particle physics. Hadron collisions at high energies involve scattering between the constituents of the hadrons (gluons, quarks and anti-quarks), which carry only a fraction of the collider centre-of-mass energy. The initial states are, therefore, not defined, and most interactions occur at relatively low energy, generating a very large background of uninteresting events. These scattering processes at high energy colliders can be classified either as hard or soft based on the momentum transfer (Q^2) between the scattered partons. QCD is the underlying theory for all such processes; however, some additional concepts are necessary to make meaningful predictions for the final state of such processes.

The calculation of a physical observable at a hadron collider, for example, the cross-section of a particular process, strongly relies on several concepts. As mentioned before, the coupling strength in QCD is dynamic in nature and becomes negligible at very high energies. As a result, the dynamics of the hard (high energy and short-distance) interactions can be considered separately from the dynamics of the soft (low energy, long-distance) interactions. In other words, hard and soft interactions can be factored into two different parts and considered separately – this is called *factorisation.* For the hard processes, the rates and event properties can be predicted with good precision using perturbation theory. For soft processes, however, the rates and properties are dominated by non-perturbative QCD effects, which are less well understood. A separate prediction based on phenomenological models, describing the transformation of the partons into colourless hadrons is called *fragmentation.* A lattice gauge theory formulated on a grid of points in space-time, called *Lattice QCD* is an example of a non-perturbative approach to solve QCD at low energies numerically [19].

If $\sigma_{pp\to X}$ is the cross-section for an arbitrary final state X produced during pp collisions then:

$$\sigma_{pp\to X} = \int_0^1 \mathrm{d}x_1 \int_0^1 \mathrm{d}x_2 \sum_{ij} f_i(x_1, \mu_F), f_j(x_2, \mu_F)\, \hat{\sigma}_{ij}(x_1 x_2 s, \mu_R), \tag{1.36}$$

where i, j goes over all possible initial state partons, i.e gluon, quark, anti-quark flavours, x_1, x_2 are the momentum fractions of the two partons w.r.t. the initial protons and μ_F and μ_R are the factorisation and the renormalisation scales. The probability of finding a parton i with momentum fraction x_i within a proton is described by the Parton Distribution Function (PDF) $f_i(x_i, \mu_F)$. The squared centre-of-mass energy is denoted by s. Perturbative calculations are done for determining the cross-section of the hard process σ_{ij}. Proton being a complex system, the PDFs cannot be calculated from first principles, and differential equations relate different energy scales.

One can simulate such hadron-hadron collisions using Monte Carlo (MC) methods, which provide a procedure to estimate the PDFs through simulation of actual physical processes involved. *Evolution functions* are used to transfer observed PDFs to the scale of new collider experiments. In the case of proton-proton collisions, two partons undergo hard scattering primarily, while the remnants of the initial protons give rise to additional activities, as shown in Figure 1.3. The big red circle indicates the hard scattering (HS) vertex.

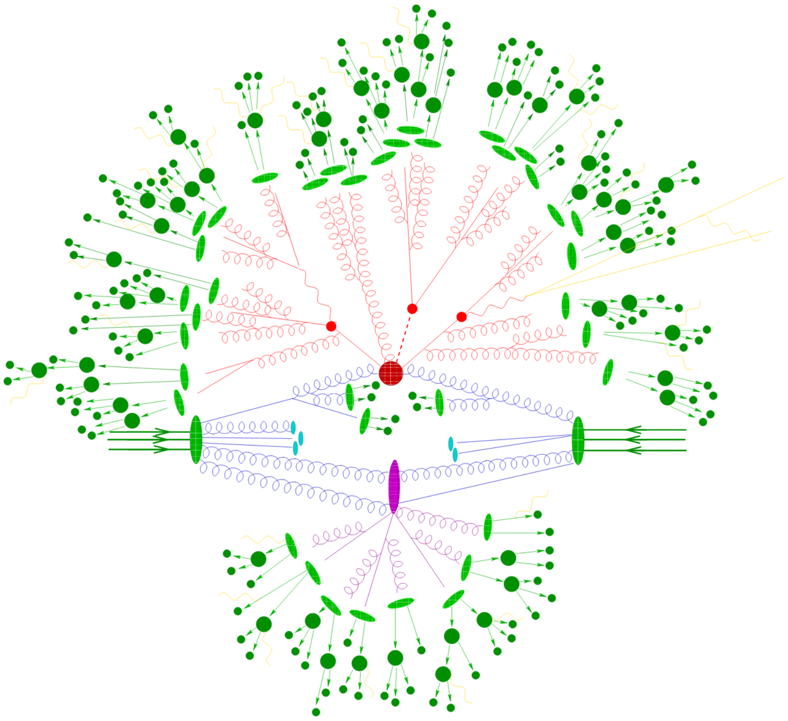

Figure 1.3: Illustration of a pp collision in the case of a $t\bar{t}H$ event. Two partons ($t\bar{t}$) from the incoming protons (large green ellipses) radiate ISR and undergo hard interaction/hard scattering (HS) (big red circle). This follows the decay of the partons along with the produced Higgs boson (small red circles). A parton shower from hard QCD radiation emerges (red) and a secondary interaction from the beam remnants (blue) takes place (purple ellipse) before the final-state partons hadronize (light green ellipses) and the hadrons decay (dark green circles). Electromagnetic radiation (yellow) can be emitted by charged particles at any stage [20].

Additional QCD radiation can be produced, both before and after parton interaction, by gluon splitting ($g \rightarrow gg$, $g \rightarrow q\bar{q}$) or by gluon radiation from quarks ($q \rightarrow qg$, $\bar{q} \rightarrow \bar{q}g$). Depending on the stage at which the radiation is emitted, it is referred to as Initial State Radiation (ISR) or Final State Radiation (FSR). The products from the hard process further emit QCD radiation repeatedly in a chain-like fashion, called *parton shower* (red). The process of *hadronisation* follows parton shower in which the coloured particles ultimately combine to form colourless hadrons (green circles). These primary hadrons finally decay into the so-called *stable* particles, which are eventually detected in the detector. Additional activities in addition to the hard interaction results due to the interaction between the proton remnants (indicated by the purple ellipse). Similar to the hard process, a parton shower followed by hadronisation and decay into stable particles takes place with the only difference that these processes are typically much softer than the hard collisions and are part of the *underlying event*.

1.2.1 Coordinate System

Before proceeding further, the co-ordinate system used in this thesis is described. A right-handed co-ordinate system with its origin at the nominal Interaction Point (IP) of the colliding particles is used;[6] see, for example, Figure 1.4. The positive x-axis points from the IP to the centre of the collider ring, the y-axis points upwards and the z-axis points along the beam pipe of the collider. The azimuthal angle ϕ is measured around the z-axis (beam pipe), with $\phi = 0$ along the positive x-axis and increasing clockwise. The polar angle θ is measured w.r.t. the z-axis. For a particle of momentum $p = (E, p_x, p_y, p_z)$, pseudorapidity is defined as:

$$\eta = -\ln \tan(\theta/2). \tag{1.37}$$

For massive objects the rapidity $y = \frac{1}{2}\ln\left(\frac{E+p_z}{E-p_z}\right)$ is sometimes used instead of the pseudorapidity. Projections of quantities into the $x - y$ plane (transverse plane) are denoted by a subscript T, for instance, $p_\mathrm{T} = \sqrt{p_x^2 + p_y^2}$ denotes the transverse component of the momentum.[7] A distance parameter between two points ($i = 1, 2$) with coordinates (η_i, ϕ_i) in the $\eta - \phi$ plane is defined as:

$$\Delta R = \sqrt{\Delta\eta^2 + \Delta\phi^2}, \tag{1.38}$$

$$\text{where } \Delta\eta = \eta_2 - \eta_1, \tag{1.39}$$

$$\text{and } \Delta\phi = \phi_2 - \phi_1. \tag{1.40}$$

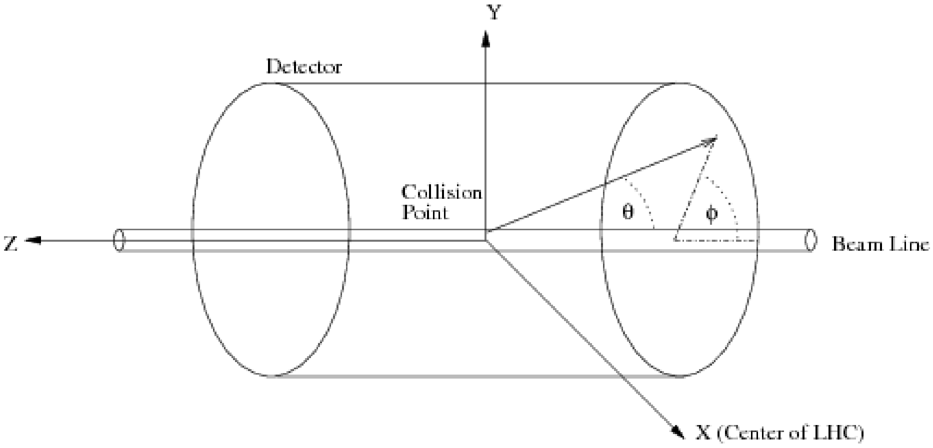

Figure 1.4: Right-handed coordinate system used by the two general purpose experiments at the LHC [21].

1.3 Jets

After hard scattering, quarks and gluons follow a branching process (fragmentation) and then hadronise to form colourless hadrons. A collimated bunch of hadrons (that can be seen as proxies of high energy quarks and gluons) is observed as a characteristic signal in

---

[6] The nominal interaction point is the place designed for the collision to happen inside the detector.

[7] Natural units are used for the measurement of the energy, mass and momentum of particles.

a detector (giving indirect information about the initial partons) and is termed as a *jet.* Jets are involved directly or indirectly in almost all physics analyses.
Studying jets and its properties is crucial for getting an insight into the underlying process of an event, primarily because the events at hadron colliders are dominated by QCD jets.

There are different 'levels' at which jets are used generally and based on this level they are classified as: parton-level jets, particle-level jets, and calorimeter jets. Parton-level jets, as the name suggests involve the kinematics of the partons (before hadronisation) and are generally used in perturbative QCD calculations and are also referred to as *theory jets.* Particle-level jets are formed by clustering a bunch of collimated hadrons (the stable particles) without detector information.[8] Calorimeter jets are clusters of energy deposited by a collimated bunch of hadrons and are purely experimental.[9] Reconstructing individual particles in the shower is unfeasible and, therefore, *jet clustering algorithms* provide a quantitative mapping between the jets (final state hadrons) and the initial partons / hadrons / calorimeter cell deposits. Besides, they must contain a robust jet definition that is stable on all jet levels. The following section discusses the most commonly used jet clustering algorithms.

1.3.1 Jet Clustering Algorithms

There are two different types of jet clustering algorithms, namely, *cone-based* and *sequential recombination* algorithms. A brief introduction to the two types of jet algorithms is given in the subsections below. A successful jet algorithm should fulfil two important requirements:

- Jet algorithms must be *infrared (IR) safe*, that is to say, they should be insensitive to (or robust against) emission of soft particles from the hard partons. Infrared sensitivity is illustrated in Figure 1.5(a), where one can see that additional soft radiation between two jets (right) may cause the merging of the otherwise distinct jets (left), thus, leading to a different set of final state jets. An IR safe jet algorithm will not change the configuration of the jets with the emission of another soft particle.

- Jet algorithms should be *collinear safe*, that is to say, the close angle parton splittings should not affect the jet definition. Figure 1.5(b) illustrates the collinear sensitivity of a cone based jet algorithm which does not construct a jet as no seed was found to pass the threshold due to energy splitting between calorimeter clusters (left) while a jet is found due to the narrow energy distribution in the calorimeter that passes the threshold (right).

In addition to the above two requirements, the jet algorithm should be invariant under boosts and is particularly important for pp (or $p\overline{p}$) collisions where the longitudinal boost of the hard interaction is in general not known. Besides, insensitivity of jet algorithms to higher-order QCD and hadronisation corrections are desirable.

---

[8] Energy resolution effects are generally also included at this level.

[9] In addition to calorimeter jets from real experimental data, they are very often emulated and simulated in order to include real detector effects in phenomenological studies.

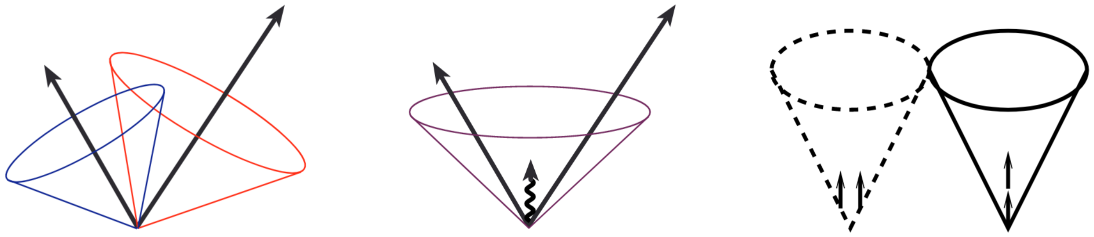
(a) (b)

Figure 1.5: Illustration of infrared sensitivity (a) and collinear sensitivity (b) of cone cone algorithm jets. The arrows represnt the seeds used for constructing jets and the length of the arrows are proportional to their energies [22].

Cone Algorithms

Cone algorithms are generally based on the idea of defining a jet as an angular cone around the direction of dominant energy flow. These dominant energy flow directions are identified by some particles passing a threshold as 'seeds' that gives a trial direction. New particles whose trajectories lie within a circle of fixed radius defined by Equation 1.38 in the $\eta - \phi$ plane are associated with the initial seed (trial cone), and the sum of their 4-momenta sets the new direction of the cone. The procedure is iterated using the new cone as seed until a stable cone is found. This is based on the so-called Snowmass scheme [23].

The need to define seeds for an iterative procedure to find stable cones introduces infrared and collinear unsafety. For example, this procedure might result in overlapping cones such that particle energies are shared between different jets. In such cases, the particles in the overlap region are assigned to the jet whose direction vector in the $\eta-\phi$ plane is closest, or the jets are merged depending on the shared momentum fraction w.r.t. p_{T} of the highest p_{T} jet. Several refinements of the simplest cone algorithm have been done to improve the infrared safety of the cone algorithms. A rather recent development from 2007, known as the Seedless Infrared-Safe Cone (SISCone) jet algorithm [24] is a seedless cone algorithm that is both infrared and collinear safe. It uses a non-iterative approach and finds all possible cones (these are defined by the radius and a pair of particles on the boundary) for a given radius . Next, the stability of the cones is checked by requiring the centroid (weighted with the p_{T} of the particles) to be within the cone radius, and finally, the final jets are selected using a spit-merge method (for details, refer to Reference [24]).

Sequential Recombination Algorithms

The sequential recombination algorithms are based on a measure of how likely it is for two partons to arise from a QCD splitting. These algorithms are therefore infrared and collinear safe by construction. At first, the distance between all possible combinations of the input particles i, j (partons or calorimeter cell energy deposits) and their distance

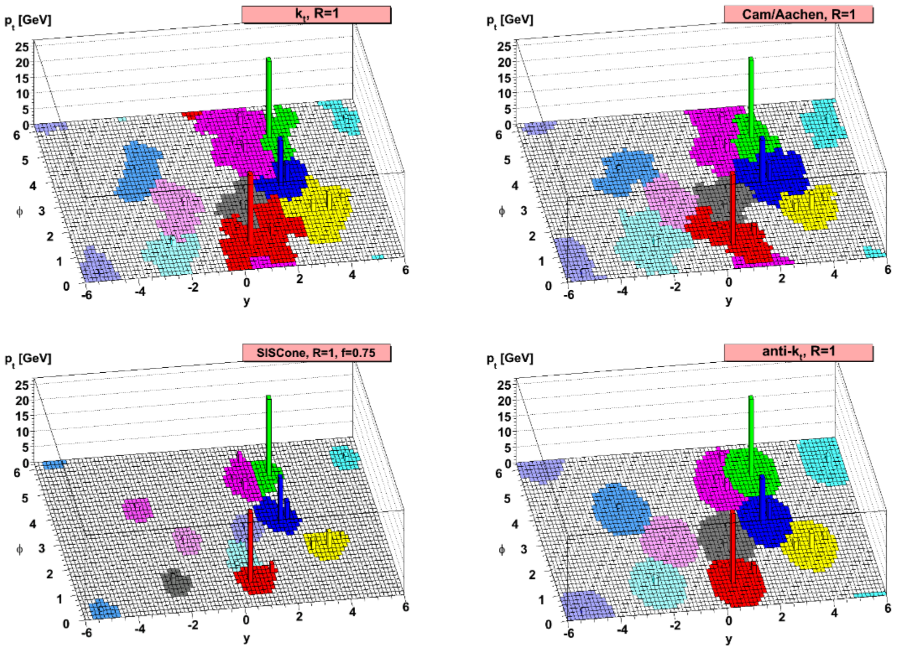

Figure 1.6: Comparison of active area of the hard jets obtained using several jet reconstruction algorithms with radius parameter $R = 1.0$. The different colours correspond to different jets. Many random soft particles are overlaid to highlight the boundaries of the jets [27].

w.r.t. the beam is determined using:

$$d_{ij} = \min\left(k_{t,i}^{2p}, k_{t,j}^{2p}\right) \frac{\Delta R_{ij}^2}{R^2}, \tag{1.41}$$

$$\text{and} \quad d_{iB} = k_{t,i}^{2p}, \tag{1.42}$$

where k_t denotes the transverse momentum, ΔR_{ij} is the distance parameter between two objects i, j defined in Equation 1.38 and R is the jet radius parameter (typically chosen to be 0.4 for small radius jets and 1.0 for large radius jets). p is an additional parameter that provides a distinction between different recombination algorithms. There are three most commonly used recombination algorithms, namely, k_t [25] ($p = 1$), Cambridge/Aachen [26] ($p = 0$), and anti-k_t [27] ($p = -1$) algorithms. If the smallest of all the d_{ij}'s is less than the beam distance d_{iB}, the two objects i and j are combined to form a *proto-jet*. On the contrary, if the smallest d_{ij} is greater than d_{iB}, the object i is removed from the list of objects and tagged as a final jet. Next, the distances are re-calculated, and the above procedure is repeated until no objects are left.

In the past, cone-based jet algorithms were preferred over sequential recombination algorithms as the latter suffered from a poor computational performance. Over the years, much more efficient implementation of the recombination jet algorithms, for example, in FASTJET package [28] based on `C++`, has made them the first choice for jet clustering in hadron collider experiments. From amongst the most commonly used recombination algorithms, the anti-k_t jet clustering algorithm gives the best performance (and is also the one used in this thesis). From Figure 1.6 one can see that the jet areas as a result of anti-k_t algorithm are more regular in the $\eta-\phi$ plane. This is an advantage from the experimental point of view, both for jet energy calibration and subtraction of underlying event and pile-up (defined in Section 1.4.3). The boundaries of k_t and Cambridge/Aachen jets are sensitive to soft radiation, although the ordering to cluster soft and collinear branchings first, with the high p_{T} particles clustered only at the end allows an easier interpretation of jet substructure in terms of QCD.

1.3.2 b-Jets

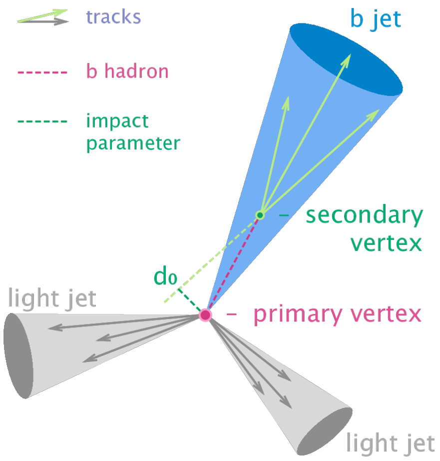

Figure 1.7: Schematic explaining b-jet identification [29]. The distinct nature of b-jets (blue) in comparison to the jets arising from other light quarks or light-jets (grey) is illustrated. A peculiar characteristic of b-jets is the presence of displaced tracks with a secondary vertex as shown in the blue coloured jet.

Many of the physics analyses carried out at High Energy Physics (HEP) experiments contain physics signals that lead to final states with jets arising from heavy flavour quarks. For example, the Higgs boson predominantly ($\sim 58\,\%$) decays into a $b\bar{b}$ pair (see Section 1.5). Also, top quarks dominantly decay into a W boson and a b quark. Moreover, some BSM-models, predict some heavy resonances decaying to a pair of heavy quarks, for example, $Z' \to t\bar{t}$, $Z' \to b\bar{b}$. Identifying jets originating from the hadronisation of heavy quark flavours (especially those from b-quarks) is, therefore, crucial for precision measurements of various SM processes and new physics searches BSM.

At hadron colliders, a b quark hadronises into a b-flavoured hadron (B-hadron). The B-hadrons have distinct properties that allow for tagging them differently from other jets as '*b-jets*'. Some of these properties include, for instance, their relatively large lifetime of $\sim 1.5\,\mathrm{ps}$ that allows them to travel a measurable distance from the IP before they decay, which leads to displaced tracks forming secondary vertices. Formation of the secondary vertex (due to decay of a B-hadron) at a distance away from the primary vertex is shown in Figure 1.7.[10] Another interesting feature is that their high mass also leads to decay

---

[10] The hadrons produced from c quarks also tend to have lifetimes of around a picosecond. This means that the C-hadrons can also travel far enough to give a secondary vertex and displaced tracks. As a result, c-jets are easily misidentified as b-jets. More advanced techniques, for example, the use of

products with larger p_T (relative to the jet axis) than the ones typically found in light-jets. Besides, the heavy hadrons have a relatively higher branching ratio for semi-leptonic decays. Hence the presence of soft leptons (high track multiplicities) in the jets serves as another tool for tagging b-jets. There are different kinds of b-tagging algorithms that make use of one or more of the distinct characteristics of the b-jets. Some of the b-tagging algorithms used in the two general-purpose LHC experiments are given in Reference [30].

The B-hadron generally decays after about a centimetre at the LHC with a centre-of-mass energy of 13 TeV [31]. At a 100 TeV hadron collider, this distance is expected to be several 10′s of centimetres; see Reference [32], where a simulation study for a 100 TeV hadron collider shows that more than 50 % of the B-hadrons with $0.5\,\mathrm{TeV/c} < p_\mathrm{T} < 5\,\mathrm{TeV/c}$ decay after a distance of 10 cm. Thus, tagging a b-jet requires excellent track vertex resolution (especially in the transverse plane) to clearly identify the secondary vertex produced due to B-hadron decay.

1.4 Collider Physics and Pile-up

At hadron colliders, pp collisions occur when two bunches of protons are smashed together (also called Bunch Crossing (BX)) to maximize the collision probability between protons every time they are smashed. A beam of these bunches with a certain bunch spacing between them is accelerated to high energies by the particle colliders to attain very high centre-of-mass energies before they are smashed. The physics processes that are of great interest to us have cross-sections that are several orders $\sim \mathcal{O}(11-15)$ of magnitude smaller than the total pp cross-section. The probability of a hard interaction of a certain physics process (hard process) to occur depends on the centre-of-mass energy of the colliding protons and the beam luminosity. Some of the frequently used useful collider parameters are introduced in the sub-sections below.

1.4.1 Luminosity

Luminosity (L) is one of the most important parameters characterizing the performance of a particle accelerator. It is a measure of the number of collisions produced per cm^2 per second. The luminosity for a collision of two (bunched) beams with Gaussian profiles with an RMS of σ_{ix} (σ_{iy}) for $i = 1, 2$ in horizontal (vertical) direction is given by:

$$\mathsf{L} = \frac{N_1 N_2 f_\mathrm{rev} N_\mathrm{b}}{2\pi\sqrt{\sigma_{1x}^2+\sigma_{2x}^2}\sqrt{\sigma_{1y}^2+\sigma_{2y}^2}} \cdot R \cdot W, \tag{1.43}$$

where N_1 and N_2 are the number of particles in the N_b colliding bunches of beam 1 and beam 2, and f_rev is the frequency of revolution around the collider ring.[11] The factors R and W are introduced to account for the reduction in luminosity due to a final crossing angle of the two beams and the transverse offset at the IP, respectively. For approximately

---

boosted decision trees with additional kinematics allow rejecting c-jets in b-tagging algorithms.

[11] The bunch lengths are assumed to be equal in Equation 1.43.

equal transverse beam sizes, i.e. $\sigma_{1x} \approx \sigma_{2x}$, $\sigma_{1y} \approx \sigma_{2y}$, and head-on collision, Equation 1.43 reduces to:

$$\mathsf{L} = \frac{N_1 N_2 f_{\text{rev}} N_{\text{b}}}{4\pi\sigma_x\sigma_y}. \tag{1.44}$$

$\sigma_{x(y)}$ depends on the transverse emittance ϵ and the β function (which describes the focusing properties of the accelerator at the IP):

$$\sigma_{x(y)} = \sqrt{\epsilon_{x(y)}\beta_{x(y)}}. \tag{1.45}$$

The emittance is a measure of the beam′s average spread in position and momentum space. It has units of length (or length × angle) and is determined by the initial conditions at the injector alone. From Equation 1.44, one can see that large beam luminosities require transverse beam sizes (hence β) as small as possible, in addition to a large number of particles per bunch for fixed f_{rev} and N_{b}. The β function at the IP is minimized using strong focusing quadrupole magnets.

The integral of the delivered luminosity over time is called the integrated luminosity ($\mathcal{L}$):

$$\mathcal{L} = \int \mathsf{L} \mathrm{d}t. \tag{1.46}$$

It gives a measure of the total collected data size and is expressed in inverse of cross-section, i.e. fb^{-1} or pb^{-1}.

1.4.2 Event Rate

Physics analyses aiming to measure specific hard processes involve measurement of the total number of events observed for that process. The expected number of events per unit time (event rate) for a given process with cross-section σ_{event} is directly proportional to the instantaneous luminosity and is given by:

$$\frac{\mathrm{d}N}{\mathrm{d}t} = \sigma_{\text{event}} \cdot \mathsf{L}. \tag{1.47}$$

Therefore, the total number of expected events is determined by:

$$N = \sigma_{\text{event}} \cdot \underbrace{\int \mathsf{L} \mathrm{d}t}_{\text{integrated luminosity}}. \tag{1.48}$$

1.4.3 Pile-up – The real enemy

Higher the rate of *pp* collisions higher are the chances of measuring interesting hard processes. There are several ways in which one can increase the collision rate of the protons, for instance, by increasing the number of protons per bunch or by improving the beam optics so that the beams are better focalised at the IP. The net effect of increasing the collision rate results in several *pp* collisions occurring simultaneously in a single BX. The overall final-state observed by the detectors is therefore not just the collision involving the highest momentum transfer (hard collision) but a superposition of several other soft collisions primarily consisting of low energy QCD processes. These additional soft collisions are referred to as pile-up [33], and the events with these pile-up collisions are often referred to as minimum bias events. The average number of interactions per bunch crossing ($\langle\mu\rangle$) depends on the instantaneous luminosity (L), the inelastic pp scattering cross-section (σ_{inel}), the number of colliding bunches (N_{b}) and the revolution frequency (f_{rev}):

$$\langle\mu\rangle = \frac{\mathsf{L}\cdot\sigma_{\text{inel}}}{N_{\text{b}}\cdot f_{\text{rev}}}. \tag{1.49}$$

In practice, the actual number of interactions in a given BX fluctuates following a Poisson distribution around its average $\langle\mu\rangle$.

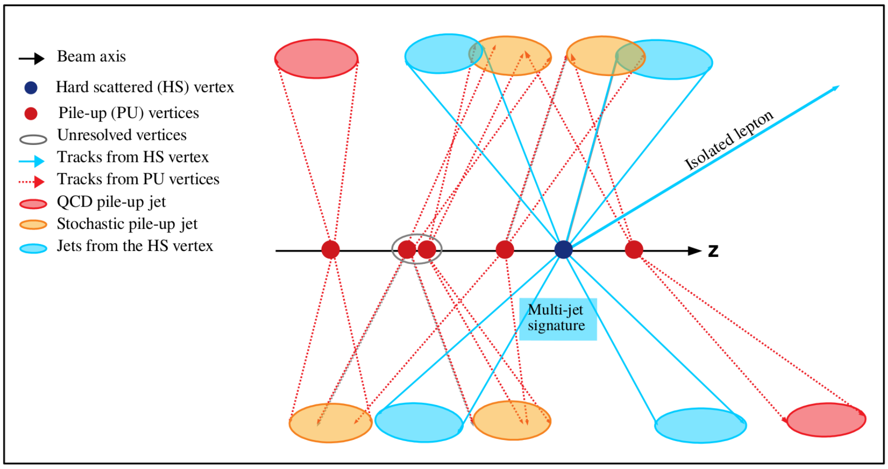

Figure 1.8: Illustration of a pp Bunch Crossing (BX) event, with one hard scattering (HS) vertex (dark blue circle) and five pile-up vertices (red circles). Particle tracks are indicated using arrows and jets from particles originating from various collision vertices are shown using a cone. For simplicity, most particles within the jet cone are omitted unless necessary. The objects resulting from the HS vertex are shown in light blue while those resulting from pile-up vertices are shown in red and orange.

A large number of soft final-state particles from the pile-up collisions essentially complicates the reconstruction of the hard scattered event itself. This is because final-state particles from pile-up consist of a large number of soft hadrons spread all over a detector. Amongst the different objects that are reconstructed by a detector, jets are probably the most affected by pile-up, although they are not the only ones. Reconstructed jets involving pile-up contributions from a single BX are termed as pile-up jets or more specifically in-time pile-up. In addition to in-time pile-up, out-of-time pile-up refers to the final-state contributions from previous and following bunch crossings w.r.t. the triggered event [34].[12] Figure 1.8 illustrates a BX between two proton bunches along the beam-axis resulting in a hard interaction (dark blue circle) and five soft (pile-up) collisions (red circles). Pile-up jets can be categorised as:

---

[12] Note that only in-time pile-up are considered in the results presented in this thesis. Out-of-time pile-up generally contributes to stochastic jets (see below), which can be removed to a large extent by using pile-up mitigation techniques.

- *QCD pile-up jets* (see the red ellipses), i.e. the jets that stem mostly from the particles originating from a single QCD process occurring in a single pile-up interaction, and
- *stochastic jets* (orange ellipses), i.e. the jets that stem from particles originating from different interactions in the event, without a single prevalent source.

One can see how the jets (hence hadrons) from pile-up, overlap with those from the hard collision. This means that when jets are reconstructed, energy deposits in the calorimeter from the former will be clustered together with the energy deposits from the later. Properties of the hard jets (e.g. p_T, η, and ϕ) are therefore biased by these extra energy deposits coming from the pile-up. Reconstruction of many other objects is affected due to very large pile-up. For example, reconstruction of leptons and photons usually involves an isolation criterion, i.e. a condition on the hadronic activities in the surrounding of the lepton/photon. Due to enormous pile-up, the hadronic activity around the lepton/photon increases, thereby resulting in reconstruction inefficiency. Similarly, missing transverse energy which requires reconstruction of the transverse momentum of all the measured objects in the event is also affected. Another consequence of pile-up, which is more subtle is pile-up fluctuations that result in smearing of reconstructed quantities and distributions, affecting the jet energy resolution. This is because of the fluctuation of the actual number of pile-up events around the mean ($\langle\mu\rangle$), which then results in fluctuation of the final-state hadronic activity from one minimum bias collision to another. The resolution of missing transverse energy will similarly degrade due to the fluctuation of the overall pile-up activity.

Thus, pile-up biases and smears the quantities reconstructed from the final-state of the hadron collisions, with the latter resulting in a degradation of the resolution [33]. Therefore, the effects of pile-up must be mitigated as far as possible as they often contribute significantly to the systematic uncertainties in analyses. Impact of pile-up due to a very large pile-up of ~ 1000 is discussed in Chapter 5. Its effect on physics analyses and the need for pile-up mitigation techniques at trigger level is highlighted. Results based on the use of tracks (and hence jets reconstructed from tracks) to suppress pile-up in real-time is discussed in Chapter 9 of this thesis.

1.5 Higgs production and its decay channels

The production of Higgs bosons at hadron colliders can occur via various production modes. The leading order Feynman diagrams for the most dominant production processes are shown in Figures 1.9(a-d). These include the process of gluon-gluon fusion (ggF), vector-boson fusion (VBF), Higgs-strahlung (VH) and associated production with top quarks ($t\bar{t}H$). Higgs boson production via gluon-gluon fusion is mainly mediated by the exchange of virtual, heavy top quarks. Although loop suppressed, the ggF production mode has the largest cross-section of $\sim 46.8\,\mathrm{pb}$ at N3LO for $\sqrt{s} = 13\,\mathrm{TeV}$ [35]. This dominance of Higgs production via ggF results due to the fact that the loop suppression is balanced out by the large Yukawa coupling to the heavy quark. Loop contributions from other light quarks are suppressed with the square of the quark masses (M_q^2). In the VBF production mode, scattering of a pair of quarks ($q\bar{q}$) is mediated by a pair of virtual weak bosons (W, Z), which fuse together to radiate a Higgs boson. The scattered quark gives rise to two back-to-back hard jets in the forward rapidity regions of a detector. Besides, gluon radiations from the central-rapidity region are strongly suppressed because of the colour singlet nature of the weak-gauge boson exchange. These features of the VBF process are used to distinguish them from the otherwise overwhelming QCD background more efficiently than the other production modes. The next sub-dominant Higgs production processes include its production in association with a gauge boson ($pp \to VH$, where $V = Z$ or W), and top quark pairs ($pp \to t\bar{t}H$). These associated productions of Higgs boson with other particles allow for determination of the Higgs coupling with the later. At $\sqrt{s} = 100\,\text{TeV}$, the cross-section of the $pp \to t\bar{t}$ process increases significantly (by around a factor of 50) compared to that at $\sqrt{s} = 14\,\text{TeV}$ [36]. The VH processes increase only by around a factor of 10. As a result, $t\bar{t}H$ will be the next dominating process at 100 TeV following ggF and VBF. Other rare production modes include associated Higgs boson production with: a pair of gauge bosons (VVH), and a single top quark.

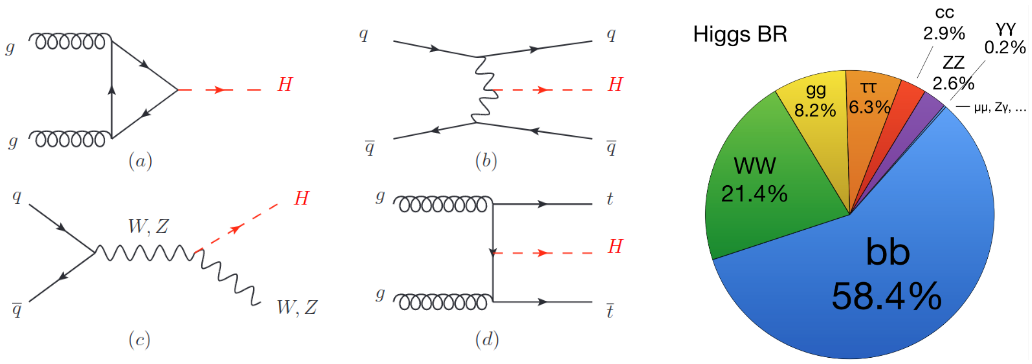

(a-d) **(e)**

Figure 1.9: Leading order Feynman diagrams contributing to Higgs production in (a) gluon-gluon fusion, (b) vector-boson fusion, (c) Higgs-strahlung (or associated production with a gauge boson), and (d) associated production with top quarks [37]. The decay channels of a Higgs boson with a mass of $\sim 125\,\text{GeV}$ is also shown(e) [38].

At tree level, the Higgs boson can decay into a fermion anti-fermion and vector boson pair. It tends to decay into the heaviest fermions and gauge bosons allowed due to the linear rise of the Yukawa coupling with the fermion mass. The 125 GeV Higgs discovered is too light to decay to a pair of top quarks ($M_t \approx 172.8\,\text{GeV}$). Therefore, it decays predominantly ($\sim 58\,\%$ of all) into a pair of the next heaviest quark, which is the bottom quark ($M_b \approx 4.2\,\text{GeV}$). The tau lepton with a mass of $\sim 1.8\,\text{GeV}$, and the charm quark with a mass of $\sim 1.5\,\text{GeV}$ are the next among the fermion-antifermion pairs that the Higgs bososn decays into. Its direct coupling to $\gamma\gamma$, $Z\gamma$ and gg is prohibited (photon and gluon being massless) and an indirect coupling is induced by loops of heavy charged particles. The branching ratios of the possible decay channels of the SM Higgs boson are shown in Figure 1.9(e) using a pie diagram. Although the $H \to b\bar{b}$ decay channel is the most dominant, the $b\bar{b}$ final state is difficult to detect due to huge QCD jet backgrounds in hadron-hadron collisions (leading to complicated detection techniques). The cleanest and easy to detect channels include those involving photons or leptons in the final state, for example, $H \to \gamma\gamma$ and the vector boson channels further decaying into two charged lepton anti-lepton pairs.

2

Physics at Future Hadron Colliders

After the discovery of the Higgs boson at the LHC, CERN in the year 2012, particle physicists around the world are now trying to address the next big question: “where is new physics?”. Although the Higgs boson completed the last missing piece of the SM of particle physics, additional particles and interactions must extend the SM to explain, for example, the abundance of matter over antimatter, the striking evidence for dark matter and the non-zero neutrino masses. Theoretical issues such as the hierarchy problem, or more in general, the apparent fine tuning that stabilizes the mass of the Higgs boson at the EW scale, likewise point to the existence of physics Beyond Standard Model (BSM).

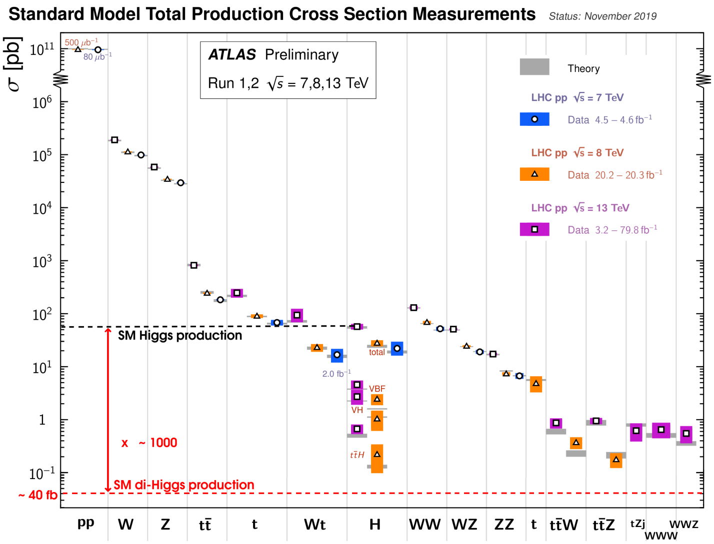

Figure 2.1: Summary of several Standard Model total cross-section measurements, corrected for branching fractions, compared to the corresponding theoretical expectations; adapted from Reference [39].

Figure 2.1 summarizes several SM total production cross-section measurements made by the ATLAS experiment at the LHC compared to the corresponding theoretical expectations [39]. The luminosity used for each measurement is indicated close to the data point.

So far the measured cross-sections are close to the SM expectations with no signs of abundance/deficit and hence new physics. Clearly, due to limited statistics and energy reach, many of the rare SM processes either have large uncertainties or are yet to be measured. For instance, Higgs pair production at $\sqrt{s} = 14\,\text{TeV}$ has a production cross-section of only $\sim 40\,\text{fb}$ which is 1000 times smaller than the measured single Higgs production cross-section. One way to increase the rate of the rare processes is to increase the luminosity of the colliding beams and thereby increase the collision probability. The HL-LHC with this goal, will collide proton bunches with $\sim$ 7 times higher luminosity, totalling to an integrated luminosity of $\sim 3\,\text{ab}^{-1}$ over a period of 10 years; see Chapter 4. Another way to increase the rate of the rare SM processes is to increase the collision energies of the proton bunches, see Figure 2.2 which shows the total production cross-section of several SM processes as a function of the proton - proton collision energies. The total (inelastic) proton-proton (pp) scattering cross-section increases only marginally from 111 mb to 153 mb (85 mb to 108 mb) when increasing $\sqrt{s}$ from 14 TeV to 100 TeV. However, the cross section for several SM processes increase more strongly, especially for jet and top-quark production. By increasing $\sqrt{s}$ to 100 TeV, a gain by more than an order of magnitude can be obtained for most of the rare SM processes (see the blue lines indicated in Figure 2.2). With this increase di-Higgs production will become accessible at 100 TeV giving insights about the nature of the Higgs potential. The production of Higgs boson from a pair of

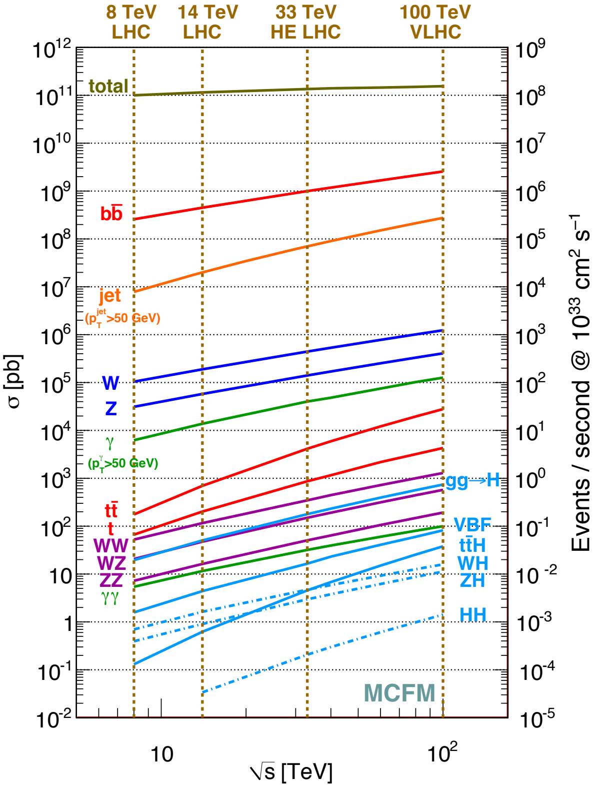

Figure 2.2: Cross-sections of various SM processes as a function of collider center-of-mass energy. The corresponding number of expected events per second is also indicated along the right axis [40].

top quarks ($t\bar{t}H$) increases by even two orders of magnitude. This will allow to study the Higgs-top couplings with greater detail.

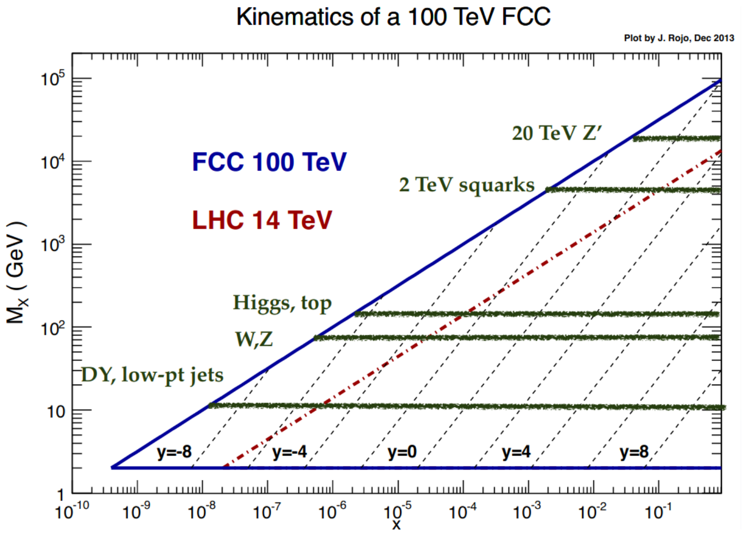

Figure 2.3: Kinematical coverage in the (x, M_X) plane of a $\sqrt{s} = 100\,\text{TeV}$ hadron collider (solid blue line) in comparison to the LHC with $\sqrt{s} = 14\,\text{TeV}$ (dot dashed red line). The dotted black lines indicate regions of constant rapidity (y) [36].

Figure 2.3 shows the mass reach of pp colliders with $\sqrt{s} = 14\,\text{TeV}$ and $100\,\text{TeV}$ in the (x, M_X) plane, where x is the fraction of the proton's momentum carried by the parton and M_X is the final state invariant mass. One can see that the mass reach for a 100 TeV hadron-hadron Future Circular Collider (FCC-hh) is highly extended compared to the LHC, especially in the central rapidity region where BSM particles up to tens of TeV can be produced (with known SM processes accessible in the forward region). Relevant M_X regions for phenomenologically important processes, from low masses (Drell-Yan, low p_T jets), electroweak scale processes (Higgs, W, Z, top), and possible new high-mass particles (squarks, Z') are also shown. Huge kinematical coverage would allow to probe PDF's down to $x \approx 5 \times 10^{-7}$ at forward rapidities. The extreme low x regions will be crucial for tuning of soft and semi-hard physics in Monte Carlo event generators [36].

In this chapter, few of the physics goals that can be addressed by a 100 TeV hadron-hadron Future Circular Collider (FCC-hh) are discussed. In Section 2.4, Higgs pair production is discussed in detail followed by a description on signal and background generation for a simple analysis on Higgs pair production in the $b\bar{b}b\bar{b}$ final sate presented in Chapter 3.

2.1 The Nature of the Higgs Potential

The shape of the Higgs potential ($\mathcal{V}$) is deeply linked to the fundamental question of Electroweak Symmetry Breaking (EWSB) in the early universe ($\sim 10^{-10}$ s after the Big Bang), allowing for a slow 2^{nd} order phase transition in the SM or a strong 1^{st} order phase transition with a modified $\mathcal{V}$. If the phase transition is strongly of 1^{st} order, it will allow one to establish the observed excess of matter over antimatter, and the possible release of detectable gravitational waves generated by the collision of bubbles of the new vacuum during the Big Bang. One of the most important next steps is therefore, to understand the properties of the Higgs boson by directly probing and constraining the couplings of the Higgs boson to the content of the SM. Of particular interest are the couplings of the Higgs boson to itself as the Higgs potential responsible for EWSB in the SM is determined by the triple (λ) and the quartic ($\tilde{\lambda}$) Higgs self-coupling:

$$\mathcal{V} = \frac{1}{2} M_{\mathrm{H}}^2 h^2 + \lambda v h^3 + \frac{\tilde{\lambda}}{4} h^4. \tag{2.1}$$

In Eq. 2.1 h is the Higgs boson field, and $v \approx 246\,\mathrm{GeV}$ is the vacuum expectation value. In the SM, λ_{SM} and $\tilde{\lambda}_{SM}(= M_{\mathrm{H}}^2/2v^2 \approx 1/8)$ are uniquely fixed by knowledge of the Higgs mass $M_{\mathrm{H}} \approx 125\,\mathrm{GeV}$. However, new physics can alter this direct correspondence and therefore, model-independently, the self-couplings λ and $\tilde{\lambda}$ can be probed only by direct measurement of multi-Higgs final states. FCC-hh targets a 5 % precision for the measurement of λ_{SM} (with enhanced precision for BSM scenarios) as compared to $\mathcal{O}(50\,\%)$ precision at the HL-LHC [41]. This 5 % precision, together with the FCC-hh discovery reach for additional particles that could affect the EWSB transition, have been shown to be necessary and sufficient to decide whether the EW phase transition was of strong 1^{st} order or not [41]. Therefore, the Higgs self-coupling λ is one of the benchmark measurements for the future hadron collider experiments. More on extraction of λ with Higgs pair production is discussed in Section 2.4.

2.2 Origin of Dark Matter

Dark Matter (DM) unlike normal matter, does not interact with the electromagnetic field, making its detection extremely difficult. It constitutes around 27 % of the universe, whereas the normal matter comprises only 5 % of the total content in the universe. Its existence has only been inferred from the gravitational effects it would have on the visible matter, for instance, the enormous speed at which galaxies in our universe are rotating, suggests that in the absence of DM the gravity generated by the visible content would have torn them apart a long time ago. A variety of theoretical models that include wide range of scenarios ranging from sub-eV axion particles to the class of heavy black holes (whose merging was recently detected by gravitational wave interferometers), explain the origin of DM. Many of these include the Weakly Interacting Massive Particles (WIMP), the most widely accepted candidates for dark matter. No experiment, at colliders or otherwise, can probe the full range of DM masses allowed by astrophysical observations. However, there is a very broad class of models for which theory motivates the GeV – 10's TeV mass scale, and which therefore could be in the range of FCC [42]. Due to their weak coupling and small production rates, only a fraction of this mass range is within the reach of the LHC [41].

Although DM itself cannot be detected in collider experiments, a large missing transverse energy ($E_{\mathrm{T}}^{\mathrm{miss}}$) associated to the DM particle (e.g. a neutralino within SUSY theory) and disappearing tracks left by the decay of the charged partner (chargino) to the DM and a soft unmeasured charged pion [43], are the typical signatures for DM searches. High p_{T} jet(s) originating from initial state radiation typically provide the means of triggering on such signatures in conjunction with $E_{\mathrm{T}}^{\mathrm{miss}}$. Another simplified model which describes the interactions between the SM partons and the invisible dark sector particles with four basic mediators, viz. scalar, pseudo-scalar, vector and axial-vector particles, allow DM searches using multi-jets [44]. At a 100 TeV collider, the sensitivity to the mediator mass typically extends up to few TeV in comparison to few hundred GeV$'s$ at LHC (for the scalar and pseudo-scalar types) or $>$15 TeV (for the vector and axial-vector types) [45]. Thus the Future hadron Circular Collider would be able to truly probe a large parameter space for a variety of dark sector scenarios.

2.3 Direct Searches for New Physics

Gaining a deeper understanding of the properties of the particles whose existence were confirmed by indirect evidences, required their direct production, for example, direct production of the Higgs boson at the LHC. Although there is no guarantee that a next generation hadron collider will be able to find new particles predicted by many of the BSM theories, it is important to be able to cover a wide phase space region of these BSM scenarios. A 100 TeV circular hadron collider delivering a total integrated luminosity of 30 ab^{-1} would allow discovery of directly produced new particles upto few 10's of TeV. Figure 2.4 shows examples of discovery reach for several new particles using a detector simulation for the baseline detector geometry of FCC-hh [42].[1] These include the Z' gauge boson decaying to SM leptonic and $t\bar{t}$ final states, excited quarks Q^* in models with composite quarks and leptons, and massive gravitons G_{RS} in the case of the warped extra dimensional model of Randall and Sundrum [46]. The gain in the discovery reach by a factor of $\sim$10 increase in luminosity (from 2.5 to 30 ab^{-1}) and by a factor of 3 (from 30 to 100 ab^{-1}), is also shown.

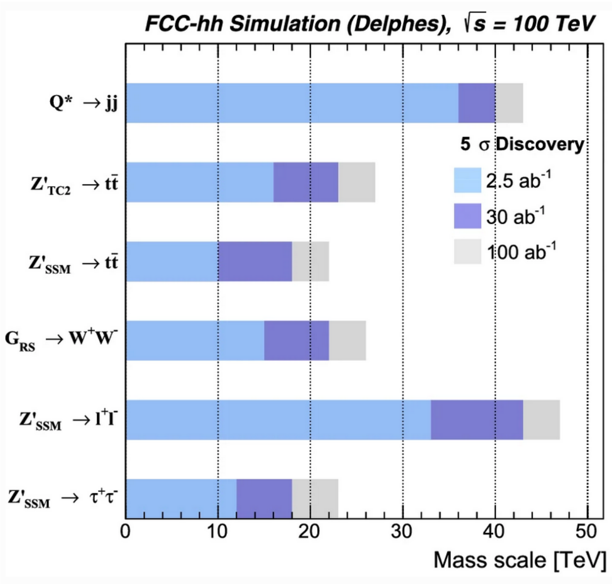

Figure 2.4: FCC-hh mass reach for different s-channel resonances for three different integrated luminosity scenarios [42].

---

[1] The baseline detector geometry is introduced in Chapter 5.

For Z' decaying to a pair of SM leptons, the reach extends to 43 TeV at the ultimate integrated luminosity of $30\,\mathrm{ab}^{-1}$ which is around five times higher than the HL-LHC reach. Similar gain of a factor of five w.r.t. HL-LHC reach have been projected for supersymmetric particles such as squarks, gluinos and stops. Thus, FCC-hh will not only span a very wide parameter space to search or exclude the existing new physics models (the known unknowns), but also hint for resonances not known by any theoretical models.

2.4 Higgs Pair Production

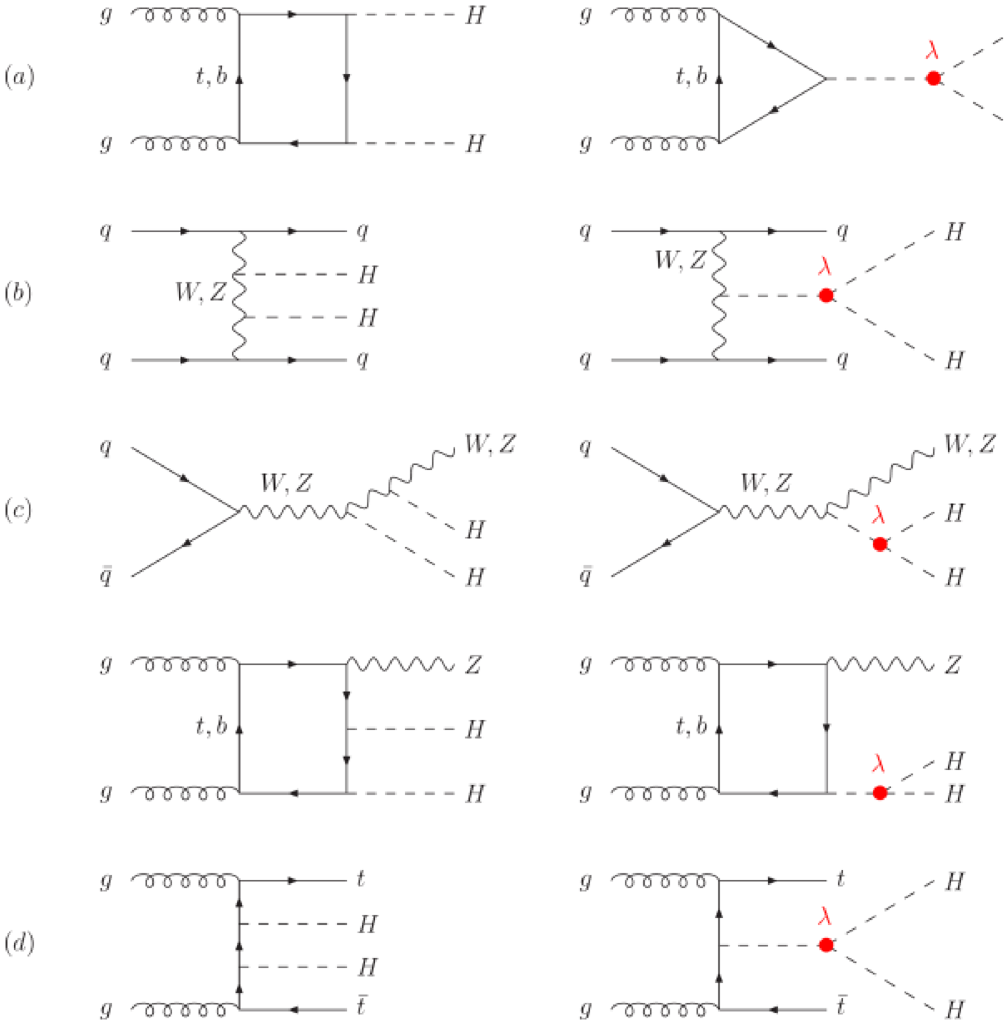

Figure 2.5: Diagrams contributing to Higgs pair production: (a) gluon-gluon fusion, (b) vector-boson fusion, (c) double Higgs-strahlung and (d) double Higgs bremsstrahlung off top quarks. The trilinear Higgs coupling contribution is marked in red [47].

Higgs pair production at high energy colliders will allow direct measurement of λ [48]. At hadron colliders, pairs of Higgs bosons can be produced through different production modes (similar to single Higgs production discussed in Section 1.5): gluon-gluon fusion (ggF), vector-boson fusion, double Higgs-strahlung (or associated di-Higgs production with a gauge boson) and double Higgs bremsstrahlung off top quarks. Examples of the Leading Order (LO) Feynman diagrams are shown in Figure 2.5, with the trilinear Higgs self-coupling marked in red. The corresponding production cross-sections in the SM – to the highest available accuracy – as a function of collider center-of-mass energy ($\sqrt{s}$) is shown in Figure 2.6. The dominant – gluon-gluon fusion – production mode for Higgs pairs is discussed in more detail in the Section 2.4.1. As mentioned earlier, new physics can modify λ_{SM} and therefore, indirect [49–51] and direct limits [52, 53] are set on the ratio (k_λ) of the Higgs boson self-coupling to its SM value where,

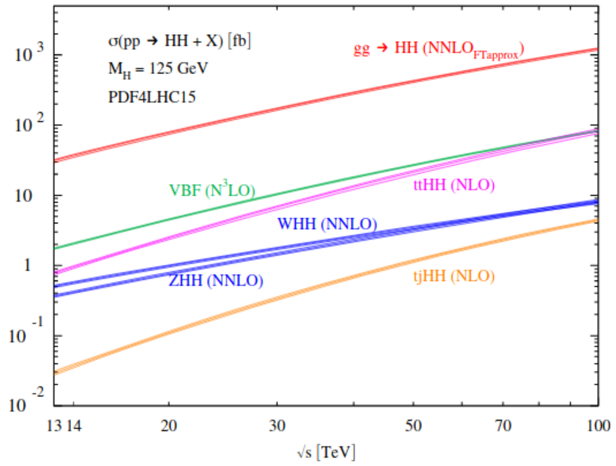

Figure 2.6: Total production cross sections for Higgs pairs within the SM via gluon fusion, vector-boson fusion, double Higgs-strahlung and double Higgs bremsstrahlung off top quarks. The width of the curve shows the total uncertainties originating from the scale dependence and the PDF + α_s uncertainties. Figure from Ref. [47]

$$k_\lambda = \frac{\lambda}{\lambda_{SM}} \tag{2.2}$$

The latest constraint is set by combining the single and the double Higgs production analyses performed with the ATLAS experiment limiting $-2.3 < k_\lambda < 10.3$ at 95 % confidence level [54].

Figure 2.7 shows the branching fractions of the main di-Higgs decay channels assuming SM Higgs boson. In Section 1.5 we saw that the SM Higgs boson has the highest probability ($\sim$ 58 %) of decaying into a $b\bar{b}$ final state. As a result, a pair of Higgs bosons have the largest branching fraction ($\sim$ 33 %) of decaying into the $b\bar{b}b\bar{b}$ final state. However, it suffers from high QCD and $t\bar{t}$ contamination. The HH $\rightarrow b\bar{b}WW$ is the channel with the second highest branching fraction of $\sim$ 25 % and suffers from a large irreducible $t\bar{t}$ background. The branching fraction decreases as one goes down the y-axis diagonally, with HH $\rightarrow \mu^+\mu^-\mu^+\mu^-$, HH $\rightarrow Z\gamma\mu^+\mu^-$, HH $\rightarrow \gamma\gamma\mu^+\mu^-$, and HH $\rightarrow \gamma\gamma\gamma\gamma$ being some of the very rare channels. The channels, HH $\rightarrow b\bar{b}b\bar{b}$ ($4b$), HH $\rightarrow WWb\bar{b}$, HH $\rightarrow b\bar{b}\tau^+\tau^-$, and HH $\rightarrow b\bar{b}\gamma\gamma$, have been identified as the golden channels in di-Higgs production and fulfil the two optimal requirements for a successful search [55]:

- one of the two Higgs bosons decays to a final state containing leptons or photons that are easy to trigger upon, to measure, and hard to fake,
- the other Higgs decays to a $b\bar{b}$ final state in order to maximize the total decay branching fraction.[2]

Therefore, the HH $\rightarrow b\bar{b}\gamma\gamma$ channel is identified as one of the purest di-Higgs decay channels, although has a very low branching fraction ($\mathcal{O}(10^{-3})$).

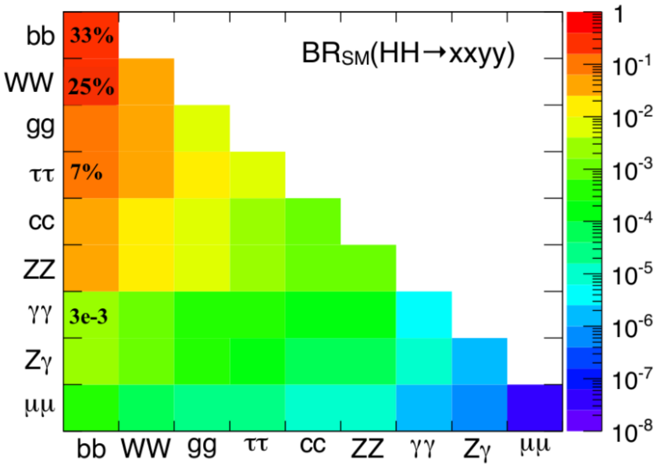

Figure 2.7: Branching fraction of the main di-Higgs decays assuming SM Higgs boson [56].

2.4.1 gluon-gluon Fusion (ggF)

The leading production mechanism for Higgs boson pairs is through loop-induced gluon-gluon fusion (ggF) that is mediated mainly by top quark loops followed by bottom quark loops. Due to the difference of the top quark propagators in the loops, the LO – box and the triangle – Feynman diagrams (see Figure 2.5 (a)) interfere destructively.

Figure 2.8 shows the di-Higgs production cross-section via ggF corrected to Next-to-Next-to Leading Order (NNLO) as a function of k_λ for $\sqrt{s}$ = 14 TeV and 100 TeV. Notice that $k_\lambda = 1$ points to the SM cross-section in Figure 2.8. The di-Higgs cross-section attains a minimum at $k_\lambda \sim 2.5$ beyond which an increase is observed in either direction. Any deviations from the predicted SM cross-section would therefore, hint existence of new physics beyond SM. At 14 TeV, the SM cross-section for HH production via ggF is rather small (∼ 37 fb), corresponding to ∼ 100 k events with an integrated luminosity of 3 ab^{-1} at the HL-LHC. Because of the rapidly growing gluon luminosity at higher energies, the HH production cross-section increases by about a factor of 35 at 100 TeV. With a projected integrated luminosity of 30 ab^{-1} at a 100 TeV hadron collider, about 350 × 100 k Higgs boson pairs will be produced. However, due to limited detector acceptance, trigger rate limitations and particle tagging efficiencies, these numbers will be significantly lower, making its measurement very very challenging. It is however very interesting to examine the

---

[2] Although the $b\bar{b}b\bar{b}$ final state does not satisfy point one, it has numerous other advantages and a generator level analysis for this channel is presented in Chapter 3.

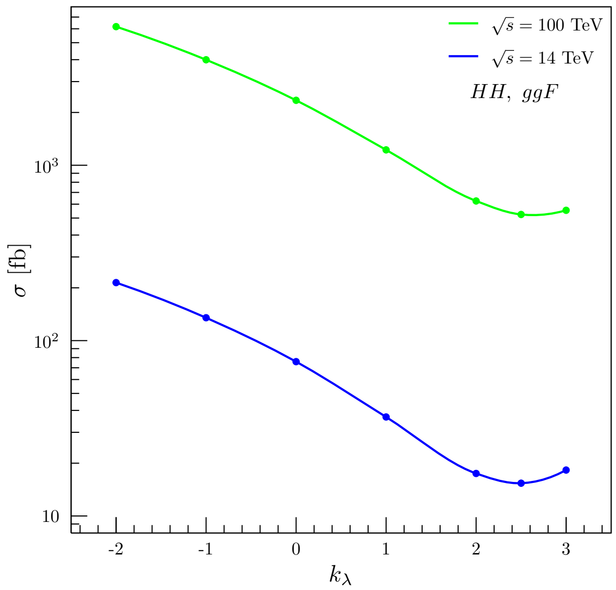

Figure 2.8: NNLO corrected cross-section for Higgs pair production via ggF as a function of k_λ at $\sqrt{s} = 100$ TeV in green and $\sqrt{s} = 14$ TeV in blue. The NNLO correction factors are taken from [47].

effect of varying k_λ on few of the kinematic distributions of the di-Higgs system and their decay products, namely, the invariant mass and the transverse momentum distributions.

The conventions used for the following figures are:

- The leading, sub-leading, 3^{rd} leading and the 4^{th} leading candidates are labelled as 1, 2, 3 and 4 respectively.
- The invariant mass distributions are denoted by the symbol M, subscripted by the candidate(s) whose distribution has been plotted.
- The transverse momentum distributions are denoted by the symbol p_{T}, subscripted by the candidate(s) whose distribution has been plotted.

The invariant mass (M_{HH}) and the transverse momentum ($p_{\mathrm{T,HH}}$) distribution of the di-Higgs system normalised to an integrated luminosity of 30 ab^{-1} at $\sqrt{s} = 100$ TeV for various values of $k_\lambda \in [-2.0, 3.0]$ is shown in Figure 2.9. A sharp cut at 250 GeV is indicative of the minimum mass required for production of a pair of Higgs bosons, each with a mass of 125 GeV. Apart from the increase in the total cross-section with decreasing k_λ in both the distributions, a characteristic dip in the low mass region in the M_{HH} distribution for $k_\lambda > 1$ can be seen. A similar dip in the p_{T} distributions of the leading (H_1) and sub-leading (H_2) Higgs candidates is also observed, see Figure 2.10. This is due to the destructive interference between the triangle and the box diagrams in the ggF production mode with the triangle contribution dominating in the low mass region (see Figure 1.3 from [47]). Neglecting background, this implies that the sensitivity for measuring λ, which comes from the triangle contribution, is much higher in the low mass region as compared to the high mass region. The transverse momentum of the individual Higgs bosons becomes softer for $k_\lambda < 1$ and features a second peak at low transverse momenta for $k_\lambda > 1$. These

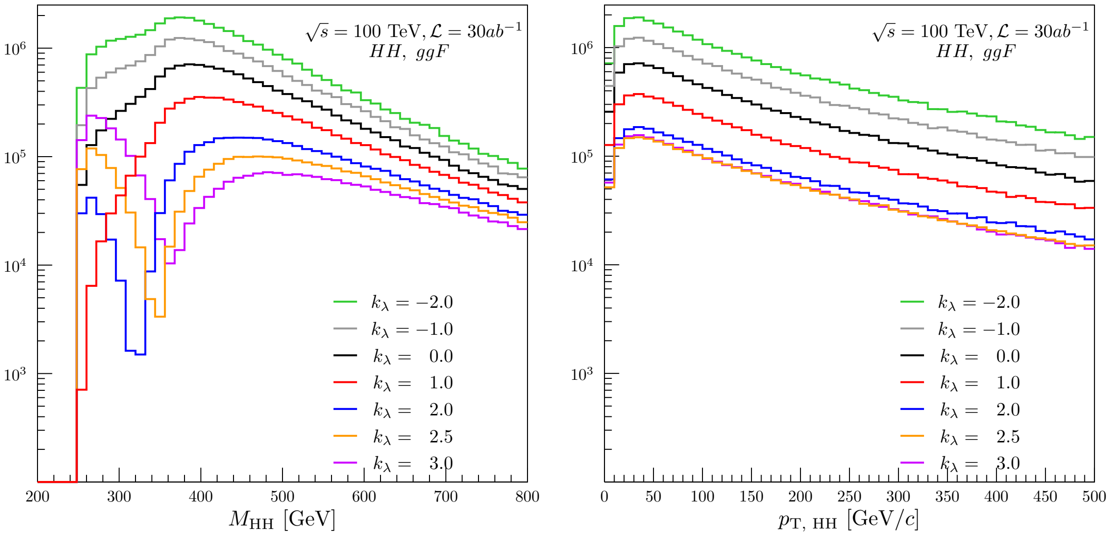

(a) **(b)**

Figure 2.9: Invariant mass (a) and transverse momentum (b) of the di-Higgs system in the gluon-gluon fusion process for different values of k_λ. Both the distributions are normalised to an integrated luminosity of $30\,\mathrm{ab}^{-1}$ for $\sqrt{s} = 100\,\mathrm{TeV}$.

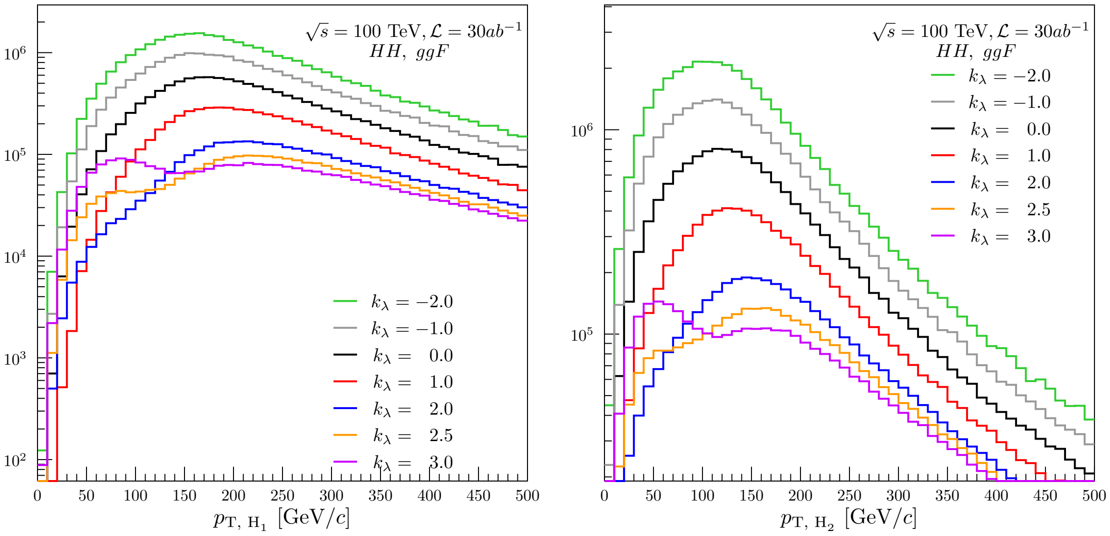

(a) **(b)**

Figure 2.10: Transverse momentum of the leading Higgs - H_1 (a) and the sub-leading Higgs - H_2 (b) in Higgs pair production via gluon-gluon fusion process for different values of k_λ. Both the distributions are normalised to an integrated luminosity of $30\,\mathrm{ab}^{-1}$ for $\sqrt{s} = 100\,\mathrm{TeV}$.

studies suggest that there are a lot of interesting physics in the low p_{T} region $\sim 30 - 80\,\mathrm{GeV/c}$, which should be studied in detail and, therefore, must not be filtered out at trigger level or during event selection. The analysis presented in Chapter 3 assumes 100 %

trigger efficiency.

The following section introduces the signal and the background samples used for the parton level analysis presented in Chapter 3.

2.4.2 Signal and Backgrounds

The LHC proton-proton collisions produce enormous amount of data at a rate of 40 MHz. However, not all of these can be read out and stored for offline analysis at 40 MHz due to various limitations in the experiments (discussed in more detail in Section 5.2). Therefore, experiments like ATLAS and CMS have a trigger system, based on calorimeter jets (calo-jets) to filter and keep only the interesting physics data. The goal of this thesis is to study and evaluate achievable trigger rate reductions in high to very high pile-up environment using the reconstructed tracks in addition to the calo-jets, at the very first trigger level. In particular, the focus is on multi-jet signatures which in the presence of pile-up are difficult to trigger by calo-jets alone. In this context, the Higgs pair production process with the $4b$ final state i.e. $gg \rightarrow \mathrm{HH} \rightarrow (b\bar{b})(b\bar{b})$ is chosen as the signal sample, which also is the most dominant final state in di-Higgs production.

In order to keep the analysis simple for the trigger study, and to get a rough estimate on the sensitivity to measure k_λ, only the irreducible QCD $4b$ multi-jet production, i.e. $pp \rightarrow b\bar{b}b\bar{b}$ is considered as background. Some of the other irreducible background processes that can mimic $\mathrm{HH} \rightarrow b\bar{b}b\bar{b}$ signal process includes the production of a Z boson in association with a pair of b quarks – $Z(\rightarrow b\bar{b})b\bar{b}$, associated single Higgs production with a Z boson – $H(\rightarrow b\bar{b})Z(\rightarrow b\bar{b})$ and associated single Higgs production with a pair of top quarks – $H(\rightarrow b\bar{b})t\bar{t}(\rightarrow b\bar{b})$. The cross-section of these background processes are much smaller than the QCD backgrounds and can, therefore, be neglected [57, 58]. In the case of top quark pair production, only the fully hadronic final states are relevant as the leptonic decays of the top quarks can be removed by requiring a lepton veto. Also, the backgrounds involving top quarks can be efficiently reduced by using the much evolved top quark reconstruction criteria.

There are several additional QCD processes that may contribute as reducible background due to mis-identification of the c-jets and light jets as b-jets, for example, the QCD $2b2j$ and $4j$ production. Although the cross-section of these processes is higher than the QCD $4b$ process, a significant suppression of their cross-section can be achieved by b-tagging, assuming light-jet and c-jet mis-identification rates of $\sim 1\,\%$ and $10\,\%$ as already obtained with the detectors at LHC [59].

Event Generation:

Events for the $gg \rightarrow \mathrm{HH} \rightarrow (b\bar{b})(b\bar{b})$ signal process are generated in two steps. At first, a pair of Higgs via ggF are generated at LO with `MadGraph5_aMC@NLO` [60] 2.6.6. A *Universal FeynRules Output (UFO)* [61] model package HeavyScalar that gives the freedom to modify a wide range of parameters including the parameter k_λ related to the Higgs self-coupling, is used to generate the Les Houches event (lhe) files.[3] k_λ was set to 1.0 for SM HH $\rightarrow b\bar{b}b\bar{b}$ sample production. The NNPDF2.3LO set [62] with strong coupling $\alpha_S(m_Z^2) = 0.119$ interfaced with `LHAPDF6` [63] is used and the factorization and the re-normalization scales are set to $H_\mathrm{T}/2$, i.e. $\mu_F = \mu_R = H_\mathrm{T}/2$ with

$$H_\mathrm{T} \equiv \sum_i^n \sqrt{(M_{\mathrm{T},i})^2 + (p_{\mathrm{T},i})^2},$$

where n is the final-state matrix-element multiplicity, and $M_{\mathrm{T},i}$ and $p_{\mathrm{T},i}$ are the transverse mass and transverse momentum of the i^{th} final-state parton (b quraks in this case) [60]. The latest available (SM) Higgs pair production cross-section at NNLO is listed in Table 1.1 of Reference [47] and is equal to 1224 fb at $\sqrt{s} = 100$ TeV. Therefore, an NNLO/LO K-factor of 1.43 on the LO inclusive cross-section is applied. Following the parton-level event generation, each of the Higgs bosons are made to decay to $b\bar{b}$ and the lhe files are showered with `PYTHIA8` Monte Carlo generator [64] v8.234, using the same PDF set as before and default Monash 2013 Tune [65, 66]. A vertex smearing of $\sigma_z = 57$ mm, $\sigma_{x(y)} = 6.8 \times 10^{-3}$ mm was used at the generator level. The same procedure was used to produce a total of seven different signal samples using seven different values for $k_\lambda = -2.0,\ -1.0,\ 0.0,\ 1.0,\ 2.0,\ 2.5,\ 3.0$.

Generation of the QCD $4b$ background sample is similarly done in two steps. $pp \rightarrow b\bar{b}b\bar{b}$ events at LO were produced using `MADGRAPH5` followed by parton shower using `PYTHIA8`. For the parton-level events, the `LHAPDF6` [63] set NNPDF3.0NLO [67] with $\alpha_S(m_Z^2) = 0.118$ and $n_f = 4$ flavour scheme was used. μ_F and μ_R were set to $H_\mathrm{T}/2$. An NLO K-factor of 1.6 was estimated using `MADGRAPH5_aMC@NLO`, with the same settings and cuts as used for generation of $pp \rightarrow b\bar{b}b\bar{b}$ at LO. For parton shower, the same PDF set, tune, and vertex smearing was used as for the signal events. Each of the final state partons are required to have a minimum transverse momentum of $p_\mathrm{T} > 20$ GeV/c and to be located within $|\eta| < 3.0$. In addition, a minimum separation of $\Delta R = 0.1$ is also required between the final state partons; see Table 2.1.

Table 2.1: LO cross-section for background and signal processes at $\sqrt{s} = 100$ TeV with the parton level cuts used during generation. In this table, j refers to light quarks and gluons, b to bottom quarks. A minimum separation of $\Delta R = 0.1$ is required between the final state partons in the background sample. The matrix element generator used, the number of events generated and the K-factors used for higher order corrections to σ_{LO} are also indicated

Process	Program	N_{events}	Cuts	σ_{LO}[fb]	K-factor
$pp \rightarrow 4b$	`aMC@NLO`	1M	$p_{\mathrm{T,j\,(b)}} \geq 20$ GeV/c $\lvert\eta\rvert \leq 3.0$ $\Delta R_{bb\,(jj,\,jb)} \geq 0.1$	14.552×10^6	1.6
$gg \rightarrow$ HH	`aMC@NLO`	0.5M	-	853.8 (SM)	1.43

The cross-section for the signal and the background events along with the generator level cuts and K-factors used are listed in Table 2.1. Note the overwhelming amount of back-

---

[3] In this UFO model, the parameter k_λ is denoted as ctr. In addition, there are a few other parameters – the coupling of the Heavy Higgs, to two SM Higgs (ctrH) and to the top quark (cyH) – that are set to a very small value to get rid of the resonant contribution.

ground cross-section in comparison to the signal cross-section. Together with pile-up, this poses a big challenge to measure such rare physics processes.

Parton-level jets and b-tagging:

After parton shower, the final state particles – from both signal and background samples – are clustered into jets using the anti-k_t jet clustering algorithm of the FASTJET [28] package, with radius parameter $\Delta R_{\mathrm{jet}} = 0.4$.[4] A minimum p_{T} threshold of 20 GeV/c is required for each of the clustered jets. An energy smearing of 50 % is applied to the jet-energies to account for detector resolution effects. All the resulting jets in an event have to then pass through a very simple b-tagging algorithm which assumes 80 % b-tagging efficiency. A jet is tagged as a b-jet if it contains at least one b quark with $p_{\mathrm{T}} \geq 15\,\mathrm{GeV/c}$, i.e. $\Delta R_{\mathrm{jet,\,b}} \leq 0.4$. For highly boosted events, two of the b-quarks might lie in a single jet cone of radius 0.4, resulting in multiple b-tags for this jet. As a result, the number of b-jets for highly boosted events is smaller than expected (four). This can be visualised with the help of the Figure 2.11(a-c), which illustrates the three different categories, namely, the resolved, intermediate, and the boosted category, in which the final states of HH → $b\bar{b}b\bar{b}$ physics channel can be reconstructed. While four b-tagged jets are obtained in the resolved category, only three and two b-tagged jets are obtained in the intermediate and the boosted categories, respectively.

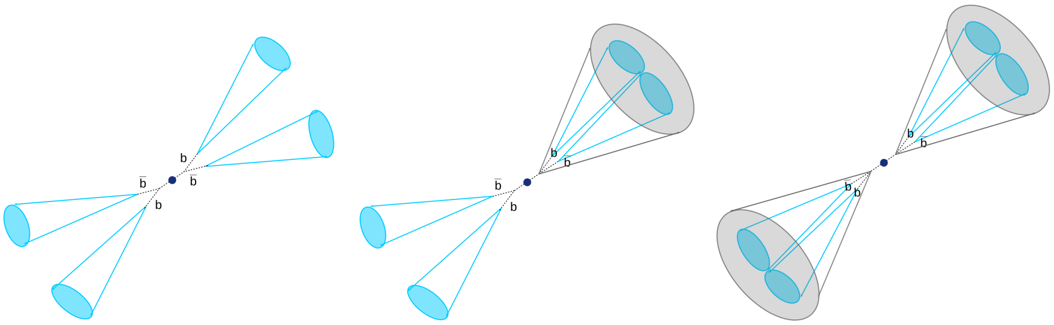

(a) Resolved **(b)** Intermediate **(c)** Boosted

Figure 2.11: Illustration of resolved (a), intermediate (b), and boosted (c) category of final state b-jets in the HH → $b\bar{b}b\bar{b}$ physics channel.

---

[4] The open source FASTJET v 3.3.2 software package was used.

3

Generator Level Analysis for $\mathrm{HH} \rightarrow b\bar{b}b\bar{b}$ at a $100\,\mathrm{TeV}$ *pp* collider

A typical High Energy Physics (HEP) experiment involves analyses of large data samples, which basically contain the measurements of the position of particle trajectories or energy releases in the detector, time of particles arrival, etc. Advanced *statistical methods* are extensively used for obtaining physics results or *inferring* physics from these experimental data samples. As mentioned before, most of the high rate particle experiments do not record all the data produced after particle collision, and instead use a trigger based system to store only the events of interest into these data samples for future analyses. In the absence of real data samples from the experiments, statistical methods can also be used on the so-called *Monte Carlo (MC) samples* that are samples of simulated events. Section 2.4.2 briefly summarised the choice of signal ($\mathrm{HH} \rightarrow b\bar{b}b\bar{b}$) and background ($pp \rightarrow b\bar{b}b\bar{b}$) processes, and the generation of the corresponding MC samples for a $\sqrt{s} = 100\,\mathrm{TeV}$ pp collider. The goal of this chapter is to get a first estimate on the measurement of the Higgs pair production process in its $b\bar{b}b\bar{b}$ final state, and hence estimate the precision to measure λ at a $100\,\mathrm{TeV}$ FCC-hh assuming negligible systematic uncertainties.

In the following an introduction to the statistical significance of data samples is presented which is followed by the event selection strategy (Section 3.1), significance studies (Section 3.2) and sensitivity studies (Section 3.3) for the $\mathrm{HH} \rightarrow b\bar{b}b\bar{b}$ physics channel at FCC-hh.

A selection procedure (also known as the *event selection strategy*) is defined to discriminate signal and background events in both data and MC samples. In experimental data, the presence of signal events is not known from before and in order to confirm whether or not the data samples contain some physics events different from the already known background events, two different hypotheses can be defined.

- A *null hypothesis*, also called as the *background-only hypothesis* H_0, that claims the data sample to contain *only background*.
- An *alternative hypothesis* H_1, that claims the data sample to contain *signal + background*.

The most natural and simple event selection strategy involves application of a series of cuts to optimise a parameter computed from the data sample that discriminates between the two hypotheses H_0 and H_1. *Statistical significance* is the parameter optimised in the analysis presented here. In particle physics, the statistical significance of a sample of events gives an estimate on how consistent the sample is with a given hypothesis. In the case of measurement of di-Higgs production with the $b\bar{b}b\bar{b}$ final state, the significance level will determine how strongly the processes that mimic the same final state (background processes) could be rejected.

From experimental data, one determines the *observed significance* of rejecting the (known) background-only hypothesis. In other words, if B is the expected number of (background) events and N ($> B$) is the total number of events observed after all analysis cuts (event selections), then the *observed significance* Z quantifies the probability of the excess S ($= N - B$) being the result of a new process (different from the background) or a plain statistical fluctuation. This probability, also referred to as the p-value is given by:

$$p = \frac{1 - \mathrm{erf}(Z/\sqrt{2})}{2}, \tag{3.1}$$

where erf(y) is the error function given by:

$$\mathrm{erf}(y) = \frac{2}{\sqrt{\pi}} \int_0^y e^{-x^2} \mathrm{d}x. \tag{3.2}$$

For counting experiments following Poisson statistics, signal significance maps the above probability to observe N events when only B events are expected and can be simply approximated by:

$$Z = \frac{N - B}{\sqrt{N}} = \frac{S}{\sqrt{N}} \tag{3.3}$$

$$\approx \frac{S}{\sqrt{B}}, \tag{3.4}$$

for $S/B \ll 1$ and well determined B. A translation between the p-values and Z for 1σ to 5σ deviations is given in Table 3.1. Lower the p-value (higher the Z); greater is the probability of rejecting the assumed (background-only) hypothesis. A signal significance of 5σ is conventionally used in HEP to claim discovery and 3σ for evidence when testing against a hypothesis [68].

Table 3.1: one sided Gaussian p-values from 1σ to 5σ

Z	1σ	2σ	3σ	4σ	5σ
p-value [%]	15.85	2.28	0.14	3.16×10^{-5}	2.87×10^{-7}

In the absence of a real experiment (as in the case of a future hadron collider with $\sqrt{s} = 100$ TeV), one tries to estimate the expected signal significance of a particular process (for a projected integrated luminosity $\mathcal{L}$) by using MC events. The *expected significance* can be determined by Equation 3.4, with the only difference that now both S and B are well defined.[1] Since S and B, both scale with the luminosity, one way to enhance the signal significance is to collect more data (as $S/\sqrt{B} \propto \sqrt{\mathcal{L}}$). A smart selection of analysis cuts that rejects a large number of background events also enhances the signal significance.

3.1 Event Selection and Analysis Strategy

Event selection in an experiment is partly done online using one or more of the variety of triggers in a detector, and partly offline while doing analysis. The trigger thresholds of these triggers are set based on several factors, for example, signal efficiency, bandwidth limitations, etc. For the analysis presented in this chapter, a trigger-less readout system is assumed. In other words, the trigger efficiency is assumed to be 100 % and only offline thresholds are considered. The η distribution of the final state b quarks for the SM signal and background processes after the parton level cuts (listed in Table 2.1) are shown in Figures 3.1(a and b).[2] Notice that the 4^{th} central b quarks peak at a much higher η value than the remaining three b quarks. Hence, in order to have a high signal efficiency, a large tracker acceptance of a detector is essential. Since the trigger studies in this thesis are based on a barrel type detector triplet, tracker acceptance of $|\eta| < 2.5$ is chosen for the rest of the analysis.[3] About 60 % of the signal events can be reconstructed with a tracker

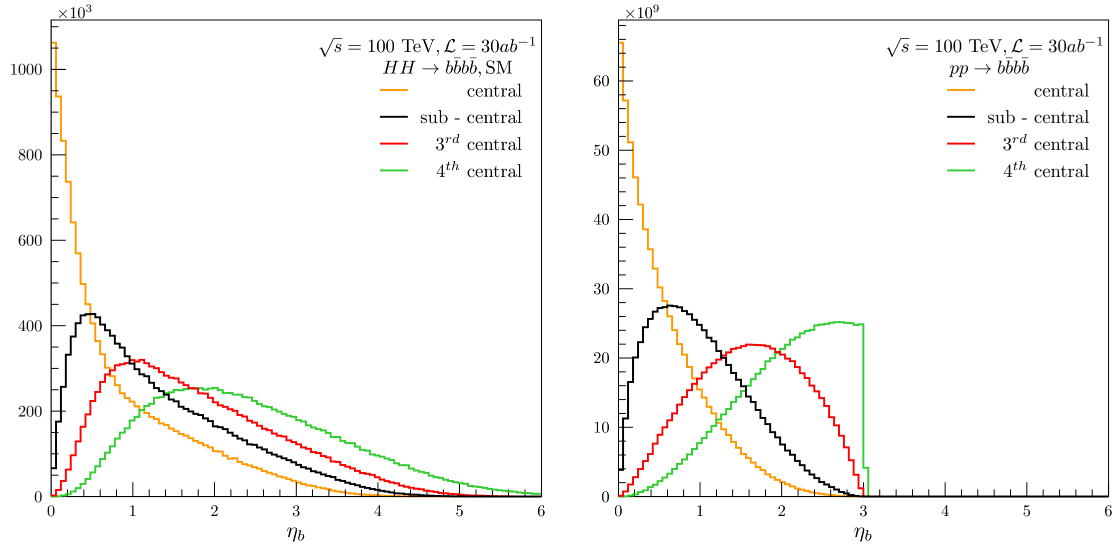

(a) **(b)**

Figure 3.1: Pseudorapidity of the four b quarks in: (a) HH → $b\bar{b}b\bar{b}$ and (b) $pp \to b\bar{b}b\bar{b}$ QCD multi-jet background with generator level cuts as given in Table 2.1.

---

[1] Note that it is important to consider all possible background processes to correctly determine the expected signal significance. However, to get a first-approximation of expected Z, one usually considers the most dominant background processes, as is the case in this thesis.

[2] Note that the branching ratio for HH → $b\bar{b}b\bar{b}$, ≈ 0.336 has been included in the normalization used for a total integrated luminosity of 30 ab^{-1} in all the distributions in this Chapter.

[3] It would be useful to do a more realistic study with endcap rings extending from $|\eta| = 1.5$ to $|\eta| = 6$ as the effects of multiple scattering are larger in this region for a barrel type geometry.

acceptance of $|\eta| < 2.5$.

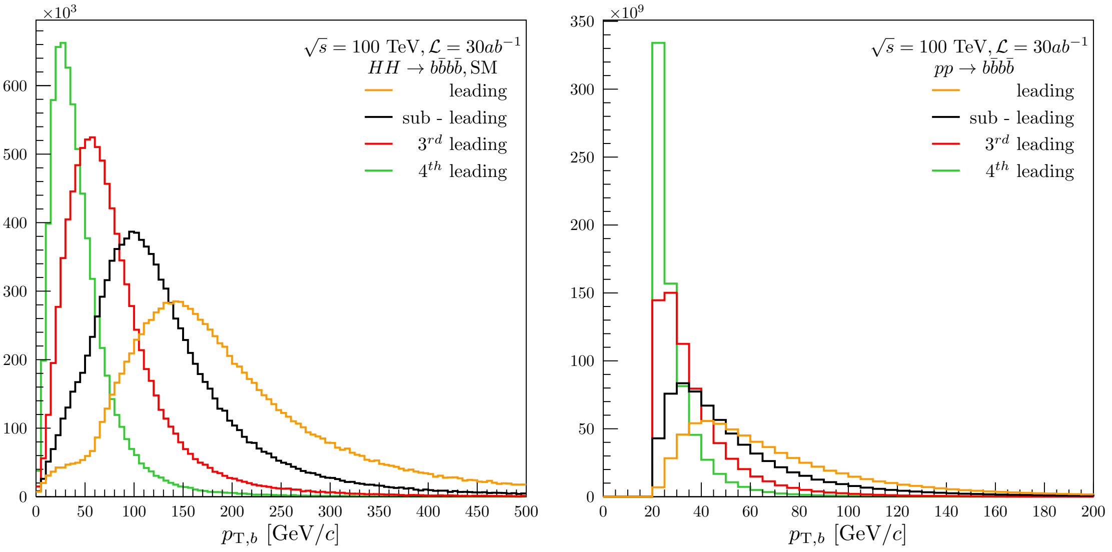

(a) **(b)**

Figure 3.2: Transverse momentum of the four b quarks in: (a) HH → $b\bar{b}b\bar{b}$ process and (b) $pp \to b\bar{b}b\bar{b}$ QCD multi-jet background after tracker acceptance cut of $|\eta| < 2.5$.

The triggers that are interesting for the signal process considered in this thesis are single-, di-, or multi-jet triggers with one, or several b-tags, depending on the analysis. The single- and the di-jet triggers in the case of multi-jet signatures are mainly used to select highly boosted events.[4] This analysis, however focusses on the resolved regime and a minimum of four jets with $\Delta R_{\text{jet}} = 0.4$ above a particular p_{T} threshold (defined by the trigger architecture) are required. For the HL-LHC upgrade with $\langle\mu\rangle = 200$, a four-jet trigger with an offline p_{T} threshold of at least 65 GeV/c has been projected for the ATLAS experiment [69].[5] In other words, only those events with at least four jets, each with $p_{\mathrm{T}} \geq 65$ GeV/c will be triggered. Assuming the same four-jet p_{T} thresholds at FCC-hh,[6] more than 80 % of the signal events will be lost. This can be seen from the p_{T} distributions of the four leading b quarks for the SM signal and background processes, with $|\eta| < 2.5$ in Figure 3.2. Although, the background can be heavily suppressed at high thresholds, less than 20 % of the events have a 4^{th} leading b quark with $p_{\mathrm{T}} \geq 65$ GeV/c in the SM signal sample. Evidently, a large fraction of signal events will be lost if the multi-jet trigger thresholds are too high. Unlike the $pp \to b\bar{b}b\bar{b}$ process, the leading b quark peaks at $\sim$ 150 GeV/c in the signal compared to $\sim$ 40 GeV/c in the background. Similarly, the sub-leading and the 3^{rd} leading b quarks in the signal sample also peak at a higher p_{T} value than in the background. This implies that asymmetric trigger thresholds for the first

---

[4] Mostly fat jets with $\Delta R_{\text{jet}} \geq 1.0$ are used as trigger objects, in the boosted analysis for multi-jet signatures.

[5] A further reduction of the trigger threshold to 55 GeV/c using regional tracking information from a hardware based track trigger is also being considered.

[6] This is a very optimistic assumption, as the trigger rates for calorimeter objects will be much higher with $\langle\mu\rangle = 1000$

few leading jets will allow an efficient background rejection. For example, a threshold of 55 GeV/c on the leading jet p_T will reject $\sim 60\,\%$ of background events while maintaining a signal efficiency $\sim 80\,\%$. A similar logic is applicable to the sub-leading and the 3^{rd} leading jets. Thus, the basic event selection is required to have:

- at least four $\Delta R_\mathrm{jet} = 0.4$ anti-k_t jets, with $|\eta| \leq 2.5$ and
- the leading jet $p_\mathrm{T} \geq 55$ GeV/c,
- sub-leading jet $p_\mathrm{T} \geq 40$ GeV/c,
- 3^{rd} leading jet $p_\mathrm{T} \geq 35$ GeV/c,
- and the 4^{th} leading jet $p_\mathrm{T} \geq 20$ GeV/c.

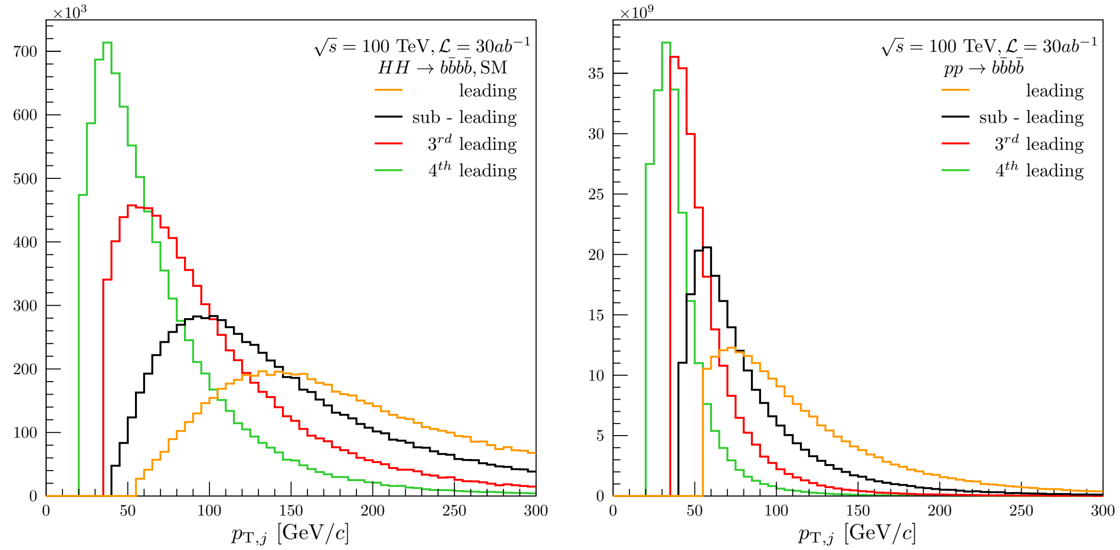

(a) **(b)**

Figure 3.3: Transverse momentum of the four leading jets in: (a) HH $\to b\bar{b}b\bar{b}$ process and (b) $pp \to b\bar{b}b\bar{b}$ QCD multi-jet background after basic cuts.

In addition to the jets from the hardronization of b quarks arising from the hard process, jets originating from, e.g. ISR and FSR are also detected. The jet reconstruction process employed for the parton-level analysis in this chapter was briefly discussed in Section 2.4.2. Figure 3.3 shows the p_T distribution of the four leading jets for the SM signal and background with the basic selection cuts. A sharp rise is observed for each of the leading p_T jets at their respective p_T thresholds. The above cuts result in reduction of the background by $\sim 90\,\%$ compared $\sim 30\,\%$ in signal. An increase in the number of events for the 4^{th} leading jet p_T distribution in comparison to that of the b quarks is indicative of the presence of the jets arising from radiations.

Figure 3.4 shows the invariant mass distributions of the first four leading jets for the SM signal and background processes. A clear peak in the invariant mass distribution of the first two leading jets suggests the presence of a large number of boosted events in the signal sample, wherein jets from two different b quarks – coming from the Higgs decay – merge into a single jet. All these events are filtered out in the next step of the analysis, where at least four b-tagged jets satisfying the basic cuts are required. The p_T distributions of the

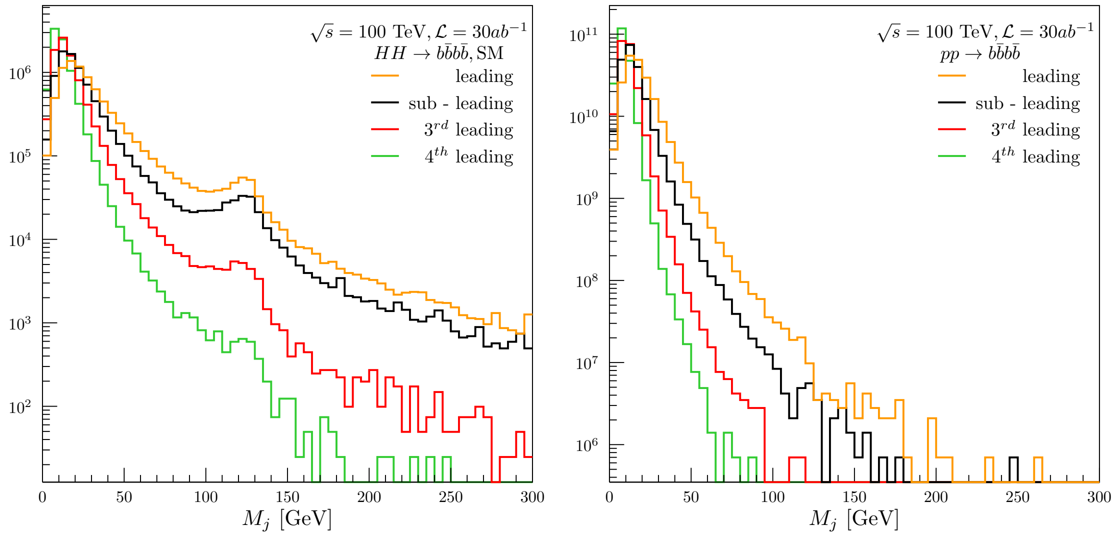

(a) **(b)**

Figure 3.4: Invariant mass distribution of the four leading jets in: (a) HH → $b\bar{b}b\bar{b}$ process and (b) $pp \rightarrow b\bar{b}b\bar{b}$ QCD multi-jet background after basic cuts.

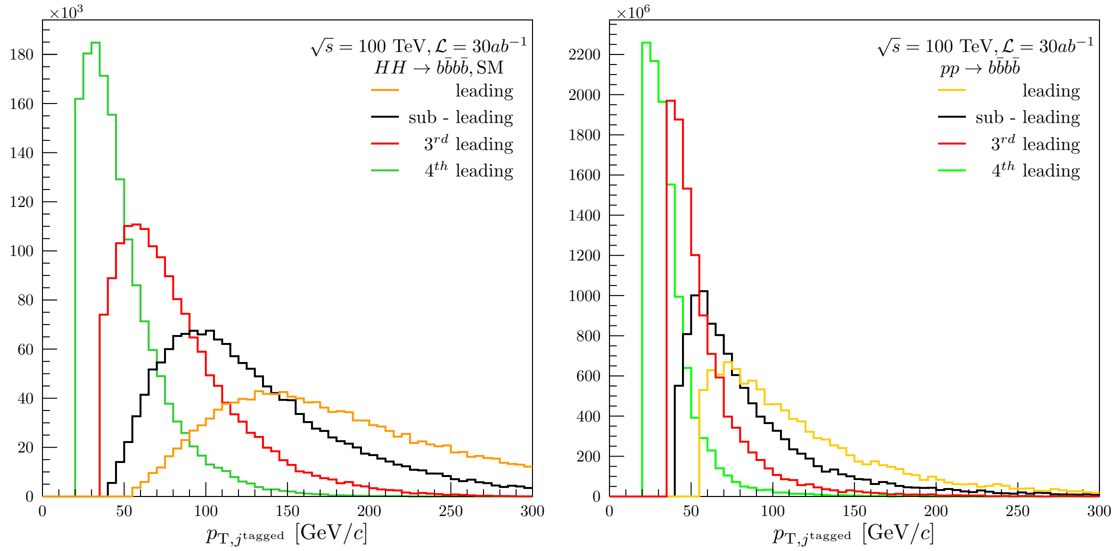

(a) **(b)**

Figure 3.5: Transverse momentum of the four leading b-jets in: (a) HH → $b\bar{b}b\bar{b}$ process and (b) $pp \rightarrow b\bar{b}b\bar{b}$ QCD multi-jet background after b-tagging.

four leading b-tagged jets for the SM signal and background are displayed in Figure 3.5. Notice the large drop in the number of events after requiring at least four b-tagged jets in a event, which is mostly due to the rejection of the boosted events and party due to 20 % b-tagging inefficiency.

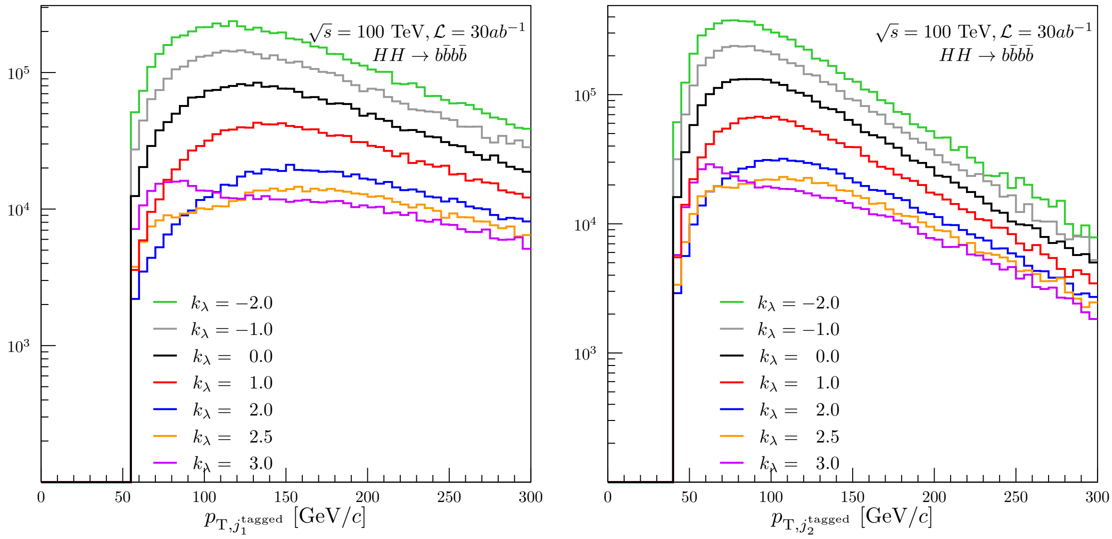

(a) leading b-jet **(b)** sub-leading b-jet

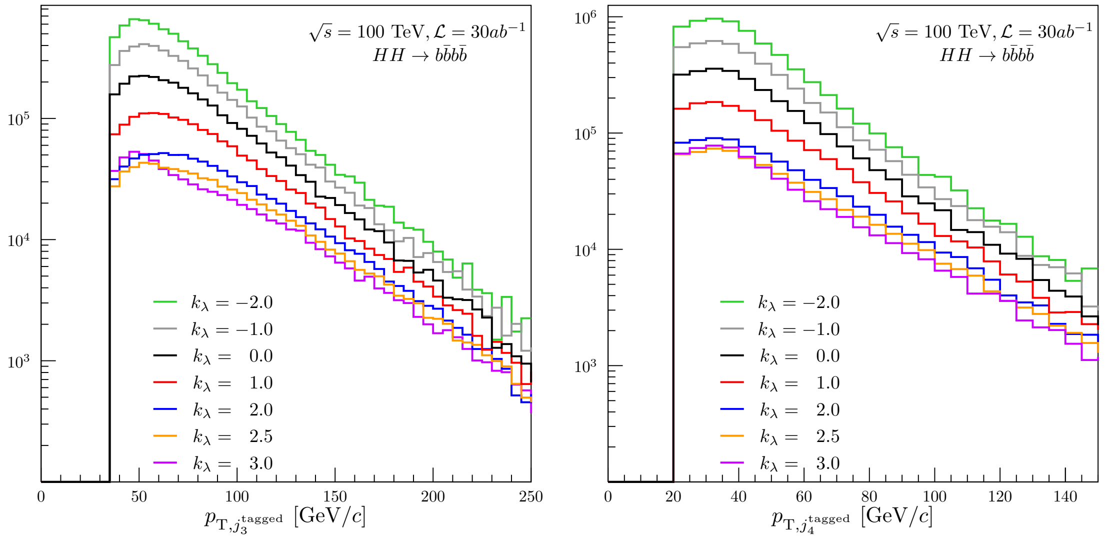

(c) 3^{rd} leading b-jet **(d)** 4^{th} leading b-jet

Figure 3.6: Transverse momentum of the four leading b-jets in: (a) HH $\to b\bar{b}b\bar{b}$ process and (b) $pp \to b\bar{b}b\bar{b}$ QCD multi-jet background after b-tagging.

In Figures 3.6(a-d), the p_T distributions for the first four leading b-jets are compared for various values of k_λ. b-jets with lower values of k_λ tend to have a softer p_T except for $k_\lambda > 2.5$, where the dominant triangle component is visible at low p_T as in the case of $p_{\mathrm{T,H}_{1(2)}}$ distributions given in Figure 2.10. With four b-jets, six b-jet pair combinations (or six Higgs candidates) are possible, i.e. $jj_{12}^{\mathrm{tagged}}$, $jj_{13}^{\mathrm{tagged}}$, $jj_{14}^{\mathrm{tagged}}$, $jj_{23}^{\mathrm{tagged}}$, $jj_{24}^{\mathrm{tagged}}$, $jj_{34}^{\mathrm{tagged}}$. With these six Higgs candidates, there are three possible di-Higgs candidates, viz. $jj_{12}^{\mathrm{tagged}}jj_{34}^{\mathrm{tagged}}$, $jj_{13}^{\mathrm{tagged}}jj_{24}^{\mathrm{tagged}}$, and $jj_{14}^{\mathrm{tagged}}jj_{23}^{\mathrm{tagged}}$. Figure 3.7 shows the correlation between the reconstructed invariant masses of the two Higgs candidates, for each of the

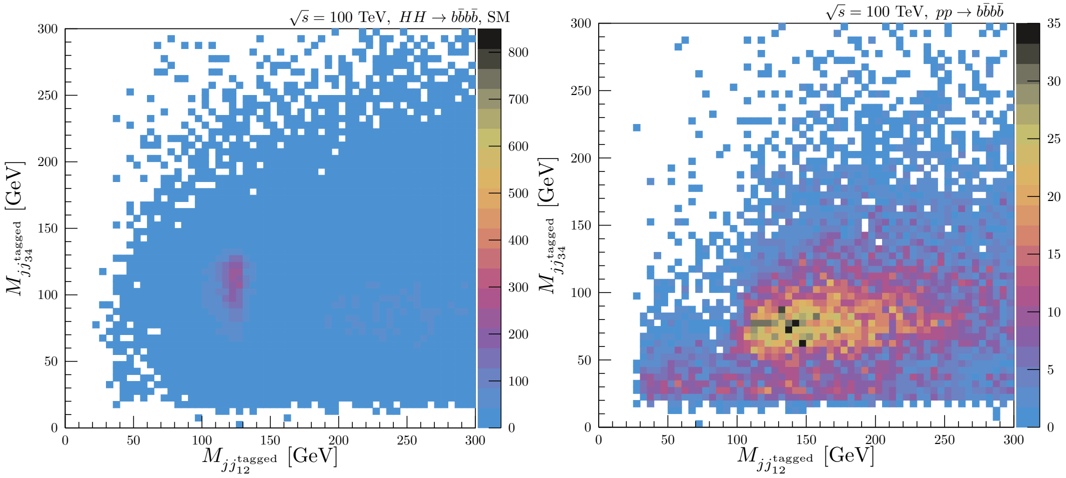

(a) $M_{jj_{34}^{\text{tagged}}}$ vs. $M_{jj_{12}^{\text{tagged}}}$: Signal **(b)** $M_{jj_{34}^{\text{tagged}}}$ vs. $M_{jj_{12}^{\text{tagged}}}$: BG

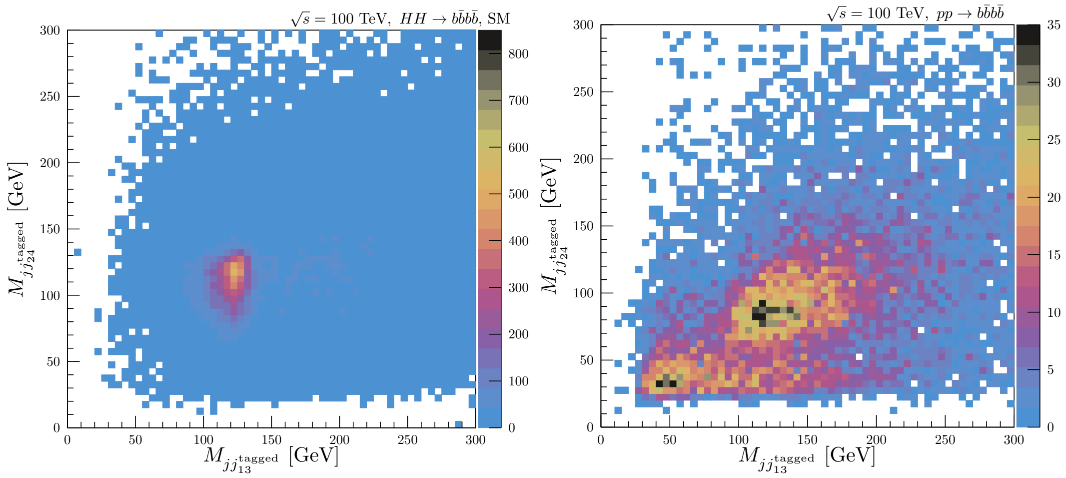

(c) $M_{jj_{24}^{\text{tagged}}}$ vs. $M_{jj_{13}^{\text{tagged}}}$: Signal **(d)** $M_{jj_{24}^{\text{tagged}}}$ vs. $M_{jj_{13}^{\text{tagged}}}$: BG

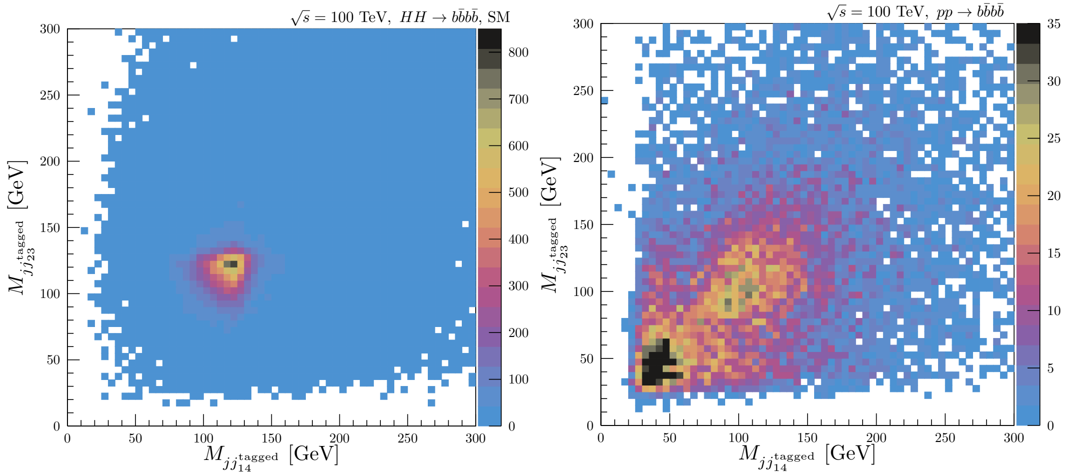

(e) $M_{jj_{23}^{\text{tagged}}}$ vs. $M_{jj_{14}^{\text{tagged}}}$: Signal **(f)** $M_{jj_{23}^{\text{tagged}}}$ vs. $M_{jj_{14}^{\text{tagged}}}$: BG

Figure 3.7: Scatter plots of the reconstructed invariant masses of the Higgs candidates for three possible di-Higgs combinations in the SM signal:(a), (c), (e) and in QCD multi-jet background: (b), (d), (f).

three possible Higgs pair combinations in the SM signal (left), and in QCD multi-jet background (right). The colour axis indicates the number of events.[7] One can see that the third combination of Higgs candidates, i.e. $jj_{14}^{\text{tagged}} jj_{23}^{\text{tagged}}$ occurs more often than the other two. For the SM signal, majority of the events have pairs of reconstructed Higgs candidates with invariant mass very close to the Higgs mass (as the b-jets are the decay products of the Higgs bosons). On the contrary, since the b-jets in the background events arise from partons that cover a wide mass range, pairs of reconstructed Higgs candidates also tend to have a wide range of invariant masses. The p_{T} cuts on the four leading jets (implemented to select more signal-like events) result in two distinguishable high density regions in these scatter plots for the background sample. Because of the high p_{T} cut of (55 + 40) GeV/c on the candidate jj_{12}^{tagged}, only one wide high density region in Figure 3.7(b) is prominent. In Figure 3.7(d), the p_{T} cut on the candidate plotted on the x-axis is (50 + 35) GeV/c as opposed to (40 + 20) GeV/c on the y-axis, resulting in two different high density regions. In Figure 3.7(f), a large number of low invariant mass combinations are seen due to the relatively low p_{T} cuts $\sim 70\,\text{GeV/c}$ for both the candidates plotted on the x and the y axes.

From these three di-Higgs combinations, the one with each of the Higgs candidates having an invariant mass lying in a 60 GeV mass range symmetric around the nominal Higgs mass, i.e $|M_{H_{1(2)}^{\text{cand.}}} - 125| \leq 60\,\text{GeV}$ is selected. If more than one combinations satisfy the above requirement, the combination with a minimum relative difference between the two Higgs candidates is selected as the final di-Higgs candidate. The Higgs boson with the largest p_{T} is termed as the leading Higgs (H_1) and the other one is termed as sub-leading Higgs (H_2). From Figure 3.7, one can see that the invariant mass cut is very effective in suppressing a large fraction of background events.[8] Thus, the HH → $b\bar{b}b\bar{b}$ signal is finally extracted by measuring the peak in the M_{jj}^{tagged} vs. M_{jj}^{tagged} plane, whereas a (signal free) side-band region defined around this peak would then define the background in data. This is usually achieved by using templates or other advanced analysis techniques. For measuring differential distributions, this extraction could be done for various values of an observable, for example, the transverse momentum or the invariant mass of the leading, sub-leading, 3^{rd} leading or the 4^{th} leading b-tagged jets.

The reconstructed invariant mass of the leading and the sub-leading Higgs candidates for the SM signal and the background processes are shown in Figure 3.8. Note that the background distribution has been scaled by 10^{-3}. A clear peak at 125 GeV is visible for the SM signal, especially for the leading Higgs. The width of the Higgs mass peak can be attributed to the energy smearing of the anti-k_t jets (mentioned in Section 2.4.2) to account for detector resolution effects and the QCD effects such as ISR and out-of-cone radiation. The smearing of the invariant mass distribution for the sub-leading Higgs in SM signal is mainly due to the out-of-cone radiation effects of the reconstructed decay products (the b-jets), reducing the reconstructed mass. Even after all the selection cuts, the background distribution heavily dominates the signal distribution by $\sim \mathcal{O}(10^3)$. However, the expected statistics with an integrated luminosity of $30\,\text{ab}^{-1}$ is sufficiently large to test for di-Higgs production in the $4b$ final state. Besides, the relevant quantity to investigate in order to

---

[7] Note that the distributions in Figure 3.7 are not scaled to the integrated luminosity of $30\,\text{ab}^{-1}$.

[8] Notice that the invariant mass cut is kept loose and further improvements are possible with advanced analysis techniques.

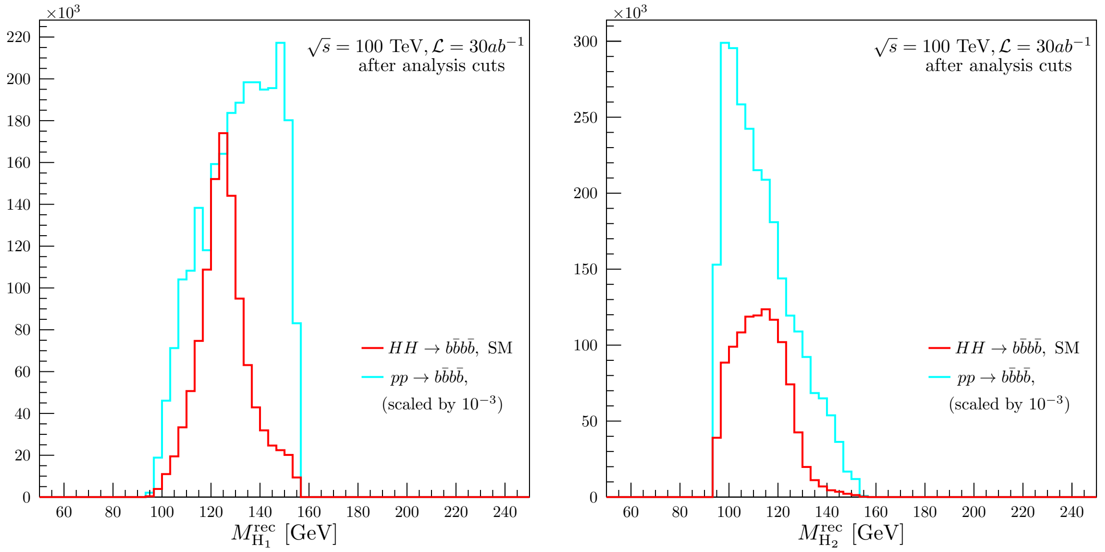

(a) **(b)**

Figure 3.8: Reconstructed invariant mass of the leading Higgs, $\rm H_1$ (a) and the sub-leading Higgs, $\rm H_2$ (b) in signal (red) and background (cyan) processes after analysis cuts.

see whether a measurement of something different from the background can be made is the signal significance, which will be discussed in more detail in Section 3.2.

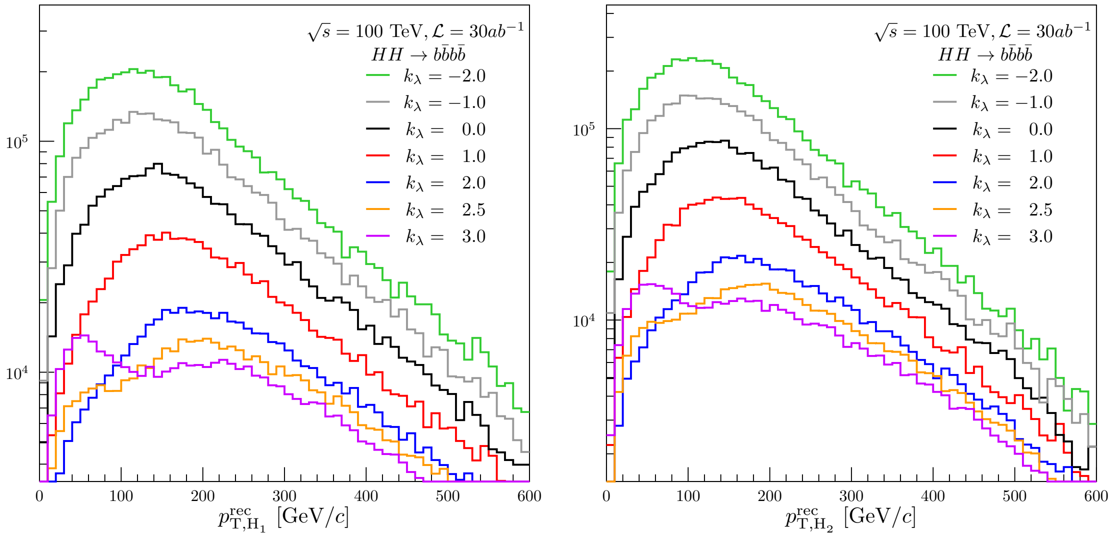

(a) **(b)**

Figure 3.9: Reconstructed transverse momentum of the leading Higgs, $\rm H_1$ (a) and the sub-leading Higgs, $\rm H_2$ (b) in HH → $b\bar{b}b\bar{b}$ process after analysis cuts for different values of k_λ .

The $p_{\rm T}$ distributions of reconstructed $\rm H_1$ and $\rm H_2$ for various values of k_λ are presented in Figure 3.9. They tend to become softer with decreasing k_λ except for $k_\lambda \geq 2.5$, after which a second peak at very low p_T is observed, similar to their truth distributions (see Figure 2.10). Deviations from the SM prediction show excess or deficiency in the total number of events and hence in the measured cross-section.

The reconstructed invariant mass and transverse momentum of the di-Higgs system for signal and background are shown in Figure 3.10. Note that the background distributions displayed are scaled by 10^{-3}. The $M_{\mathrm{HH}}^{\mathrm{rec}}$ distribution for the background events is rather soft compared to that of the signal events for all values of k_λ. Note that at parton-level the M_{HH} distribution shows a sharp kinematic cut-off at the minimum mass required to produce a pair of Higgs bosons (250 GeV); see Figure 2.9. This is no longer visible and the reconstructed invariant mass is smeared out due to parton shower and detector resolution effects. Clearly, the very high invariant mass region is insensitive to any deviations from the SM predictions, as for all k_λ values, the $M_{\mathrm{HH}}^{\mathrm{rec}}$ distribution by far remains indistinguishable. In the low invariant mass region, apart from differences in measured number of events for various values of k_λ, some peculiar features are visible for $k_\lambda > 2$. Therefore, the low invariant mass region is crucial to look for BSM scenarios. The $p_{\mathrm{T,HH}}^{\mathrm{rec}}$ distribution in Figure 3.10(b) shows that the background has a very steeply falling behaviour compared to the signal events with various values of k_λ. Also, the high p_T region has very low background as compared to that at low p_T, but is still higher than the number of signal events (note the large error bars and the scaling used for the background distribution in these plots). These differences of the $M_{\mathrm{HH}}^{\mathrm{rec}}$ and $p_{\mathrm{T,HH}}^{\mathrm{rec}}$ distributions between signal and background can be used as an input to some more advanced analysis techniques, e.g. a multivariate analysis (as shown in Reference [57]), to make a clear distinction of signal from background.

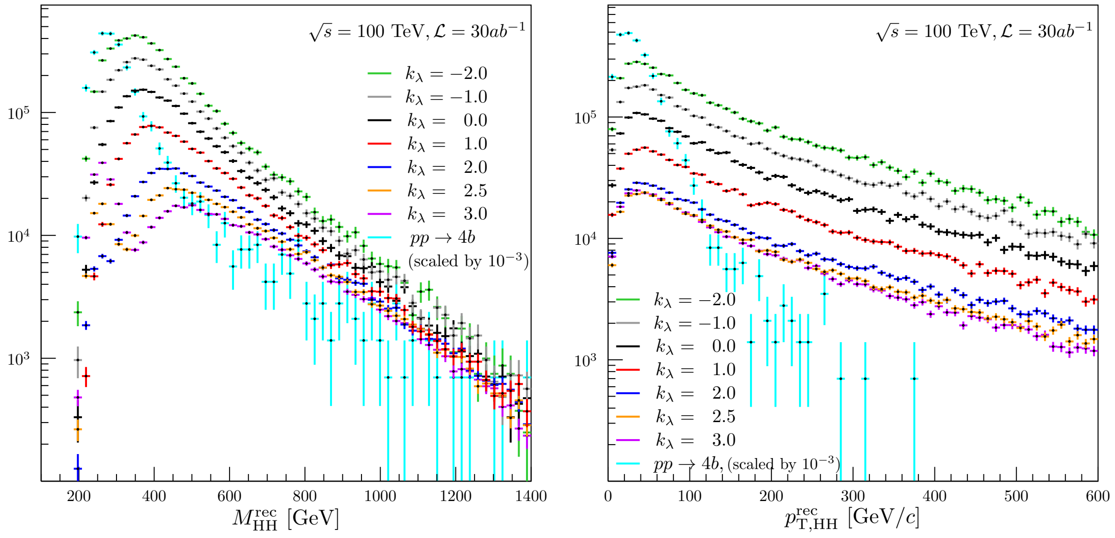

(a) **(b)**

Figure 3.10: Reconstructed invariant mass (a) and transverse momentum (b) of the di-Higgs system after analysis cuts in signal for various values of k_λ, and background.

The entire analysis chain is explained with the help of a flow chart in Figure 3.11 and

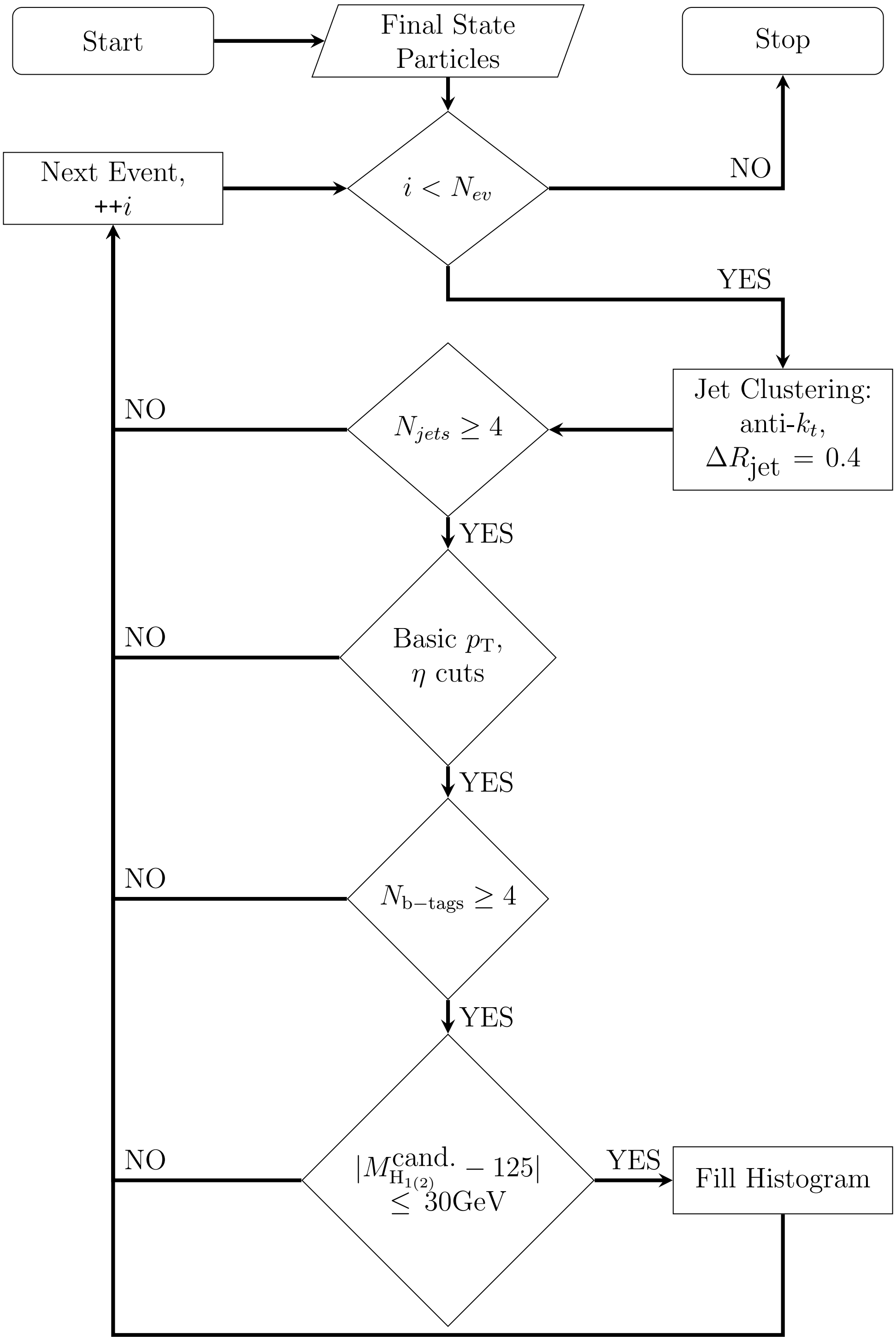

Figure 3.11: Flow chart of the anlysis strategy used.
]

Table 3.2: Cut-flow table indicating the number of background and signal events remaining after application of various cuts at each step in the analysis. A total of 1M background and 0.5M signal events (with the generator level cuts given in Table 2.1 included) were considered before starting the analysis.

Cuts, $S/\sqrt{B}$ †	$pp \to 4b$	$k_\lambda = 1.0$	$k_\lambda = 0.0$	$k_\lambda = -1.0$	$k_\lambda = -2.0$	$k_\lambda = 2.0$	$k_\lambda = 2.5$	$k_\lambda = 3.0$
Basic p_T, η cuts	305420	360717	351031	343662	339583	368173	360449	341091
$S/\sqrt{B}$	–	19.294	35.990	60.001	91.596	10.065	8.252	8.250
$N_{\text{b-tags}} \geq 4$	15888	63150	59844	57890	56472	66192	63448	57682
$S/\sqrt{B}$	–	14.810	26.901	44.314	66.785	7.934	6.369	6.117
$\lvert M^{\text{cand.}}_{\text{H}1(2)} - 125\rvert \leq 30$	3680	43789	41694	40684	39590	45587	44047	40265
$S/\sqrt{B}$	–	21.338	38.943	64.710	97.284	11.354	9.187	8.872

† Note that the number of events indicated are not normalised to $\mathcal{L} = 30\,\text{ab}^{-1}$ however the significances computed include the signal and the background normalisations.

the resulting number of events (unnormalised) and the signal significances at each step of the analysis is presented in a cut-flow Table. 3.2. The total number $pp \to b\bar{b}b\bar{b}$ events are reduced by about 70 % of the initial 1M events, only after application of the basic p_T and η cuts. This indicates that the irreducible QCD multi-jet background comprises of a large number of very low p_T jets unlike the signal events. Also an asymmetric selection of p_T cuts improves the signal selectivity. A huge drop in the number of events for both the signal ($\sim$ 83 % - SM) and background ($\sim$ 95 %) occurs after requiring at least four b-tagged jets. One also sees that there is a drop in the signal significance after this step. This is expected, as this analysis considers only the resolved regime and as explained earlier, this significant drop is mainly due to a large number of boosted events and partly due to the 20 % b-tagging inefficiency considered in this analysis. This cut is, however, crucial in a resolved analysis as it allows for identification of the four b-jets coming from the Higgs bosons. The following invariant mass cut about the SM Higgs mass would not make sense without identifying these b-jets in an event. One of the most crucial selection cuts, discriminating the signal from background is the invariant mass requirement on the possible Higgs candidates. One can see that after this step the lost significance is recovered and also improves slightly, although the gain is small. However, the invariant mass cut gives an important handle on background estimation, which plays a crucial role in determination of systematic uncertainties.

The p_T distributions of the four leading b-tagged jets for background and signal processes, after application of all the analysis cuts is shown in Figure 3.12. As also noted for other kinematic distributions, clearly the number of background events dominates the total number of signal events selected, for all the k_λ values considered. However, the above simple set of selection cuts alone allowed for an improvement of the signal to background ratio by about an order of magnitude. Further improvements can be achieved by the use of advanced analysis techniques. The leading and sub-leading jets show a distinct peak at around 80 GeV/c for signal events with $k_\lambda \geq 2.5$. The background events tend to have a steeper p_T distribution compared to the signal distributions with different values of k_λ.

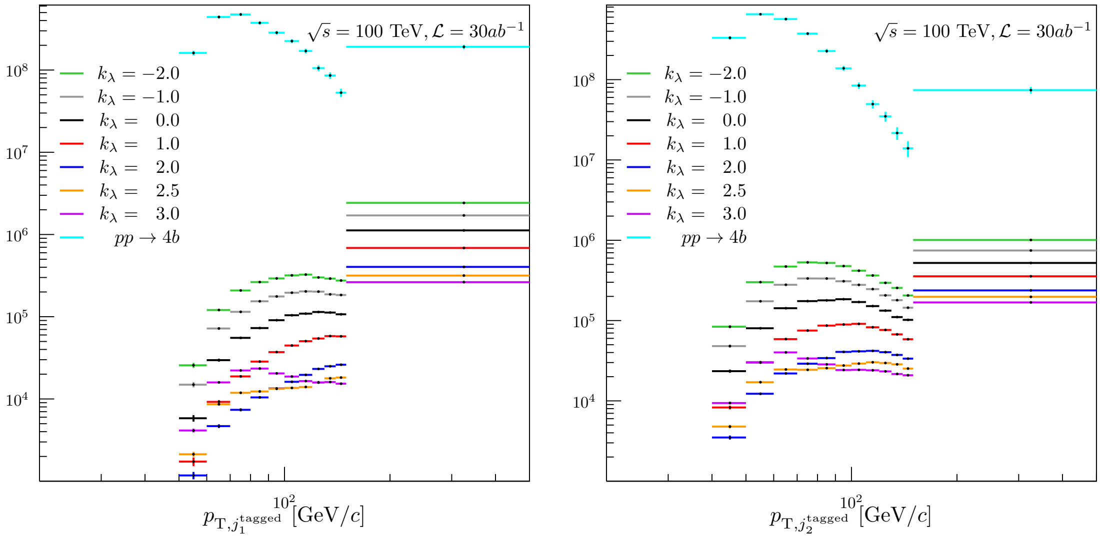

(a) leading b-jet **(b)** sub-leading b-jet

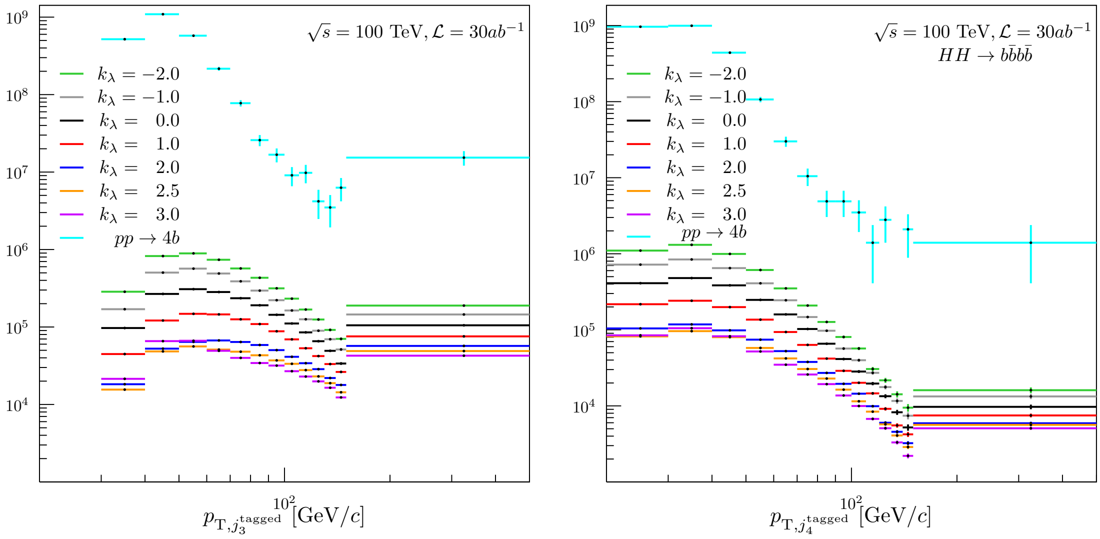

(c) 3^{rd} leading b-jet **(d)** 4^{th} leading b-jet

Figure 3.12: Transverse momentum of the four leading b-jets after all the analysis cuts in background and signal processes for various values of k_λ.

This information can be used by a neural network, for instance, to further improve the signal selectivity. A quantitative discussion on the improvement of significances of signal events in the presence of background and the sensitivity to measure deviations from SM predictions, as a function of the 4^{th} leading b-tagged jet in an event is presented in the following sections.[9]

---

[9] Notice the large error bars for the background distributions with increasing p_T. Last few bins are combined into one to avoid the large statistical errors in determining the signal significance and sensitivity as a function of 4^{th} b-jet p_T.

3.2 Signal Significance Studies

An introduction to the signal significance with its quantification in terms of number of standard deviations to confirm or reject a null hypothesis was given at the beginning of this chapter. It was mentioned that one of the ways to enhance the signal significance is by making a smart choice of selection cuts. Yet another way to enhance the signal significance is by taking a quadratic sum of the significances over several bins of a discriminant. Let's consider the transverse momentum of the 4^{th} leading b-jet, i.e. $p_{\mathrm{T,j4}}^{\mathrm{tagged}}$ as the discriminant. A histogram of $p_{\mathrm{T,j4}}^{\mathrm{tagged}}$ for signal and background will result in S_i and B_i events in the i^{th} bin. One can now determine the significances for each of the i^{th} bins (Z_i), and the quadratic sum of the individual significances over all the bins can be written as:

$$Z = \sqrt{\sum Z_i^2}, \tag{3.5}$$

$$\text{where } Z_i^2 = S_i^2/B_i. \tag{3.6}$$

Figure 3.13(a) shows the i^{th} bin contributions to the total significance Z (determined by

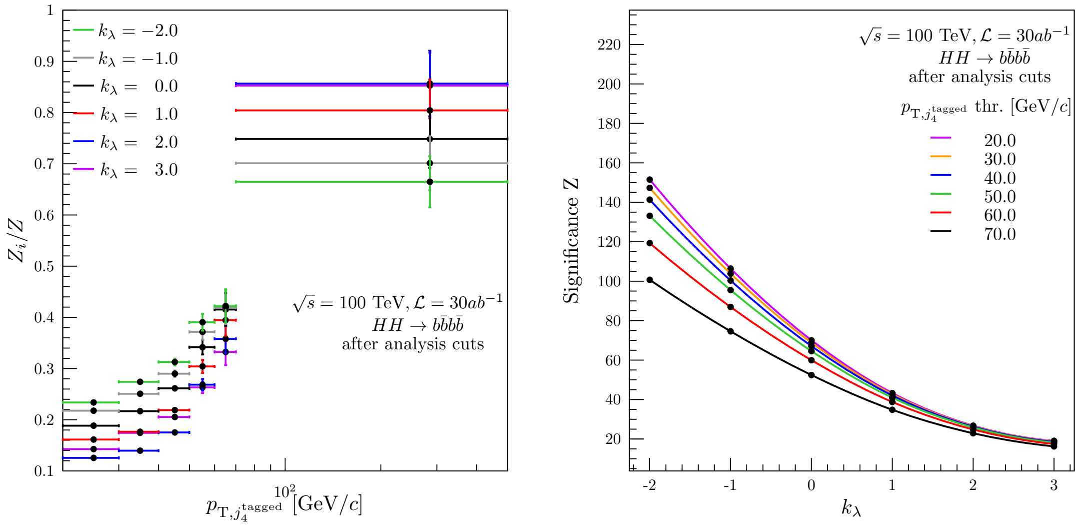

(a) **(b)**

Figure 3.13: (a) Contribution of different p_T bins to total significance for various values of k_λ in HH → $b\bar{b}b\bar{b}$ and (b) Total significance as a function of k_λ at various p_T thresholds of the 4^{th} leading b-jet.

setting $p_{\mathrm{T,j4}}^{\mathrm{tagged}}$ threshold to 20 GeV/c) for six different values of k_λ (indicated by different colours). The lower edge of each bin indicates the $p_{\mathrm{T,j4}}^{\mathrm{tagged}}$ threshold. Although the maximum contribution to Z comes from the highest p_T bin $\in [70, 500)$ (due to the highest signal to background ratio owing to the steeply falling background p_T), the contributions from the remaining bins are non-negligible ($> 10\,\%$) for all values of k_λ.

This strongly motivates the need to keep the trigger threshold for the 4^{th} *b-jet as low as possible.*

Figure 3.13(b) presents the total expected signal significance of HH $\rightarrow b\bar{b}b\bar{b}$ after all the analysis cuts, as a function of k_λ for a 100 TeV pp collider with a total integrated luminosity of 30 ab^{-1}. The $p_{\mathrm{T,j4}}^{\mathrm{tagged}}$ thresholds, starting from a minimum of 20 GeV/c (as used in the analysis) to a maximum of 70 GeV/c in steps of 10 GeV/c, are indicated by different colours. For the SM signal, $Z \sim 43$ with $p_{\mathrm{T,j4}}^{\mathrm{tagged}}$ threshold of 20 GeV/c. The significance increases with decreasing k_λ and becomes as high as 150 for $k_\lambda = -2$ (with $p_{\mathrm{T,j4}}^{\mathrm{tagged}}$ threshold = 20 GeV/c) owing to the much larger signal cross-section than the SM cross-section. A significance gain of a factor of ~ 1.5 is obtained for $k_\lambda = -2$, by switching from a $p_{\mathrm{T,j4}}^{\mathrm{tagged}}$ threshold of 70 GeV/c to 20 GeV/c. The gain in Z decreases as k_λ increases and is ~ 1.25 for the SM when switching from a $p_{\mathrm{T,j4}}^{\mathrm{tagged}}$ threshold of 70 GeV/c to 20 GeV/c.

Table 3.3: Summary of the signal significances for six different values of k_λ after application of all the analysis cuts. The results are summarised only for the resolved category and using the irreducible QCD 4b background alone.

k_λ	-2	-1	0	1	2	3
$Z_{\text{one bin}}$	97.28	64.71	38.94	21.34	11.35	8.87
$Z_{p_\mathrm{T}=20\,\mathrm{GeV/c}}$	151.51	106.39	70.05	43.27	26.74	19.08
$Z_{p_\mathrm{T}=70\,\mathrm{GeV/c}}$	100.71	74.59	52.42	34.81	22.91	16.27

Table 3.3 summarises the signal significances in the resolved category for six different values of k_λ. The significances are quoted for two different p_T thresholds on the 4^{th} leading b-jet. Signal significances determined with unbinned data are also presented for comparison and shows enhancement in Z by taking a quadratic sum over the significances in the individual bins. There are some important points to be noted when referring to the significances quoted in Table 3.3 for a future 100 TeV pp collider:

- The quoted Z values will reduce slightly as only the most dominant irreducible QCD $4b$ background for the HH $\rightarrow b\bar{b}b\bar{b}$ physics channel has been considered in the present analysis. The analysis presented in Reference [57] focusses on the HL-LHC scenario for Higgs pair production in the $4b$ final state and shows that the significance reduces by around 20 % in the resolved category by considering other background processes, for example, QCD $2b2j$, $4j$ and $t\bar{t}$ production (with hadronic final states). The reduction is more pronounced for the boosted category where the inclusion of the above background processes reduces Z by half. For the resolved analysis presented here, even a 30 % drop in Z due to other backgrounds would still result in significances well above the 5σ discovery reach. In particular, for the SM signal, Z will reduce to around 30, which is six times higher than the 5σ significance required for discovery. Therefore, the final significance will largely depend on the b-tagging efficiency and light and charm jet misidentification rates.

- The effects of a very high pile-up will also reduce Z to some extent. Reference [57] shows that the effect of pile-up on the final results of the analysis will be mild for the HL-LHC scenario with an average pile-up of 200. The effects of an average pile-up of ~ 1000 might be different, and hence pile-up suppression techniques (both online and offline) will be crucial for carrying out a good analysis.

- The results presented in this chapter are based on a simple traditional cut based analysis. Use of the state-of-the-art analysis techniques, for example, multivariate analysis (MVA) techniques or more advanced machine learning techniques can improve the results significantly. In Reference [57], a gain of > 4 in the significance determined by cut based analysis is obtained following the application of MVA.

- A further improvement of the signal significance can be achieved by including the intermediate and the boosted categories.

- Final measurements would also depend largely on the systematic uncertainties, especially for those associated with background estimation. Generally, two different methods are used for estimating the background events for a given signal process. One is by extrapolation of data from a signal free side-band region (*data-driven background estimation*) and other is by using MC simulations. Use of simulations for estimating QCD background introduces large normalisation uncertainties as many higher order corrections are not considered by the MC generators. The first method has the advantage of not relying on potentially incorrect simulations, but it usually does not predict the shape of the background underneath a signal distribution. Some of the other common sources of systematic uncertainties include the uncertainties introduced due to b-tagging and mis-tagging of jets, energy calibration and resolution uncertainties, theory uncertainties that result from variations of renormalisation and factorisation scales, PDF set uncertainties, and uncertainties in modelling of the underlying event and hadronic showers (hence varying ISR and FSR), uncertainties from the integrated luminosity recorded, etc.

3.3 Sensitivity Studies

The trilinear Higgs self-coupling λ is one of the key benchmark measurements that future hadron collider experiments are aiming for. As mentioned earlier, its measurement is extremely challenging owing to the smallness of di-Higgs production cross-section and very high background cross-section. Besides, a further complication in the extraction of λ from di-Higgs cross-section arises due to the destructive interference between the diagrams that are related to λ (the triangle diagram), and those that are not (the box diagram in Figure 2.5(a)). Enhanced cross-sections for di-Higgs production for certain BSM trilinear Higgs couplings allows putting a limit on the precision with which k_λ can be measured. The relevant question to ask here is whether the dataset is compatible with a model described by a parameter λ (or k_λ) or not? Let's assume that the number of signal events in each of the i^{th} bins can be linearized as a function of k_λ (expected hypothesis), i.e.

$$\begin{aligned} S_i(k_\lambda) &= S_i(k_\lambda^{\mathrm{SM}}) + \frac{\mathrm{d}S_i}{\mathrm{d}k_\lambda}\Delta k_\lambda \\ &= S_i^{\mathrm{SM}} + c_i \Delta k_\lambda, \qquad (3.7) \\ \text{with } k_\lambda &= k_\lambda^{\mathrm{SM}} + \Delta k_\lambda. \qquad (3.8) \end{aligned}$$

To measure the discrepancy between data and the expected hypothesis a sensitivity to the parameter k_λ can be defined as

$$\text{Sensitivity} = \frac{\mathrm{d}\chi}{\mathrm{d}k_\lambda}, \tag{3.9}$$

$$\text{for } \chi^2 = \sum_{bins=i}^{N} \frac{(x_i - (S_i(k_\lambda) + B_i))^2}{\sigma_i^2}, \tag{3.10}$$

where $\sigma_i^2 = S_i(k_\lambda) + B_i$ and x_i is the number of measured events in the i^{th} bin. Using Equation 3.7, the total sensitivity over all the N bins can be written as:

$$(\text{Sensitivity})^2 = \sum_i^N \frac{c_i^2}{\sigma_i^2} = \sum_i^N \frac{c_i^2}{S_i^{\mathrm{SM}} + B_i}. \tag{3.11}$$

Figure 3.14(a) shows the sensitivity as a function of k_λ for six different 4^{th} leading jet p_T thresholds (shown with different coloured lines).[10] Since S_i for a given k_λ is proportional to the corresponding cross-section (which has a quadratic behaviour as a function of k_λ; see Figure 2.8), c_i has a linear dependence on k_λ. As a result, the sensitivity varies linearly as a function of k_λ. Once again, one can see the importance of keeping the 4^{th} leading jets p_T threshold low, allowing to cover a large phase space for the signal events and enhancing the sensitivity. Figure 3.14(b) shows the bin by bin contribution to the total sensitivity (obtained by setting the $p_{\mathrm{T,j4}}^{\mathrm{tagged}}$ threshold = 20 GeV/c). As expected, the most significant contribution comes from the highest p_T bin as the signal to background ratio is the highest

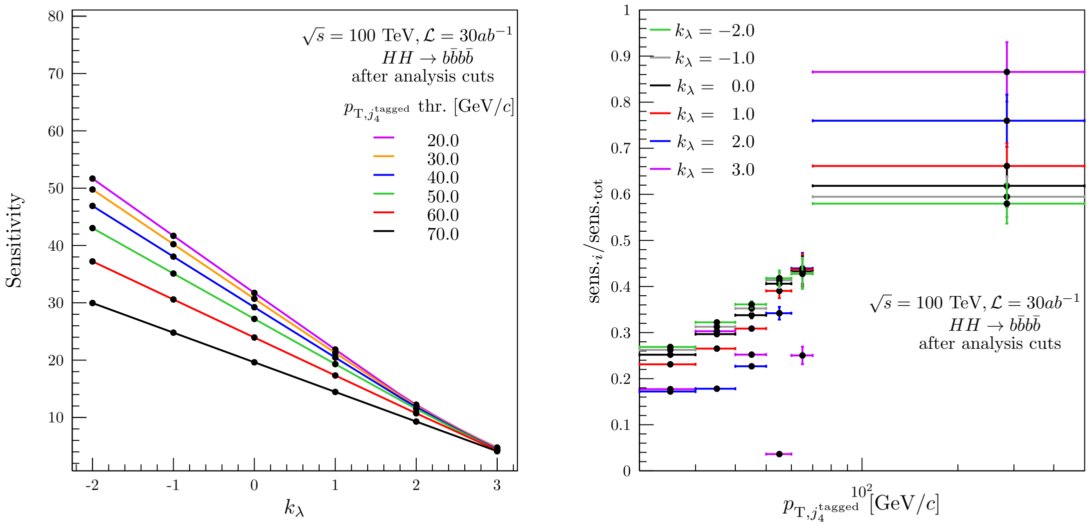

(a) **(b)**

Figure 3.14: (a) Total sensitivity as a function of k_λ at various p_T thresholds of the 4^{th} leading b-jet and (b) Contribution of different p_T bins to total sensitivity for various values of k_λ in HH → $b\bar{b}b\bar{b}$.

---

[10] One can similarly investigate the impact of the first three leading b-jet p_T thresholds on signal significances and sensitivities, however this is left for future studies.

in this bin. The contributions from most of the bins are $\geq 20\,\%$ for all the k_λ values considered here, except for $k_\lambda \geq 2$, where the contributions from the first few bins are much lower. In particular for $k_\lambda = 3$, one sees large fluctuations in the bin contributions with more than $10\,\%$ rise in the sensitivity contribution from the bin $30 - 40$ GeV/c and the least contribution from the bin $50 - 60$ GeV/c. This can be understood by recalling the two peak structure (dips) due to the destructive interference between the triangle and the box diagrams in the p_T distributions of the pair of Higgs's (see Figure 3.9) for $k_\lambda > 2$.

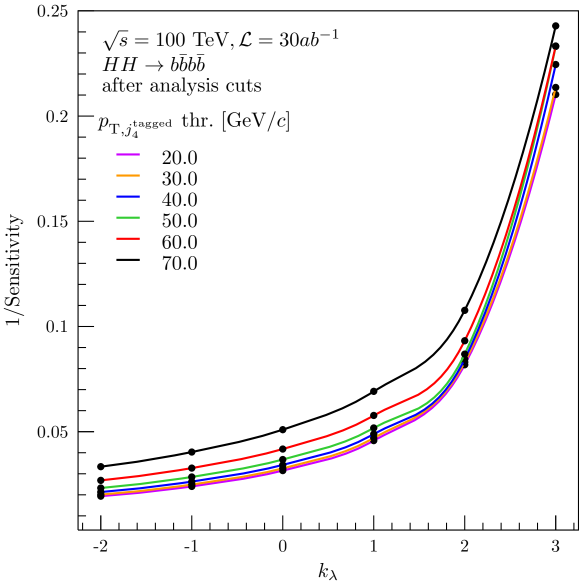

Figure 3.15: Precision as a function of k_λ at various p_T thresholds of the 4^{th} leading b-jet in $\mathrm{HH} \to b\bar{b}b\bar{b}$.

The inverse of the sensitivity would give the *precision* on the measurement of k_λ. Figure 3.15, shows the precision with which k_λ can be measured for various $p_{\mathrm{T,j_4}}^{\mathrm{tagged}}$ thresholds (indicated by different colours), without systematic uncertainties. The Higgs self-coupling for the SM signal can be measured with around $5\,\%$ at a 100 TeV pp circular collider with a total integrated luminosity of $30\,\mathrm{ab}^{-1}$, if the systematic uncertainties are minimal, and the trigger thresholds are kept low.

To summarise, this chapter presented a very simple cut-based generator level analysis for the resolved category of $\mathrm{HH} \to b\bar{b}b\bar{b}$ physics channel in the ggF production mode, for a 100 TeV pp collider with a total integrated luminosity of $30\,\mathrm{ab}^{-1}$ (with a huge scope for improvement with the existing advanced analyses techniques – beyond the scope of this thesis). This physics channel sees an enormous QCD multi-jet background, which dominates even after the event selection cuts, and the signal to background ratio is $\mathcal{O}(10^{-3})$ or lower for the various k_λ values considered here. However, the huge statistics available – because of an integrated luminosity of $30\,\mathrm{ab}^{-1}$ – makes this small S/B still very useful. One can conclude to a first approximation that despite the overwhelming amount of QCD multi-jet background associated with the Higgs pair production process in the $b\bar{b}b\bar{b}$ final state, it can be measured with a significance well above the 5σ requirement and a precision of $\sim 5\,\%$, provided the trigger thresholds are low enough to allow a wide phase space region coverage and the systematic uncertainties, especially those related to b-tagging efficiency and background estimation are not very high.

The next part of the thesis introduces two of the future hadron collider experiments and briefly discusses the challenges and the assumptions for various parts of the experiment due to the enormous instantaneous luminosity of the colliding beams.

Part II

Future Hadron Colliders

4

The High Luminosity LHC

A major luminosity upgrade for the Large Hadron Collider (LHC) after Run3 (2021 – 2024) aims to crank up the performance of the LHC to fully exploit its intensity frontier at the maximum possible centre-of-mass energy of 14 TeV until the end of its lifetime. Hence, the LHC will collide proton-proton (pp) beams with a peak instantaneous luminosity (L) of five times the design luminosity of the LHC ($1 \times 10^{34}\mathrm{cm}^{-2}\mathrm{s}^{-1}$).[1] This new phase of the LHC has been named as High Luminosity LHC (HL-LHC). Large instantaneous luminosity implies an increase in data rate and pile-up and therefore, demands upgrade of some of the present detector technologies, electronics and data acquisition system to cope with the challenging environment. Such a high luminosity upgrade will allow accumulation of a total integrated luminosity of up to $3000\,\mathrm{fb}^{-1}$ after HL-LHC's operation for a decade starting from 2027. This corresponds to more than ten times the total integrated luminosity accumulated by the LHC in its first 12 years of operation.

This chapter starts with an introduction to the LHC, along with the accelerator chain preceding it, in Section 4.1. The challenges and the technological limitations for the HL-LHC phase are briefly discussed in Section 4.2. In Section 4.3, one of the two general-purpose experiments of the LHC, i.e. the ATLAS experiment, w.r.t. the HL-LHC is discussed, and some important numbers w.r.t. its tracker and the Trigger and Data Acquisition (TDAQ) system are listed.

4.1 The Large Hadron Collider

The LHC [5] is the largest and the most powerful particle accelerator in the world built by the European Organization for Nuclear Research (CERN). It is installed in the tunnel of the former Large Electron-Positron Collider (LEP) [70], which has a circumference of 26.7 km and lies $\sim$ 100 m beneath the Swiss-French border near Geneva; see Figure 4.1. It is designed to collide pp beams with a centre-of-mass energy ($\sqrt{s}$) = 14 TeV. There are four major experiments at the LHC: the two general-purpose experiments - A Toroidal LHC ApparatuS (ATLAS) [6] and Compact Muon Solenoid (CMS) [7], and two more specific experiments - A Large Ion Collider Experiment (ALICE) [8] and Large Hadron

---

[1] Design margins should allow for an ultimate peak instantaneous luminosity of $\sim 7.5 \times 10^{34}\mathrm{cm}^{-2}\mathrm{s}^{-1}$ [12].

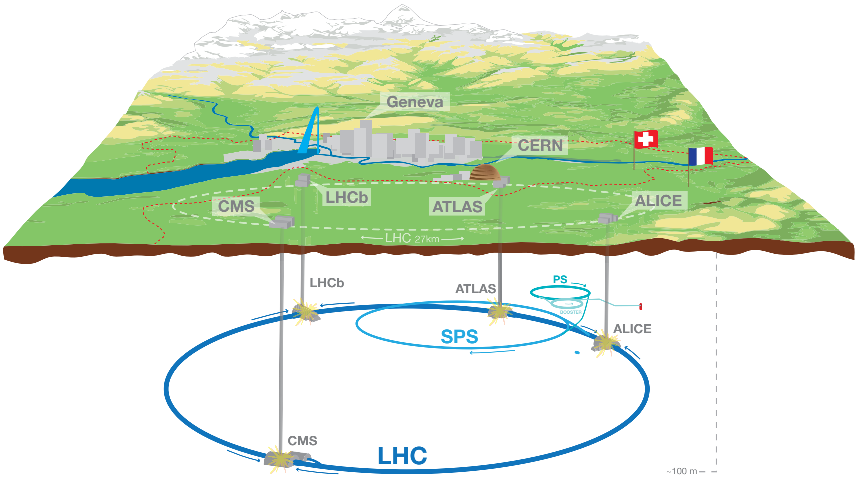

Figure 4.1: Overall view of the LHC, including its four major experiments [71].

Collider beauty (LHCb) [9] focussed mainly on quark-gluon plasma and b-physics studies. In addition to these four, there are three more small experiments at the LHC namely, Total Elastic and diffractive cross-section Measurement (TOTEM) [72], Large Hadron Collider forward (LHCf) [73] and Monopole and Exotics Detector At the LHC (MoEDAL) [74].

The LHC smashes lead-lead (Pb-Pb) and proton-Pb beams in addition to the *pp* beams. To accelerate these particles to their final energies a chain of particle accelerators is used; see Figure 4.2. In the case of *pp* collisions, protons are obtained by stripping off electrons

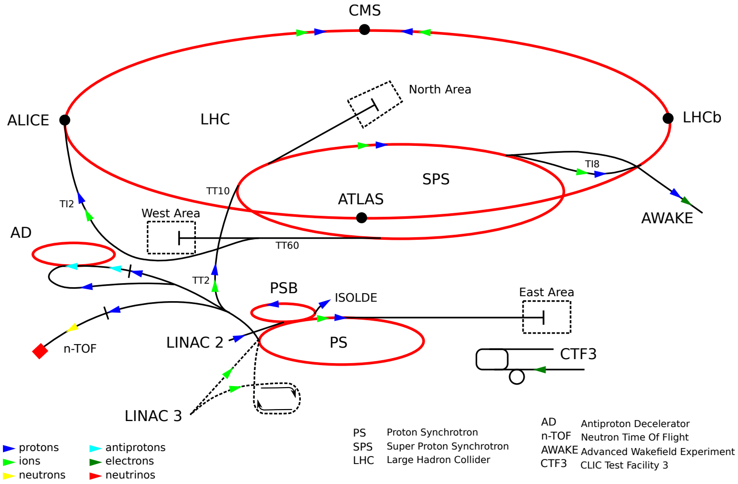

Figure 4.2: Schematic of the CERN accelerator complex [75].

from pure hydrogen gas. These protons enter the first acceleration stage Linear Accelerator 2 (Linac 2), where they are accelerated to the energy of 50 MeV. They are further accelerated to 1.4 GeV by injecting them into the Proton Synchrotron Booster (PSB). The PSB has a radius of 25 m and consists of a stack of four synchrotrons sharing a common main magnet and focussing quadrupoles, a common main power converter and vacuum system [76]. These 1.4 GeV protons are then injected into the Proton Synchrotron (PS) to be accelerated to 25 GeV. The PS is one of the key components in CERN's accelerator complex and was CERN's first synchrotron becoming operational on 24 November 1959. It has a circumference of 628 m and consists of 277 conventional electromagnets, including 100 dipoles to bend the beams round the ring.[2] Protons are then fed to the second largest machine in CERN's accelerator complex, the Super Proton Synchrotron (SPS), where they are accelerated to 450 GeV. The protons from the SPS are finally injected to the two beam-pipes of the LHC. The SPS measures nearly 7 km in circumference and provides accelerated beams not only to the LHC but also to other experiments like the SPS Heavy Ion and Neutrino Experiment (NA61/SHINE) and NA62 experiments, and the Common Muon and Proton Apparatus for Structure and Spectroscopy (COMPASS) experiment [77]. Both the PS and the SPS have been used to accelerate protons, anti-protons, electrons, positrons and heavy ions. One of the major breakthroughs for the SPS, however, occurred when it operated as a proton-antiproton collider leading to the Nobel-prize-winning discovery of the W and the Z bosons [78, 79].

The LHC consists of a total of 1232 superconducting Niobium-Titanium dipole magnets with a magnetic length of 14.3 m each to bend the beams, and 392 quadrupole magnets (5 – 7 m in length) to focus the beams. The bending radius of the beams is therefore given by: $\rho = 1232 * 14.3/(2\pi) = 2804\,\text{m}$. ρ together with the magnetic field $B = 8.33\,\text{T}$ of the superconducting magnets limit the maximum energy of the proton beams in the LHC. The maximum energy of the proton beams in each of the two beam-pipes is given by: $p = 0.3B\rho = 7\,\text{TeV}$. The proton beams entering the LHC are not continuous but are in the form of several bunches, with each bunch containing up to 1.15×10^{11} protons. Each consecutive bunch is separated by 7.5 m which move close to the speed of light inside the 27 km ring. This results in a bunch spacing of ($7.5\,\text{m}/3 \times 10^{8}\,\text{m}\,\text{s}^{-1}$) 25 ns and ∼2808 bunches. Thus, bunch collisions at the four main experiments occur every 25 ns during LHC's operation. It takes 4 min 20 s to fill each LHC ring, and around 20 min for the protons to reach an energy of 6.5 TeV [80].[3]

4.2 Increased Luminosity and Challenges

The LHC circulated the proton beams for the first time on 10 September 2008. During Run2 (2015 to 2018) of data taking, i.e. after the first long shutdown (LS1), the LHC managed to reach its design centre-of-mass energy of 14 TeV and a peak instantaneous luminosity (L) of $2.1 \times 10^{34}\text{cm}^{-2}\text{s}^{-1}$. The second long shutdown (LS2) is underway at the time of writing this thesis. An astonishing increase in the total integrated luminosity of $4000\,\text{fb}^{-1}$ using the ultimate value of L will be achieved in a little more than a decade after

---

[2] Before 26 May 1972 (when the PSB received its first beam), 50 MeV protons from the Linac 2 were directly injected into the PS.

[3] Under normal operating conditions, the beams circulate for several hours inside the LHC beam-pipes.

LS3. Figure 4.3 shows the projected instantaneous and the integrated luminosities in red and blue, respectively, over several years. This will significantly increase the mass reach up to TeV scale to answer some pressing questions in particle physics, as seen in Chapter 2.

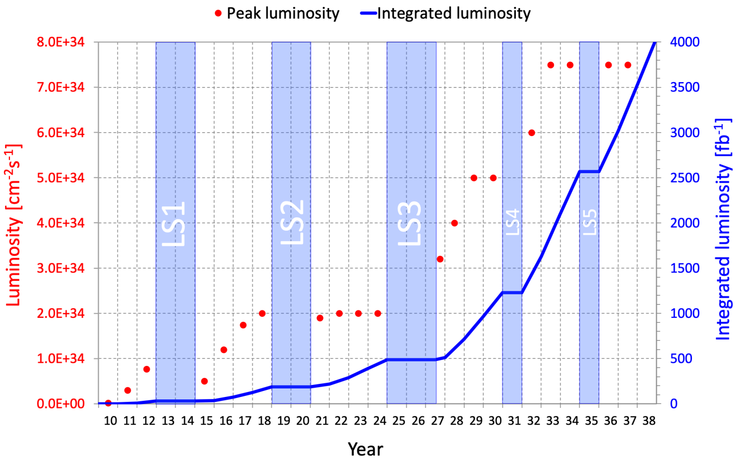

Figure 4.3: Instantaneous and integrated luminosities for Run1 and Run2 including projections for Run3 and the HL-LHC using the ultimate instantaneous luminosity at HL-LHC [81].

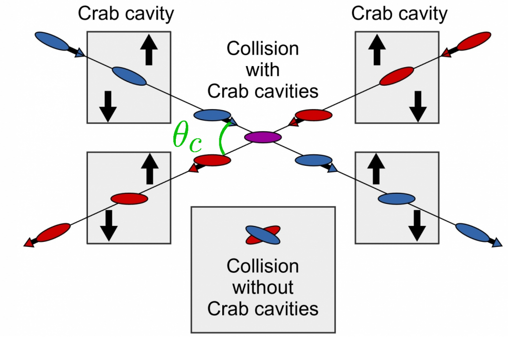

Figure 4.4: Depiction of beam manipulation using superconducting radio frequency (RF) crab cavities (CC) (the arrows indicate the torque on the bunch generated by the transverse RF field). Bunch collision at IP without CC is also shown. Figure adapted from [82].

From Equations 1.44 and 1.45, one sees that an increase in L requires reduction of β at the IP (β^*), the transverse normalized emittance ϵ_n, and (or) the number of particles per bunch. Therefore, the number of particles for each of the 2808 bunches revolving with $f_{\text{rev}} = 11.2\,\text{kHz}$ and 25 ns bunch spacing in the LHC ring will be increased from 1.15×10^{11} to 2.2×10^{11} for the HL-LHC. ϵ_n and β^* will be reduced to 2.5 µm and 20 cm for the HL-LHC as opposed to 3.75 µm and 55 cm for the LHC [12]. Reducing β^* is particularly challenging as small β^* requires large crossing angle (θ_c) between the colliding bunches, which results in the reduction of the geometrical factor R. This challenge has been addressed by using superconducting radio frequency (RF) crab cavities (CC) to compensate for R in a very efficient and elegant way by generating transverse electric field to provide a torque to the beam. This causes each of the bunches to rotate by $\theta_c/2$, allowing perfect overlap and hence head-on collision between the two bunches at the IP; see Figure 4.4.

Since the LHC and its experiments were designed to handle a nominal luminosity of 1×10^{34} cm^{-2}s^{-1}, a huge upgrade was planned in three different phases for the HL-LHC project. The HL-LHC will produce collisions at a rate of about 5×10^9 s^{-1}. The resulting particles from these collisions and the radioactivity they would induce in the material of the (non-upgraded) detectors and the on-board electronics would significantly damage them, thereby leading to progressive degradation of the detector performance.

In addition to the high radiation dose, a major challenge to the LHC experiments will be the overwhelming number of pp collisions per BX (pile-up). The expected average pile-up ($\langle\mu\rangle$) for an ultimate instantaneous luminosity of 7.5×10^{34}cm^{-2}s^{-1} and $\sigma_{\text{inel}} = 85$ mb at $\sqrt{s} = 14$ TeV can be determined using Equation 1.49 and is around 200 compared to only ~ 34 in Run2. Figure 4.5(a) and (b) show $\langle\mu\rangle$ per BX for the Run2 data taking period of the present ATLAS detector and event display of $t\bar{t}$ event with an expected $\langle\mu\rangle = 200$ using an upgraded ATLAS simulation for HL-LHC, respectively. The dense environment very close to the beamline (in Figure 4.5(b)) is indicative of the intensity of the challenges put forth for the experiments. The enormous amount of pile-up results in very large data rates and occupancies, which therefore demands upgrade not only of the detector elements but also of the read-out electronics, the trigger and the data acquisition (TDAQ), and the storage systems. Section 4.3 briefly discusses the major upgrades of the ATLAS detector for the HL-LHC project.

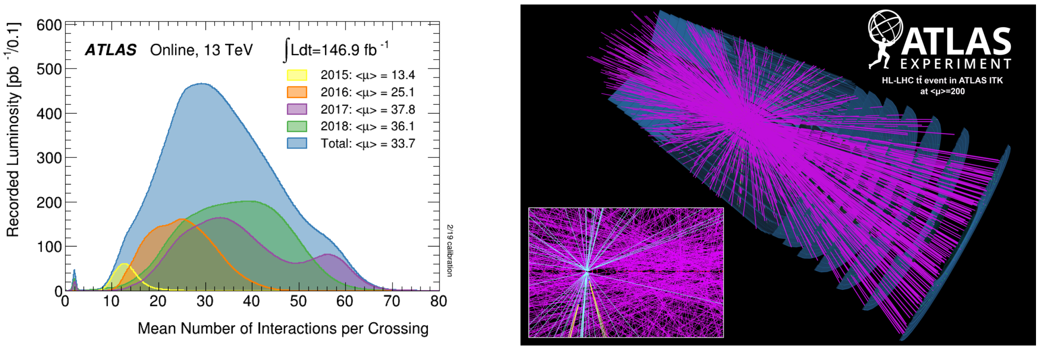

(a) **(b)**

Figure 4.5: (a) Average pile-up per BX during Run2 data taking [83] and (b) simulated event display of $t\bar{t}$ event with an average pile-up of 200 collisions per BX in the ATLAS experiment for HL-LHC [84].

4.3 The ATLAS Experiment at the HL-LHC

The ATLAS experiment [6] is a multi-purpose particle physics experiment at the LHC. Its detector has a length of 44 m, a diameter of 25 m and weighs around 7000 tonnes. A computer generated image of the ATLAS detector before the HL-LHC upgrade is shown in Figure 4.6. The IP lies at the centre of the detector and a right-handed coordinate system with its origin at the IP (see Section 1.2.1) is used. Several types of particle detectors are combined to ensure a hermetic coverage in solid angle. The central part of the detector has a barrel shape, and the forward part consists of disc-shaped detectors (also called the endcap detectors) in order to detect particles with directions close to the beam-axis. With increasing radial distance from the IP, the present ATLAS detector consists of the Inner Detector (ID) surrounding the beamline, followed by the solenoid magnet, the calorimeters and the muon spectrometer.

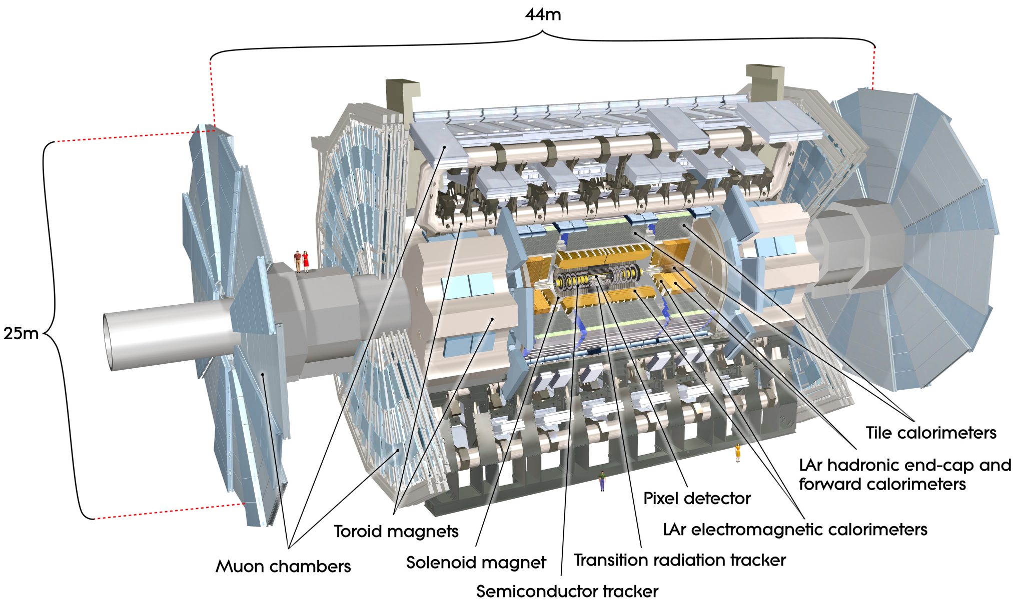

Figure 4.6: Computer generated image of the whole ATLAS detector before HL-LHC upgrade [85].

The ID [86] comprises three independent sub-detectors, namely, the pixel detector located very close to the IP, followed by the Semiconductor Tracker (SCT) and the Transition Radiation Tracker (TRT). The ID is enveloped by a solenoid magnet which creates a magnetic field of 2 T parallel to the beamline, allowing bending of all the charged tracks for momentum determination.

Surrounding the solenoid magnet are the calorimeters that record the energy deposits of particles undergoing various kinds of interaction by stopping them within the calorimeter. Muons being minimum ionising in nature make very little interaction with the detector material and pass through the calorimeter to be detected by the muon spectrometer which is completely surrounded by massive air-core toroids producing magnetic fields of approximately 0.5 – 1.0 T. In addition to the above detectors, the ATLAS experiment also features detectors for luminosity monitoring (Luminosity measurement using a Cherenkov Integrating Detector (LUCID)) and total cross-section measurements (Absolute Luminosity For ATLAS (ALFA)) [87].

The upgrade of the ATLAS detector to deal with the harsher radiation environment and higher detector occupancies at the HL-LHC is planned in three phases: Phase-0, Phase-I and Phase-II.

- The Phase-0 upgrade of the ATLAS detector (LS1: 2013 – 2014) mainly involved the installation of a new ID cooling system, a new neutron shielding of the muon spectrometer and a new aluminium based beam-pipe replacing the old one based on stainless steel.[4] The central upgrade activity in Phase-0 was the installation of the new Insertable B-layer (IBL) [88] at a radius of 33 mm in between the beam-pipe (R = 25 mm) and the innermost pixel layer (also called the B-layer at R = 50.5 mm) of the ID. Due to its proximity to the IP, the IBL allowed improvement of vertex resolution and b-tagging, hence extending the reach of the physics analysis.

- The Phase-I upgrade of the ATLAS detector (LS2: 2019 – 2020) involves the installation of one of the two New Small Wheel's (NSW) [89] replacing the first endcap station of the muon spectrometer,[5] and installation of new trigger schemes. It also involves upgrading the level-1 trigger processors along with the installation of electronic cards for the TDAQ system.

- By the end of Run3 some of the existing sub-detector components will reach the end of their lifetime due to radiation damage. A few others are not capable of handling the extreme conditions due to very high occupancies and data rates at the HL-LHC. Therefore, during the Phase-II upgrade of the ATLAS detector (LS3: 2025 – 2027), most of the sub-detectors, including the TDAQ system, will undergo upgrade. Since the focus of this thesis is future hadron collider experiments, the ATLAS detector for the Phase-II upgrade of the HL-LHC is detailed in the following sections. Previous sub-detectors are mentioned whenever necessary.

4.3.1 Inner Tracker (ITk)

One of the major changes to the existing ATLAS detector for the Phase-II upgrade involves the complete replacement of the ID by an all-silicon tracking detector called the Inner Tracker (ITk). Similar to the ID, the ITk will have pixel and strip subsystems; see the latest ITk layout (at the time of writing this thesis) shown in Figure 4.7.[6] Due to very large occupancies expected for the TRT during Run4 (post HL-LHC upgrade), its operation is unfeasible for the HL-LHC [92].

The pixel subsystem [94] of the ITk (shown in red) consists of five flat barrel layers and five layers of inclined or vertical rings covering a pseudorapidity range of $|\eta| < 4.0$ (compared to $|\eta| < 2.5$ in ID). The innermost pixel barrel consists of single-chip modules and sits at a radius of 39 mm, while the remaining four pixel barrel layers consist of quadruplet (quad) modules comprising 2×2 readout chips located at radii of 99 mm, 160 mm, 228 mm and 291 mm, respectively. The expected radiation fluence for the innermost and the outermost pixel layers are $\sim 1.5 \times 10^{16} \mathrm{n_{eq}cm^{-2}}$ and $\sim 3 \times 10^{15} \mathrm{n_{eq}cm^{-2}}$ respectively; see Figure 4.8(a). Total Ionizing Dose (TID) of as large as 1×10^{7} Gy are expected for a total integrated luminosity of $3000\,\mathrm{fb}^{-1}$; see Figure 4.8(b). Therefore, the traditional

---

[4] The aluminium based beam-pipe lead to 10–20 % reduction in backgrounds for the muon spectrometer.

[5] Although the initial plan was to install two NSW in the forward regions, only one is installed during LS2 as the assembly of the other NSW will not be complete before the end of LS2.The plan is to install the 2^{nd} NSW in the next Year End Technical Stop (YETS) [90].

[6] Note that the barrel layers of all the sub-detector systems in ATLAS are divided into two halves with a small gap at $z = 0$.

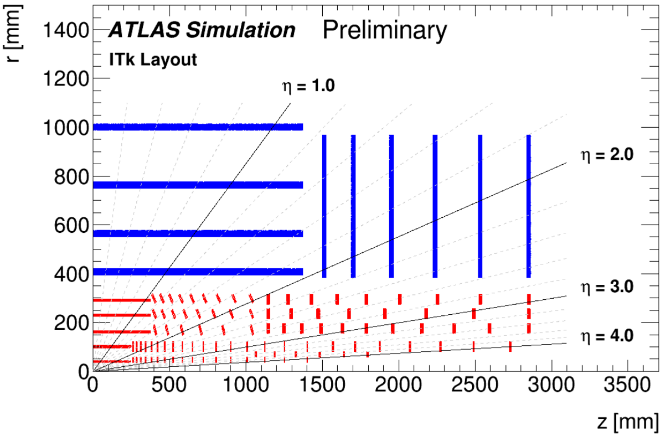

Figure 4.7: A schematic depiction of the ITk Layout for the HL-LHC. Only active detector elements in one quadrant are shown. The active elements of the strip detector are shown in blue, and those of the pixel detector are shown in red. The horizontal axis is along the beam line with zero being the interaction point. The vertical axis is the radius measured from the interaction region [91].

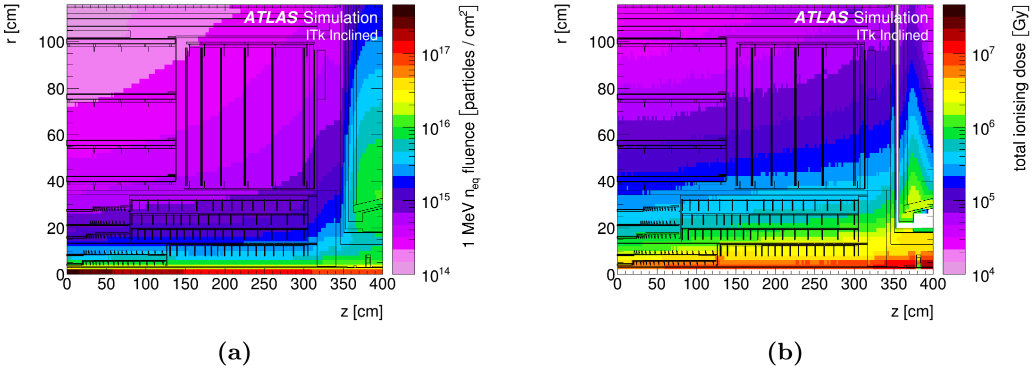

(a)

(b)

Figure 4.8: Simulated Non-Ionizing Energy Loss (NIEL) fluence (a) and Total Ionizing Dose (TID) (b) distributions for the ATLAS ITk layout for an integrated luminosity of 3000 fb^{-1} [93].

hybrid pixel sensor technology is used for the entire pixel detector although monolithic sensor technology (owing to its low cost due to commercial production) was considered as an option for the outermost pixel layer.[7] Two different pixel dimensions: $50 \times 50\mu\text{m}^2$ and $25 \times 100\mu\text{m}^2$, are under consideration at the time of writing this thesis.[8]

The strip subsystem [93] (shown in blue) comprises four strip layers in the central barrel region and six endcap discs on each side of the barrel, covering a pseudorapidity range of $|\eta| < 2.7$. It extends from -1372 mm to $+1372$ mm along the z-axis and from 399 mm

---

[7] Monolithic pixel sensors combine the sensor and the readout electronics into a single unit, thereby reducing the material budget to a large extent unlike hybrid pixel sensors, where the sensor is bump bonded to the readout chip. Presently, monolithic pixel sensors can tolerate fluences of $\sim 2 \times 10^{15} \text{n}_{\text{eq}}\text{cm}^{-2}$ [95]. A brief discussion on the two technologies is made in Section 6.1.

[8] Pixel size of $25 \times 100\mu\text{m}^2$ has been used for the results presented in Chapters 7 and 8.

(endcap: 385 mm) to 1000 mm in radius.[9] The length of the strips ranges from 19.0 mm to 60.1 mm depending on their proximity to the beamline. The basic element of the ITk strip detector is the silicon strip module, which consists of a silicon micro-strip sensor and readout electronics. The ITk strip sensors are around ten times more radiation tolerant than the ones in the ID, which is good enough to maintain the strip detector performance until the end of HL-LHC. These strip modules are mounted on either side of light and sturdy mechanical support structures called staves in the barrel part and petals in endcap region. Many staves (petals) – staggered to give a hermetic coverage – together form a barrel (endcap) layer. A stereo angle of 52 mrad (40 mrad) between the strips on the opposite sides of the stave (petal) provides 2D space points to be used for tracking.

The ITk will offer more extensive rapidity coverage, higher readout bandwidth, higher granularity and higher radiation tolerance compared to the ID. A charged track passing through all the layers of the ITk would ideally result in five pixel hits and eight hits from the double sided strips. The ATLAS track reconstruction algorithm for the ITk requires at least 9 pixel + strip hits in the central pseudorapidity region, $|\eta| < 2.0$, with at least one of them being a pixel hit and a possibility of one missing hit (called as a hole). Track parameters are reconstructed using an iterative, combinatorial track reconstruction algorithm called Kálmán Filter [96]. A minimum track p_{T} of 900 MeV, maximum transverse impact parameter (d_0) of 2 mm and longitudinal impact parameter (z_0) of 200 mm are required in addition. An all-silicon based ITk for the ATLAS Phase-II detector is expected to perform as good and even better than the ID in many cases, in a significantly difficult tracker environment [91].

4.3.2 Trigger and Data Acquisition System

The Trigger and Data Acquisition (TDAQ) system is one of the most crucial parts of the ATLAS experiment. A trigger is a system that uses simple criteria to rapidly decide which events to keep when only a small fraction of the total can be recorded. The data produced at a rate of 40 MHz is reduced by more than $\mathcal{O}(10^3)$ to be stored for offline analysis by the TDAQ system at a rate of 1 kHz within $\mathcal{O}(1\,\mathrm{s})$ (Run3) [97].

The TDAQ architecture for the ATLAS Phase-II upgrade will be re-designed completely as the Run3 TDAQ system does not have the scalability required to cope with a factor of more than twenty increase in bandwidth requirement resulting from increased event size and higher data rates. The TDAQ upgrade is mainly motivated by the broad physics programme of the ATLAS during the HL-LHC, which includes a wide range of topics including some of the very rare physics channels. The physics requirements are a set of p_{T} threshold and acceptance rate requirements from MC analysis and projections – for the relevant objects, e.g. e, μ, τ, jet, invariant masses, etc. – that motivate the trigger requirements.

The baseline TDAQ system [69] consists of a Level-0 Trigger System (L0), the Data Acquisition (DAQ) system, and the Event Filter (EF) system; see Figure 4.9. The Level-0 trigger

---

[9] The radii at which the barrel layers are located and the z-positions of the endcap disks are chosen to optimise the number of hits on a track and the p_{T} resolution [93].

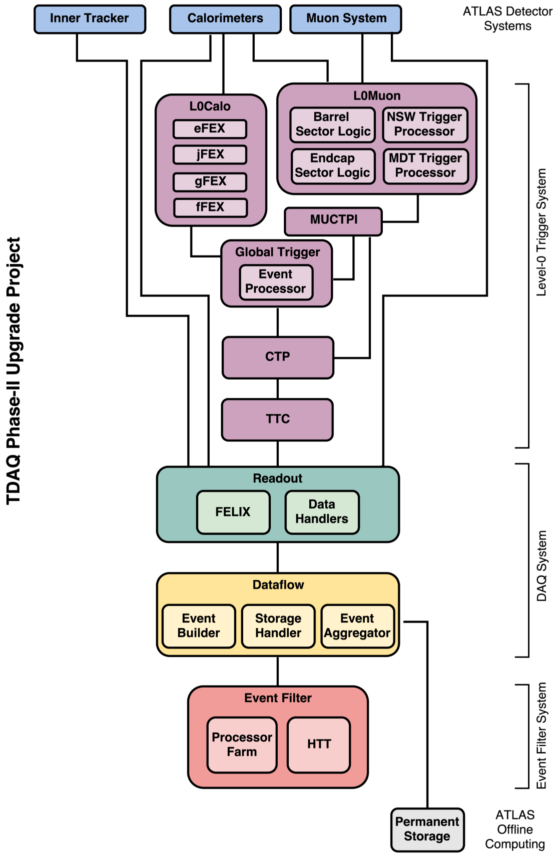

Figure 4.9: Functional block diagram of the baseline TDAQ Phase-II upgrade architecture, highlighting the three main sub-systems: Level-0 Trigger, DAQ, and Event Filter. Direct connections between each Level-0 trigger component and the readout system are suppressed for simplicity [69].

system comprises of several trigger sub-systems, namely, the L0Calo, L0Muon, Global Trigger and the Central Trigger Processor (CTP). L0Calo and L0Muon are similar to the L1 system of Phase-I that use information from the calorimeter and the muon subsystems at 40 MHz to apply an initial event selection to be subsequently examined by the next trigger sub-system.[10] The Global Trigger is a new sub-system in the L0 trigger, which will use full granularity calorimeter data, for example, to perform offline-like algorithms. The CTP will provide the final L0 decision at an acceptance rate of 1 MHz in 10 µs (compared to 100 kHz in 2.5 µs during Phase-I), taking into account the physics (trigger threshold), and dead-time requirements.[11] The resulting trigger data and detector data are transmitted through the DAQ system at 1 MHz. A large EF processor farm is needed to cope with the 1 MHz input rate. It consists of a CPU-based event processing complemented by a fast hardware based track reconstruction sub-system, called the Hardware Track Trigger (HTT). Based on the L0 trigger, the EF uses regional and global tracking information from the ITk to further refine the reconstructed objects to be transferred for permanent

---

[10] L0Calo will have minor upgrades, while the L0Muon will be upgraded significantly compared to the Phase-I, receiving data from all the muon sub-systems and a part of TileCal.

[11] This limit is generally set by many factors, for instance, the storage capacity, readout bandwidth, radiation hardness of the front-end and back-end electronics.

storage at 10 kHz. The raw output event size is expected to be ~ 6 MB, and hence a total bandwidth of $60\,\mathrm{GB\,s^{-1}}$ is expected out of the system.

For Run4, the four-jet trigger threshold will be set to 100 GeV and to 65 GeV with two of the four jets being b-tagged (relevant for the HH $\rightarrow b\bar{b}b\bar{b}$ analysis) with an L0 acceptance rate of 100 kHz [69]. Without an upgrade of the TDAQ system, the four-jet trigger threshold with two b-tags would be 100 GeV with a significantly smaller L0 acceptance rate. As seen from Chapter 2, such high four-jet thresholds will make the measurement of trilinear Higgs self-coupling from the HH $\rightarrow b\bar{b}b\bar{b}$ physics channel alone extremely challenging during the HL-LHC.

4.3.3 Calorimeters

The calorimeter system in ATLAS consists of Liquid Argon (LAr) EM calorimeters, the LAr Forward Calorimeters (FCal), the scintillating tile hadronic barrel detectors (TileCal) and the Hadronic Endcap Calorimeter (HEC); see Figure 4.10. They would maintain their required performance under HL-LHC conditions and therefore do not need replacement, unlike the ITk. The calorimeters in ATLAS are built out of alternating detector layers of material that initiate particle showers followed by material that allow measurement of the energy deposits (sampling calorimeters). The present electromagnetic and hadronic calorimeters are briefly discussed below.

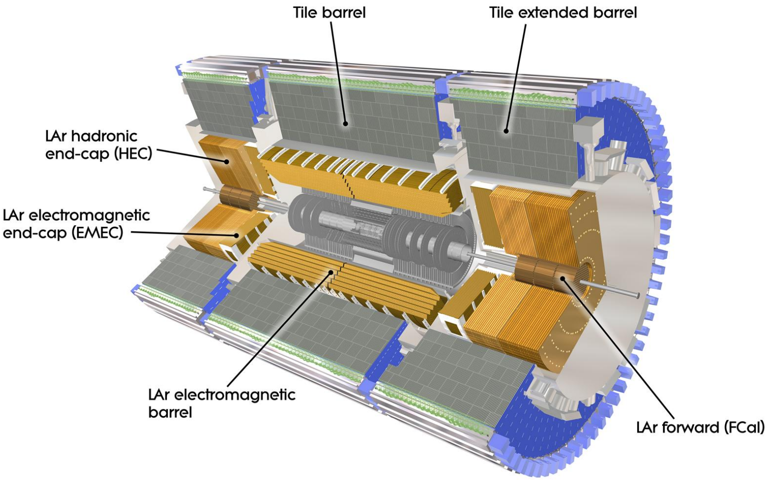

Figure 4.10: Computer generated image of the ATLAS calorimeter [98].

The LAr EM calorimeter consists of two half-barrels (with a small gap at $z = 0$) covering a pseudorapidity range of $|\eta| < 1.475$ and two endcaps (also called Electromagnetic Endcap Calorimeter (EMEC)) on each side of the barrel within $1.375 < |\eta| < 3.2$. Each of the half-barrels measure 3.2 m in length, weigh ~ 57 t and a thickness of 53 cm and are housed in the same cryostat as the solenoid magnet. The endcaps are divided into two coaxial wheels that are 63 cm thick, have a radius of 2.077 m and are placed in independent endcap cryostat's together with the HEC.

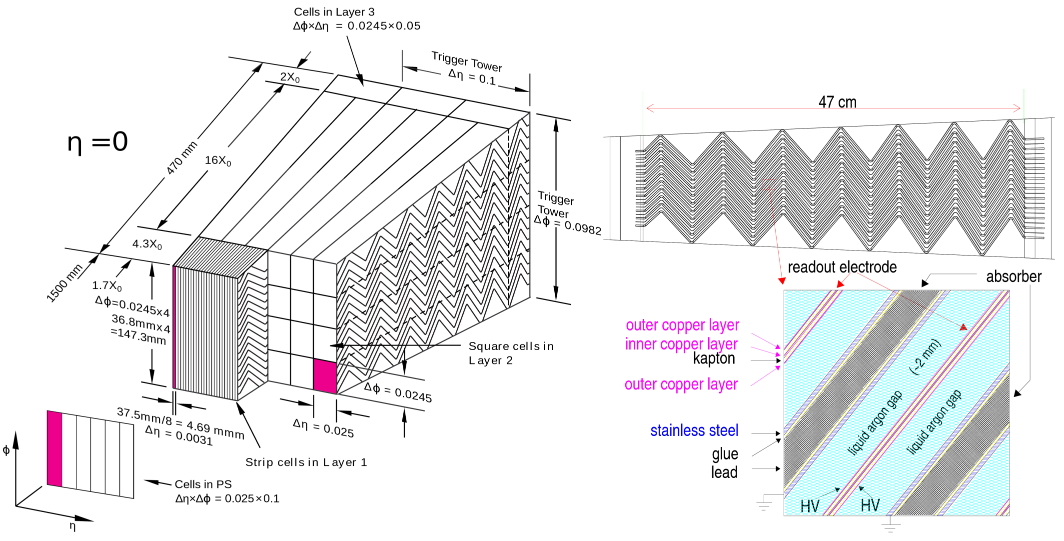

(a) (b)

Figure 4.11: (a) Sketch of an Electromagnetic Barrel (EMB) module with different layers whose granularity in ηandϕ is also shown. (b) Small sector of the EMB in a plane transverse to the beam-axis showing its accordion structure (top) and a magnified view of its small section (bottom) [99].

The Electromagnetic Barrel (EMB) comprises accordion-shaped copper-kapton electrodes positioned between lead absorber plates and kept in position by honeycomb spacers while the system is immersed in LAr at $-183\,°\mathrm{C}$;[12] see Figure 4.11. The lead absorber plates with a thickness between 1.13 mm and 2.5 mm initiate particle showers. The EM calorimeter is divided into three longitudinal layers (indicated as Layer 1, Layer 2, and Layer 3 in Figure 4.11(a)) up to $|\eta| < 2.5$ and is finely divided in the lateral section to provide a precise measurement of electron and photon energies. It has an energy resolution of $\sigma_E/E = 10\,\%/\sqrt{E} \oplus 0.7\,\%$, where E has units in GeV. Particles traversing the gap between the lead absorbers plates, filled with ~ 4 mm of LAr undergo ionization to from the shower, and the electron current is measured with the readout electrodes; see Figure 4.11(b).

The hadronic calorimeter sits just outside of the EM calorimeter and is characterized by its coarse granularity for jet reconstruction together with LAr calorimeter. The hadronic TileCal consists of a cylindrical barrel part with a length of 5.8 m, extending from R = 2.28 m to R = 4.25 m and covering a pseudorapidity range up to $|\eta| < 1.0$. An extended barrel provides an additional pseudorapidity coverage between $0.8 < |\eta| < 1.7$. The TileCal is designed for a jet energy resolution of $\sigma_E/E = 50\,\%/\sqrt{E} \oplus 3\,\%$. It captures approximately 30 % of jet energy and plays an important role in the measurement of jet- and missing-energy, jet substructure, electron isolation, and triggering (including muon information) [100]. It is a sampling calorimeter constructed of $4-5$ mm thick steel plates and 3 mm thick scintillating tiles as absorber and active material, respectively. Ionizing particles produce UV scintillation light in the polystyrene-based material which is doped with fluorine to convert UV scintillation light to the optical spectrum. A wavelength shifter further shifts the light to longer wavelengths which are then read out by photo-multiplier tubes (PMTs).

---

[12] LAr is chosen as active material because of its linear response and intrinsic radiation hardness.

Situated right behind the EMEC are two additional wheels instrumented by the LAr/copper calorimeter modules forming the Hadronic Endcap Calorimeter (HEC) the region $1.5 < |\eta| < 3.2$. The very forward pseudorapidity regions $3.1 < |\eta| < 4.9$ are covered by LAr Forward Calorimeters (FCal). Since the radiation levels in the very forward pseudorapidity regions are very high, the FCal's are placed further away from the ID at $z = 4.7\,\mathrm{m}$ to reduce the radiation initiated by the neutrons reaching the ID. This effect is further mitigated by making a very dense design choice for the FCal.

Upgrades:

The Phase-II upgrades for the calorimeter system involve the upgrade of its readout electronics which have already begun during LS2 (Phase-I). The readout electronics of the LAr calorimeters will be upgraded to provide higher-granularity, higher-resolution and longitudinal shower information from the calorimeter to the trigger at the very first level (L1 trigger). The improved calorimeter readout electronics will allow usage of more sophisticated algorithms (used at higher level trigger) at the L1 trigger to restrict the L1 trigger rates to the maximum of 110 kHz supported by the present front-end (FE) and back-end (BE) electronics.

Since the Phase-I upgrade of ATLAS is limited to a few sub-detectors only, the readout of most of the sub-systems will remain unchanged, thereby, limiting the enhancement of some of the L1 trigger system parameters, for example, the maximum rate (110 kHz) and maximum latency (2.5 µs). The large integrated luminosity during the Phase-II upgrade imposes radiation tolerance requirements on all front-end components, beyond the qualification for the operation of the existing electronics. Therefore, all existing readout and trigger electronics, on- and off-detector, will be replaced to adapt to the new overall trigger architecture and the new requirements in terms of radiation tolerance. Similarly, for the TileCal, the scintillating tiles and the PMTs will not be replaced during the Phase-II upgrade. However, to meet the demands of the new trigger architecture, the present analog electronics will be replaced, and complete digital information from the TileCal will be sent to the trigger system at 40 MHz with a maximum latency of 1.7 µs. The new scheme also demands a large number of optical links ~ 2048 (compared to 256 now) with a bandwidth of 9.6 Gbps (compared to 640 Mbps).

4.3.4 Muon Spectrometer

The Muon Spectrometer (MS) is the outermost detector system of the ATLAS experiment, muons being the only detectable particles that are not stopped by the calorimeters. It covers a pseudorapidity range up to $|\eta| < 2.7$. Figure 4.12 shows the different sub-systems of the MS, namely, the Muon Drift Tubes (MDT), the Cathode Strip Chambers (CSC), the Resistive Plate Chambers (RPC) and the Thin Gas Chambers (TGC) immersed in a magnetic field of $\sim$0.5 T (1 T) generated by a system of one (two) air-core toroid magnets in the barrel (endcap) region. The deflection of the muon trajectories in the magnetic field is measured using the hits in the three MDT layers for $|\eta| < 2$ and in one CSC together with two MDT layers for $2.0 < |\eta| < 2.7$. Three layers of RPC's in the barrel ($|\eta| < 1.05$) and three to four layers of TGC's in the endcaps ($1.05 < |\eta| < 2.4$) provide fast measurements for muon trigger and also measure the muon trajectory in the non-bending coordinate of the toroid magnets. The muon first-level hardware trigger is based on hit coincidences between different RPC or TGC detector layers inside programmed geometrical windows that define the muon p_{T}.

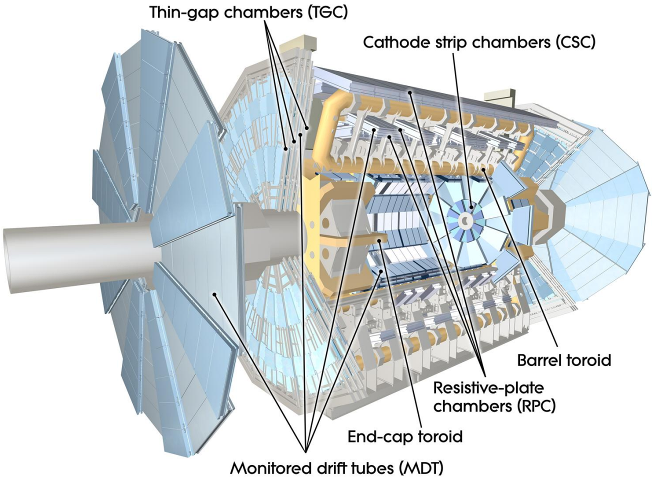

Figure 4.12: Computer generated image of the ATLAS Muons sub-system [101].

The muon spectrometer Phase-II upgrade comprises the installation of new chambers, the replacement of some existing chambers by new ones, and the replacement of a large part of the front-end and trigger and readout electronics [102]. These include the installation of new RPC chambers with increased rate capability to maintain high trigger efficiency. Some of the TGC chambers in the endcap region will be replaced with finer readout granularity TGC to obtain a high purity for triggered muons. The trigger and the readout chain of the RPC and the TGC trigger chambers will be completely re-designed to be compatible with the new Phase-II trigger and readout scheme. Besides, the low-voltage and high-voltage power system of the MS will be replaced as well due to ageing, radiation damage and outdated components.

4.3.5 High Granularity Timing Detector

A completely new detector system that will be installed in the ATLAS experiment during LS3 (Phase-II upgrade) is the High Granularity Timing Detector (HGTD) [103]. It will be housed in the small space available between the LAr calorimeter and the tracking detectors at $z = \pm 3.5\,\mathrm{m}$. It is based on a silicon-based hybrid pixel sensor technology of low gain avalanche diodes (LGAD) and extends from 120 mm to 640 mm (active area) along the radial coordinate covering a pseudorapidity range of $2.4 < |\eta| < 4.0$. These LGAD pixels are $1.3 \times 1.3\,\mathrm{mm}^2$ with an active thickness of 50 µm to which custom application-specific integrated circuit (ASIC) will be bump bonded. They have a very good time resolution per track of around 30 ps. Such an excellent time resolution will help to use the timing information together with the z_0 measurement from the tracker in assigning tracks to vertices and mitigate the impact of a high vertex density in the forward pseudorapidity region of the ATLAS experiment.

5

The Future Circular Hadron Collider

The Future Circular Collider (FCC) [104] is a potential successor of the LHC that is planned to collide particles in a tunnel that is about four times as large as the LHC tunnel. The total circumference of the collider is 97.75 km. The first series of Conceptual Design Reports (CDRs) [13] was delivered at the end of 2018, acting as an input to the European Strategy for Particle Physics Update (ESPPU) 2019/2020. In its latest meeting held in June 2020 [105], the ESPPU highlights the need to pursue an “electron-positron Higgs factory” as the highest-priority facility after the LHC. The FCC study considers a staged research program, similar to the LEP-LHC programme, starting with an electron-positron collider (FCC-ee) followed by a hadron-hadron (proton-proton and heavy ion) collider (FCC-hh) and a possible intermediate electron-hadron collider (FCC-eh). The FCC-ee [106] is planned to operate for around 15 years at four different centre-of-mass energies. Increasing from $\sqrt{s} \sim 91\,\text{GeV}$ (producing $\approx 5 \times 10^{12}$ Z-bosons), it will be followed by $\sqrt{s} \sim 160\,\text{GeV}$ (producing $\approx 10^{8}$ WW pairs), $\sqrt{s} \sim 240\,\text{GeV}$ (producing $> 10^{6}$ Higgs bosons) and $\sqrt{s} \sim 360\,\text{GeV}$ (producing $> 10^{6}$ $t\bar{t}$ pairs).

The goal of the FCC is to push the energy and the intensity frontiers of particle colliders to a large extent in the search for new physics. The FCC-hh, with this goal, will collide proton-proton beams with energies as large as 100 TeV, and (instantaneous) luminosities of more than an order of magnitude larger than LHC’s design luminosity. A dipole field of $\sim 16\,\text{T}$ superconducting Nb_3Sn-based magnets, is required to keep the beams on the circular orbit. The existing accelerator complex with the 26.7 km LHC ring as a possible final stage of the injector chain, called the High Energy Booster (HEB), will allow acceleration of the proton bunches to 50 TeV. The other tunnels that can be used as an HEB include the SPS, which could reach 1.3 TeV if 6 T superconducting magnets are used, and a 3.3 TeV HEB with iron-dominated 1 T superferric magnets housed in the FCC itself [107]. The Linac 4, the PSB, the PS, the SPS and the HEB will constitute the injector chain for FCC-hh; see Figure 5.1. The HEB should be capable of filling the 97.75 km FCC ring with more than $10,000$ proton bunches of 3.3 TeV by accelerating the 450 GeV proton bunches from the SPS. Two different bunch spacing scenarios are under consideration, namely, 5 ns and a baseline of 25 ns.[1]

Two main high luminosity experiments are located at opposite insertion points along the FCC ring, similar to ATLAS and CMS in the LHC. Two additional lower luminosity

---

[1] The results presented in this thesis use the baseline scenario of 25 ns bunch spacing.

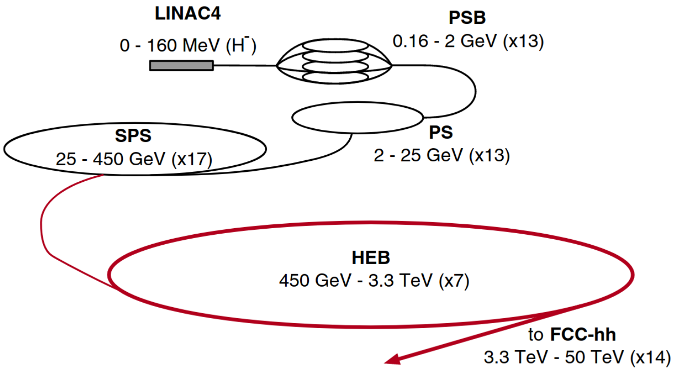

Figure 5.1: Schematic view of the CERN accelerators system viewed as injectors of the future hadron collider (FCC-hh). [41].

experiments are also under consideration. A reference detector design for the FCC-hh experiments is discussed in Section 5.1. The FCC-hh plans to deliver *pp* collision data at $\sqrt{s}$ = 100 TeV with an initial beam luminosity of $5 \times 10^{34}\,\mathrm{cm^{-2}s^{-1}}$ during the first ten years of its operation. The beam luminosity will then be increased to its nominal value of $30 \times 10^{34}\,\mathrm{cm^{-2}s^{-1}}$, with a goal to collect a total integrated luminosity of $30\,\mathrm{ab^{-1}}$ (10× the expected value by the end of HL-LHC operation) over the project lifetime $\sim 25-30$ years. The limitations and the challenges arising due to very high beam luminosity and energy are presented in Section 5.2. Section 5.3 summarises the input parameters considered/assumed for FCC-hh study. Finally, Section 5.4 describes the effect of a very high pile-up on a calorimeter trigger emulated using the baseline calorimeter specifications of the FCC-hh reference detector.

5.1 Reference Detector of the FCC-hh

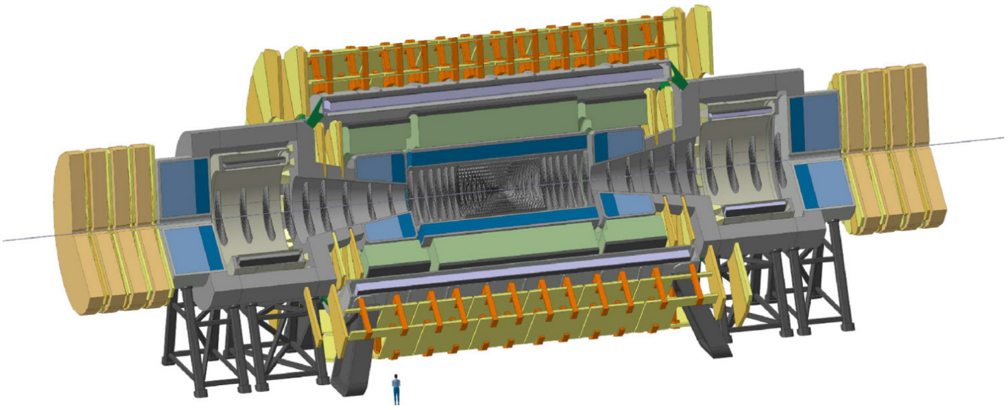

Figure 5.2: The FCC-hh reference detector with an overall length of 50 m and a diameter of 20 m. It comprises different sub-systems: the tracker (grey) surrounding the beampipe, followed by the electromagnetic (blue) and the hadronic calorimeter (green). A 4 T solenoidal magnet followed by the muon system (yellow/orange) surrounds the calorimeter system [41].

A reference detector for the FCC-hh experiments (shown in Figure 5.2) has been designed to serve as a concrete example for detector sub-system and physics studies.[2] It has dimensions comparable to that of the ATLAS detector with an overall length of 50 m and a diameter of 20 m. It has a pseudorapidity coverage of up to $|\eta| \approx 6$; see also Figure 5.3, which shows the layout of one quadrant of the FCC-hh reference detector along the $y-z$ plane. Starting from the IP (also the centre of the detector), going radially outwards, the FCC-hh reference detector comprises the following systems (similar to that of the LHC experiments):

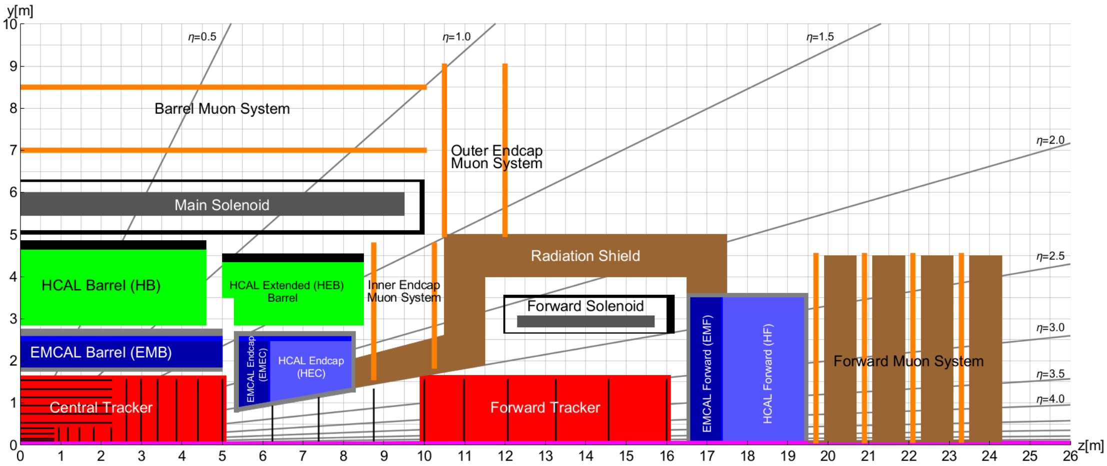

Figure 5.3: Layout of one quadrant of the FCC-hh reference detector along the $y-z$ plane. Different sub-systems are indicated by various colours [41].

- A central tracking system that is modelled according to the HL-LHC Phase-II trackers of the ATLAS and the CMS detectors to provide precision momentum spectroscopy for charged particles up to $|\eta| = 2.5$. A forward tracker extending up to $|\eta| \approx 6.0$ with a forward solenoidal magnet is inspired by the present ALICE and LHCb detectors. The baseline tracker layout for the FCC-hh reference detector is discussed in more detail in Section 5.1.1.

- A calorimeter system (surrounding the tracker volume) consisting of an Electromagnetic Calorimeter (ECAL) and Hadronic Calorimeter (HCAL) for energy measurements of electromagnetic and hadronic showers up to $|\eta| \approx 6$. The ECAL and the HCAL together ensure 98 % containment of high energy showers. A brief overview of the assumed calorimetry for the FCC-hh reference detector is presented in Section 5.1.2.

- A magnet system consisting of a central solenoid and two forward solenoids housing the tracker and the calorimeter system to provide a 4 T field for momentum spectroscopy in the entire tracking volume. It is based on the same superconducting material, i.e. Al stabilised Nb – Ti/Cu Rutherford cables, as used in the ATLAS and CMS magnet systems. The superconductors have to be cooled down to 4.5 K using liquid He. It extends from $z \approx -15$ m to $z \approx 15$ m along the beam-axis. The central (main) solenoid has a 10 m diameter bore while the two forward solenoids have 5 m

---

[2] This detector does not represent the final implementation for FCC-hh experiments.

diameter bores. The main solenoid weighs about 2 kt and can store magnetic energy of about 12.5 GJ compared to 1.6 GJ and 2.7 GJ for the ATLAS and the CMS magnet systems, respectively. An alternative of two dipoles (similar to ALICE and LHCb) with a magnetic field integral of ≈ 4 T m is also being studied for the forward region to improve the tracking performance in the high pseudorapidity region. The detector cavern housing the magnet system will not contain an active shielding for the proposed magnet system due to its size and huge cost. Therefore, the service cavern must be adapted to the significant stray fields which reaches the 5 mT level at $z \approx 70$ m and $R \approx 55$ m.

- A muon system (for muon momentum spectroscopy and trigger) consisting of a barrel, an outer endcap located outside the main solenoid, an inner endcap situated within the main solenoid covering pseudorapidity up to $|\eta| = 2.2$, and a forward muon sub-system extending up to $|\eta| = 6.0$. More details are discussed in Section 5.1.3.

5.1.1 Baseline Tracker

The baseline tracker of the FCC-hh reference detector is an all-silicon tracker and consists of a central tracker in the region $|\eta| < 2.5$ and a forward tracker with tracking capabilities up to $|\eta| \approx 6$. It extends from the beampipe (r > 20.8 mm) up to 1.6 m in the radial direction. In the longitudinal direction, the central tracker extends up to $z = 5$ m while the forward tracker extends up to $z = 16$ m from the IP. Figure 5.4 shows two different layouts considered for the FCC-hh baseline tracker, namely, the tilted layout (left) based on the current ATLAS and CMS Phase-II upgrade, and the more traditional flat layout (right). In the tilted layout, the detector modules are inclined in the $r - z$ plane such that the particles passing through them make almost a normal incidence, minimising the amount of material traversed by the particle. This reduces the effect of multiple scattering in comparison to that in the flat tracker layout while keeping the number of measured hits high. It results in a significant improvement in tracking performance. The total silicon surface amounts to 430 m^2 for the flat layout and 391 m^2 for the tilted layout compared to around 250 m^2 for the Phase-II trackers of ATLAS and CMS.

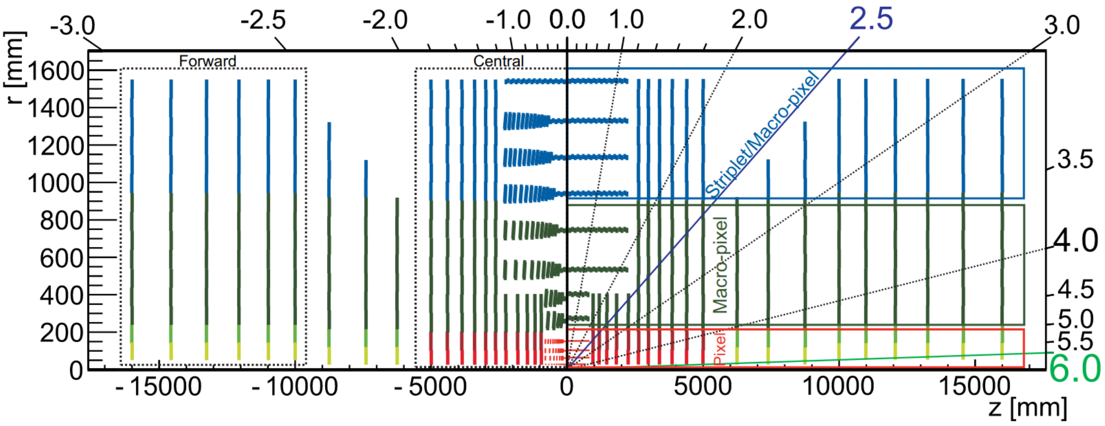

Figure 5.4: Tracker layout using the so called "tilted geometry" (left) and "flat geometry" (right) [41].

Charged particles trace a helical motion in the uniform magnetic field of 4 T generated by the solenoid magnet that envelops the tracker. Their tracks are reconstructed using 12 measurement points (hits) from 12 different layers of this tracker. The tracking system has been designed by keeping several constraints in mind. As the produced particle momenta could reach tens of TeV's in the FCC-hh scenario, a requirement for a relative momentum resolution of 20 % for $p_{\mathrm{T}} = 10\,\mathrm{TeV/c}$ is set. The relative momentum resolution depends on a hit uncertainty term (dominant at high p_{T}) and a multiple scattering uncertainty term (dominant at low p_{T}) for a particle traversing through N detector layers. Using Gluckstern's formula [108] and Highland's approximation for multiple scattering uncertainty [109] the relative momentum resolution can be approximated by:

$$\sigma_{\delta p_{\mathrm{T}}/p_{\mathrm{T}}} \propto \underbrace{\frac{\sigma_t}{\sqrt{NBL^2}}p_{\mathrm{T}}}_{\text{hit uncertainty}} + \underbrace{\frac{\mathrm{K_{MS}}}{\sqrt{\sin(\theta)}}}_{\text{MS uncertainty}} \,, \tag{5.1}$$

where $B = 4\,\mathrm{T}$, $L \approx 1.6\,\mathrm{m}$ and $\mathrm{K_{MS}}$ depends on the material budget of the tracker; see Appendix B. The hit uncertainty term has a direct dependence on the lateral hit uncertainty (σ_t), which has to be around 9 µm with $N = 12$ detector layers and material budgets as mentioned in Table 5.1 to meet the 20 % p_{T} resolution requirement. The above requirement – together with a general goal of keeping the channel occupancy below 1 %, and to allow for the separation of two close-by tracks within a jet (double track resolution) – is used to define the granularity of the tracking layers. Since the innermost layers are used for vertex determination (that is crucial, for instance, for b-tagging and pile-up suppression), they are composed of very fine granularity pixels; see the red coloured layers in Figure 5.4. The pixel sub-system lies within a radius of 20 cm with the innermost layer positioned at a radius of 2.5 cm and consist of pixels with dimensions in the range of $25-33.3\times50-400\,\mu\mathrm{m}^2$; see Table 5.1. Following the pixel sub-system, in the range 20 cm < r < 90 cm lies the

Table 5.1: Summary of the spatial dimensions of the detector elements of different sub-systems in the baseline tracker for FCC-hh. The relative radiation length (X/X_0) per layer in also indicated.

sub-system	layout	dimensions	X/X_0 per layer
pixel	Flat & Tilted	$25 \times 50\,\mu\mathrm{m}^2$ ($1^{st} - 4^{th}$ BRL)	1 %
		$25 \times 50\,\mu\mathrm{m}^2$ (1^{st} EC ring)	1.5 %
		$33.3 \times 100\,\mu\mathrm{m}^2$ (2^{nd} EC ring)	
		$33.3 \times 400\,\mu\mathrm{m}^2$ ($3^{rd} - 4^{th}$ EC ring)	
macro-pixel	Flat & Tilted	$33.3 \times 400\,\mu\mathrm{m}^2$	2 %
striplets	Flat	$33.3\,\mu\mathrm{m} \times 50\,\mathrm{mm}$ (BRL)	2.5 %
		$33.3\,\mu\mathrm{m} \times 10\,\mathrm{mm}$ (EC)	
	Tilted	$33.3\,\mu\mathrm{m} \times 1.75\,\mathrm{mm}$ (BRL, EC)	
		$33.3\,\mu\mathrm{m} \times 50\,\mathrm{mm}$ (12^{th} BRL layer)	

macro-pixel sub-system with elements consisting of slightly coarse granularity (shown in green). The macro-pixels have a dimension of $33.3 \times 400\,\mu\text{m}^2$. The outermost part of the tracker consists of the striplets with dimensions $33.3\,\mu\text{m} \times 2 - 50\,\text{mm}$. The striplet sub-system extends from around 90 cm to 160 cm along the radial axis. The assumptions regarding the detector technology for the baseline tracker of the FCC-hh is discussed later in Section 5.3.1.

5.1.2 Baseline Calorimetry

Similar to the LHC experiments, the FCC-hh baseline calorimeter system consists of the electromagnetic calorimeter (ECAL) followed by the hadronic calorimeter (HCAL). It gives a measure of the energy deposited by particles undergoing electromagnetic and hadronic interactions in the respective calorimeters. The energy resolution of a calorimeter, in general, can be parametrised in terms of a *stochastic term (a)* due to shower fluctuations and sampling, a *noise term (b)* due to electronic noise and pile-up, and a *constant term (c)* due to numerous effects like shower leakage, construction uniformity and cell-to-cell calibration variations [41]:

$$\frac{\sigma_E}{E} \approx \frac{a}{\sqrt{E}} \oplus \frac{b}{E} \oplus c. \tag{5.2}$$

It lies within the solenoidal magnetic field of 4 T up to $|\eta| = 2.5$ and beyond $|\eta| = 2.5$ it is outside the B field.

Electromagnetic Calorimeter

The ECAL has a thickness of around 30 radiation lengths (X_0) and consists of three parts, namely, the Electromagnetic Barrel (EMB), the Electromagnetic Endcap Calorimeter (EMEC) and the Electromagnetic Forward (EMF). The EMB and the EMEC extend up to $|\eta| = 2.5$, while the EMF covers the region $2.5 \leq |\eta| \leq 6$. The maximum 1 MeV neutron equivalent fluence expected at the ECAL is $\sim \mathcal{O}(10^{16})\,\text{neq/cm}^2$. Therefore, the FCC-hh ECAL is based on Liquid Argon (LAr) due to its intrinsic radiation hardness (inspired by the ATLAS ECAL introduced in Section 4.3.3). It is a sampling calorimeter consisting of alternate 2 mm steel-plated lead absorbers followed by multilayer printed circuit board (PCB) readouts. The ECAL cells are two to four times more granular than the ATLAS LAr calorimeter. The granularity of the EMB is chosen to be $\Delta\eta \times \Delta\phi = 0.01 \times 0.009$ with an exception for the second layer, which has very fine division along the pseudorapidity axis of $\Delta\eta = 0.0025$ (for efficient π_0 rejection). Due to this high granularity of the EMB, it uses plates inclined by 50° in the radial direction; see Figure 5.5(a) (unlike in ATLAS, where the LAr calorimeter had an accordion structure). Since LAr has to be cooled, all calorimeters are enclosed within an aluminium cryostat. The EMB has an inner radius of 185 cm and outer radius of 272 cm, including a cryostat thickness of 5 cm in the front and 10 cm at the back of the ECAL. In the endcap region, the EMEC and the HEC share the same cryostat. The EMEC uses 1.5 mm steel-plated lead absorbers with 0.5 mm LAr gaps in a direction perpendicular to the beamline; see Figure 5.5(b). The geometry of the EMF is similar to EMEC except that the absorbers are now 1 cm copper plates with 0.1 mm LAr

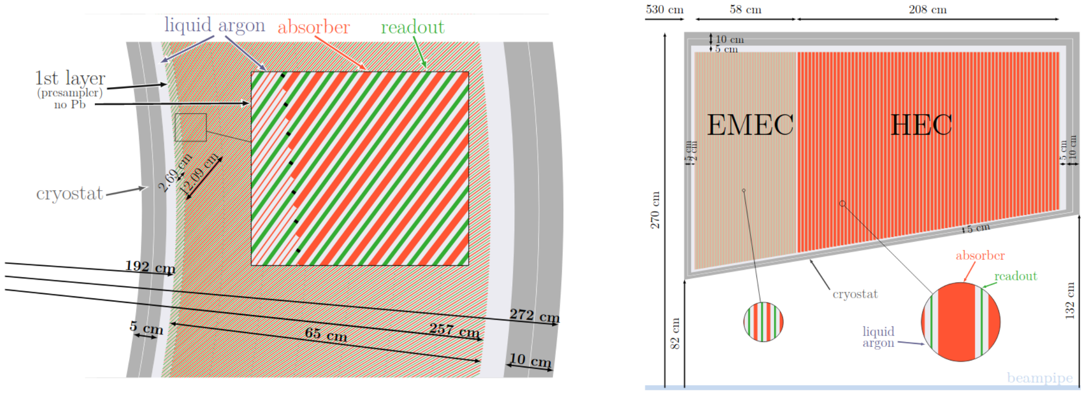

(a) EMB **(b)** EMEC & HEC

Figure 5.5: Geometry of the LAr Electromagnetic Barrel (EMB) (a) and the endcap (b) calorimeter of the FCC-hh reference detector [41].

gaps. Besides, the EMF uses a coarser granularity of $\Delta\eta \times \Delta\phi = 0.025 \times 0.025$ compared to the EMB and EMEC.
A full simulation of ECAL using single electrons results in an energy resolution of $\sigma_E/E \approx 8.2\,\%\sqrt{\text{GeV}} \oplus 0.15\,\%$ at $\eta = 0$ [41]. The noise term is estimated ($\sim 1.3 - 2.7\,\text{GeV}$) using an optimal cluster-size for pile-up simulations, and capacitances of the readout electrodes scaled to the ATLAS values.

Hadronic Calorimeter

In Chapter 2, it was shown how a 100 TeV pp collider would open up new opportunities for the discovery of new heavy particles (gauge bosons) in addition to the precise measurements in the Higgs sector. These high mass gauge bosons may decay into highly boosted jets ($\sim 5-20\,\text{TeV}$), which contain a significant fraction of highly energetic hadrons. Therefore, the calorimeter should have an excellent energy resolution and posses high transverse and longitudinal granularity to distinguish close by boosted objects [110]. It should also be able to contain the highly energetic hadron showers. Similar to the ECAL, the HCAL is divided into three parts, namely, a central barrel (HB), two extended barrels (HEB) covering a pseudorapidity range of $|\eta| \leq 1.81$ and two LAr based parts. The LAr based calorimeters include the HCAL endcap (HEC) and HCAL forward (HF) and cover a pseudorapidity range of around $1.8 \leq |\eta| \leq 6$. The radiation levels are similar to the HL-LHC levels in the region where the HB and the HEB are situated. Therefore, organic scintillating tile-based calorimeter TileCal (similar to the one used in ATLAS) is used for the HB and the HEB of the FCC-hh reference detector. The TileCal for the FCC-hh reference detector uses a mix of scintillator and steel oriented orthogonal to the beamline. It offers an effective calorimeter depth of 9λ for containing the hadronic showers. The scintillating light signals are transported by wavelength shifters to be read out by silicon photo-multipliers (SiPMs). There are 8 and 10 longitudinal layers in the HEB and the HB respectively, with cell granularity of $\Delta\eta \times \Delta\phi = 0.025 \times 0.025$. Single pion simulations result in an energy resolution of $48\,\%/\sqrt{E} \oplus 2.2\,\%$ and within a target goal of a maximum constant term

$b = 3\,\%$ [41]. However, the presence of the magnetic field in the hadronic calorimeter degrades the energy resolution to some extent due to energy losses at the cryostat wall. Topological clustering algorithms are used to account for the effect of electronic noise and pile-up, thereby, further worsening the energy resolution to $114\,\%/\sqrt{E} \oplus 2.1\,\%$ at $\eta = 0.36$ and $\langle\mu\rangle = 200$. Improvements in the energy resolution are expected by combining the tracking information with the calorimeter information (using particle flow algorithms).

5.1.3 Baseline Muon System

Unlike the ATLAS detector that hosts a stand-alone muon system for excellent muon momentum spectroscopy, the focus of the FCC-hh muon system will be more on muon trigger and muon identification aspects, as there is little doubt that precise muon spectroscopy can be done close to the IP (with the large scale silicon trackers). The stand-alone muon momentum resolution is limited by multiple scattering in the calorimeters and is expected to be $\sim 4\,\%$ for tracks with $p_{\mathrm{T}} \in [10, 1000]\mathrm{GeV/c}$, $\sim 6\,\%$ for $2\,\mathrm{TeV/c}$ tracks and $24\,\%$ for $10\,\mathrm{TeV/c}$ tracks. Assuming $50\,\mu\mathrm{m}$ position resolution for the muon system up to $|\eta| = 2.5$ the combined muon momentum resolution improves significantly in comparison to the stand-alone system with p_{T} resolution $\sim 6\,\%$ event at p_{T} as high as $10\,\mathrm{TeV/c}$.[3] In the forward pseudorapidity region with $|\eta| > 2.5$, the momentum resolution goes beyond $100\,\%$ for $p_{\mathrm{T}} > 1\,\mathrm{TeV/c}$. Therefore, the forward muon sub-system of the FCC-hh reference detector can only be used for muon identification and not for triggering. For a good momentum resolution in the forward region, the alternative option of dipole magnets instead of the solenoid must be used in the forward region (as is the case in the ALICE and LHCb experiments).

Due to a large number of highly boosted objects expected at the FCC-hh, the energy deposited in the calorimeters increases strongly in the forward region. A large number of low energy neutrons are produced inside the forward calorimeter due to the shower and the absorption processes. Therefore, a heavy radiation shield is placed around the forward solenoid magnets to cover the gap between the endcap and forward calorimeters and to prevent the neutrons from entering the muon system and the detector cavern. The capture of neutrons immerses the muon system and the detector cavern in a gas of high energy photons that then convert to electrons in the muon system material. These electrons have relatively low energy and contribute significantly to the charge particle rate in the muon system, which is a key number to help decide for the choice of muon system technology and granularity. The charge particle rate is expected to be in the range from around $1 - 250\,\mathrm{kHz/cm^2}$ for the FCC-hh muon system, which is comparable to the rates at the muon systems of some of the LHC experiments. Hence, technologies that are planned to be used during the HL-LHC Phase-II upgrade of the ATLAS detector, for example, the small-diameter Muon Drift Tubes (sMDT) chambers can be used for the muon system of FCC-hh. These chambers consist of drift tubes filled with a gas mixture of $\mathrm{Ar} : \mathrm{CO_2}$ $(93 : 7)$, which have $0.4\,\mathrm{mm}$ thick aluminium walls and a small diameter of $15\,\mathrm{mm}$ [111]. Two layers consisting of four rows of sMDT's can provide an angular resolution of $60\,\mu\mathrm{m}$ and a spatial resolution of $40\,\mu\mathrm{m}$. 250 of these sMDT chambers will allow covering a total area of $1150\,\mathrm{m^2}$

---

[3] Combined momentum resolution here corresponds to momentum measurement with tracker and muon system combined.

of the muon system. Thin gap RPC's with 0.5 ns time resolution might be combined with these sMDT chambers to allow bunch crossing identification.

5.2 Limitations and Challenges

Around seven times higher centre-of-mass energy and about thirty times higher luminosity than the design values of the LHC, not only lead to a significant increase in the discovery potential and measurement precision but also increases the challenges manifold. Some of the main challenges related to the experiments at the FCC-hh are discussed below.

5.2.1 Pile-up

As discussed in Section 1.4.3, the number of simultaneous pp collisions in a BX depends mainly on the proton-proton collision rate and hence the luminosity. Increasing the beam luminosity by a factor of 5–7 for the HL-LHC is already quite challenging and involved a major upgrade of the accelerator system. The key is to reduce β^* and normalised transverse emittance (ϵ) of the beam while keeping the crossing angle at the IP small. Besides, the beam luminosity is also directly proportional to the number of bunches (N_b) and the number of particles per bunch. For FCC-hh, the plan is to have $\epsilon = 2.2\,\mu\text{m}$, $\beta^* = 20\,\text{cm}$ and $N_b = 10600$ ($\sim$ five times of that at LHC) to achieve a peak instantaneous luminosity (L) of $\sim\ 30 \times 10^{34}\,\text{cm}^{-2}\text{s}^{-1}$. For each of the 10600 bunches – revolving with a bunch revolution frequency of $\sim 3\,\text{kHz}$ around the 97.75 km collider ring – the number of protons will be 1×10^{11}. Using pp inelastic cross-section of 108 mb at $\sqrt{s} = 100\,\text{TeV}$, an average pile-up of ≈ 1030 is expected in a bunch spacing of 25 ns within a length of around 6 – 10 cm luminous region; see Equation 1.49. This is more than five times higher than that expected at the HL-LHC, making the environment close to the beamline very dense and packed. On average, around 5 – 8 collisions are expected every mm.

Referring to Figure 1.8 and increasing the red points (pile-up vertices) from five to one thousand, one can imagine how densely packed the collision vertices would be. The effect of pile-up on the reconstructed objects (as discussed in Section 1.4.3) will also increase significantly. Identification of the HS vertex from such a dense environment of so many closely spaced vertices is going to be a real challenge if mitigation of pile-up is not carried out at the trigger level. In experiments like ATLAS and CMS, which have a two-level trigger system, pile-up mitigation algorithms [112–118] are usually employed only at the second (software) level trigger or mostly offline during analyses. One of the main reasons for these algorithms not being implemented at the very first trigger level is the unavailability of information from the track at this level; see Chapter 6. Besides, calorimeters are almost blind at pointing to a PV/HS vertex.[4]

Broadly, these pile-up mitigation methods are based on vertex information from charged tracks, the event pile-up density, and the local distribution of pile-up w.r.t. particles from the HS vertex. For the HL-LHC Phase-II upgrade, ATLAS and CMS have a dedicated

---

[4] CMS for its HL-LHC upgrade will use a High Granularity Calorimeter (HGCAL) [119] to point to vertices using a very good timing resolution

timing detector in the forward rapidity region, namely, the HGTD [103] and HGCAL [119], respectively, to exploit the timing information for pile-up mitigation. Besides, the CMS outer tracker will be upgraded to provide track parameter information at the first trigger level and thereby, implement one of the software level pile-up mitigation algorithms called Pile-up Per Particle Identification (PUPPI) [118] in the Level 1 trigger [120, 121]. With unprecedented pile-up at FCC-hh experiments and in the limit of vertex resolution, it is clear that timing information together with the longitudinal vertex information will be crucial for a substantial pile-up suppression. Chapter 7 of this thesis introduces a concept of a track trigger based on detector triplets that allows a significant pile-up suppression using the longitudinal vertex (z_0) and the transverse momentum information. Trigger performance studies in the particular case of multi-jet signatures, where multiple jets point to the same vertex (see the blue cones in Figure 1.8), is presented in Chapter 9.

5.2.2 Radiation Environment

A large increase in the peak pp collision rate from about 0.8 GHz (4 GHz) at the LHC (HL-LHC) to around 30 GHz at the FCC-hh, 30 times higher integrated luminosity goals, having silicon detector layers very close to the beamline and increased detector acceptance along pseudorapidity, will expose some parts of the experiments to extreme radiation fluences. Figure 5.6 (a) shows the 1 MeV neutron equivalent fluence for the FCC-hh reference

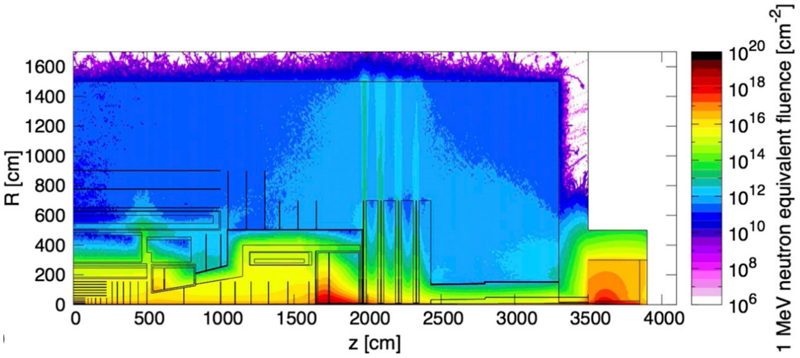

Figure 5.6: 1 MeV neutron equivalent fluence for the FCC-hh reference detector [41].

detector in the $r - z$ plane. It is expected to be around $5 - 8 \times 10^{17}\,\mathrm{neq/cm^2}$ at the layer closest to the beam-pipe i.e. at R = 2.5 cm. This is around one order of magnitude higher than that expected at experiments at the HL-LHC and even two orders of magnitude higher than the present LHC detectors. However, some of the innermost part of the forward calorimeters at $z > 1.5$ m are exposed to extreme fluences with values of up to $5 \times 10^{18}\,\mathrm{neq/cm^2}$. Dedicated research and development efforts are underway to design detector technologies that can withstand such extreme radiation level. The fluences for the other outer regions (R > 40 cm) are similar to the fluences expected at the HL-LHC experiments. Therefore the detector technologies used for the HL-LHC phase-II can be used. Besides, the detector elements and the electronics should also be radiation tolerant to long term damage that can occur due to their exposure to the total ionizing dose (TID) from an integrated luminosity of $30\,\mathrm{ab^{-1}}$. The TID expected at FCC-hh (270 Gy) is about twenty times higher (at R = 2.5 cm) than the TID expected at the HL-LHC experiments (13 Gy).

5.2.3 Data Rate, Trigger and Computational challenges

The proposed reference calorimeters for the FCC-hh have around two to four times higher granularity than the calorimeters at ATLAS and CMS, for instance. Higher granularity, in addition to the increased acceptance along η, will result in about 250 TB/s of data from the calorimeters and the muon systems, which is more than $\sim$ 10 times higher than in the ATLAS and CMS Phase-II scenarios. Reading out this huge amount of data using a trigger-less readout system (see Section 5.3.2) is challenging. Although, it might be possible to cope up with such high data rates by the time FCC-hh comes into operation.

The total number of charged tracks per collision changes by a little less than a factor of two when going from $\sqrt{s} = 14$ TeV to 100 TeV. However, the charged particle rate per unit area changes by almost an order of magnitude with around 10 GHz/cm^2 at R = 2.5 cm. This is mainly because of the thirty times higher luminosity and hence the massive amount of pile-up ($\sim$ 1000). This number drops to around 3 MHz/cm^2 at the outer radii of the tracker. The occupancies in the innermost tracker layers are therefore enormous, resulting in increased combinatorics; see Chapter 6 for general track reconstruction techniques. A data rate of about 1 – 2 PB/s from the tracker system of the FCC-hh reference detector is expected. Whether this huge amount of data can be read out using a trigger-less system even in 20 – 30 years from now is a big question. Assuming that if optical link technology for full tracker readout is available and affordable, the amount of material that will be added due to the required number of radiation hard optical links ($\sim$ 300 k), will significantly affect the physics performances. Therefore, most probably a trigger system similar to ATLAS and CMS, with a level 1 trigger to reduce the data output rate from 40 MHz to around 1 – 4 MHz before being fed to a software-based HLT will be needed. With a trigger system similar to the ATLAS and the CMS Phase-I trigger (based on coarse granularity information from the calorimeter and the muon system), the trigger thresholds to operate the muon, electron/photon and jet triggers at a rate of 100 kHz are raised from 25/30/120 GeV to 78/150/300 GeV with $\langle\mu\rangle = 140$ [41]. The effect of $\langle\mu\rangle = 1000$ on a trigger solely based on calorimeter – by emulating a calorimeter with the specifications mentioned in Section 5.1.2 – is presented in Section 5.4.

Moreover, reconstructing offline quality tracks with more than $\sim$ 30 M activated pixels will be computationally challenging and expensive. If the trigger-less readout isn't an option for the FCC-hh detector, the trigger system in place along with the available storage space will limit the data readout rate due to bandwidth and latency requirements to reduce the dead time between event readout. It also demands high-capacity and high throughput data processing infrastructures needed for running advanced software, for example, pattern recognition and track reconstruction in the event filter. Since the occupancies are lower at large radii, a track trigger concept (with a triplet of pixel detector layers) that will allow rate reductions by more than an order of magnitude at the very first level of the trigger is proposed in Chapter 7. Such a triplet track trigger allows for identification of $\sim$ 60 % (82 %) of HH $\rightarrow b\bar{b}b\bar{b}$ events at a trigger rate of 1 MHz (4 MHz) in the central pseudorapidity region of $|\eta| < 1.5$; see Chapter 9 for details. Efforts for using machine learning techniques at trigger level are also underway.

5.3 Input Parameters for FCC-hh Study

This section summarises the different input parameters assumed for the FCC-hh and its reference detector. A summary of a few of the key parameters for the FCC-hh (mentioned in the sections above) in comparison to the LHC and the HL-LHC is presented in Table 5.2.

Table 5.2: A few of the key parameters for the FCC-hh in comparison to the LHC and the HL-LHC.

Parameter	LHC	HL-LHC	FCC-hh
circumference [km]	26.7		97.75
$\sqrt{s}$ [TeV]	14		100
σ_{tot} (σ_{inel}) [mb]	111 (85)		153 (108)
number of bunches	2808		10600
bunch spacing [ns]	25		
peak nominal (ultimate) L [10^{34}cm^{-2}s^{-1}]	1 (2)	5 (7.5)	30
Goal integrated luminosity $\mathcal{L}$ [ab^{-1}]	0.3	3	30
$\langle\mu\rangle$	34	200	1026
peak *pp* collision rate [GHz]	0.8	4	31
1 MeV neq-fluence at 2.5 cm [10^{16}neq/cm^2]	0.4	3.9	60
TID at 2.5 cm [MGy]	1.3	13	300

5.3.1 Detector Technologies

With increasing pile-up and particle rates, the demand for highly granular (position and timing) detectors is rising. This, however, has to be accompanied by radiation tolerant and low material budget technologies, especially for the innermost and forward detector layers. Besides, there is a need for cost-effective and commercially available devices using new detection technologies. As mentioned in the respective sub-sections of Section 5.1, some of the detector technologies planned to be used for the HL-LHC phase can withstand the radiation requirements at the FCC-hh. Table 5.3 summarises the assumed and possible candidate technologies for different systems of the FCC-hh reference detector.

Table 5.3: Summary of the assumed and possible detector technologies for different systems of the FCC-hh reference detector.

Detector system	assumed/possible technologies	advantages	R & D needed
Tracker	CMOS Silicon detectors, for outer layers. LGAD (timing)	low-mass, high-resolution sensors, affordable and potential to cover large surface area	radiation tolerance
Calorimeter	LAr, Tile Calorimeter SiPMs	highly granular, timing capabilities	radiation tolerance, dark count rate
Muon	Gas detectors, e.g. sMDTs, RPCs	large area coverage, moderate cost	choice of gases and environmental compatibility

Also, application-specific electronics and high-rate, high throughput, data transmission for applications with severe constraints (e.g. radiation, power consumption, heat dissipation and space limits, accessibility, cable path limitations) will be needed [41].

5.3.2 Trigger

The trigger system for the FCC-hh reference detector has not been decided yet, as the trigger design strongly depends on the detector technology, the front-end and the readout electronics, the computational power and the data storage capacity. For now, a trigger-less readout using only a software level trigger, similar to that planned for the LHCb Run 3 data taking period [122] has been assumed. Such a trigger system is highly flexible and has an advantage that it can be easily adapted for different physics requirements. However, the expected data rates $\sim \mathcal{O}(1\,\mathrm{PB/s})$ and the amount of data links required to read out such a massive amount of data places a big question on the trigger-less readout scheme; see Section 5.2.3.

For the studies presented in the following parts of this thesis, two different trigger rates for the first level trigger have been anticipated (or assumed), namely, 1 MHz and 4 MHz.

5.4 Effect of very high pile-up on Calorimeter Trigger

Increasing pile-up and limitations to full detector readout in very high rate experiments demand the need for a trigger system allowing careful reduction and analysis of an enormous quantity of data. Assuming that trigger-less readout is not feasible for the FCC-hh experiment, a calorimeter trigger is emulated for its baseline detector geometry with the following specifications, as mentioned in the previous sections and Reference [41].

5.4.1 Emulation of a calorimeter trigger

According to the baseline detector design for FCC-hh, the calorimetry starts at a radius, $\mathrm{R_{calo}} \sim 2\,\mathrm{m}$ and is enveloped by a solenoidal magnetic field $B = 4\,\mathrm{T}$. The finest granularity from amongst the ECAL and HCAL, i.e. $\Delta\eta \times \Delta\phi = 0.01 \times 0.009$ for $|\eta| < 2.5$, is chosen to construct a 2D histogram representing the $\eta - \phi$ cells of the calorimeter. Imagine ~ 1000 pp collisions at $\sqrt{s} = 100\,\mathrm{TeV}$ in 25 ns producing a variety of particles with initial parameters (E, p_T, η_i, ϕ_i). Charged particles above a minimum transverse momentum and all neutral particles (barring neutrinos) deposit their energy in the calorimeter cells. This minimum p_T depends on the location of the calorimeter and the magnetic field that the charged particles traverse through (see Figure 5.7(a)) and is given by:

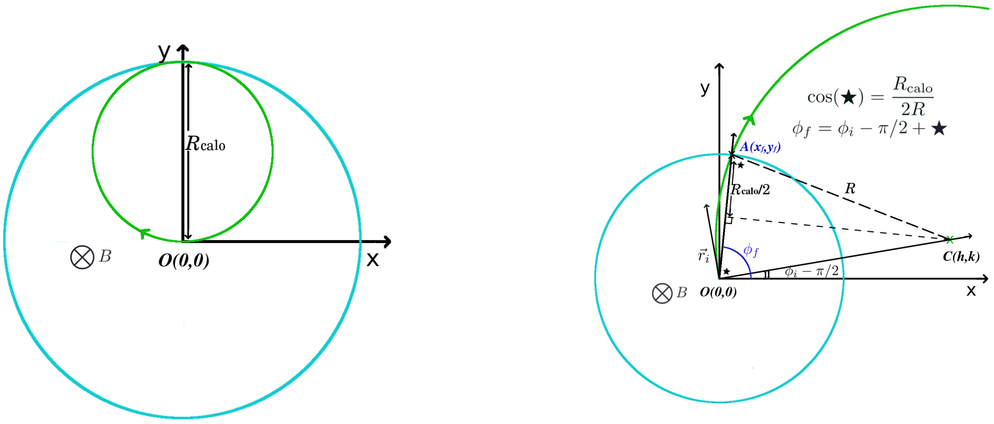

(a) (b)

Figure 5.7: Shown in the sketch above is a calorimeter (in cyan) at radius $\mathrm{R_{calo}}$ and a particles circular trajectory (in green) of radius R in the transverse plane. Figure (a) shows the minimum radius required for a charged particle to reach the calorimeter at $\mathrm{R_{calo}}$ and Figure (b) explains the determination of the final polar angle, ϕ_f at $\mathrm{R_{calo}}$, of a particle traversing in a uniform magnetic field, B.

$$\sim 0.3\,\mathrm{B}\,\mathrm{R_{calo}}/2\,[\mathrm{T \cdot m}] = 1.2\,\mathrm{GeV/c}. \tag{5.3}$$

Due to the bending of the charged particles in the transverse plane, their polar angles are re-calculated at $\mathrm{R_{calo}} = 2\,\mathrm{m}$ using the following equation (see Figure 5.7(b)):

$$\phi_f = \phi_i - \arcsin\left(\frac{\mathrm{R_{calo}}}{2\,\mathrm{R}}\right), \tag{5.4}$$

where $\mathrm{R}\,[\mathrm{m}] = p_\mathrm{T}/(0.3\,\mathrm{q}\;\mathrm{B})\,[\mathrm{GeV/c \cdot T^{-1}}]$ is the radius of the charged particle. η_i is kept unchanged assuming straight line in the longitudinal ($s - z$) plane. For each event,[5] the energies in each of the $\eta - \phi$ cells are accumulated and smeared by an energy resolution of 50 % before being fed to the anti-k_t jet algorithm to produce the so called "*emulated calo-jets*". The resulting transverse momentum in the $\eta - \phi$ cells of the emulated calorimeter for a single pile-up 1000 event is shown in Figure 5.8 (a). Although, the minimum bias events

---

[5] An event here refers to all the particles resulting in 25 ns bunch crossing.

have a steeply falling p_T spectrum peaking at $p_\mathrm{T} << 10\,\mathrm{GeV/c}$, many $\eta - \phi$ cells show large p_T due to overlapping energy deposits from from different minimum bias collisions.

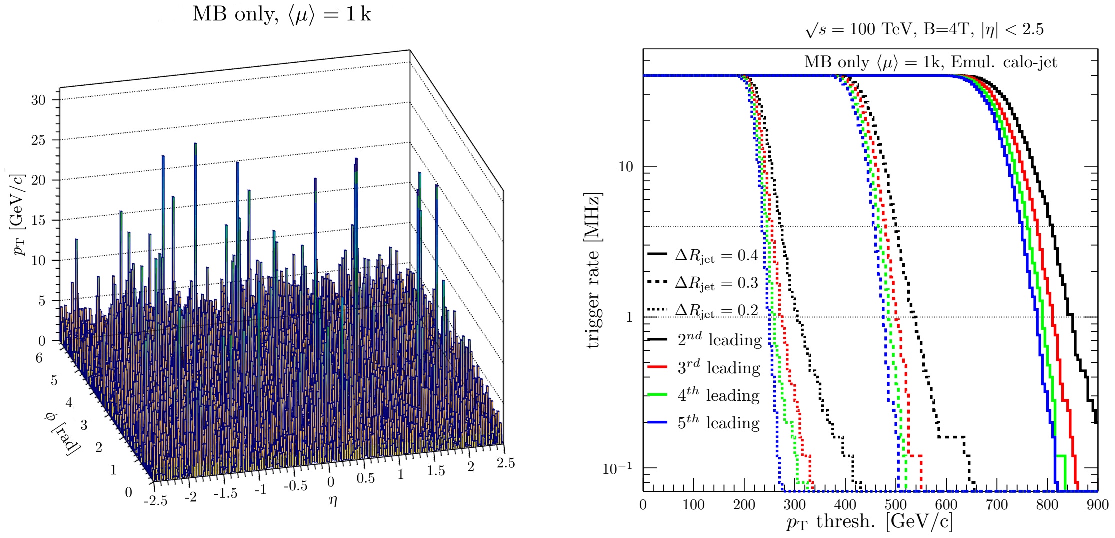

(a) **(b)**

Figure 5.8: Transverse momentum recorded in the $\eta - \phi$ cells for a minimum bias event with $\langle\mu\rangle = 1\mathrm{k}$ (a) and trigger rate as a function of trigger threshold (b) using a calorimeter (with a granularity of $\Delta\eta \times \Delta\phi = 0.01 \times 0.009$) emulated at $R_\mathrm{calo} = 2\,\mathrm{m}$ for FCC-hh experiment.

Shown in Figure 5.8 are the (trigger) rates of the 2^{nd}, 3^{rd}, 4^{th} and 5^{th} leading p_T emulated calo-jets (in minimum bias sample with $\langle\mu\rangle = 1\,\mathrm{k}$) as a function of their p_T for three different jet radius parameters $\Delta R_\mathrm{jet} = 0.2$, 0.3 and 0.4. Even with a trigger rate of 4 MHz (a factor of 10 less than the full readout rate of 40 MHz), trigger thresholds as high as 720 GeV/c on the 5^{th} leading jet – clustered with ΔR_jet of 0.4 – will be needed. Although, clustering jets with radii smaller than 0.4 results in relatively lower trigger thresholds, the thresholds are high enough to cause a significant loss in acceptance of various signal processes, especially those involving multi-jet final sates. Besides, a very small jet radius will result in loss of the FSR emissions from the hard scattering decay products. An optimum jet radius must, therefore, be chosen to eliminate the effects of pile-up on the hard processes; this, however, goes beyond the scope of this thesis.[6] Also, jets with p_T as high as 0.9 TeV/c in minimum bias events are possible due to a random combination of particle energies from various pile-up collisions. This effect can be dramatically reduced by identifying the vertex (origin) of these particles. Trackers can provide this information for the charged particles, which can then be linked to the objects in the calorimeter to obtain a tremendous suppression of pile-up. Hence, track triggers are on the wish-list for many experiments as a key trigger to harvest interesting physics.

Chapter 6 gives an overview of some of the most common track reconstruction techniques

---

[6] Note that many pile-up removal techniques have been devised. However, these are employed mostly at the software level of the trigger system or during offline analyses and not at the very first level of the trigger.

used in high energy physics followed by Chapter 7 which introduces a track trigger that can be used at the very first level.

6

Track Reconstruction in High Energy Physics Experiments

Track reconstruction is one of the fundamental parts of event reconstruction in High Energy Physics (HEP) experiments. It involves reconstruction of trajectories of charged particles that traverse through the tracking detector layers and leave a trace in the form of electronic signals (*hits*) on the sensitive detector elements. It is one of the the most complex and CPU consuming parts of event reconstruction in HEP, especially in hadron collider experiments, where the number of instantaneous hadron collisions (pile-up) is kept high for a high integrated luminosity in a short period of time. Broadly, it can be divided into the procedure of finding track candidates, pattern recognition, and estimation of the parameters that describe the particle trajectory (*track fit*). Pattern recognition involves finding a collection of hits arising from a single particle. The found collection (or pattern) of hits are further processed in the track fit to estimate the parameters describing a track. Care is taken to avoid misidentified hits (*fake hits*), as they usually decrease the final track resolution or lead to wrong track signatures.

This chapter briefly discusses the various steps involved in the most commonly used track reconstruction algorithms in HEP. The trajectory of a particle, however, cannot be measured directly, but only a localisation (with a given uncertainty) of the particle at several discrete points in the detector volume can be done [123]. Tracking detector technologies are mainly divided into two types, namely, the solid state semiconductor detectors and the gaseous detectors. The semiconductor detectors are generally used in the innermost part of the tracking system for precise measurements and vertexing. Section 6.1 introduces some of the silicon-based modern detector technologies which facilitate the measurement of hits in the inner tracking layers. Gaseous detectors on the contrary are used for outer tracking (covering large surface areas) due to their relatively lower cost, e.g. drift tubes, Resistive Plate Chambers (RPC), Gas Electron Multiplier (GEM).

6.1 Silicon based Modern Tracking Detectors

Silicon detectors caught the eye of particle physicists in the 1980's and the NA11 experiment at the CERN's SPS used a set of silicon strip detectors for tracking and vertex measurements in charm quark production studies. With the rapid evolution of micro-electronics (which allowed the development of Application Specific Integrated Circuits (ASIC), and progress in the interconnection technologies (such as micro bonding)), silicon strip detector systems were miniaturized and subsequently used by almost all collider experiments.

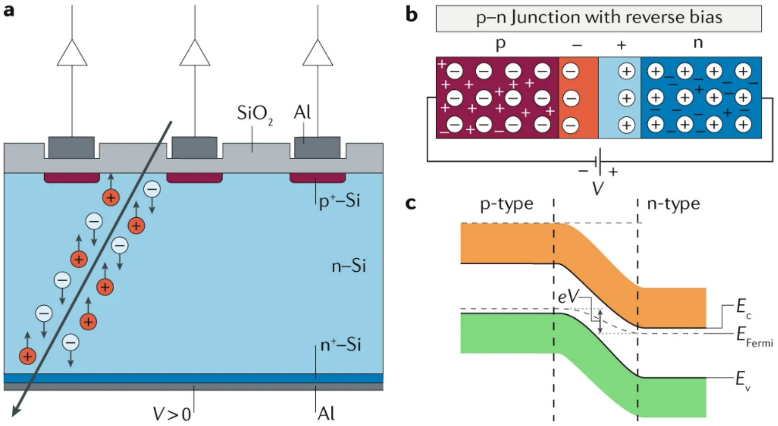

Figure 6.1: (a) Illustration of charge collection when a charged particle passes through a depleted detector creating electron-hole pairs. (b) and (c) show the development of the depletion region at the junction in reverse bias. E_c, E_v, E_{Fermi} denote the energies of the conduction band, valence band and Fermi level, respectively [124].

Its working principle is based on charge collection due to creation of electron-hole pairs on passage of a charged particle through the silicon bulk; see for example, a n-type silicon bulk material in light blue in Figure 6.1(a).[1] A p-n junction is created by establishing an interface between a p- and n-type semiconductors such that a potential barrier is created as the free charge carriers diffuse from one side to the other. This potential barrier is depleted of free charge carriers (hence also called depletion region), making it almost non-conductive. The basic building block of a silicon sensor in HEP is a p-n junction in reverse bias mode, i.e. the n- and the p-type sides are connected to the positive and the negative terminals, respectively, with the detecting medium being the depletion region; see Figure 6.1(b and c). The width of the potential barrier increases with decrease in the effective doping concentration and with increase in the reverse voltage applied across the p-n junction. The electron-hole pairs created (by any charged particle) in the depletion region, drift towards the electrodes at which the induced current is amplified and recorded giving the position of the charged particle.

Most of the silicon detectors used in HEP comprises strips or pixels. Strips have a coarse granularity along one of their dimension ($\mathcal{O}(1)$cm) compared to the pixels and provide 2D measurements. Pixels on the other hand have a very fine granularity ($\sim 100 \times 100\,\mu\text{m}^2$) and provide 3D measurements. Silicon pixel detectors broadly are of two types, namely, the more traditional hybrid pixel detectors and the monolithic pixel detectors.

---

[1] Semiconductors have four electrons in their valence shell. An n-type (p-type) semiconductor is obtained by adding pentavalent (trivalent) impurities to an intrinsic/pure semiconductor material, such that there are excess free electrons (holes) in the valence band due to creation of energy states close to the conduction (valence) band.

6.1.1 Hybrid Pixel Detectors

Hybrid pixel detectors are characterised by detection elements implemented as an array of silicon diodes bump-bonded to a readout ASIC, i.e. every pixel is connected to the readout ASIC via its own solder bump; see Figure 6.2 (a). They have an advantage of optimising readout and sensor as two separate entities. Furthermore, they allow for large signal sizes and are radiation hard. Hybrid pixel detectors are therefore the default option for trackers in HEP. The disadvantage however, is that it adds a lot of material to the detector, enhancing multiple scattering effects. Also, the size of the pixels is limited to $\sim 50\,\mu\text{m}$ because of the solder bump size. Based on the shape and the orientation of the depletion region, the hybrid pixel sensors are of two types: planar and 3D pixel sensors.

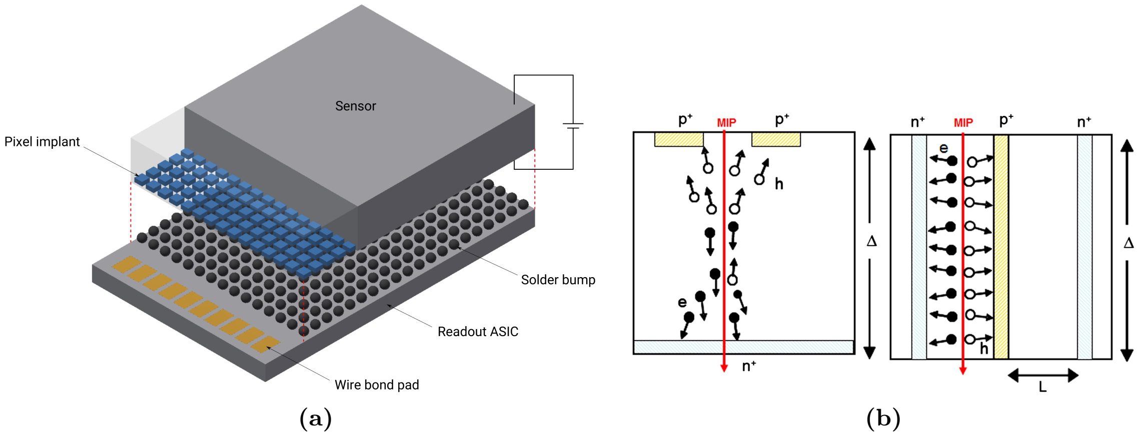

Figure 6.2: (a) Illustration of hybrid pixel detector concept [95]. (b) Schematic cross-sections of a planar sensor (left) and a 3D sensor (right). The substrate thickness and the electrode distance are denoted by Δ and `L`, respectively [125].

The standard planar sensors have the electrodes implanted on the top and bottom surfaces of the wafer, such that the depletion region grows vertically; see Figure 6.2(b-left). The full depletion voltage, therefore, depends on the thickness (Δ) of the substrate. In case of the 3D sensors, the depletion region grows laterally between the electrodes; see Figure 6.2(b-right). The distance between these electrodes (`L`) is much smaller than the substrate thickness and hence full depletion voltage can be dramatically reduced w.r.t. the planar sensors. The number of electron-hole pairs (and hence the charge) generated by a minimum ionising particle (MIP), for the same substrate thickness, is the same for both type of sensors. However, shorter charge collection distances in 3D sensors compared to the planar sensors makes the 3D sensors less prone to charge collection inefficiencies after irradiation due to charge trapping.[2] Besides, shorter charge collection distances in 3D sensors also reduces the charge collection time and makes it more radiation hard compared to the planar sensors. 3D (planar) pixel sensors are proven to achieve detection efficiencies of above 97 % with fluences up to $2.8 \times 10^{16}\ \text{n}_{\text{eq}}/\text{cm}^2$ ($1 \times 10^{16}\ \text{n}_{\text{eq}}/\text{cm}^2$) at bias voltages of around 150 V

---

[2] High-energetic particles can interact with the nuclei in the silicon bulk and cause displacement w.r.t. their lattice position (lattice defects) in the crystal. Charge trapping refers to the localisation of electrons or holes at lattice defects leading to charge collection deficiency and increased leakage current.

(600 V) [126, 127]. 3D sensors are chosen as the baseline technology for the two innermost layers of the ITk in ATLAS [94].

6.1.2 Monolithic Pixel Detectors

Monolithic pixel detectors integrate the sensor array and the front-end readout electronics on the same silicon substrate unlike the hybrid technology. They do not require the expensive bump-bonding process employed for hybrid pixel detectors. This allows them to be relatively thin ($50 - 100\,\mu\mathrm{m}$), reduces the effects of multiple scattering and hence improves the tracking performance.

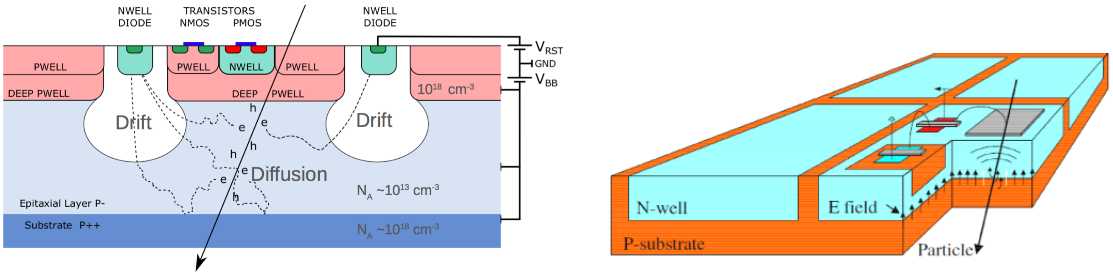

(a) **(b)**

Figure 6.3: (a) Schematic cross-section of an ALPIDE pixel. The diffusion of the electron-hole pair in the moderately p-doped expitaxial layer until they reach the depletion region where they drift to be collected by the n-well diode is also shown [128]. (b) 3D-view of four pixels in HV-MAPS with electronics implanted in deep n-well [129].

There are two broad categories of monolithic pixel detectors, namely, the Charge-Coupled Devices (CCDs) and the Monolithic Active Pixel Sensors (MAPS). CCDs require a minimum of in-pixel electronics to transfer collected charge through successive pixels to be processed on the chip. This allows for very thin ($\sim 20\,\mu\mathrm{m}$) and small pixel sizes ($\sim 2 \times 2\,\mu\mathrm{m}^2$). However, charge transport over long distances makes them prone to radiation damages. MAPS are made in CMOS technology and benefit from the development in the field. It consists of the moderately p-doped epitaxial layer on top of a highly doped p++ substrate and below a few p-well implants of the front-end electronics. The n-well implant is used for charge collection here. One can see that the epitaxial layer is not fully depleted and signal charges move mainly by diffusion; see Figure 6.3(a). MAPS (Mimosa28) (w/o the deep p-well) were first used in the vertex detector of the STAR experiment at RHIC. Based on the same concept but using a smaller feature size (180 nm) CMOS process, the ALPIDE sensor is developed for the new Inner Tracking System (ITS) of the ALICE experiment at the LHC.[3] The small feature size will allow for a higher integration density and improve the readout speed. A deep p-well in addition enables full implementation of CMOS logic without interfering with the charge collection process. The ALPIDE sensors are also shown to have a low power consumption ($< 40\,\mathrm{mW/cm^2}$). However, they cannot tolerate fluences well above 2.5×10^{13} $\mathrm{n_{eq}/cm^2}$ without accounting for significant inefficiency and noise [128]. A process modification to obtain full depletion of the epitaxial layer (and

---

[3] The ALICE ITS is being installed at the time of writing and will cover a large area of about $10\,\mathrm{m}^2$.

hence charge collection by drift) using a low dose blanket n-type implant in the pixel array is suggested in Reference [130]. First results show a significant improvement in timing performance and radiation tolerance of up to 1×10^{15} $\mathrm{n_{eq}/cm^2}$.
Another way to achieve charge collection via drift is to implant large collection electrodes (deep n-wells) housing the electronics; see Figure 6.3(b). This creates a low doped p-n junction which is biased with a high reverse voltage (80–100 V) leading to depleted area that is about an order of magnitude higher than in a standard CMOS chip. These chips are called High Voltage Monolithic Active Pixel Sensors (HV-MAPS) and have been prototyped for several experiments, e.g. Mu3e [131], ATLAS and CLIC with different readout architectures. They provide time resolutions of a few nanoseconds and are radiation tolerant (2×10^{15} $\mathrm{n_{eq}/cm^2}$) [132].
Thus, contrary to the hybrid pixel detectors, monolithic detectors offer advantages in terms of detector assembly, detector capacitance, low material and production cost. Therefore, they are promising not only for pixel detectors but also for full tracking detectors.

6.2 Track Reconstruction Algorithms

A charged particle with charge q moving with velocity $\vec{\boldsymbol{v}}$ in a magnetic field ($\vec{\mathbf{B}} = B\hat{z}$) experiences a Lorentz force which is given by:

$$\frac{\mathrm{d}\tilde{\mathbf{p}}}{\mathrm{dt}} = q(\vec{\mathbf{v}} \times \vec{\mathbf{B}}), \tag{6.1}$$

where natural units ($\hbar = c = 1$) are assumed. Assuming a uniform magnetic field in a direction parallel to the beam-axis, the charged particles trace a helical trajectory through the detector layers; see Figure 6.4. Its projection on the transverse and the longitudinal plane can be described by a circle and a straight line, respectively. The standard track reconstruction algorithms employed in experiments with high track multiplicity generally consist of the following steps:

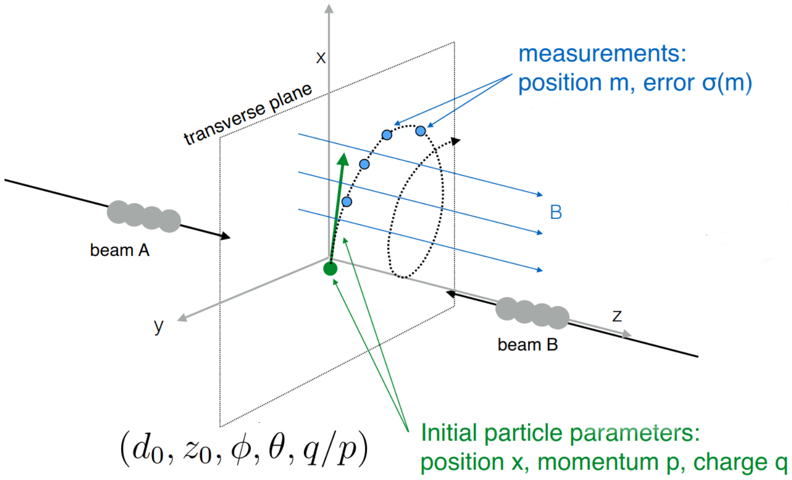

Figure 6.4: Illustration of motion of a charged particle in a uniform magnetic field parallel to the beam-axis. Figure adapted from Reference [133].

6.2.1 Space-point formation

Track reconstruction begins with creation of 3D space-points from the raw detector measurements. The silicon pixel detectors already provide 3D measurements, whereas in case of strips, two strips with a stereo angle (double sided strips) can be used to extract the 3D information (as in the case of the ATLAS detector). However, the charge on a sensor is often collected over multiple pixels due to the incident angle of the particles w.r.t. the sensor, diffusion of electrons and holes in the sensor, drift of charge generated along the track in the direction of the Lorentz angle, multiple particles passing through close-by pixels and emission of δ rays. Neighbouring hit pixels are grouped to form cluster and information from all pixels is used to estimate the position using a linear approximation [134]. In dense environment, however, the chances of several particles passing through close-by pixels to form a single merged pixel is large. Split cluster positions are obtained in this case, for example, by using neural networks to estimate the probability that a cluster was created by one or many particles and to split the cluster when possible [134].

6.2.2 Seed Search

The next step in track reconstruction is to identify a minimum number of space-points (henceforth referred to as hits for simplicity) in several tracking layers to form a track seed. It usually consists of hits from three detector layers or from two detector layers if additional constraints (e.g. if IP is assumed to be the origin of the track) are required. These hits must be selected such that they originate from the same particle track. One can either search for a seed from the inner most tracking layers and propagate outwards (inside-out approach) or from the outermost tracking layers and propagate inwards (outside-in approach). Both approaches have some pros and cons given high detector occupancies (leading to overlapping hits) and the fact that particles undergo different kinds of interactions with the detector material (leading to absence of hits, for example, due to inelastic nuclear interactions). Hence, finding the initial seed is a challenge, especially in high pile-up environment due to very high combinatorial possibilities. Combining all the hits from a

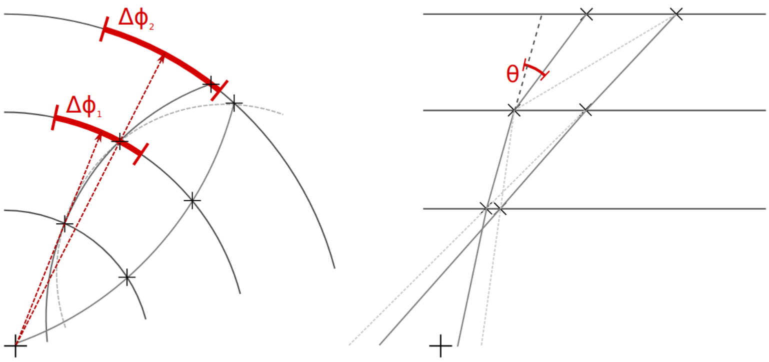

Figure 6.5: Example of search windows in the transverse and the longitudinal plane for building three-hit seeds in a barrel detector. The search windows in the second and the third layer are defined w.r.t. the space-point in the first layer. Solid lines indicate true seeds, dashed lines indicate combinatorial background [135].

tracker in high rate experiments for seed formation is highly unfeasible. Therefore, a combinatorial seed finder builds a seed based on search windows defined around the azimuthal and zenith angles of a hit. The above two cuts are motivated by the assumed helical track model with the azimuthal window determining the highest allowed curvature or lowest transverse momentum, while the polar angle requiring consistency for true track candidates as a result of the linear longitudinal movement; see Figure 6.5. One of the biggest single CPU consumers of track reconstruction is the seed building from space-points and, therefore, the search windows must be optimised to allow fast seed finding. Besides, an additional detector hit is required sometimes to reduce fake seed formation.

6.2.3 Track Fitting and Hit Linking

The helical trajectory of a charged particle can be described using five parameters, namely, two local coordinates defining the current position of the particle, two angles giving the direction of the trajectory, and one parameter specifying its curvature. It is necessary to define a track model that describes the state of a particle track in the magnetic field by taking the material effects and hit resolution of the detector into account. For example, in the absence of magnetic field or homogeneous magnetic field, an analytical track model can be applied. For every track seed, an initial estimate of track parameters is made using a track fit, which is further propagated to other detector layers where additional hits are searched for. The five track parameters include the transverse and the longitudinal distance parameters (d_0, and z_0), the azimuthal and the zenith angles (φ and θ) and the curvature given by the charge to momentum ratio (q/p). The seed builds into a track candidate by linking hits from the successive detector layers to the original track seed. Along with the track parameters, the track fit also takes the track parameter uncertainties into account to decide for linking the successive hits to a track prototype.[4]

At each measurement layer k, a track can be described by a 5-component state vector $\boldsymbol{q}_k$. A track model relates the track parameters at layer k w.r.t. the state on a different layer i by means of a track propagator $\boldsymbol{f}_{k|i}$, such that

$$\boldsymbol{q}_k = \boldsymbol{f}_{k|i}(\boldsymbol{q}_i); \tag{6.2}$$

see Figure 6.6. The standard linear error propagation gives the covariance matrix ($\boldsymbol{C}$) of the track parameters between layers i and k,

$$\boldsymbol{C}_k = \boldsymbol{F}_{k|i}\boldsymbol{C}_i\boldsymbol{F}_{k|i}^{\mathrm{T}}, \tag{6.3}$$

where $\boldsymbol{F}_{k|i} = \partial\boldsymbol{q}_k/\partial\boldsymbol{q}_i$ is the Jacobian matrix of the propagation from layer i to k.

The most commonly used track fitting techniques include, the *Least Squares Method* (also known as *Global* χ^2 *fit*) and the Kálmán filter [96]. The least squares method uses a global fitting approach, i.e. all the hits are fitted once with an assumed track model. A residual for each layer i is obtained by determining the difference between the predicted measurement ($\boldsymbol{m}_i^{\mathrm{pred}}$) and the actual measurement ($\boldsymbol{m}_i$) from the track state vector at layer i. The

---

[4] A track prototype is defined as an incomplete track candidate which has usually more than three hits.

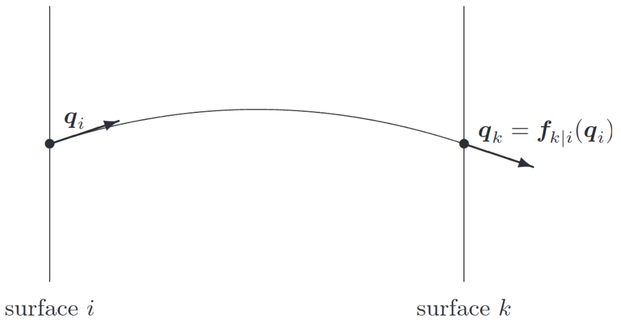

Figure 6.6: Illustraction of the propogation of a state vector $\boldsymbol{q}$ from layer i to layer k using a propagator $\boldsymbol{f}_{k|i}$ defined by a track model [136].

optimal estimate of the initial state vector is determined by minimizing the residuals and the so-called χ^2 function of the track fit is defined as

$$\chi^2 = \sum_i \frac{(\boldsymbol{m}_i - \boldsymbol{m}_i^{\text{pred}})^2}{\sigma_i^2}, \tag{6.4}$$

where σ_i is the measurement uncertainty at layer i. The covariance matrix determination involves inverting large matrices due to the large number of measurement layers involved leading to a high computational cost (scales by $\sim \mathcal{O}(n^3)$).

A recursive formulation of the above method, the Kálmán filter, requires inversion of only small matrices (scales by $\sim \mathcal{O}(n)$), as the track state and covariance matrix is needed only at a single point. It proceeds by progressively including the measurements in the track fit, layer by layer and treats material effects such as multiple scattering and energy loss locally. It includes the following three steps:

- At first a *prediction* of the track state vector at a future stage is made by using the estimated state vector determined by all the measurements from the previous track prototype. The predicted state vector at layer i using all the measurements up to $i-1$ layers can be written as:

  $$\boldsymbol{q}_{i|i-1} = \boldsymbol{f}_{i-1}\boldsymbol{q}_{i-1}. \tag{6.5}$$

  The covariance matrix is similarly predicted by considering the covariance matrix ($\boldsymbol{Q}_i$) of multiple scattering after layer $i-1$ up to layer i:

  $$\boldsymbol{C}_{i|i-1} = \boldsymbol{F}_{i-1}\boldsymbol{C}_{i-1}\boldsymbol{F}_{i-1}^{\mathrm{T}} + \boldsymbol{Q}_i \tag{6.6}$$

- The *update* step (also referred as *filtering*) corrects the predicted state vector by estimation of the present state vector using all the previous and the present measurement into account. The χ^2 of the fit is incremented with inclusion of each of the additional measurements, which is helpful in getting rid of outliers or falsely assigned measurements to the track.

- The third step is *smoothing* of the state vector by estimation of the final state vector considering all the measurements of the track obtained after filtering. Thus, smoothing proceeds backwards and is referred to as backward Kálmán Filter, while filtering proceeds forward and referred to as forward Kálmán filter.

The Kálmán filter is the primary track fitting algorithm used in HEP experiments. Its progressive nature allows for its use already at the pattern recognition stage, for example, the combinatorial Kálmán filter where several Kálmán filters run in parallel; see Reference [137].

Some of the other track fitting algorithms that are used for track reconstruction not discussed here include the helix fit which uses the Karimäki circle fit [138], the general broken lines fit [139, 140] and the triplets fit suitable for high multiple scattering environment [141, 142]. Although the Kálmán filter allows for a precise determination of the track state vector with a lower computational cost compared to the global χ^2 fit, it involves many iterative steps, making track fitting and hit linking the most computationally expensive steps of track reconstruction.

6.2.4 Fit Quality

Certain quality criteria must be met by the reconstructed track candidates. These include, for example, a minimum number of linked hits (layers), minimum track length, and minimum track quality. The ratio of χ^2 and the number of degrees of freedom (n_{dof}) obtained from the track fit is a good parameter for distinguishing between good and bad tracks.

6.2.5 Arbitration/Ambiguity Solving

Arbitration is a process to reduce dependence on the starting point and to decrease the vulnerability of a reconstruction algorithm against stochastic influences. For instance, the seed finding step must not strictly depend on a single set of layers from where the seed is selected, as this would lead to loss of tracks if one of the seeding layers happens to be inefficient. Hence, one normally uses several combination of layers for seeding to be redundant against device inefficiencies. Similarly, the track finding step usually allows for a few missing hits while propagating through the detector layers. For example, branches from track prototypes are created in the case where more than one hit is present rather than immediately discarding the hits not closest to the predicted hit. However, all these branch extensions may lead to vast combinatorics which will explode with increasing hit densities. As a result, an ambiguity solving algorithm resolves these problems by scoring the tracks in a reward/penalty schema with respect to one another to finally achieve the best track collection. The main aim is to apply loose requirements during the previous steps to obtain high efficiency and find the best candidates by solving for ambiguities using a scoring mechanism. In general, each hit associated with the track leads to a better score value to favour fully reconstructed tracks rather than small track segments [123]. The hits from different sub-detector parts are in general weighted with different scores, preferring the precision measurements (e.g. pixel clusters) and downgrading measurements from less precise detector parts. In the case with many branches, the branch candidate with the best score and fit quality is kept while the remaining ambiguous branches are revaluated or discarded. Multiple track candidates arising due to detector overlap are also taken care of in this step by selecting the best track candidate and discarding the remaining (also called as duplicate removal).

6.3 Performance and Speed Requirements

Tracks are used in almost all analysis channels of HEP experiments, sometimes as an indicator of background events and sometimes as an important part of signal events. Therefore, a track reconstruction algorithm in general aims to achieve the best correspondence between the true particle and reconstructed tracks. This correspondence is never perfect and therefore some quality criteria are defined to quantify the performance of a track reconstruction algorithm. An ideal reconstruction algorithm should be able to reconstruct all the particle tracks passing through the detector with as few false (fake) tracks as possible. Besides, the reconstructed tracks should have an excellent track parameter resolution, i.e. best estimate of the track parameters. Therefore, the performance of a track reconstruction algorithm is generally quantified using the following: the reconstruction efficiency, fake rate or track purity, and track parameter resolution. Depending on the goal of an analysis, one may focus on different performance aspects of the reconstruction. For instance, some analyses need minimum combinatorial fake rate compensating the efficiency or vice versa, while some need the best momentum or vertex resolution. Chapter 8 presents track reconstruction performance using the concept of Triplet Track Trigger (discussed in Chapter 7) for the ATLAS ITk and FCC-hh.

The event rate including the trigger and the DAQ system adds limitations to the memory usage and time within which the tracks must be reconstructed. With the growing need for tracks to be used at the very first stage of a trigger system, the demand for very fast track reconstruction algorithm is also increasing. Therefore, the best track reconstruction algorithm for high rate experiments with ad hoc limitations (coming from storage space and detector electronics) should fulfil the quality performance within the runtime and memory consumption budget available. The execution time is the CPU time spent in reconstructing tracks and is sometimes also referred to as computational performance. One of the most time consuming parts of track reconstruction are the track finding and the track fitting steps mainly due to the iterative procedure. Massive parallelisation efforts including novel techniques (e.g. use of neural networks) are underway to speed up the different steps in track reconstruction. However, with increasing hit densities, the execution time for the seed search process is also increasing dramatically. The processing time for seed search using n layers with $\mathrm{N}_{\mathrm{hit}}$ hits scales with $(\mathrm{N}_{\mathrm{hit}})^n$. This is one of the reasons why seed searches often use the outside-in approach, especially for very high detector occupancies. Different approaches can be used to reduce the hit combinatorial problem in the seed search and in the successive track finding process by use of more advanced algorithms like cellular automaton [143], Hough transforms [144], or use of lookup tables or associative memories.

7

Triplet Track Trigger (TTT)

The effect of the enormous amount of pile-up on calorimeter triggers was highlighted in Section 5.4. It was shown that a vast pile-up forces an increase in the calorimeter trigger thresholds for jets substantially. This, together with various detector related limitations, will tremendously affect the signal efficiencies and thereby, forbid the possibility to carry out good physics analyses using calorimeter trigger alone (especially for physics channels with multi-jet final states). Track triggers are therefore a must for substantial pile-up suppression at an early stage in the trigger system. However, as discussed in Chapter 6, track reconstruction in high rate experiments is very challenging and computationally intensive due to a large number of possible combinations of hits from different layers. Consequently, it technically limits the access to the reconstructed track parameters at a very early stage of the trigger system in the high rate experiments like ATLAS and CMS [145].

In this context, a generic concept of a triplet track trigger that can be implemented in any experiment is introduced in Section 7.1. It uses a very simple and fast track reconstruction algorithm, which is presented in Section 7.2. In the following sections, results from full Geant4 based detector simulation for the baseline detector design of the FCC-hh, and the ATLAS experiment in context of the HL-LHC scenario, are presented.

7.1 A Generic Concept of Triplet Track Trigger

The concept of *Triplet Track Trigger (TTT)* was proposed for reconstructing tracks in real-time at high rate experiments [146], where reconstructing tracks is very expensive in time. It uses a very simple and fast track reconstruction algorithm based on a detector triplet. A *detector triplet* is defined as a stack of three closely spaced, highly granular pixel detector layers (preferably MAPS due to their low production cost and the possibility to instrument large areas) placed at large radii (>40 cm).

When a charged particle passes through such a detector triplet in a uniform magnetic field B, its trajectory is *helical* in 3D; see Figure 6.4. Its projection in the transverse $(x - y)$ plane is a *circle* of radius R, and in the longitudinal $(s - z)$ plane it is a *straight line*.[1] Close

---

[1] s corresponds to the arc length of a circular trajectory with radius R subtending an angle Φ at its centre.

stacking at a large radius ($\mathrm{R_{TTT}}$) ensures that the trajectory of the particles between the layers of the detector triplet is almost a straight line (for $\mathrm{R} \gg \mathrm{R_{TTT}}$), thereby providing enough redundancy to reduce combinatorial background efficiently. Besides, an excellent spatial resolution of pixels allows for determination of z-vertex with very high precision.

The TTT concept relies on the assumption that all particles originate from the *beamline* $(0,\ 0,\ z_0)$ or have a small transverse impact parameter, $\mathcal{O}(1)$cm if they originate from secondary decays. The large radius of a detector triplet not only ensures a good curvature resolution and hence momentum resolution of the reconstructed tracks, but also reduces the impact parameter dependence of secondary particles in momentum reconstruction. Also, significantly lower hit occupancies at large radii $> 40\,\mathrm{cm}$ (see Figure 7.4), allow to speed up the seed search step in track reconstruction and reduce hit combinatorics significantly.

The track reconstruction algorithm used is extremely fast, involves no complicated calculations and is detailed in the following section. Its simplicity allows for its implementation in hardware, e.g. in an FPGA[2]. It gives track parameters in real-time to be used in a trigger, for instance, to trigger various objects like single and multi-jets (tracks) with the precise z-vertex information. Trigger studies using the TTT concept are discussed in greater detail in Chapter 9.

7.2 Triplet Track Reconstruction Algorithm

Consider a TTT in a uniform magnetic field B comprising layers l_1, l_2 and l_3, a section of which is shown in Figure 7.1. Let d be the radial distance between each of the layers, henceforth called as the *gap-size* of the TTT.[3] A charged particle passing through it is detected with coordinates (x_i, y_i, z_i) in the i^{th} layer, where $i = 1, 2, 3$. Let the measured hit azimuthal angle (as measured from the beamline), and the absolute radial co-ordinates corresponding to the i^{th} hit be:

$$\phi_i = \arctan\left(\frac{y_i}{x_i}\right), \tag{7.1}$$

$$r_i = \sqrt{x_i^2 + y_i^2} \tag{7.2}$$

Its trajectory is reconstructed using the following three steps: *triplet hit selection, triplet track reconstruction, final selection cuts.*

7.2.1 Triplet Hit Selection

In this step, a triplet of hits is selected (one from each of the three layers) to reconstruct a track. Due to a lower hit occupancy in the outermost layer, l_3 of the detector triplet compared to the other two, a search window in $\Delta\phi = |\phi_3 - \phi_1|$ and $\Delta z = |z_3 - z_1|$ is

---

[2] Field-Programmable Gate Array (FPGA) is an integrated circuit designed to be configured by a customer or a designer after manufacturing.

[3] Note that in this thesis, an equidistant spacing between the TTT layers is assumed.

introduced w.r.t. the hit co-ordinates in l_3 to look for hit candidates in l_1 of the detector triplet.[4]

$$\Delta\phi < \phi_{13}^{\text{cut}} \tag{7.3}$$

$$\Delta z < z_{13}^{\text{cut}} \tag{7.4}$$

ϕ_{13}^{cut} takes into account bending of a track in a magnetic field and therefore, indirectly depends on the minimum transverse momentum that can be reconstructed by the TTT at radius $\mathrm{R}_{\mathrm{TTT}}$. z_{13}^{cut}, on the other hand, depends on the longitudinal acceptance of the detector. Tracks can already be reconstructed at this stage using the beamline constraint (see Section 7.2.2).[5]

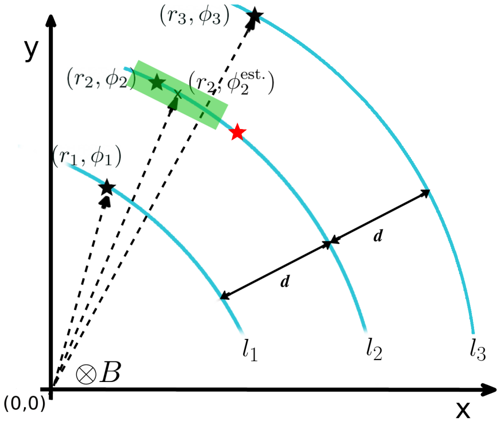

Figure 7.1: Pre-selection of triplet hit candidates in the transverse plane. Shown in the figure are the hits recorded by the TTT in addition to an estimated hit position in l_2.

Since the trajectory between l_1 and l_3 is more or less a straight line for small gap sizes and large radii of the TTT, a cut on the residua of the hit in the middle layer is applied both in the $x-y$ and the $s-z$ planes:

$$|\mathrm{d}\phi_2| = |\phi_2 - 0.5\,(\phi_1 + \phi_3)| < \mathrm{d}\phi_2^{\text{cut}} \tag{7.5}$$

$$|\mathrm{d}z_2| = |z_2 - 0.5\,(z_1 + z_3)| \; < \mathrm{d}z_2^{\text{cut}} \cdot \sin(\theta)^{n_z}. \tag{7.6}$$

A polar angle dependence of θ is introduced to cut on $|\mathrm{d}z_2|$ assuming multiple coulomb scattering as one of the main sources of uncertainty, in contrast to $|\mathrm{d}\phi_2|$ which depends mainly on the minimum transverse momentum to be reconstructed. The optimal value for n_z can be determined using error propagation and is found to be 1.5. Equation 7.5 can be visualised with the help of a sketch in Figure 7.1. The green band corresponds to $\mathrm{d}\phi_2^{\text{cut}}$ around the estimated hit in l_2, $(r_2, \phi_2^{\text{est.}})$, where $r_2 = \sqrt{x_2^2 + y_2^2}$ and $\phi_2^{\text{est.}} = 0.5\,(\phi_1 + \phi_3)$.[6] A hit lying outside of this green band, e.g. the red point is rejected using Equation 7.5.

---

[4] Note that the hit search order is not strict and one can instead introduce these search windows in $\Delta\phi$ and Δz w.r.t. the hit co-ordinates in l_1 or l_2.

[5] beamline constraint assumes that the particles originate from (0, 0, z_0)

[6] The estimated hit positions here are based on the assumption that the triplet detector layers are equidistant barrel layers.

The hit combinatorial problem is largely reduced at this stage, and this makes a triplet design superior compared to the tracker designs based on doublets. The cut parameters $d\phi_2^{\text{cut}}$, dz_2^{cut} and n_z are optimised using simulated HH → $b\bar{b}b\bar{b}$ events for a given geometry. Optimisation of all the selection cuts for TTT in the context of a modified tracker of the FCC-hh baseline detector design is discussed further in Section 7.3.2.

7.2.2 Triplet Track Reconstruction

The triplet hit candidates selected above are used to determine the track parameters analytically by solving for a circle and a straight line in the $x - y$ and the $s - z$ planes, respectively. The following five track parameters can be extracted using the TTT:

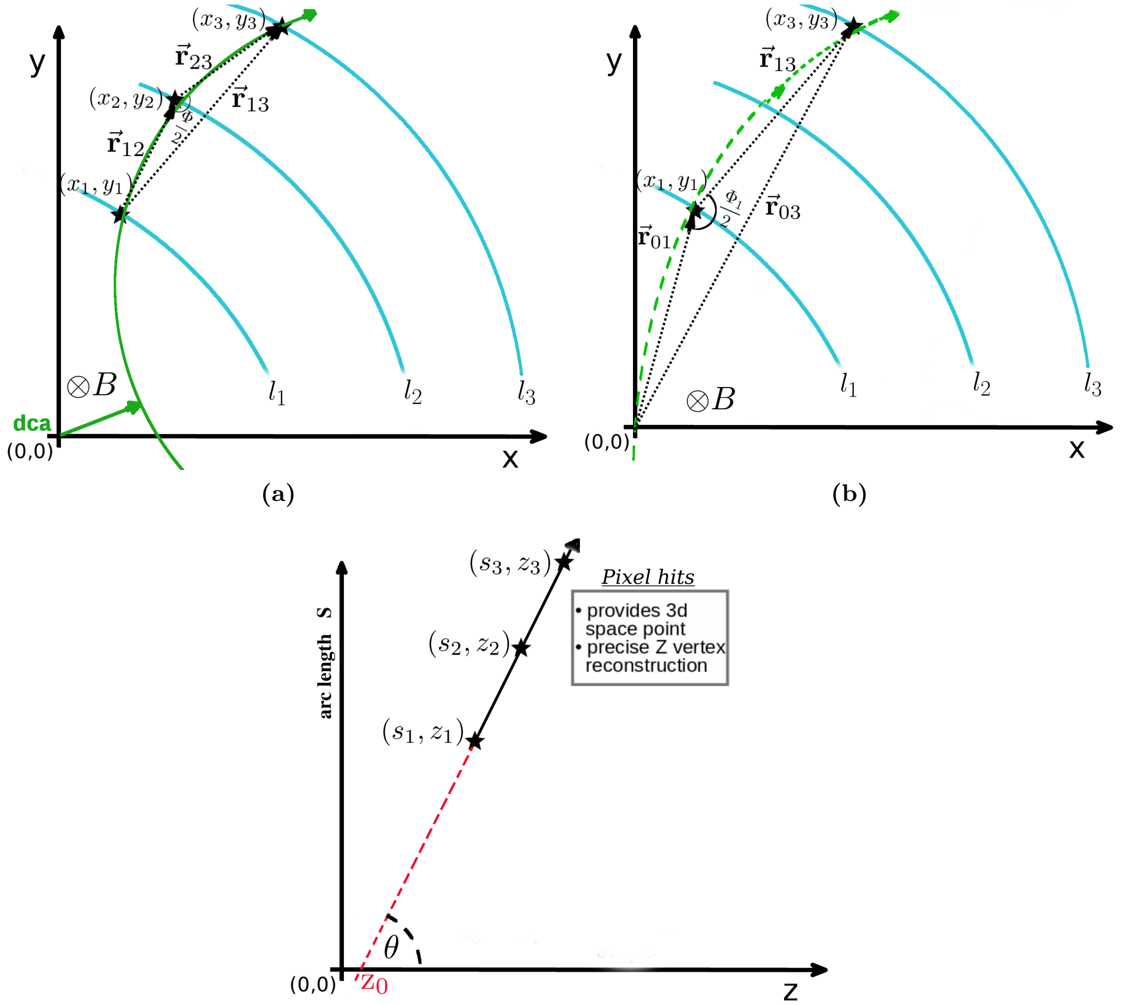

(a) **(b)**

(c)

Figure 7.2: Reconstruction of a charged particle's track in a uniform magnetic field B, in the transverse plane – (a) without beamline constraint and (b) with beamline constraint – and in the longitudinal plane (c).

1. the transverse momentum p_{T} determined by the track curvature κ,
2. pseudo-rapidity η,
3. the initial direction of a particle in the $x-y$ plane φ,
4. the longitudinal impact parameter z_0 and
5. the transverse impact parameter or the distance of closest approach *dca*.[7]

At first, κ and *dca* are determined using two independent methods: with and without beamline constraint.

Without beamline constraint calculations:

In this method, hits from all the three layers l_1, l_2 and l_3, are used; Figure 7.2(a).[8] Let Φ be the angle subtended by the chord joining the first and the third hit at the centre of the circular trajectory traversed by a particle,[9] then the bending angle between the first and the third layer is given by:

$$\Phi/2 = \arcsin\left(\frac{\vec{\mathbf{r}}_{23} \times \vec{\mathbf{r}}_{12}}{|\vec{\mathbf{r}}_{23}|\,|\vec{\mathbf{r}}_{12}|}\right) \tag{7.7}$$

where $\vec{\mathbf{r}}_{ij}$'s are the position vectors pointing from hit i to j, and its magnitude $|\vec{\mathbf{r}}_{ij}| = \sqrt{(x_j - x_i)^2 + (y_j - y_i)^2}$ (see Figure 7.2(a)). The transverse momentum is then determined by:

$$\kappa_{123} = \frac{1}{\mathrm{R}_{123}} = \frac{2\,\sin(\Phi/2)}{|\vec{\mathbf{r}}_{13}|} = \frac{2\,(\vec{\mathbf{r}}_{23} \times \vec{\mathbf{r}}_{12})}{|\vec{\mathbf{r}}_{23}|\,|\vec{\mathbf{r}}_{12}|\,|\vec{\mathbf{r}}_{13}|} \tag{7.8}$$

$$p_{\mathrm{T},123}[\mathrm{GeV/c}] = \frac{0.3\,B}{\kappa_{123}}[\mathrm{T}\cdot\mathrm{m}] \tag{7.9}$$

Notice that κ (hence p_{T}) determination does not involve the sine term and involves only simple arithmetic operations which can be easily implemented in hardware. The sign of κ indicates the direction of movement of a particle. $\kappa > 0$ and $\kappa < 0$ correspond to the clockwise and anti-clockwise motion of the particle along the circle, respectively. The centre co-ordinates (c_x, c_y) of this circle can be determined using the following equations:

$$c_x = \frac{(y_2 - y_1)\,(r_3^2 - r_1^2) - (y_3 - y_1)\,(r_2^2 - r_1^2)}{2\,(\vec{\mathbf{r}}_{23} \times \vec{\mathbf{r}}_{12})} \tag{7.10}$$

$$c_y = \frac{(x_2 - x_1)\,(r_3^2 - r_1^2) - (x_3 - x_1)\,(r_2^2 - r_1^2)}{2\,(\vec{\mathbf{r}}_{12} \times \vec{\mathbf{r}}_{23})} \tag{7.11}$$

---

[7] *dca* is in the transverse plane, the shortest distance between the circular trajectory and the beamline (0, 0, z_0) (see Figure 7.2(a))

[8] Note that a subscript 123 is used for the parameters determined without beamline constraint, and a subscript 013 is used for parameters determined with beamline constraint.

[9] Using inscribed angle theorem, $\frac{\Phi}{2}$ is the angle inscribed on the circle by this chord. Also, note that, three different types of the Greek character phi have been used in this chapter. ϕ refers to the azimuthal angle of a hit, φ refers to the initial direction of a track, and Φ refers to bending angle of a particle in a magnetic field.

The distance of closest approach (the tangential distance between the radius and the co-ordinate (c_x, c_y)) is then given by:

$$dca = \begin{cases} |\frac{1}{\kappa_{123}}| - \sqrt{c_x^2 + c_y^2}, \text{ for } \kappa_{123} > 0 \\ \\ \sqrt{c_x^2 + c_y^2} - |\frac{1}{\kappa_{123}}|, \text{ for } \kappa_{123} < 0 \end{cases} \tag{7.12}$$

Notice that *dca* is a signed quantity and its sign is indirectly determined by the product $\kappa_{123} \cdot dca$. A positive value of the product indicates the origin of the transverse co-ordinate system $(0, 0)$ to be located outside the circular track (as shown in Figure 7.2(a), for instance), and a negative value of the product would indicate the origin to be located inside the circular track.

With beamline constraint calculations:

In this method, the track curvature is calculated using hits in l_1 and l_3, and a pseudo-hit $(x_0, y_0) = (0, 0)$ is used as the third hit; see Figure 7.2(b). The bending angles at (x_1, y_1) and (x_3, y_3) denoted by $\Phi_1/2$ and $\Phi_3/2$ can be determined with equations similar to Equation 7.7. Referring to Figure 7.2(b), Φ_1 and Φ_2 can be written as:

$$\Phi_1/2 = \arcsin\left(\frac{\vec{\mathbf{r}}_{01} \times \vec{\mathbf{r}}_{13}}{|\vec{\mathbf{r}}_{01}|\,|\vec{\mathbf{r}}_{13}|}\right) \tag{7.13}$$

$$\Phi_3/2 = \arcsin\left(\frac{\vec{\mathbf{r}}_{03} \times \vec{\mathbf{r}}_{13}}{|\vec{\mathbf{r}}_{03}|\,|\vec{\mathbf{r}}_{13}|}\right). \tag{7.14}$$

The transverse momentum, similar to Equation 7.9, is given by:

$$\kappa_{013} = \frac{1}{\mathrm{R}_{013}} = \frac{2\,\sin(\Phi_1/2)}{|\vec{\mathbf{r}}_{03}|} = \frac{2\,(\vec{\mathbf{r}}_{01} \times \vec{\mathbf{r}}_{13})}{|\vec{\mathbf{r}}_{01}|\,|\vec{\mathbf{r}}_{13}|\,|\vec{\mathbf{r}}_{03}|} \tag{7.15}$$

$$p_{\mathrm{T},013}[\mathrm{GeV/c}] = \frac{0.3\,B}{\kappa_{013}}[\mathrm{T \cdot m}]. \tag{7.16}$$

Notice that *dca* is zero by construction and the lever arm $|\vec{\mathbf{r}}_{03}|$ determining the curvature, is much larger compared to $|\vec{\mathbf{r}}_{13}|$ in the previous method. As a result, κ_{013} and hence the momentum resolution determined is much more precise with this method (for particles originating from close to $(0, 0)$). The centre co-ordinates (c'_x, c'_y) are given by:

$$c'_x = \frac{y_3\, r_1^2 - y_1\, r_3^2}{2\,(\vec{\mathbf{r}}_{01} \times \vec{\mathbf{r}}_{03})} \tag{7.17}$$

$$c'_y = \frac{x_3\, r_1^2 - x_1\, r_3^2}{2\,(\vec{\mathbf{r}}_{03} \times \vec{\mathbf{r}}_{01})}, \tag{7.18}$$

from which the initial direction of the particle φ_{013} can be determined. It is orthogonal to the line joining the origin (0, 0) and (c'_x, c'_y), hence:

$$\varphi_{013} = \arctan\left(\frac{-c'_x}{c'_y}\right). \tag{7.19}$$

In the longitudinal plane, the z-vertex (z_0), and θ are extrapolated from the straight line joining the hits in l_1 and l_3 (see Figure 7.2(c)). If s_1 and s_3 are the arc lengths at the 1^{st} and the 3^{rd} hit positions, then

$$s_1 = \mathrm{R}_{013}\,\Phi_1 \tag{7.20}$$

$$s_3 = \mathrm{R}_{013}\,\Phi_3 \tag{7.21}$$

$$slope = \frac{s_3 - s_1}{z_3 - z_1} \tag{7.22}$$

$$\theta_{013} = \arctan\left(slope\right) \tag{7.23}$$

$$\eta_{013} = -\ln\ \tan\left(\theta_{013}/2\right) \tag{7.24}$$

$$z_0 = z_1 - \frac{s_1}{slope} \tag{7.25}$$

7.2.3 Final Selection Cuts

As a final step, a few more selection requirements are imposed on the precise parameters obtained with beamline constraint. The reconstructed z_0, η_{013} and $p_{\mathrm{T},013}$ are constrained based on the luminous region of the colliding proton beams, the η acceptance of the TTT and minimum transverse momentum to be reconstructed. Besides, yet another powerful constraint can be defined based on the design specifications of the TTT (for example, the gap-size between the layers of the TTT, the material thickness and pixel dimensions).

Momentum consistency cut:

The momentum consistency cut – in addition to the redundancy cuts imposed on the residua of the hit in the middle layer – rejects a significant number of wrongly reconstructed tracks by making a consistency check on the curvatures determined by two independent methods. This is done by studying the so-called pull distribution:

$$\frac{\mathrm{d}\kappa}{\sigma_\kappa} = \frac{\kappa_{123} - \kappa_{013}}{\sigma_\kappa}, \tag{7.26}$$

where σ_κ is the curvature uncertainty. σ_κ can be determined analytically using the uncertainties on the spatial hit co-ordinates and multiple scattering [142].

$$\left(\frac{\sigma_\kappa}{\kappa}\right)^2 = \left(\frac{\sigma_\kappa}{\kappa}\right)^2_{\mathrm{Hit}} + \left(\frac{\sigma_\kappa}{\kappa}\right)^2_{\mathrm{MS}} \tag{7.27}$$

From Equation B.10 in Appendix B, the expected hit uncertainty is given by:

$$\left(\frac{\sigma_\kappa}{\kappa}\right)^2_{\mathrm{Hit}} = \left(\frac{\sqrt{6}\,\sigma_t}{d^2\cdot\kappa}\right)^2, \tag{7.28}$$

where $\sigma_t = w/\sqrt{12}$, w being the width of the pixel. If t is the thickness of the middle layer, then the expected multiple scattering uncertainty at the middle layer is given by the Highland Formula [109]:

$$\sigma_{\mathrm{MS}} \approx \frac{13.6\ \mathrm{MeV/c}}{\beta p}\sqrt{\frac{X}{X_0}} = \frac{13.6\,\mathrm{MeV/c}}{\beta p}\sqrt{\frac{t}{X_0\ \sin(\theta_{013})}}, \tag{7.29}$$

where p is momentum, $\beta \approx 1$ is the particle velocity, and t/X_0 is the material thickness given in units of radiation length. From Equations 7.8 and 7.15, one can see that the uncertainty $\delta\kappa_{013} << \delta\kappa_{123}$, since the lever arms $|\vec{\mathbf{r}}_{03}| >> |\vec{\mathbf{r}}_{13}|$. Therefore, the curvature κ_{013} reconstructed with the beamline constraint is much more precise than κ_{123}, and allows determination of σ_κ using κ_{013}.

$$\left(\frac{\sigma_\kappa}{\kappa}\right)^2_{\mathrm{MS}} = \left(\frac{\sigma_{\mathrm{MS}}}{d \cdot \kappa \cdot \sin(\theta_{013})}\right)^2 \tag{7.30}$$

Using Equations 7.28 and 7.30, the curvature uncertainty is

$$\sigma_\kappa^2 = 0.5\left(\frac{w}{d^2}\right)^2 + \frac{t}{X_0\,\sin\left(\theta_{013}\right)}\left(\frac{13.6\,\mathrm{MeV/c}\,\kappa_{013}}{0.3\,B \cdot d}\right)^2,$$

or simply:

$$\sigma_\kappa^2 = \mathrm{K}^2_{\mathrm{Hit}} + \left(\frac{\mathrm{K}_{\mathrm{MS}}\,\kappa_{013}}{\sqrt{\sin(\theta_{013})}}\right)^2. \tag{7.31}$$

Having determined σ_κ, the pull distribution in Equation 7.26 must have a mean of zero and a standard deviation of one. A momentum consistency cut can then be defined as:

$$|\mathrm{d}\kappa| < n \cdot \sigma_\kappa, \tag{7.32}$$

where n is an acceptance cut in units of the standard deviation (typically chosen in the range $3 - 5$).

The following section details the implementation of the TTT in a full Geant4 [147] based:
– stand-alone detector simulation for the baseline FCC-hh detector and
– ATLAS official simulation, in context to the HL-LHC scenario.

7.3 TTT for HL-LHC (in ATLAS) and FCC-hh

As mentioned in Chapters 4 and 5, for the experiments at HL-LHC and FCC-hh, pile-up is one of the main hindrances preventing a good signal efficiency for many of the physics channels, especially those involving jets. Availability of vertex information from tracks at trigger level can greatly help to suppress pile-up. In this context, full simulations are performed for the modified trackers of the ATLAS detector and the FCC-hh baseline detector, including the TTT at a radius of 85.7 cm.[10] Details of the simulations and optimisation of the selection cuts used in triplet track reconstruction are discussed below.

---

[10] The choice of $\mathrm{R}_{\mathrm{TTT}} = 85.7\,\mathrm{cm}$ comes from a small pseudorapidity gap between the barrel and the 1st endcap detector layer in ATLAS, and a TTT at this radius would cover this gap. Detailed studies for a barrel completion layer at this same radius were performed w.r.t. the ATLAS detector; see Reference [148].

7.3.1 Full Geant4 based Detector Simulation

The first step to carry out a realistic detector simulation, is the choice of certain detector parameters, for example, the technology to be used, its dimensions and material properties, number of modules, etc. Some of these are summarised in Table 7.1 for the ATLAS and FCC-hh experiments. CMOS monolithic pixel sensors are used as the active detector elements of the TTT due to their extremely low material budget and cost-effectiveness to construct large area pixel detectors. Note that radiation tolerance of CMOS monolithic pixel sensors is not an issue at $R_{\mathrm{TTT}} = 85.7\,\mathrm{cm}$, where the projected fluences for FCC-hh scenario are of the order of $\sim\ 10^{15}\mathrm{n_{eq}/cm^2}$ [41]. The latest results for HV-MAP sensors, namely, ATLASPix1_Simple show efficiencies above 98 % for fluences of up to $2 \times 10^{15}\mathrm{n_{eq}/cm^2}$ at high bias voltages of up to 80 – 85 V [132].

Table 7.1: Geometry specifications of the TTT in the ATLAS and FCC-hh experiments.

	Experiments					
TTT Specs.	ATLAS	FCC-hh				
Radius [mm]	857	857				
η coverage	1.5	2.5				
X/X_0 /layer [%]	1.5	1.5				
gap-size [mm]	20	20	25	30	35	40
# staves along ϕ	70	58	58	58	60	60
# sensor modules along z	$2 * 17$	104				
Stave [mm^3]	$80 \times (80 \times 2 * 17) \times 5^{\dagger}$	$100 \times (100 \times 104) \times 5$				
Sensor module [mm^3]	$80 \times 80 \times 0.05$	$100 \times 100 \times 0.05$				
Pixel [mm^2]	0.05×0.05	0.04×0.04				
Radial offset [mm]	±4	±4				

[†] Note that the stave dimensions are given as width × (length) × height and the multiplicative factor 2 here corresponds to the two half barrels in ATLAS.

Table 7.2: Material composition of the TTT stave.

Element	Mass per mole [g/mole]	fraction used [%]
Carbon	12.011	70.0
Aluminium	26.98154	20.0
Hydrogen	1.00794	6.0
Oxygen	15.9994	3.0
Copper	63.546	1.0

Detector geometry setup for FCC-hh

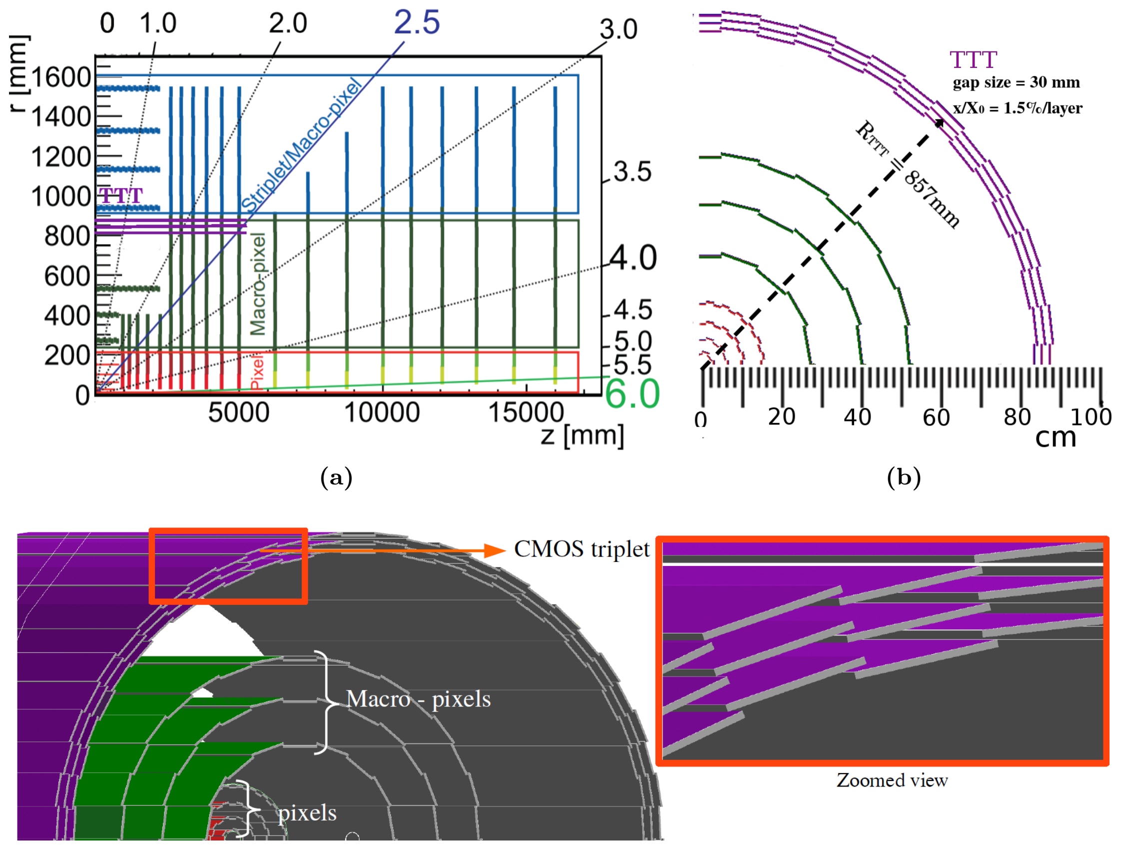

(a)

(b)

(c)

Figure 7.3: (a) Modified tracker layout with the TTT, (b) transverse section of the castellated tracker in Geant4 and (c) solid detector geometry with the castellated design in Geant4, for the FCC-hh experiment.

The simulation of the FCC-hh baseline detector is based on stand-alone G4 simulations and therefore allows for easy modifications to its tracker layout. The baseline tracker geometry of the FCC-hh in the stand-alone simulation is slightly modified to position the middle layer of the TTT at a radius of $R_{\mathrm{TTT}} = 857\,\mathrm{mm}$ (as shown by the violet coloured layers in Figure 7.3). Notice the unrealistic length of the TTT barrel extended to $\eta = 2.5$ in Figure 7.3(a). The purpose is to have $\sim 60\,\%$ of the signal events from $\mathrm{HH} \to b\bar{b}b\bar{b}$ within the acceptance of the TTT.[11] All the strip layers above the TTT are not included in this modified geometry; see Figure 7.3(b and c). The pixel layers below the TTT are placed at radii as indicated in the tracker layout and Table 7.3, acting as dead material in front of the TTT.[12] Besides, these layers are extended to $\eta = 2.5$ and have material budget according to the specifications in the CDR of the FCC [41] (also listed in Table 7.3).

---

[11] Ideally, one would place endcap TTT rings beyond $\eta \sim 1.5$ however, it goes beyond the scope of this thesis.

[12] Note that the layer right below the TTT was removed as it would lie very close to the innermost layer of the TTT, adding to unnecessary material scattering.

Table 7.3: Geometry specifications of the FCC-hh modified tracker with the TTT covering a pseudorapidity of $|\eta| < 2.5$.

	Layers							
Properties	l_1	l_2	l_3	l_4	l_5	l_6	l_7	TTT
Radius [mm]	25	60	100	150	270	400	520	857
Sensor/module [mm^3]	$20 \times 20 \times 0.05$				$100 \times 100 \times 0.05$			
# sensors/modules along z	100				65			104
Stave thickness [mm]	3.3		5.0		6.6			5.0
X/X_0 /layer [%]	1.0		1.5		2.0			1.5

For simplicity, single barrels are constructed in $\eta \in [-2.5, 2.5]$, unlike two half barrels followed by endcap discs in ATLAS. The barrel layers are constructed by placing many staves (ϕ modules) along the polar angle at $\mathrm{R}_{\mathrm{TTT}}$ with a slight overlap between the consecutive staves.[13] Three of these staves separated by a radial distance equal to the TTT gap-size form a triplet module. A castellated design – with a radial offset of ±4 mm between the consecutive triplet modules – for the TTT barrels was chosen to realise the overlaps ($\sim 4 - 10$ mm) and to ease the trigger mechanism by ensuring all the three hits (required to reconstruct the TTT tracks) lie in the same triplet module. Each stave comprises 104 sensor modules (100 mm wide) along the beam-axis measuring $100 \times (100 \times 104) \times 5\,\mathrm{mm}^3$. The material composition of the stave is the same as that used in the ATLAS simulation and consists of a mixture of elements, with their densities adjusted to give a radiation length of 1.5 %/layer (see Table 7.2).[14] The sensor modules are composed of active Si sensors and have dimensions $100 \times 100 \times 0.050\,\mathrm{mm}^3$, which are backed with inactive Si of the same dimensions. The sensors are $20 \times 20\,\mathrm{mm}^2$ and are composed of pixels with $40 \times 40\,\mu\mathrm{m}^2$. The TTT has been simulated for five different gap-sizes in this setup, i.e. 20, 25, 30, 35 and 40 mm, and an optimum gap-size is chosen based on the track reconstruction performance (see Section 8.4).

Final state particles from the $\mathrm{HH} \to b\bar{b}b\bar{b}$ produced from pp collisions with $\sqrt{s} = 100\,\mathrm{TeV}$ are then simulated using the above setup in a uniform solenoidal magnetic field of 4 T. These particles interact with the detector volume, e.g. electromagnetically or hadronically or undergo decay, to give hits. In Geant4, a *hit* is a snapshot of a physical interaction or an accumulation of interactions of a particle or particles in a "sensitive" detector component [147]. Similarly, the minimum bias samples (soft pp collision events) are also simulated using the FCC-hh setup. An average pile-up of $\langle\mu\rangle = 1000$ is added to each event of $\mathrm{HH} \to b\bar{b}b\bar{b}$ by adding hits of ≈ 1000 minimum bias events in one $\mathrm{HH} \to b\bar{b}b\bar{b}$ event; see Appendix A for details.

---

[13] The overlap ensures 100 % detection efficiency by overlapping the inactive area (housing the digital part) of one stave by the active area of the other stave. For simplicity, no dead area has been introduced in the pixel sensors.

[14] The same stave material composition as used for the official ATLAS ITk simulations is used here.

Cluster formation:

Since multiple pixels might record a hit from a single particle traversing the pixel detectors (due to charge sharing effects), hit clusters are formed before being fed to the TTT reconstruction algorithm. The hits from the neighbouring pixels (if any) are combined into a cluster object, and only the very first hit (from a list of hits) belonging to this cluster object is used to approximate the cluster position. The remaining hits of the formed cluster object are discarded and not used in the TTT reconstruction. This clusterisation method used for the FCC-hh setup is very simple and can be improved further, for example, by approximating the cluster position as an average of all hit positions in a cluster object. However, this has not been implemented for the results presented in this thesis. Huge pile-up (hence large hit occupancies) might result in very large cluster objects from multiple particles passing through very close pixels. In this situation, the above approximation leads to small reconstruction inefficiencies which can be mitigated to some extent by splitting it into smaller cluster objects (not used in this thesis).

Figure 7.4 shows the cluster occupancies /event/cm^2 for different detector layers in the FCC-hh tracker as a function of its radius, namely for, no pile-up, a pile-up of 200 and 1000. As expected, the cluster occupancy increases with increasing proximity of the layers to the beamline and increasing pile-up. As a rule of thumb, not more than 1 hit/event/cm^2 can be read out with the currently available links, making it almost impossible to have a complete readout of all hits/event at 40 MHz. In terms of physical data links for events produced at a rate of 40 MHz and 32 bit/hit, occupancies of 1 hit/event/cm^2 would correspond to a data rate of 1.28 Gbit/s every cm^2. That means more than four 1.25 Gbit/s electrical links will be needed to read out a single sensor of $2 \times 2\,\text{cm}^2$. This is a huge number and is one of the reasons why the TTT has to be situated at a large radius ($> 40 - 50\,\text{cm}$).

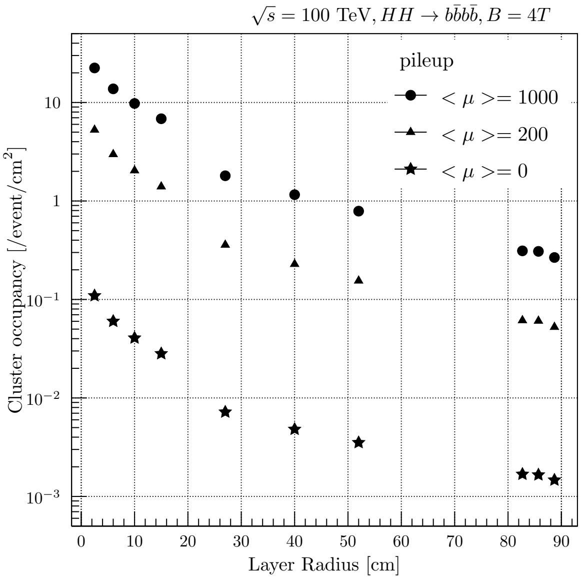

Figure 7.4: Cluster occupancies as a function of layer radius for the HH → $b\bar{b}b\bar{b}$ events with three different pile-up configurations using FCC-hh modified tracker geometry.

TTT geometry setup in ATLAS for HL-LHC

The TTT layers in the ATLAS setup for HL-LHC also have a castellated design, as shown in Figure 7.5. Since the ITk in the central rapidity region consists of two half barrels, the TTT layers situated between the last two strip layers also comprise of two half barrels. The sensor modules consist of active Si sensors and measure $80 \times 80 \times 0.050\,\text{mm}^3$. These are backed with inactive Si of the same dimensions. Each of the two ITk half barrels is 1372 mm long. Hence, a sensor module with a width of 80 mm corresponds to $1372/80 \sim 17$ sensor modules in a line sitting on a simple stave with dimensions $80 \times (80 \times 17) \times 5\,\text{mm}^3$, for each of the half barrels. The pixel dimensions for the ATLAS setup is $50 \times 50\,\mu\text{m}^2$. The 5 mm thick staves have the same material composition as used for the FCC-hh setup; see Table 7.2. Three of these staves make a triplet module with an equidistant spacing of 20 mm. Several of these triplet modules are staggered with a radial offset of ±4mm about the surface of a logical (invisible) cylinder at R_{TTT} to form TTT castellation barrels, as shown in Figure 7.5. Thus, the middle TTT barrel layer is composed of an outer castellation layer with a radius of $\text{R}_{\text{TTT}} + 4\,\text{mm}$ and an inner castellation layer with a radius of $\text{R}_{\text{TTT}} - 4\,\text{mm}$. For the outermost TTT barrel radius of 877 mm (857 + 20), a total of at least 70 staves with a width of 80 mm are required.

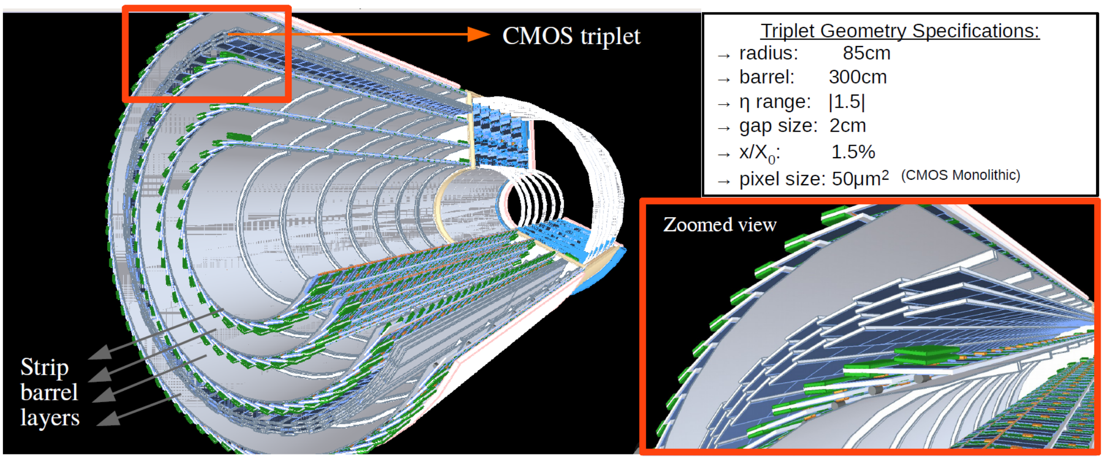

Figure 7.5: Detector geometry of the ATLAS ITk with the TTT for HL-LHC in Geant4.

With the above specifications, the TTT geometry was successfully implemented in the official ATLAS simulation using GeoModel Xml package. This allowed simulation of the complete ITk, including the TTT within the ATLAS software framework. HH $\to b\bar{b}b\bar{b}$ samples obtained from pp collisions at $\sqrt{s} = 14\,\text{TeV}$ were simulated in a uniform magnetic field of 2 T without any pile-up. The resulting pixel hits were digitised, and cluster positions were approximated by determining the average hit position and later smearing with a hit uncertainty of $50\,\mu\text{m}/\sqrt{12}$.[15]

---

[15] Due to technical difficulties, signal events with a pile-up of 200 could not be digitised for the modified ATLAS setup. Therefore, only the tracking performance studies are presented in Chapter 8 for the ATLAS setup using HH $\to b\bar{b}b\bar{b}$ signal events without pile-up.

7.3.2 Stand-alone Triplet Track Reconstruction

The digitised hits/clusters, which are 3D cartesian co-ordinates from the pixels, act as input to the track reconstruction algorithm described in Section 7.2 to yield the five track parameters as output. In this section, the optimisation of the selection cuts used in the TTT algorithm for the FCC-hh and ATLAS setup are discussed one by one. Before discussing the optimisation of cuts, however, it is important to understand the terms: *fake tracks, matched tracks and double-counted tracks.*

Matching procedure

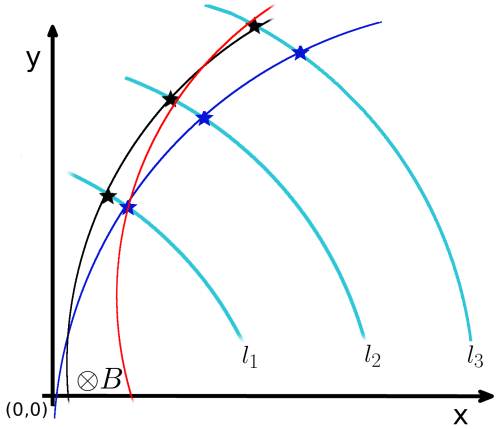

Figure 7.6: Sketch explaining matching of the reconstructed tracks to the simulated truth tracks. The blue and black coloured hits are produced when two different truth tracks pass through the TTT. The curves indicate the reconstructed tracks, with blue and black tracks being the matched tracks, while red track is a fake track.

It is important to know whether the reconstructed tracks arise from the correct combination of hits or not. Geant4 assigns a unique identifier to every simulated track in an event, let's call it trackID. All the hits associated with a given track, also have the corresponding trackID linked to them; see the black and the blue hits in Figure 7.6. This information allows tagging a reconstructed track as "*matched*" if all the hits from which this track was reconstructed have identical trackID's. If all hits (from the hit triplet) do not have identical trackID's, the reconstructed track is tagged as "*fake*" (the red curve in Figure 7.6, for example).

Dealing with double counting of tracks

If a particle passes through the active area in the overlap region of the TTT, it may get reconstructed more than once due to more than one possible triplet hit combinations satisfying the selection cuts. These reconstructed tracks would also satisfy the above matching criteria (as all these hits will have the same trackID), resulting in multiple tracks matched to a single truth track. This leads to excess reconstruction efficiency and might also affect trigger decisions. Therefore, all the tracks reconstructed more than once (double-counted tracks) are identified using their trackID and discarded.[16] For the FCC-hh setup, this number is found to be less than 1 % on average per event (in HH → $b\bar{b}b\bar{b}$ with $\langle\mu\rangle = 1000$).

Optimisation of selection cuts for the FCC-hh setup

Several pre-selection and final selection cuts were defined in Section 7.2 for early rejection of fake combinations and to speed up the seed (triplet of hits) search process. To optimise these cuts, tracks are reconstructed with very wide hit selection cuts, a p_T cut of 2 GeV/c, a luminous region cut of 10 cm and no momentum consistency cut. With the help of some control distributions, these cuts are optimised, and the final set of optimised cuts used in the TTT algorithm for the FCC-hh setup are summarised in Table 7.4 for five different gap sizes. Note that only the control distributions for the FCC-hh setup with TTT gap-size of 30 mm are shown here.

Table 7.4: Optimised selection cuts for the triplet track reconstruction algorithm in the FCC-hh and ATLAS setup for different gap-sizes of the TTT.

TTT gap-size	FCC-hh ($B = 4\,\mathrm{T}$)					ATLAS ($B = 2\,\mathrm{T}$)
d [mm]	20	25	30	35	40	20
ϕ_{13}^{cut} [rad]	0.014	0.018	0.021	0.025	0.028	0.007
z_{13}^{cut} [mm]	250	320	380	430	480	70
$\mathrm{d}\phi_2^{\mathrm{cut}}$ [rad]	3×10^{-4}					1×10^{-4}
$\mathrm{d}z_2^{\mathrm{cut}}$ [mm]	0.1	0.12	0.13	0.15	0.16	0.09
n_z	-0.9	-1.1	-1.13	-1.18	-1.3	0
$\mathrm{K_{Hit}} \cdot d^4$	0.8×10^{-3}					1.25×10^{-3}
$\mathrm{K_{MS}} \cdot d^2$	1.93					7.707

Most of these cuts depend on the detector properties and the final track parameter requirements. For instance, the strength of the magnetic field decides the extent of bending that a track with a given momentum has to undergo. This then decides how large the ϕ_{13}^{cut} needs to be for a given gap-size of the TTT. Similarly, the z_{13}^{cut} depends on the η coverage of the TTT. Figures 7.7(a and b) show the reconstructed track $p_{\mathrm{T},013}$ and $|\eta_{013}|$ as a function of differences between the azimuthal and z co-ordinates of hits in layers l_1 and l_3. From these distributions, ϕ_{13}^{cut} and z_{13}^{cut} are chosen to be 0.021 radian and 380 mm, respectively.

Figures 7.8(a and b) show the middle layer redundancy cuts (defined in Equations 7.5 and 7.6) as a function of ($\sin\theta_{013}$) for matched (blue) and fake tracks (red). The cut on $\mathrm{d}\phi_2$ can be determined by the pixel resolution and is kept rather loose $\sim 3 \times 10^{-4}$ as the momentum consistency cut takes complete care of it. Notice that most of the blue points (matched tracks) lie well below the $\mathrm{d}\phi_2^{\mathrm{cut}}$. The blue points with large $\mathrm{d}\phi_2$ correspond to the secondary matched tracks with low momentum. Multiple scattering effects at large η

---

[16] Only the very first track from the list of tracks that have the same trackID is saved and the rest count as double-counted tracks. In principle, a more optimum way to select a track (from the list of double-counted tracks) would be to compare the reconstructed track parameters (e.g. p_T) with the truth track parameters and keep the one with the smallest deviation.

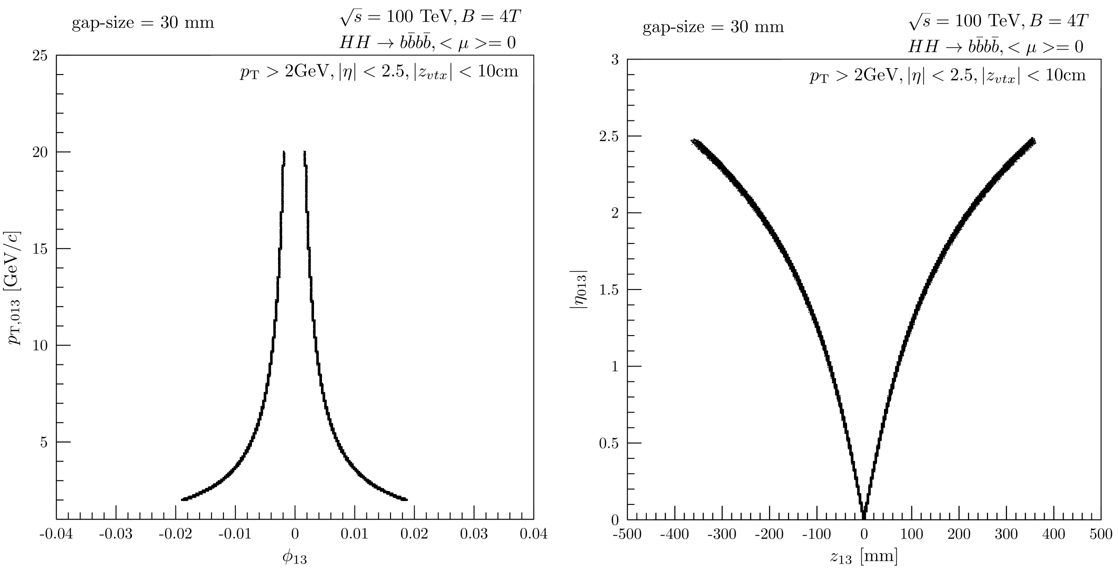

(a) **(b)**

Figure 7.7: Control distributions to set the ϕ_{13} and z_{13} pre-selection cuts for the FCC-hh setup: (a) reconstructed track p_T vs ϕ_{13} and (b) reconstructed $|\eta|$ vs z_{13}.

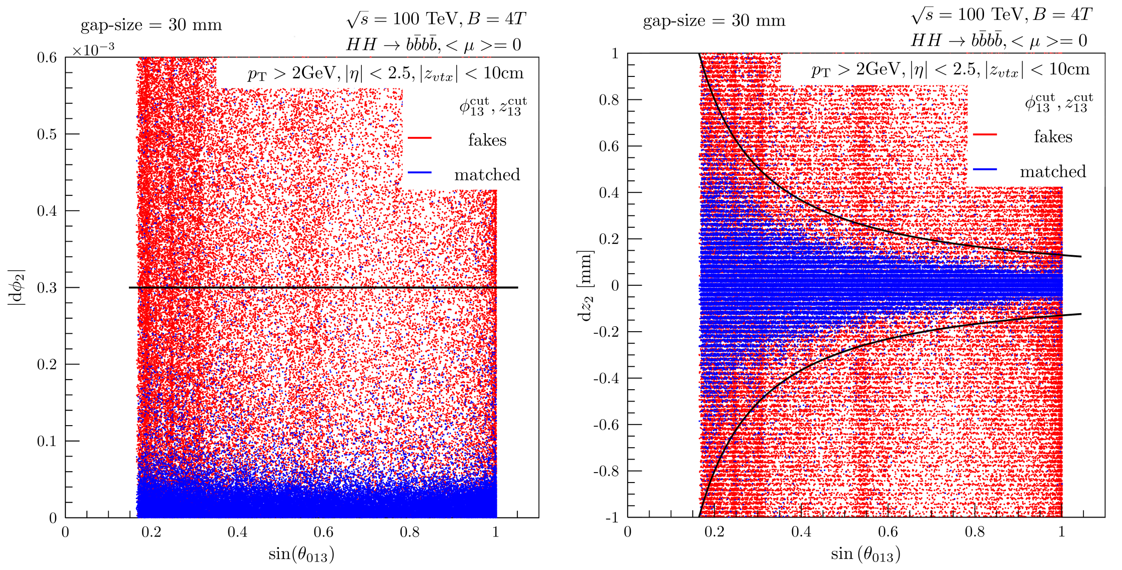

(a) **(b)**

Figure 7.8: Control distributions to set the middle layer redundancy cuts $d\phi_2^{\text{cut}}$ and dz_2^{cut} for the FCC-hh setup. Shown in the figures are the difference between the estimated and real: ϕ_2 (a), and z_2 (b) as a function of sine of the reconstructed θ.

and hence small $\sin(\theta_{013})$ are nicely visible in Figure 7.8(b). A θ dependent cut on dz_2 (shown by the black line) rejects a significant fraction of fake combinations. The stripes seen in the plots are due to the discrete pixel hits (as the hit positions were not smeared for the FCC-hh setup during the digitisation process).

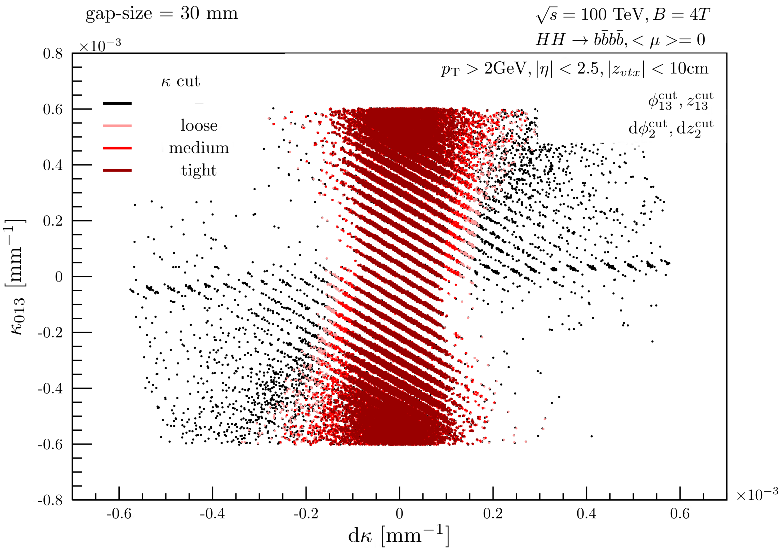

Figure 7.9: Effect of the momentum consistency cut (κ cut) for the FCC-hh setup with TTT gap-size = 30 mm. Shown in the plot is the precise curvature κ_{013} as a function of the difference between the curvatures determined using two independent methods for four different κ cuts.

The last and one of the crucial cuts to reject fake tracks is the momentum consistency cut. Figure 7.9 shows the difference, dκ, as a function of the more precise curvature κ_{013} for the following four cuts in addition to the minimum p_T, η acceptance, z-vertex, and all four pre-selection cuts (Equations 7.3 – 7.6):

1. no momentum consistency cut indicated in black,
2. $|d\kappa| < 5\,\sigma_\kappa$ (loose), indicated in light red,
3. $|d\kappa| < 4\,\sigma_\kappa$ (medium), indicated in red, and
4. $|d\kappa| < 3\,\sigma_\kappa$ (tight), indicated in dark red.

Its distribution is similar to the shape of an hourglass in 2D, and large smearing effects due to multiple coulomb scattering are clearly visible for large values of $|\kappa_{013}|$. As mentioned before, the stripes in the plot are due to pixel discretisation. Black bands (outside the hourglass structure) are visible without the momentum consistency cut. These are mainly due to the secondary electrons and positrons arising from late photon conversions at different layers of the inner tracking layers. One can see that the momentum consistency cut is quite effective not only to separate the correct hit combinations from the wrong ones but also to reject a huge fraction of secondary particles, especially those arising from late photon conversions. This effect is nicely visible in the Figures 7.10(a - d) where a large inconsistency between κ_{013} and κ_{123} is observed for the secondary electrons and positrons reconstructed (Figure 7.10(b)). Muons being minimum ionising in nature show very little inconsistency between κ_{013} and κ_{123}. The band is slightly thicker for charged pions compared to muons as they mostly undergo inelastic nuclear interactions, unlike muons. The products of nuclear interaction are, however, mostly emitted in the direction of the primary pion. Therefore, they do not form a very distinct band as in the case of electrons

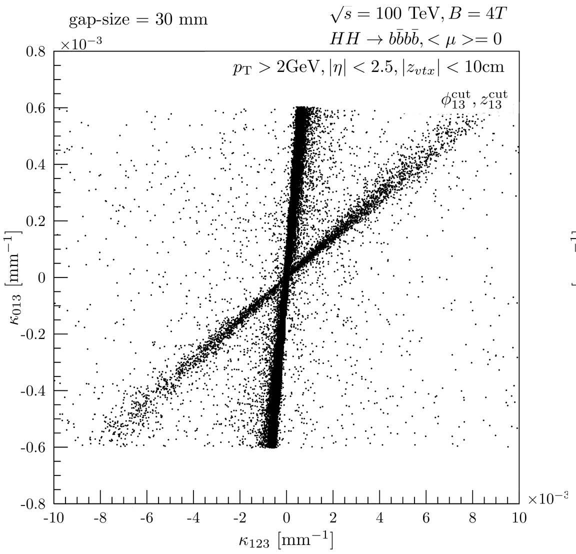

(a) all particles **(b)** e^+, e^-

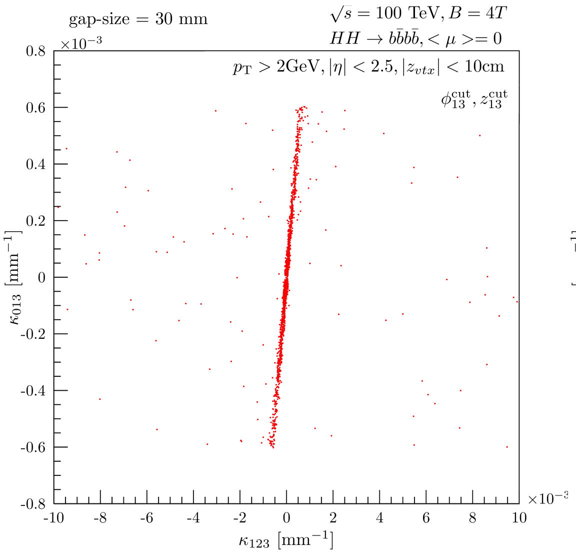

(c) μ^+, μ^- **(d)** π^+, π^-

Figure 7.10: Scatter plot of κ_{013} vs κ_{123} for (a) all particles, (b) electrons and positrons only, (c) muons and anti-muons only, and (d) pions and anti-pions only, from the HH $\to b\bar{b}b\bar{b}$ reconstructed events using the FCC-hh setup.

and positrons. The constants $\mathrm{K}_{\mathrm{Hit}}$ and K_{MS} are determined from Equation 7.31. Notice that $\mathrm{K}_{\mathrm{Hit}} \cdot d^4$ and $\mathrm{K}_{\mathrm{MS}} \cdot d^2$ are a constant for a given detector environment; see Table 7.4.

The cuts are finally fixed by maximising both, the track reconstruction efficiency and track purity (which are discussed in the following chapter).

Optimisation of selection cuts for the ATLAS setup

For the ATLAS setup, the TTT reconstruction routine was modified to be compatible with the ATHENA software framework [149], and the final reconstructed output file contained the offline reconstructed tracks (ITk tracks) and the TTT tracks. Performance comparison between the TTT tracks and the ITk tracks is presented in Chapter 8. For optimisation of the selection cuts for the ATLAS setup, same procedure as for the FCC-hh setup was adopted and the corresponding cuts are summarised in the last column of Table 7.4. Comparing the optimised cuts from the ATLAS and the FCC-hh setup for $d = 20\,\mathrm{mm}$, one can nicely see the effect of two times smaller magnetic field. The ϕ_{13}^{cut} required to reject tracks below a certain transverse momentum in the ATLAS setup is exactly half of that for the FCC-hh setup with $d = 20\,\mathrm{mm}$. The z_{13}^{cut} is significantly smaller in the ATLAS setup due to a smaller pseudorapidity coverage of $|\eta| < 1.5$ compared to $|\eta| < 2.5$ for the FCC-hh setup. A similar effect is seen on the remaining selection cuts.

The next part presents the results of the TTT track reconstruction and trigger performance studies.

Part III

Results

8

TTT Tracking Performance Studies

Quantifying and evaluating the performance of any tool based on some figure of merits, is one of the key aspects that helps decide whether or not the tool is suitable for a given environment. In this chapter, figure of merits like track reconstruction efficiency, track purity and track parameter resolutions are defined and the corresponding results for the tracks reconstructed with the modified FCC-hh tracker and ATLAS ITk are presented.[1]

Each section but last has two sub-parts, one contains the results for the FCC-hh detector setup and the other for the ATLAS detector setup. Section 8.1 discusses the TTT track reconstruction efficiency for the HH → $b\bar{b}b\bar{b}$ sample as a function of three different track parameters, viz. η, φ, and p_T. The efficiencies of the TTT tracks are compared with the offline reconstructed tracks (ITk tracks) in the 2^{nd} half of this section. Section 7.2 presents the purities of the TTT tracks as a function of η, φ, and p_T for the two detector setups, following which the TTT track parameter resolutions of $p_\mathrm{T}, \eta, \varphi, z_0, dca$ are presented as a function of η and p_T in Section 8.3. Finally, in Section 8.4, the selection of an optimal TTT gap-size for the FCC-hh setup is discussed.

Before discussing the figure of merits of the reconstructed tracks, it is essential to consider some detector effects affecting their performances. These include:

- the effect of limited detector *acceptance*, resulting in missing detector hits (also called holes) due to scattering of the particles off the detector layers (in front) to eventually lie outside the detectors reach;
- the effect of detector *inefficiencies*, for instance, the presence of a dead area containing the detector electronics, causing unrecorded hits; and
- the effect of limited detector *resolution* resulting in the measured track parameter values smeared w.r.t. its true values.

Table 8.1 lists the set of final selection cuts used for the tracking performance studies of the modified detector setups of FCC-hh and ATLAS with the TTT. Tracks are required to have a minimum momentum, $p_{\mathrm{T,min}} = 2\,\mathrm{GeV/c}$ and a z-vertex within the luminous region of the colliding proton beams, i.e. $z_{0,\mathrm{max}} = \pm 10\,\mathrm{cm}$.

---

[1] Note that the track parameters obtained from the more precise method (with beamline constraint) from Section 7.2.2 are used for TTT tracking performance. Henceforth, the track parameters $(p_{\mathrm{T},013}, \eta_{013}, \varphi_{013}, z_{013})$ will be referred to as $(p_\mathrm{T}, \eta, \varphi, z_0)$.

Table 8.1: List of selection cuts used for the tracking performance studies of the modified FCC-hh and ATLAS detector setup.

Detector setup	Selection cuts / acceptance			
	$p_{\mathrm{T,min}}$	$z_{0,\mathrm{max}}$	η_{max}	κ consistency
FCC-hh	2 GeV/c	±10 cm	±1.7	3 σ
ATLAS	2 GeV/c	±10 cm	±1.4	5 σ

For the FCC-hh setup, although some of the barrel detectors were extended to unrealistic lengths (upto $|\eta| = 2.5$), tracking performance studies are presented only for realistic barrel lengths covering a maximum pseudorapidity, $\eta_{\mathrm{max}} = \pm 1.7$. This is due to the known reason of excessive multiple scattering in the forward rapidity region for a barrel type geometry, where the traversing particle sees much more material than in the central region. Therefore, most of the experiments have disc type detectors in the forward rapidity region for a large detector acceptance. For the ATLAS setup, tracking performance studies are presented for $\eta_{\mathrm{max}} = \pm 1.4$.

8.1 Track Reconstruction Efficiency

Track reconstruction efficiency for MC events is defined as the ratio of the number of correctly (matched) reconstructed tracks to the total number of simulated tracks (truth tracks), satisfying all the selection requirements and well within the acceptance of the tracking detector. The above can be formulated in a mathematical form as:

$$\epsilon_{reco} = \frac{\#\ \text{reconstructed tracks (matched \ \&\& \ sel. \ \&\& \ acc.)}}{\#\ \text{truth tracks (sel. \ \&\& \ acc.)}}. \tag{8.1}$$

The procedure used for matching the TTT tracks with the truth tracks was discussed in Section 7.3.2.

8.1.1 Track Reconstruction Efficiency for the FCC-hh detector setup

The efficiency of the TTT tracks for the FCC-hh setup was determined using Equation 8.1 for TTT gap-size of 30 mm using the HH → $b\bar{b}b\bar{b}$ MC sample with an average pile-up, $\langle\mu\rangle = 1\,\mathrm{k}$. Figures 8.1(a-c) show the reconstruction efficiencies of the TTT tracks as a function of φ, η and p_{T} of the truth tracks. In addition to the overall reconstruction efficiency of the TTT tracks (indicated in black) in HH → $b\bar{b}b\bar{b}$, $\langle\mu\rangle = 1\,\mathrm{k}$, contributions from three different kinds of particles:

- electrons and positrons (indicated in blue),
- muons and anti-muons (indicated in red), and
- pions and anti-pions (indicated in green)

are also displayed. Clearly, the pion efficiency dominates the overall TTT tracking efficiency $\sim 80\,\%$; see Figure 8.1(a). The $20\,\%$ inefficiency in the above sample is primarily due to the following:

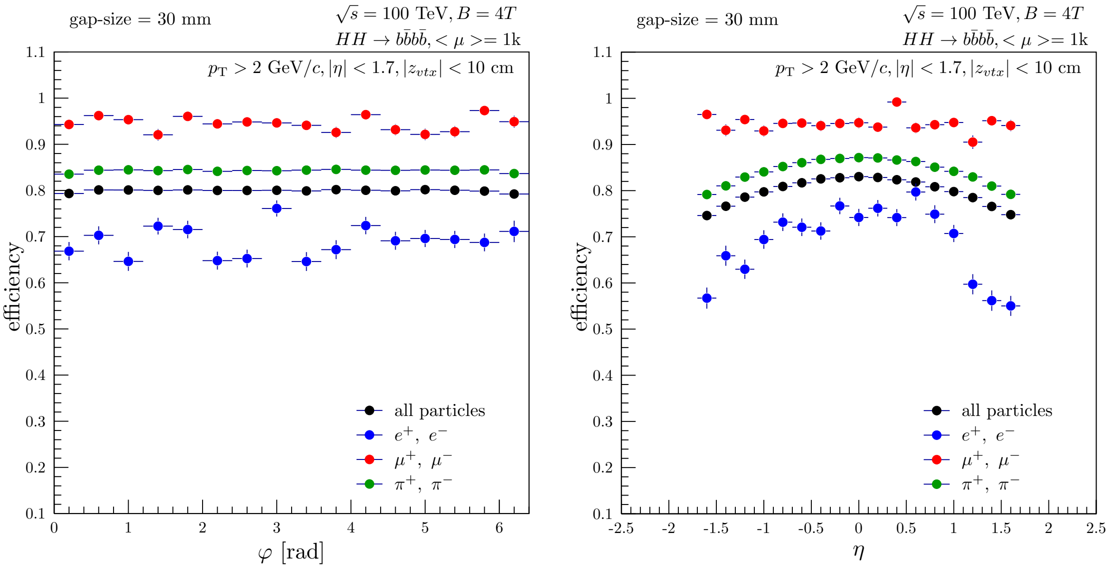

(a) reconstruction efficiency vs. φ **(b)** reconstruction efficiency vs. η

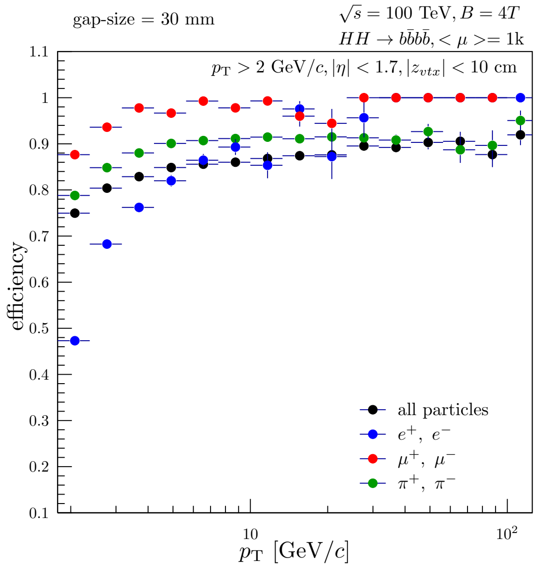

(c) reconstruction efficiency vs. p_T

Figure 8.1: TTT Track reconstruction efficiency in FCC-hh as a function of φ, η and p_T using the HH $\to b\bar{b}b\bar{b}$ signal sample in $\langle\mu\rangle = 1$ k.

1. Material interaction of the particles, in particular in the forward rapidity region; see Figure 8.1(b). Effects like radiative losses by emission of bremsstrahlung, elastic and inelastic nuclear interactions, and multiple coulomb scattering after interaction with

the detector material add to the inefficiency.

- Radiative losses are specifically high for electrons due to their low mass ($-dE/dx \propto E/m^2$), resulting in tracks with large curvature and hence low momentum.[2] Reconstruction inefficiencies of the electrons mainly result when electrons loose most of its energy via bremsstrahlung before making a hit in the detector layer.
- Unlike electrons, the energy loss of charged pions through bremsstrahlung is negligible. Instead they undergo multiple scattering and energy loss through ionisation as they pass through the tracker volume. The inefficiency in reconstruction of pions (or hadrons in general) is mainly due to elastic and inelastic nuclear interactions. Inelastic nuclear interactions are the main source of inefficiency for charged hadrons. The products of nuclear interaction are mostly emitted in the same direction as the primary hadron (especially for large pion momenta), resulting in unrecorded hits of the primary hadron.
- Muons on the contrary, have a very high tracking efficiency $\sim 95\,\%$ due to their minimum ionizing nature. Their dominant mode of energy loss is via ionization (which is essential to tracking), unlike electrons and pions. This very nature of the muons is also responsible for a flat efficiency curve as a function of η in comparison to other particles. The remaining $5\,\%$ inefficiency is explained in the next point.

2. The momentum consistency cut employed in the triplet track reconstruction algorithm is highly effective in suppressing the number of wrong hit combinations reconstructed. It, however, introduces some inefficiencies in the multiple scattering dominant (low p_T) region. A trade-off has to be made between the track reconstruction efficiency and the track purity (discussed in Section 8.2), and the optimum cuts presented in Table 7.4 are good enough to maintain a reasonable track purity. A small inefficiency ($\leq 1\,\%$) is introduced due to the track reconstruction requirement that triplet of hits (of the particles passing through the TTT) must belong to the same $\phi-$module of the TTT. This requirement together with the TTT module width of 10 cm and $B = 4\,\mathrm{T}$, results in inefficiency for all the low p_T tracks, as hit combinations with one of the hits lying in the neighbouring $\phi-$module are not reconstructed.[3] Figure 8.1(c) shows the TTT tracking efficiency as a function of the p_T of the truth tracks. The efficiency is quite low for the low p_T tracks and gradually increases with increasing momentum and reduced bending of the tracks in $B = 4\,\mathrm{T}$. The efficiency is particularly low for electrons due to the combined effect of bremsstrahlung emission, multiple scattering and momentum consistency cut, and smaller module width.[4] For $p_\mathrm{T} > 6\,\mathrm{GeV/c}$ a very high efficiency of close to $100\,\%$ is obtained for the muons and the overall efficiency rises to $\sim 85\,\%$.

It is clear from the above two points that the overall tracking efficiency depends largely on the type of sample used. Samples with a large fraction of muons and small fraction of electrons will result in much higher tracking efficiency and vice versa.

---

[2] This leads to dilution of the original track momentum, as the momentum of a high p_T truth track is diluted with the emission of bremsstrahlung.

[3] The requirement to have the triplet of hits lying in the same $\phi-$module of the TTT is to ease the trigger mechanism. It will also allow track reconstruction in parallel, in all the $\phi-$modules.

[4] Note that it is possible to increase the module width to account for the inefficiency at low p_T.

8.1.2 Track Reconstruction Efficiency for the ATLAS detector setup

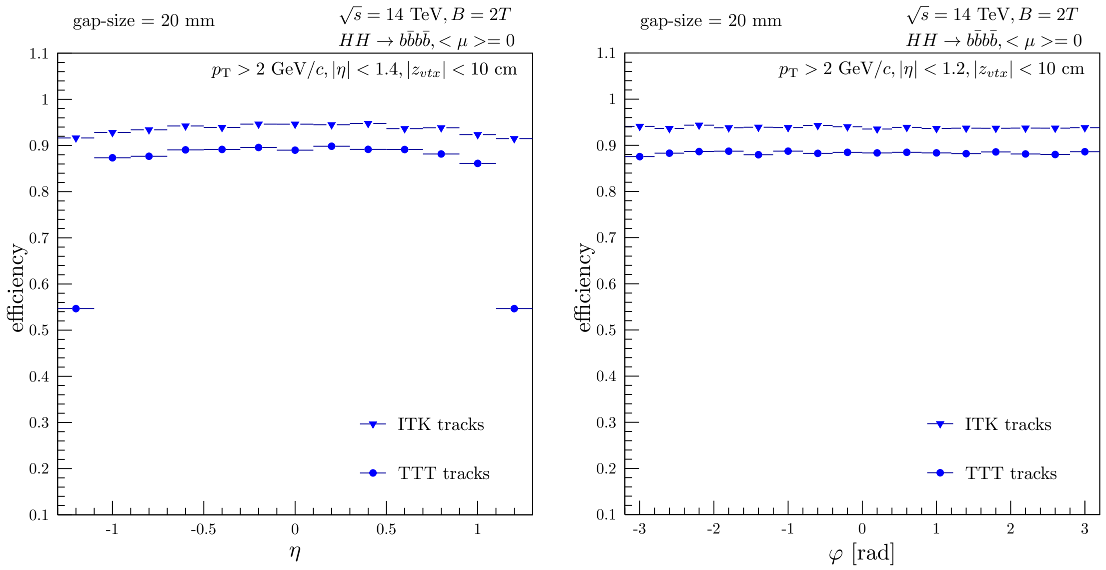

(a) reconstruction efficiency vs. η **(b)** reconstruction efficiency vs. φ

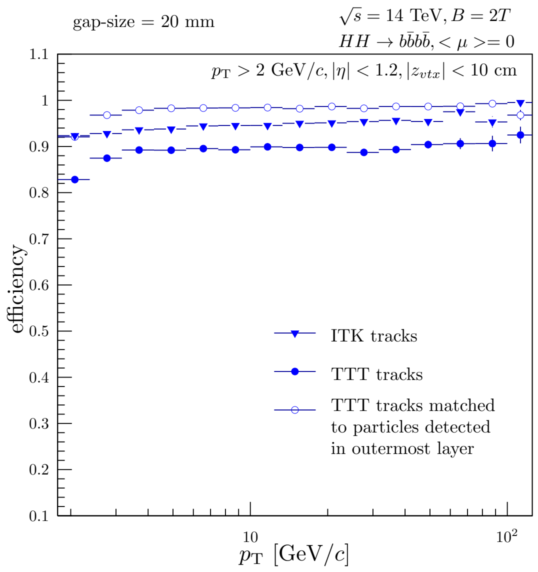

(c) reconstruction efficiency vs. p_T

Figure 8.2: Comparison of track reconstruction efficiencies between the TTT tracks (circle) and the ITk tracks (triangle) in the ATLAS setup as a function of η, φ and p_T using the HH $\rightarrow b\bar{b}b\bar{b}$ signal sample.

Track reconstruction efficiency for the TTT tracks in the ATLAS detector setup was determined in a similar fashion as discussed for the FCC-hh setup. What is different in addition to the selection cuts for the ATLAS setup (listed in Table 8.1) w.r.t. the FCC-hh setup, is the TTT gap-size (20 mm), width of the TTT module (8 cm) and the magnetic field (2 T).

Figure 8.2 shows the reconstruction efficiency of the TTT tracks (in circle) as a function of φ, η and p_{T} for the HH $\rightarrow b\bar{b}b\bar{b}$ MC sample without any pile-up.[5] In addition, the reconstruction efficiency of the ITk tracks (in triangle) reconstructed with a total of nine tracking layers is also shown.

An overall tracking efficiency of $\sim 88\,\%$ is obtained for the TTT tracks except for $|\eta| > 1.2$ where a huge inefficiency of $\sim 45\,\%$ is observed; see Figure 8.2(a). This inefficiency is due to the scattering of a fraction of particles at the edge of the barrel detector into the forward rapidity region (lying outside the reach of the TTT). These scattered particles are then detected by the endcap disc layers and hence, no significant drop in the tracking efficiency for the ITk tracks is observed for $|\eta| > 1.2$.

The reconstruction efficiency for the HH $\rightarrow b\bar{b}b\bar{b}$ sample with $|\eta| < 1.2$ is close to $94\,\%$ for the ITk tracks in comparison to $88\,\%$ for the TTT tracks; see Figure 8.2(b). This difference comes from the differences in the number of tracking layers used (9 for ITk : 3 for TTT) and the complexity of the reconstruction algorithm employed for reconstructing ITk tracks. Nine tracking layers spread more or less uniformly over a large radial distance (from 2.5 cm to 1 m) allows to keep a good track of most of the primary particles resulting from the *pp* collisions. The particles undergoing material interaction, or nuclear interaction, or hadronization, to produce secondary particles at some finite radial distance, result in the 6 ($\sim$ 8)% inefficiency for the ITk (TTT) tracks. Note that the tracking algorithm employed for reconstructing ITk tracks allows for the presence of two missing hits (or holes). As a result, particles not making through the last two strip layers, for instance, are also reconstructed as ITk tracks. On the other hand, these very particles contribute as an inefficiency for the TTT tracks. This can be understood from Figure 8.2(c), where in addition to the reconstruction efficiency of the ITk and the TTT tracks matched to all the primary particles, efficiency of the TTT tracks matched only to the particles making a hit in the outermost layer of the TTT (at 857 + 20 mm) is also displayed (with open circles).[6] With the above constraint imposed for the TTT tracks, the inefficiencies due to material effects almost disappear resulting in $\sim 98\,\%$ tracking efficiency except for tracks with p_{T} less than $\sim 4\,\mathrm{GeV/c}$.

For TTT tracks with $p_{\mathrm{T}} < \sim 4\,\mathrm{GeV/c}$, the inefficiencies arise due to the electrons emitting bremsstrahlung and due to the tracking requirement for the triplet of hits to be in the same $\phi-$module. Figure 8.3 shows the reconstruction efficiencies for single particle MC samples, i.e. muons, pions, and electrons for:

- TTT tracks reconstructed using triplet of hits selected from the same $\phi-$modules (circles), and
- TTT tracks reconstructed using triplet of hits selected from the nearest neighbour modules.

One can nicely see how after including the hits from the neighbouring $\phi-$modules, the reconstruction efficiencies of muons and pions jump to $> 98\,\%$, for p_{T} less than $\sim 4\,\mathrm{GeV/c}$. While a rise in the electron reconstruction efficiency is also observed, the inefficiencies due to the material effects remain.[7]

---

[5] Due to technical difficulties, TTT studies with pile-up included signal sample couldn't be continued in the ATLAS ATHENA software framework.

[6] Note that the efficiency curve with open circles in Figure 8.2(c) is shown for illustrative purpose only and must not be compared with the overall efficiency of the ITk tracks.

[7] Note that for single muons, 100 % reconstruction efficiency is expected for fully efficient detector layers. The 2 % inefficiency for single muons result from a very conservative design choice of having 0.4 mm

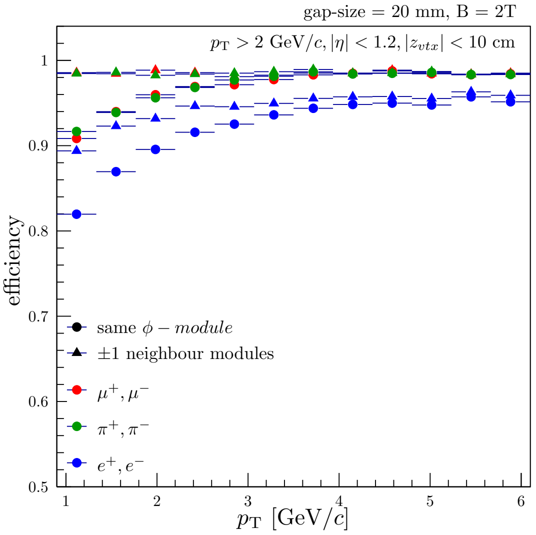

Figure 8.3: TTT track reconstruction efficiencies for single particles, namely, muons (red), pions (green), electrons (blue), illustrating the inefficiencies caused for $p_T < \sim 4\,\mathrm{GeV/c}$ by exclusion of the neighbouring $\phi-$modules during triplet hit selection.

8.2 Track Purity

Track purity is a quantity that gives an estimate on how pure the tracks reconstructed by a tracking algorithm are. In other words, it gives a measure of the possible number of fake tracks reconstructed by a given detector and track reconstruction algorithm. It is defined as the ratio of the number of correctly (matched) reconstructed tracks to the total number of reconstructed tracks, satisfying all the selection requirements and well within the acceptance of the tracking detector. It can be mathematically formulated as:

$$\text{purity} = \frac{\#\ \text{reconstructed tracks (matched \ \&\& \ sel. \ \&\& \ acc.)}}{\#\ \text{reconstructed tracks (sel. \ \&\& \ acc.)}}. \qquad (8.2)$$

The selection cuts used on the reconstructed tracks for both the FCC-hh and ATLAS detector setups are listed in Table 8.1.

8.2.1 TTT Track Purity for the FCC-hh detector setup

Track purity of the TTT tracks as a function of its reconstructed φ, η and p_T, for the FCC-hh detector setup with TTT gap-size of 30 mm, is presented in Figure 8.4. The HH $\rightarrow b\bar{b}b\bar{b}$ MC sample with an average pile-up of 1 k was used to determine the TTT track purity. Although, the presence of such a huge amount of pile-up degrades the track purity to some extent (due to the increased number of hit combinations), the triplet track reconstruction algorithm does a very good job in maintaining a high track purity ($> 95\,\%$) over the entire φ range; see Figure 8.4(a). The effect of the momentum consistency cut (κ consistency cut) in improving the track purity is also displayed for loose ($5\,\sigma_\kappa$ in light red), medium ($4\,\sigma_\kappa$ in red), and tight ($3\,\sigma_\kappa$ in dark red) cuts on the difference, $|\mathrm{d}\kappa|$ between the curvatures determined with and without beamline constraint; refer to Section 7.2.3 and

---

spacing between consecutive sensors along the length of a TTT module.

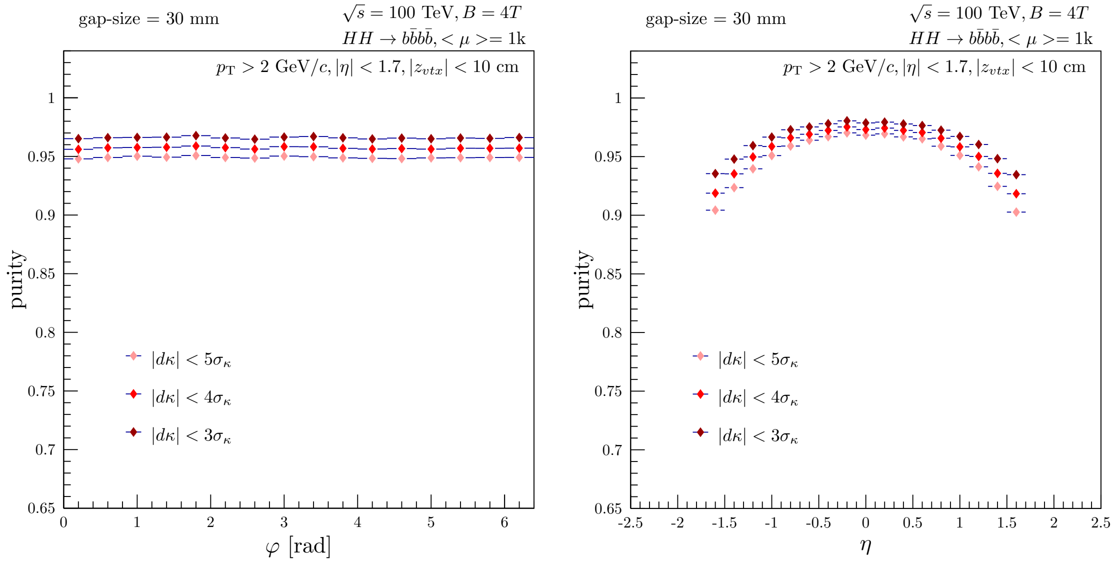

(a) track purity vs. φ **(b)** track purity vs. η

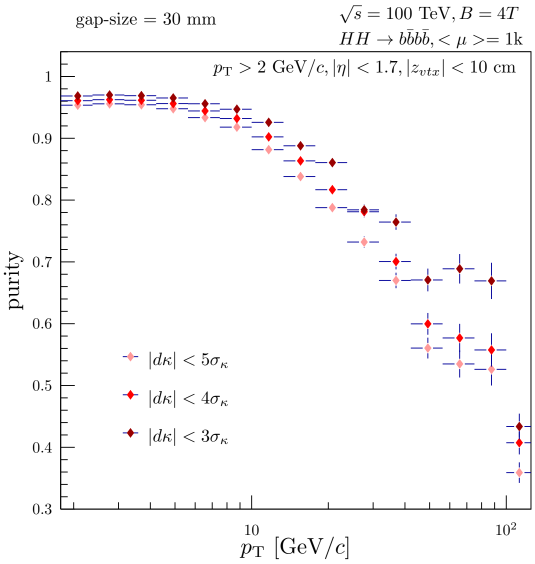

(c) track purity vs. p_T

Figure 8.4: TTT track purity in FCC-hh as a function of η, φ and p_T for three different κ cuts using the HH $\to b\bar{b}b\bar{b}$ signal sample in $\langle\mu\rangle = 1$ k.

Figure 7.9 for a discussion on the κ consistency cut. The overall gain in the track purity from $5\,\sigma_\kappa$ to $3\,\sigma_\kappa$ cut is constant along φ and is $\sim 2\,\%$.

From Figure 8.4(b) one can see that the number of fake combinations in the forward rapidity region is greater than in the central rapidity region. This is due to the increase in multiple scattering uncertainty with increasing $|\eta|$; see Equation 7.29, where $\sigma_{\text{MS}} \propto 1/\sqrt{\sin(\theta_{013})}$. As the κ consistency cut takes into account the uncertainties due to multiple scattering, the gain by cutting tighter on $|\mathrm{d}\kappa|$ in the forward rapidity region is comparatively larger than in the central rapidity region.

Figure 8.4(c) shows the TTT track purity as a function of the reconstructed p_{T} of the TTT tracks. Notice the increase in the size of the error bars with increasing p_{T}, indicating low statistics in the high p_{T} region.[8] As a result, the ratio of the number of correctly reconstructed tracks to the total number of reconstructed tracks appears to be lower, although the average number of fake tracks per event is small in the high p_{T} region as compared to that in the low p_{T} region; see Figure 8.5. The average number of fake tracks per event increases with decreasing p_{T} due to increase in multiple scattering uncertainty with decreasing p_{T}; see Equation 7.29. Besides, the number of fake tracks also increases at low p_{T} as the combinatorial background (hence the fake tracks) are flat in $1/p_{\mathrm{T}}$ (phase space).

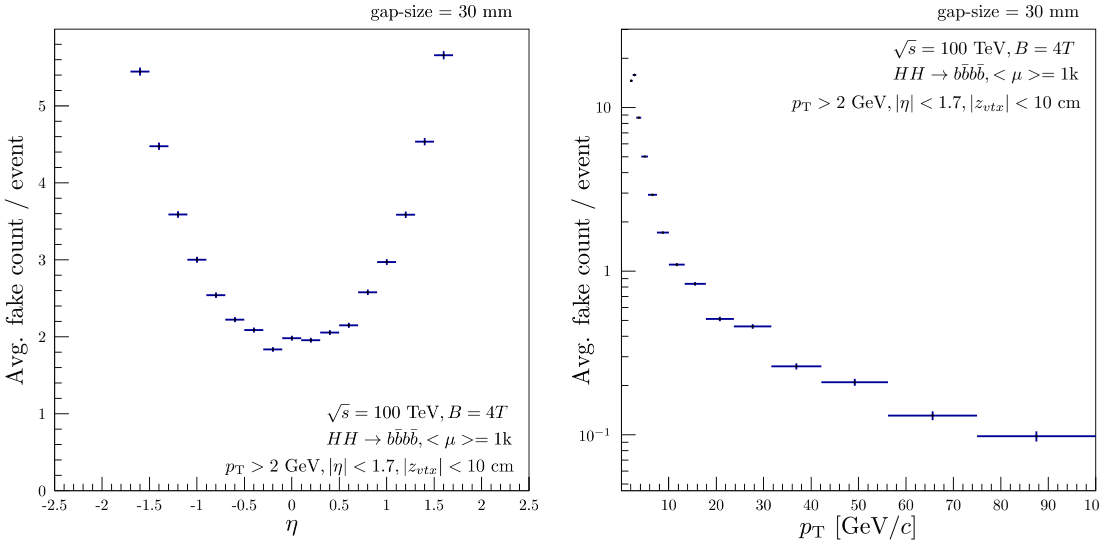

(a) Average # fake tracks/event vs. η **(b)** Average # fake tracks/event vs. p_{T}

Figure 8.5: Average number of fake TTT tracks per event for the FCC-hh setup as a function of η (a) and p_{T} (b) using the HH $\to b\bar{b}b\bar{b}$ signal sample in $\langle\mu\rangle = 1$ k.

Another interesting feature to note is the high effectiveness of the momentum consistency cut in rejecting wrong combinations, especially for tracks with large p_{T} values.[9] A wrong triplet combination determined as a high p_{T} track using the beamline constraint often turns out to originate from a low p_{T} track originating from a secondary vertex (without beamline constraint), resulting in large $|\mathrm{d}\kappa|$ and hence inconsistency between the two methods. This is what makes the TTT robust against a huge amount of pile-up.

---

[8] Low statistics at high p_{T} is due to the presence of ~ 1 k pile-up events (per bunch crossing) that have a steeply falling p_{T} distribution with almost no events with very large p_{T}.

[9] It is important to note that high p_{T} fake tracks are more dangerous than low p_{T} fake tracks especially when constructing objects (e.g. track-jets) with such high p_{T} fake tracks. A single very high p_{T} fake track can completely fake the energy-momentum of a track-jet. More detailed discussion on track-jets is done in the following chapter.

8.2.2 TTT Track Purity for the ATLAS detector setup

TTT track purity for the ATLAS detector setup is similarly determined as for the FCC-hh setup. Pure HH $\rightarrow b\bar{b}b\bar{b}$ sample without any pile-up was used with the selection cuts as given in Table 8.1.

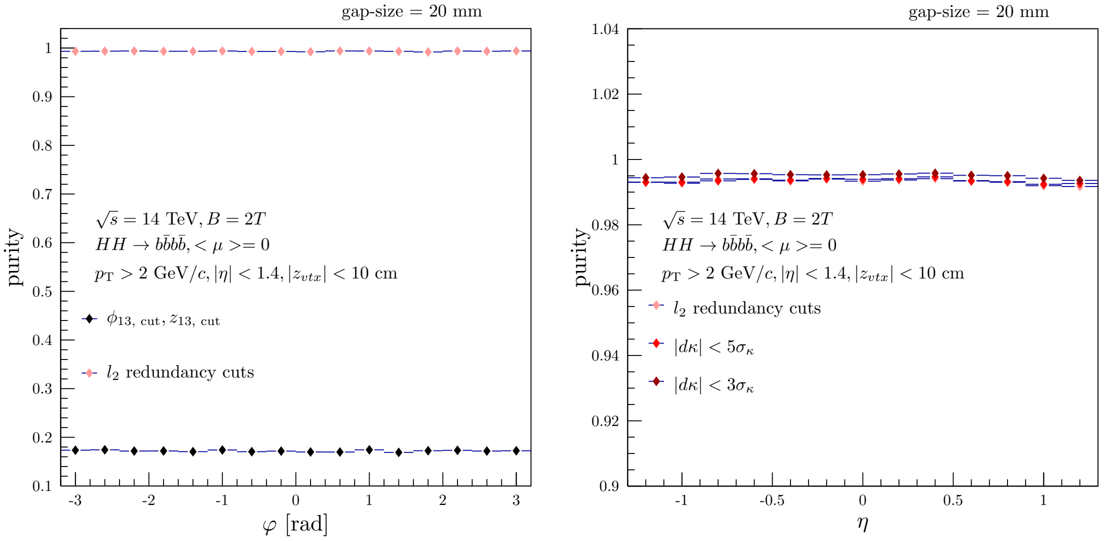

(a) track purity vs. φ **(b)** track purity vs. η

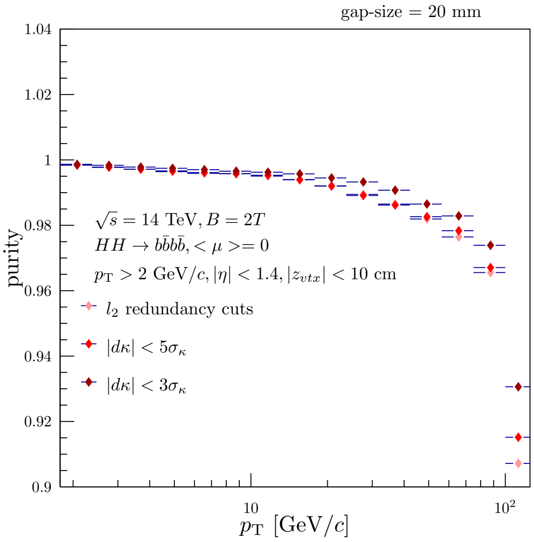

(c) track purity vs. p_T

Figure 8.6: TTT track purity in ATLAS as a function of η, φ and p_T for three different κ cuts using the HH $\rightarrow b\bar{b}b\bar{b}$ signal.

Figure 8.6(a) shows the TTT track purity as a function of its reconstructed φ at the preselection stage of the triplet track reconstruction algorithm. Highlighted in this plot is the effectiveness of the middle layer redundancy cuts to eliminate the wrong hit combinations.

The black points show the track purity after the first hit selection stage, which is purposely kept loose and allows for the possibility to form large number of wrong hit combinations. Owing to the close stacking of the detector triplet at large radius (857 mm), a gain of over 80 % in track purity is attained after implementation of the middle layer redundancy cuts. This is because extremely low momentum particles that experience the largest bending force due to the magnetic field of 2 T do not make it to the detector triplet. Particles that make it to the detector triplet, but have transverse momentum below 2 GeV/c are rejected by the pre-selection cuts. For those with $p_{\mathrm{T}} > 2\,\mathrm{GeV/c}$, the trajectory is close to a straight line both in the transverse $(x - y)$ and the longitudinal $(s - z)$ plane, thereby allowing interpolation of the hit co-ordinates in the middle layer with small uncertainty. This is what makes the triplet design so special compared to for instance, vector-based tracking. The CMS tracker for the HL-LHC upgrade will be using vector-based tracking using several doublet detector layers with a gap-size of $\mathcal{O}(1)$mm to access track parameters at trigger level for data rate reduction [150]. A triplet based tracking is far superior to doublet (or vector) based tracking, especially due to the presence of an extra layer further constraining the hit positions to reduce combinatorial background (fakes).

Figure 8.6(b, c) show the TTT track purities as a function of η and p_{T} for cuts after the pre-selection step (in light red), $|\mathrm{d}\kappa| < 5\,\sigma_\kappa$ (in red) and $|\mathrm{d}\kappa| < 3\,\sigma_\kappa$ (in dark red). The small gap-size (20 mm), the centrality in η of the TTT barrel, and the absence of pile-up, ensures an excellent TTT track purity $> 99\,\%$ already after the pre-selection stage. Although the gain in track purity after the implementation of the κ consistency cut is not large, a good fraction of the wrong combinations marked as high p_{T} tracks are rejected due to the inconsistency in the curvatures determined with and without beamline constraint.

Comparing the TTT track purities between the FCC-hh and the ATLAS setup, one sees that a smaller TTT gap-size ensures higher track purity. Besides, for the FCC-hh setup, an average pile-up of 1000 was used together with the HH $\rightarrow b\bar{b}b\bar{b}$ signal, while only the HH $\rightarrow b\bar{b}b\bar{b}$ signal sample without any pile-up was used for the ATLAS setup. This is another reason why the ATLAS setup has better track purity. However, the track parameter resolutions worsen with decrease in the TTT gap-size. Hence a compromise between TTT track purity and its track parameter resolutions is made and is discussed further in Section 8.4. Notice that the strength of the magnetic field also impacts the purity of the TTT tracks. In the FCC-hh detector environment, the tracks with a given momentum are bent with a force twice as strong as that in ATLAS detector environment. This in turn forces the selection cuts to be twice as loose as compared to the ATLAS detector setup – while maintaining a very high track reconstruction efficiency – and hence greater number of wrong hit combinations.

8.3 Track Parameter Resolution

Resolution of the parameters reconstructed via a tracking detector is another figure of merit grading the quality of the reconstructed tracks and hence the tracker. In this section, resolution of the five track parameters reconstructed by the TTT are shown for the FCC-hh and ATLAS detector setup.

Resolution of a track parameter α is estimated as the standard deviation of a Gaussian fit to the distribution of the difference between the reconstructed track parameter($\alpha_{rec,i}$) and its true value ($\alpha_{true,i}$). For track parameters whose distribution of the difference ($\alpha_{rec,i} - \alpha_{true,i}$) is non-Gaussian, the resolution is estimated using the root mean square of this difference, given by:[10]

$$\sigma_{\delta\alpha} = \sqrt{\frac{\sum(\alpha_{rec,i} - \alpha_{true})^2}{N}}. \tag{8.3}$$

8.3.1 Track Parameter Resolution for the FCC-hh setup

Figure 8.7 shows the resolution of the TTT track parameters, i.e. p_T, $1/p_\mathrm{T}$, η, φ, and z_0 – as a function of η (on the left) and p_T (on the right) – reconstructed using the FCC-hh detector setup for a TTT gap-size of 30 mm. Comparing the left and the right column of plots, one can see that all the track parameter resolutions have:

1. a quadratic behaviour along η, and
2. an inverse p_T dependence in the multiple scattering region ($p_\mathrm{T} < \sim 20\,\mathrm{GeV/c}$) followed by a constant dependence on p_T in the hit uncertainty region; except for Figure 8.7(b).

The above dependence on η and p_T can be understood by looking at the different terms contributing to the resolution of the track parameters.

The relative transverse momentum resolution has two contributions, i.e. one from a p_T dependent measurement uncertainty term and the other from a θ dependent multiple scattering term:

$$\left(\sigma_{\delta p_\mathrm{T}/p_\mathrm{T}}\right)^2 \propto \left(\frac{\mathrm{K}\,\sigma_t}{\sqrt{N}BL^2}p_\mathrm{T}\right)^2 + \left(\frac{\mathrm{K_{MS}}}{\sqrt{\sin(\theta)}}\right)^2, \tag{8.4}$$

where K is a geometry constant, $\sigma_t = w/\sqrt{12}$ is the hit resolution determined by the pixel width w, N is the number of measurement points (or detector layers), B is the magnetic field, L is the length of the lever arm used to determine the transverse momentum, and $\mathrm{K_{MS}}$ is the same multiple scattering constant as in Equation 7.31. The derivation of Equation 8.4 is given in Appendix B.

In the MS term, $1/\sqrt{\sin(\theta)}$ increases with increasing rapidity and as expected – due to the increase in the amount of material traversed by the particles – the relative p_T resolution degrades quadratically with increase in η; see Figure 8.7(a). The best $\sigma_{\delta p_\mathrm{T}/p_\mathrm{T}}(< 0.5\,\%)$ is at $|\eta| \approx 0$, where the middle layer of the TTT sees the least amount of material = 12.5 % radiation length (see Table 7.3), beyond which it increases and is $> 0.75\,\%$ for $|\eta| > 1.5$ as the amount of material thickness traversed by the particles increases to $\sim 30\,\%$ radiation length. The effect of the first term is also seen in Figure 8.7(b), where the relative p_T resolution degrades linearly with p_T in the hit uncertainty region. However, it is well

---

[10] Note that the truth tracks are required to satisfy the selection cuts listed in Table 8.1.

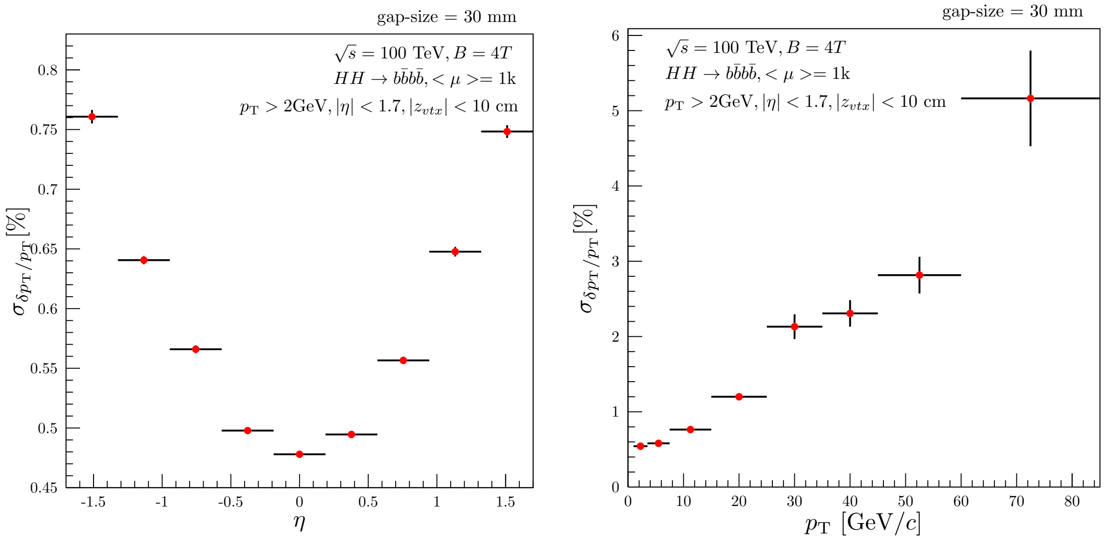

(a) relative p_T resolution vs. η **(b)** relative p_T resolution vs. p_T

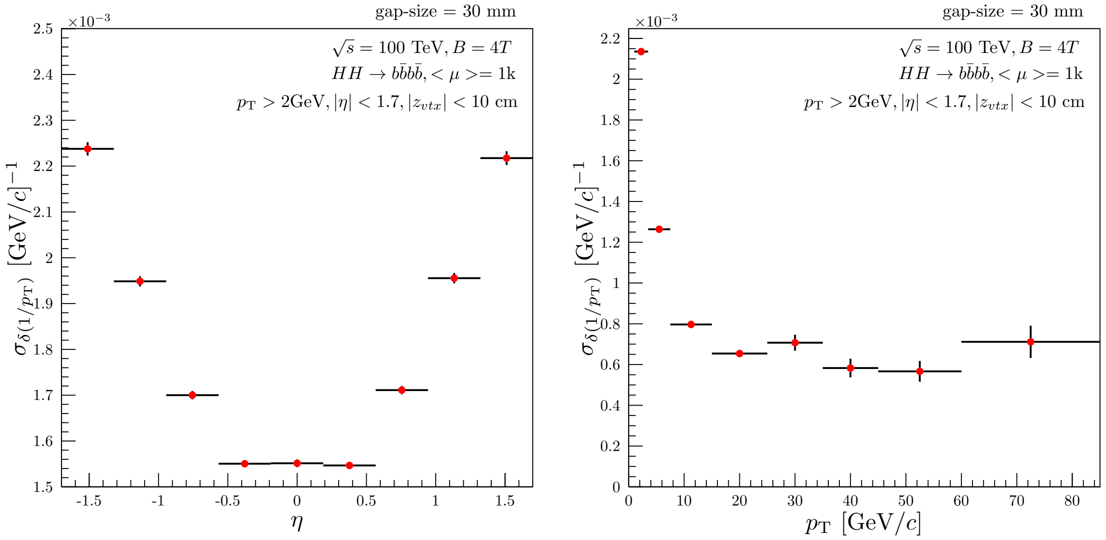

(c) inverse p_T resolution vs. η **(d)** inverse p_T resolution vs. p_T

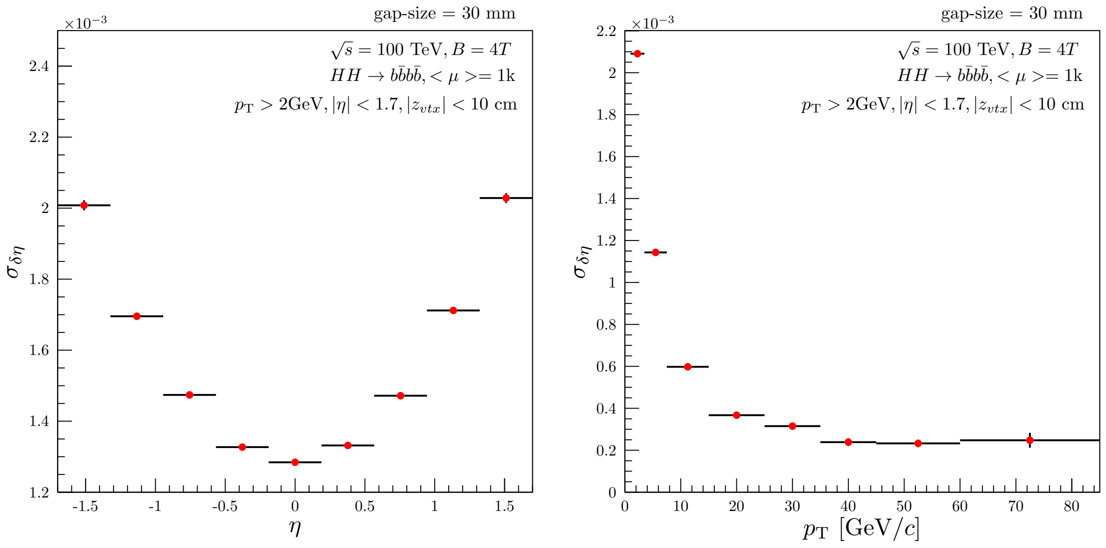

(e) η resolution vs. η **(f)** η resolution vs. p_T

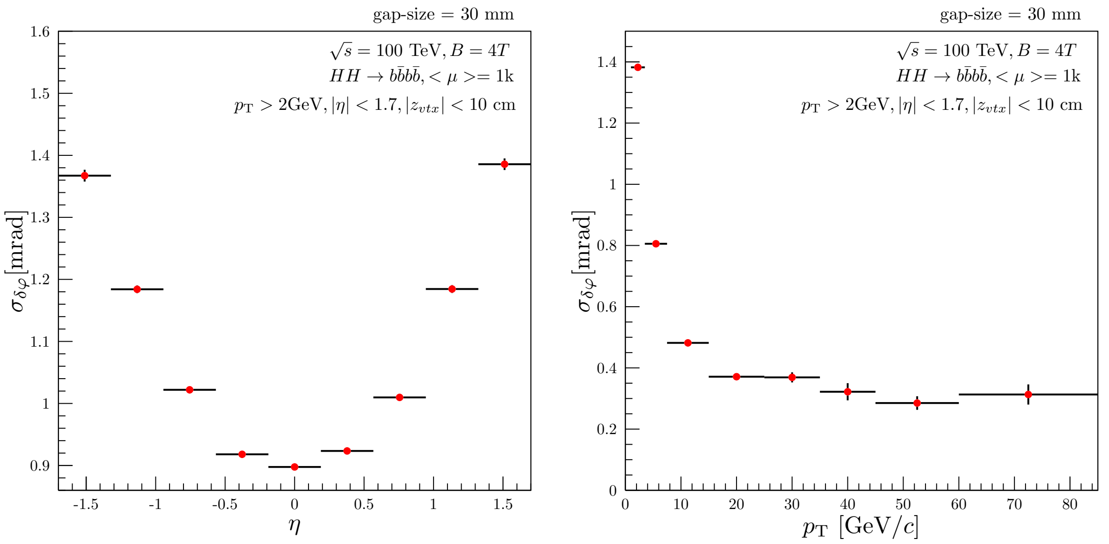

(g) φ resolution vs. η **(h)** φ resolution vs. p_T

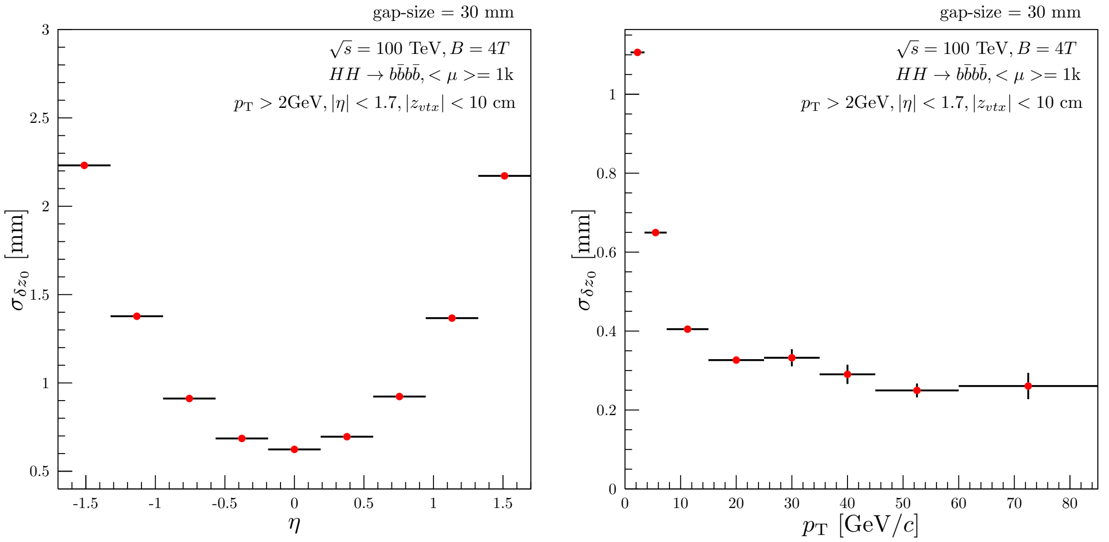

(i) z_0 resolution vs. η **(j)** z_0 resolution vs. p_T

Figure 8.7: TTT Track parameter resolutions of relative p_T (a, b), inverse p_T (c, d), η (e, f), φ (e, f), and z_0 (g, h), in FCC-hh as a function of η (left) and p_T (right) using the HH $\to b\bar{b}b\bar{b}$ signal sample in $\langle\mu\rangle = 1$ k.

below 1 % for $p_T < 15$ GeV/c and along a wide η range, implying that the relative p_T resolution as a function of η is dominated by the low-p_T tracks (due to the presence of $\langle\mu\rangle = 1$ k). This very good momentum resolution (only with three detector layers) can be attributed to the large lever arm ($L = 887$ mm for a TTT gap-size of 30 mm) measured with beamline constraint and the magnetic field (B = 4 T).

At high p_T, it is more relevant to look at the inverse p_T resolution with Gaussian errors. The inverse transverse momentum resolution similarly, has two contributions: one from a constant hit uncertainty term and the other from a p_{T} and θ dependent multiple scattering term. Using Equation 7.31, the inverse momentum resolution can be written as:

$$\left(\sigma_{\delta(1/p_{\mathrm{T}})}\right)^2 \propto \mathrm{K}^2_{\mathrm{Hit}} + \left(\frac{\mathrm{K}_{\mathrm{MS}}}{p_{\mathrm{T}}\sqrt{\sin(\theta)}}\right)^2 , \tag{8.5}$$

where

$$\mathrm{K}^2_{\mathrm{Hit}} = \left(\frac{\sqrt{6}\,\sigma_t}{d^2}\right)^2 , \text{ and } \mathrm{K}^2_{\mathrm{MS}} = \left[\frac{13.6\,\mathrm{MeV/c}}{0.3\,B\,L}\sqrt{\frac{t}{X_0}}\right]^2 , \tag{8.6}$$

with d being the distance between the consecutive equidistant detector layers.[11] The first term in Equation 8.5 explains the constant inverse p_{T} resolution in the central rapidity region ($|\eta| < 0.5$) and for $p_{\mathrm{T}} > 20\,\mathrm{GeV/c}$. In the region dominated by multiple scattering, a quadratic dependence of $\sigma_{\delta(1/p_{\mathrm{T}})}$ that degrades with $|\eta|$ and an inverse p_{T} dependence is observed in Figure 8.7(c and d).

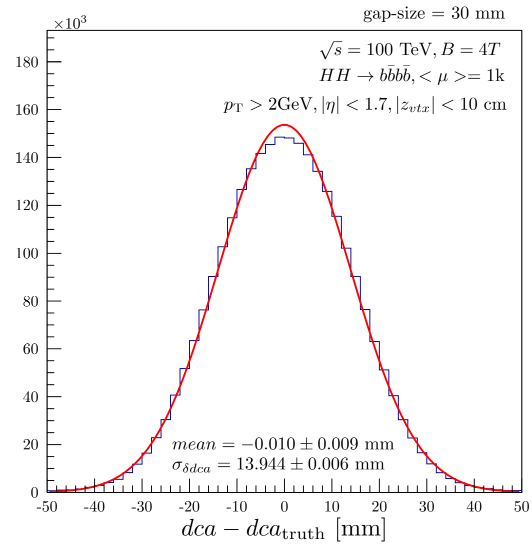

Figure 8.8: *dca* resolution of TTT tracks in the FCC-hh setup for the HH → $b\bar{b}b\bar{b}$ signal sample in $\langle\mu\rangle = 1\,\mathrm{k}$.

The resolution of the remaining track parameters, viz. η, φ and z_0 show a similar dependence on η and p_{T} due to the measurement uncertainty and contributions from MS uncertainty; see Figures 8.7(e-j). TTT has a very good η and φ resolution with $\sigma_{\delta\eta} < 2.2 \times 10^{-3}$ and $\sigma_{\delta\varphi} < 1.5\,\mathrm{mrad}$ for a wide range of η and p_{T}. Sub-mm precision in z_0 resolution are achievable using only three detector layers for a very wide range in p_{T}. Note that this sub-mm precision is mainly determined by the material in front of the TTT. Even better z_0 resolution for the TTT are possible if the material in front of the TTT can be reduced. The resolution in the forward η region degrades due to multiple coulomb scattering, however is good enough to suppress the effects of pile-up to a large extent. Use of z-vertex

---

[11] Note that $\mathrm{K}_{\mathrm{Hit}}$ includes the geometry constant K given in Equation 8.4.

information from TTT tracks to suppress pile-up and improve signal efficiency is further discussed in Chapter 9.

By design the *dca* resolution of the TTT tracks is not the best due to the large radial distance of the TTT layers from the beamline and the relatively small lever arm $\mathcal{O}(50)$mm for *dca* determination without beamline constraint. For completeness, the *dca* resolution of the TTT tracks – which is around 14 mm – is shown in Figure 8.8.

8.3.2 TTT and ITk Resolution Comparison for the ATLAS setup

In this Section, the track parameter resolutions of the TTT tracks are compared with those of the ITk tracks for the ATLAS setup. Figure 8.9 shows the resolution of reconstructed p_T, η, φ, and z_0 – using the triplet track reconstruction algorithm (red) and the ATLAS offline reconstruction algorithm (blue) – as a function of η (on the left) and p_T (on the right).

Similar to the FCC-hh setup, the reconstructed (TTT and ITk) tracks in the ATLAS setup also have track parameter resolutions that have a quadratic behaviour as a function of η and an inverse p_T dependence in the regions with high multiple scattering. The resolution of most of the ITk track parameters are almost twice or even thrice as good as the resolution of the TTT track parameters; see Figure 8.9(a-h). This can be understood using the measurement uncertainties of the track parameters (see Equation 8.4):

- Large number of detector layers and hence measurement points (N = 9 for ITk tracks compared to 3 for TTT tracks) per track.
- Smaller pixel width (25 µm) of the ITk pixels (25 × 100 $\mu\mathrm{m}^2$) compared to that of the TTT pixels (50 × 50 $\mu\mathrm{m}^2$).[12]
- An iterative and complex track reconstruction algorithm (Kálmán Filter [96, 137]) that corrects for errors in the track parameters determined, for every measurement point (hit). This is however one of the main reasons why tracks cannot be used at trigger level (see Chapter 6).

Figures 8.9(i and j) show the comparison of the z_0 resolution of ITk and TTT tracks. The z_0 resolution of the ITk tracks is more than an order of magnitude better than that for the TTT tracks. This excellent z_0 resolution is not only due to the highly granular ITk pixels but also due to the innermost pixel detector layer sitting at a radius of 25 mm compared to 837 mm (radius of the innermost layer) of the TTT.

Despite these large differences, the triplet track reconstruction algorithm is able to reconstruct tracks with a relative p_T resolution of $< 2.5\,\%$ (for $p_\mathrm{T} < 10\,\mathrm{GeV/c}$ and $|\eta| < 1.4$) and a z_0 resolution of $< 1\,\mathrm{mm}$ (for a wide range of p_T and η). In addition, the TTT can provide all the above track parameters in real time as opposed to the ITk tracks which are only available offline. The sub-mm z_0 resolution can then be exploited in real time at trigger level to trace back tracks and track-objects coming from the same z-vertex facilitating suppression of huge amount of pile-up at trigger level.

---

[12] 25 × 100 $\mu\mathrm{m}^2$ were the dimensions used for the ITk pixels in the simulation results presented here. Different dimensions e.g. 50 × 50 $\mu\mathrm{m}^2$ for ITk pixels are under consideration at the time of writing this thesis.

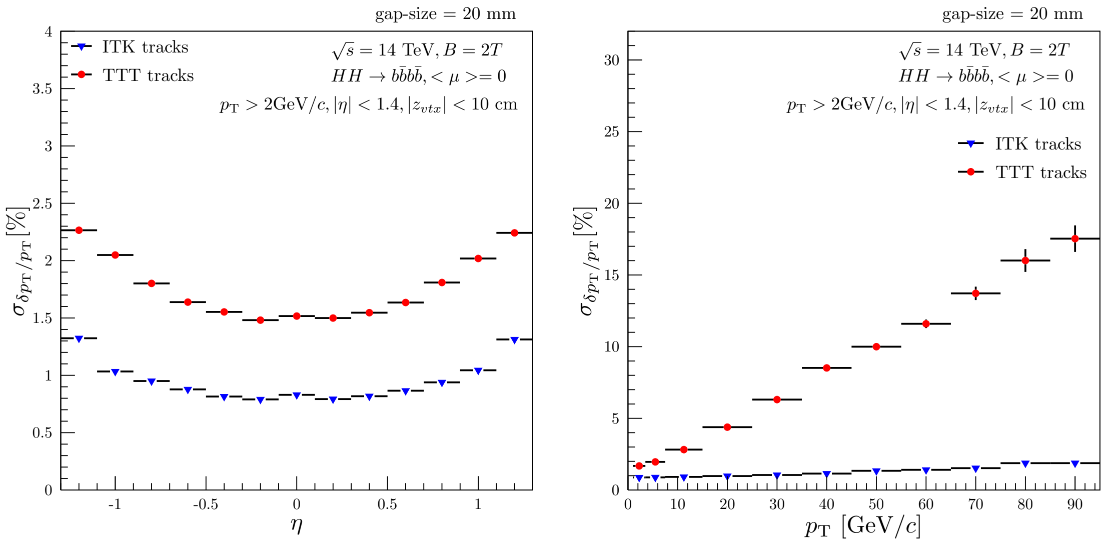

(a) relative p_T resolution vs. η

(b) relative p_T resolution vs. p_T

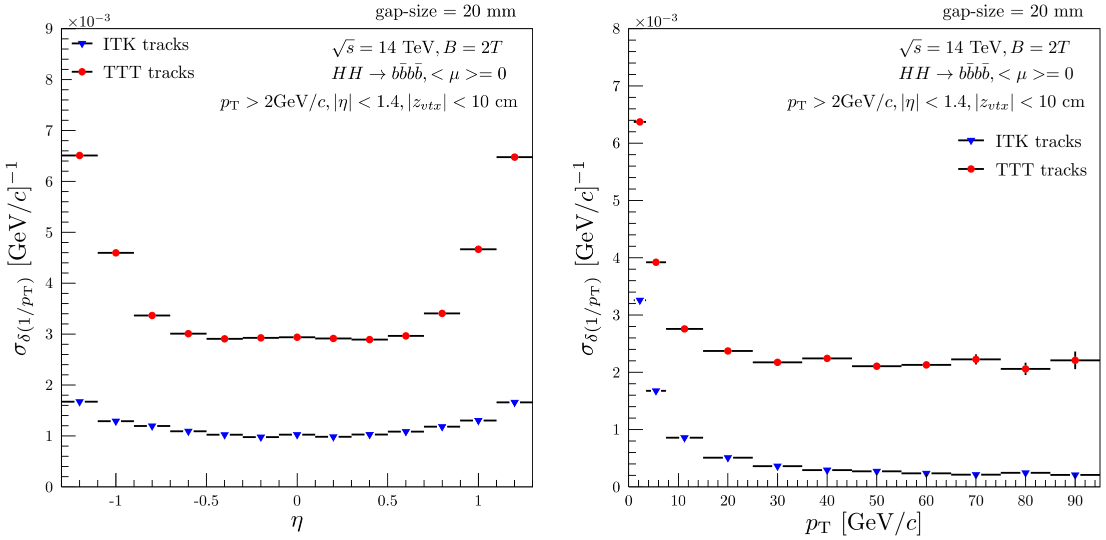

(c) inverse p_T resolution vs. η

(d) inverse p_T resolution vs. p_T

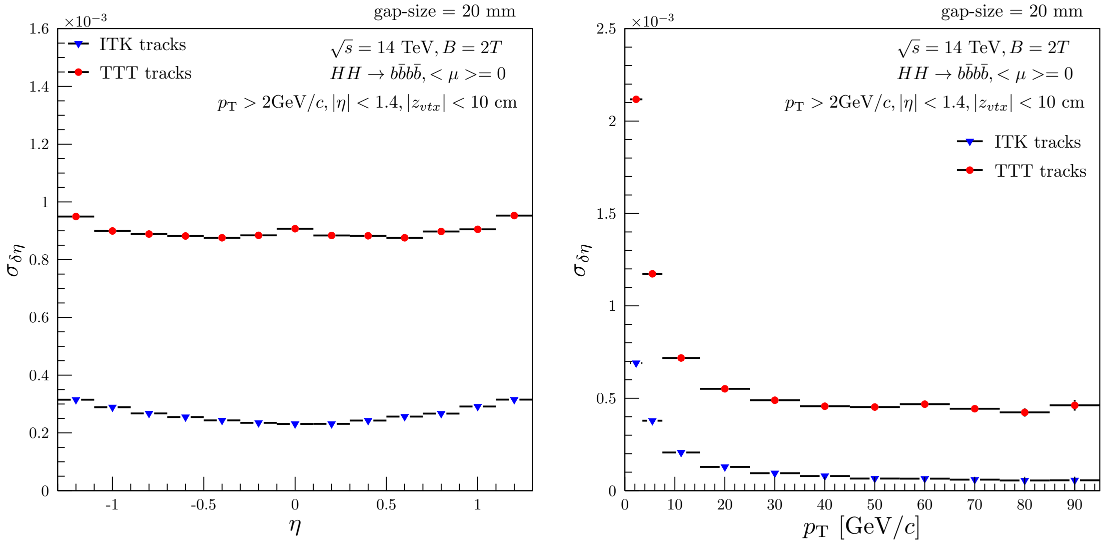

(e) η resolution vs. η

(f) η resolution vs. p_T

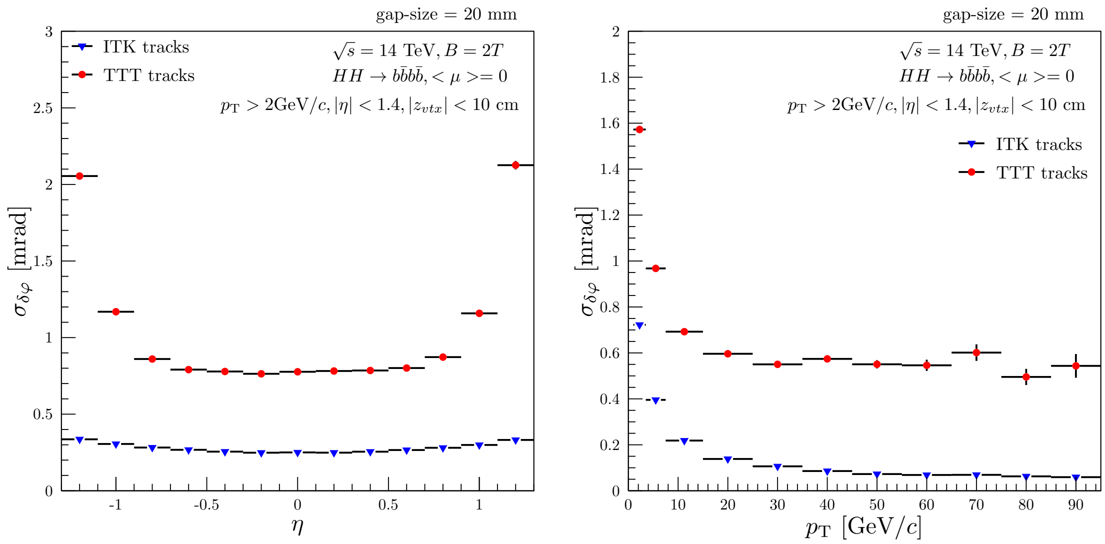

(g) φ resolution vs. η

(h) φ resolution vs. p_T

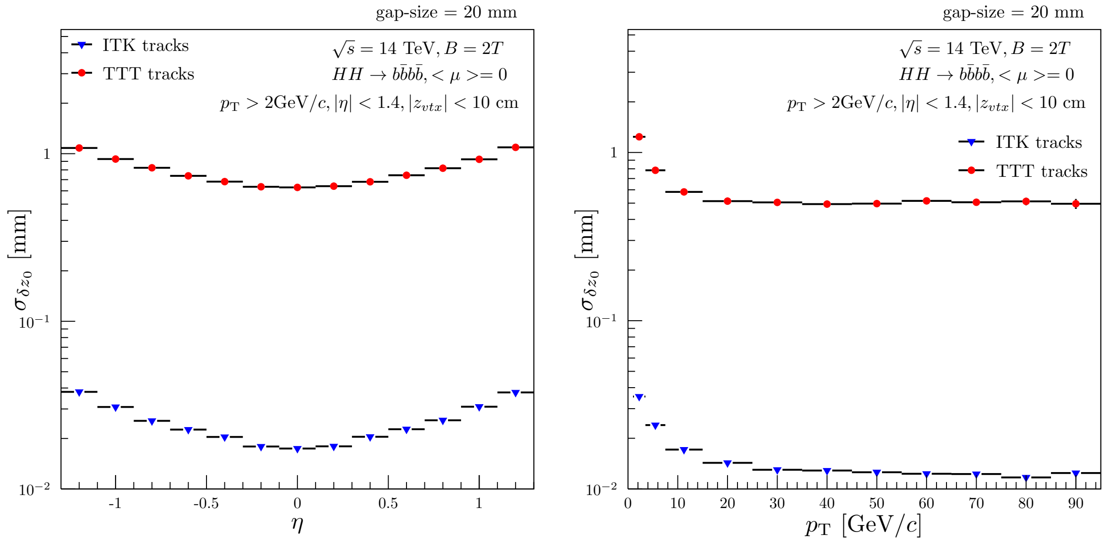

(i) z_0 resolution vs. η

(j) z_0 resolution vs. p_T

Figure 8.9: TTT (red) and ITk (blue) track parameter resolutions of relative p_T (a, b), inverse p_T (c, d), η (e, f), φ (e, f), z_0 (g, h), in ATLAS as a function of η (left) and p_T (right) using the HH $\to b\bar{b}b\bar{b}$ signal sample.

Comparing the results in this section between the FCC-hh setup and the ATLAS setup one sees that the TTT track parameter resolutions for the FCC-hh detector setup are around 2 – 3 times better than those for the ATLAS detector setup. This is mainly due to the two times stronger magnetic field and ∼ 1.25 times finer granularity of the pixels. Note that the momentum resolution depends on $1/L^2$ and hence a larger TTT gap-size of 30 mm as opposed to 20 mm also helps to improve the momentum resolution.

8.4 Optimization of TTT gap-size

Having defined the figure of merits for the reconstructed tracks in the sections above, an optimal gap-size for the TTT can now be determined. Results are presented only for the FCC-hh detector setup.

Figure 8.10(a) summarises the relative transverse momentum resolution of 10 GeV/c single pion tracks as a function of average TTT track purity for five different TTT gap-sizes (d = 20, 25, 30, 35, 40 mm), and for three different pile-up configurations of the HH → $b\bar{b}b\bar{b}$ signal sample ($\langle\mu\rangle = 0, 200, 1000$).[13] The average TTT track purity for each of the pile-up configurations was determined by taking a weighted mean of the track purities over several p_T bins in the range 10 – 100 GeV/c. As expected the relative p_T resolution improves with increasing gap-size of the TTT, with the best resolution of ∼ 0.6 % for d = 40 mm; see the orange markers. Similarly, in Figure 8.10(b), an increase in the gap-size of the TTT results in increased proximity of the TTT to the beamline, thereby improving the z_0 resolution of the TTT tracks.

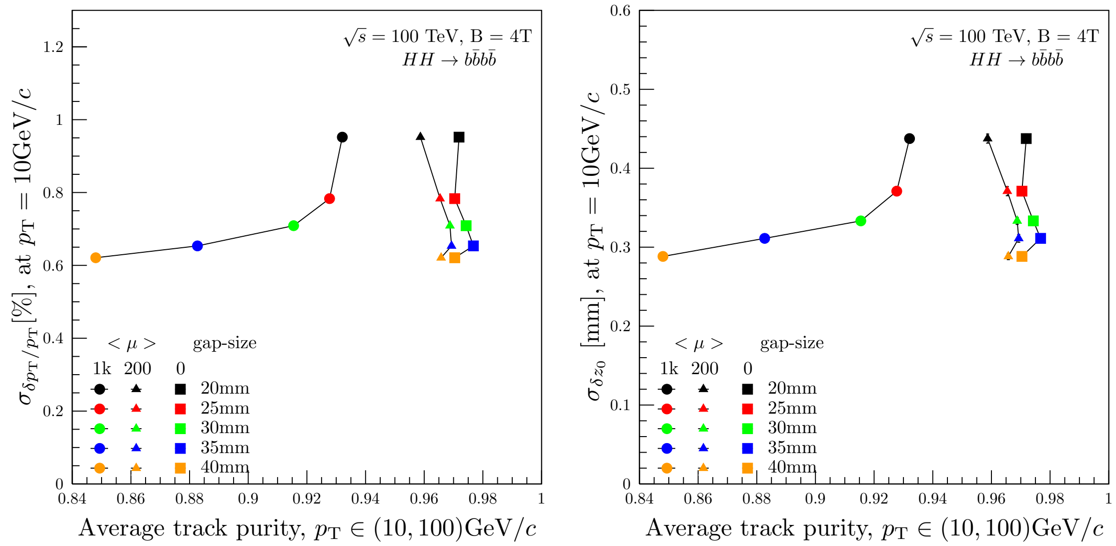

(k) **(l)**

Figure 8.10: Summary of relative transverse momentum resolution (a) and z_0 resolution (b) – of the TTT tracks in the FCC-hh setup – as a function of average track purity in HH → $b\bar{b}b\bar{b}$ for five different TTT gap-sizes and three different pile-up configurations.

The effect of increasing TTT gap-size has two different effects on the TTT track purities.

- For moderate to low pile-up environment (see $\langle\mu\rangle = 0$ (squares), 200 (triangles)), the improved track parameter resolutions due to increase in the TTT gap-size, increases the effectiveness of rejecting wrong hit combinations using the momentum consistency cut. With an increase in the gap-size of the TTT, the cuts have to be modified to be wide enough to reconstruct the tracks with a certain minimum track p_T (of 2 GeV/c

---

[13] Note that $\langle\mu\rangle = 0$ corresponds to pure HH → $b\bar{b}b\bar{b}$ signal sample.

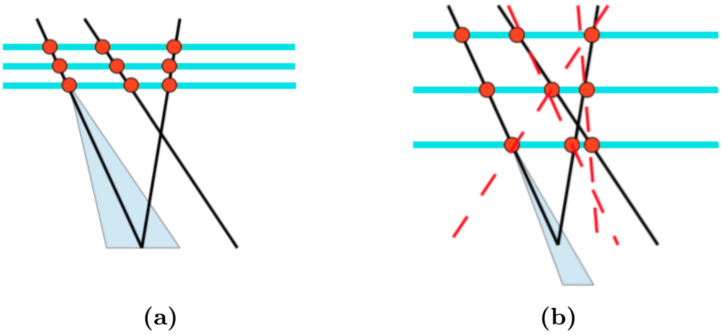

Figure 8.11: Sketch of the TTT in the longitudinal plane explaining the effect of small and large TTT gap-size on tracking performance. Shown in the figure are the hits (red points) made by the truth tracks (black lines) passing through the detector layers (cyan). Some of the possible wrong hit combinations are indicated by the red dashed lines and extrapolation of the triplet hits to the z-axis are shown by the light blue triangles

here). Widening of the cuts, however, increases the number of possible wrong hit combinations. At some point, the gap-size is so large that the momentum consistency cut can no longer adequately reject the large number of wrong hit combinations, thereby resulting in a drop in the average track purity of the TTT tracks. Therefore, the average track purity increases with an increase in TTT gap-size until $d = 35\,\text{mm}$ beyond which it starts to degrade.

- For very large pile-up (e.g. $\langle\mu\rangle = 1\,\text{k}$ (circles)) and hence large hit occupancies per layer, the probability of linking hits from different tracks is much lower for small gap-sizes than for large gap-sizes of the TTT. This explains why the average track purity decreases with increase in TTT gap-size for $\langle\mu\rangle = 1\,\text{k}$. This can be understood by comparing the Figures 8.11(a and b), where on one hand a small TTT gap-size leads to fewer wrong hit combinations compared to a large TTT gap-size, on the other hand a small TTT gap-size results in relatively lower vertex resolution. Therefore, a compromise between high track purity and high track parameter resolutions is made to choose an optimal gap-size.

For all pile-up configurations, the gain in the relative p_T and z_0 resolution from TTT gap-size of 20 mm to 25 mm is $\sim 2\,\%$ beyond which the gain is small. With the above findings, 30 mm was chosen as the optimal TTT gap-size in a detector environment with 1000 pile-up events per bunch crossing. For moderate to low pile-up environment, a TTT gap-size of 35 mm would be the best. Although the enormous amount of pile-up events affects the TTT track purity to some extent, the triplet track reconstruction algorithm remains mostly immune to a very high pile-up environment. This immunity of the TTT along with a very good track parameter resolution (for four of the five track parameters) is exploited in the following chapter to study possible trigger rate reduction using TTT track-jets while maintaining a high trigger efficiency.

9

TTT Trigger Performance Studies

In high pile-up environment, identification of objects coming from the hard interaction and hence making trigger decisions based on their energy or momentum is crucial to a trigger system. Trigger decisions are made by triggering on one or more of the first few leading jets coming from a hard interaction (*Primary Vertex (PV)*) in an event. In low pile-up environment, these leading jets from the PV can be easily known by identifying the largest energy deposits in the calorimeter. In experiments with a very high pile-up, however, the above procedure can no longer be used as energy deposits from several pile-up collisions can result in jets with energies much larger than those resulting from a PV. Therefore, trigger decisions must be preceded by very good *pile-up suppression*. Track triggers can do a great job in doing this; thanks to the availability of the track momentum and z-vertex information at trigger level.[1] In FCC-hh like detector environment, where there are ~ 1000 pp collisions within a length of $\sim 20\,\mathrm{cm}$, a z_0 resolution of $\sim 0.1\,\mathrm{mm}$ is required to assign the reconstructed tracks originating from a particular z-vertex uniquely. A z_0 resolution $> 0.4\,\mathrm{mm}$ for $p_\mathrm{T} < 20\,\mathrm{GeV/c}$ (see Figure 8.7(j)) is however not sufficient for this unique assignment. This also means that it will be challenging to identify the PV and therefore match the reconstructed tracks to it. However, at the trigger level, it is not necessary to identify the PV, and instead identification of a region in which the PV is contained (let's call it the *Primary Bin (PB)*) is sufficient, as it can dramatically reduce the effects of the pile-up.[2]

In this chapter, the reconstruction of *TTT-jets* from TTT tracks, with and without using their z_0, is discussed in Section 9.1. The correct set of the leading track-jets can be selected in many different ways by reducing the effects of pile-up in a high pile-up environment. Two such methods of event selection using the triplet track trigger, namely, the *max-bin* and the *multi-bin* event selection, are introduced in Section 9.2. These methods make use of the transverse momenta of TTT-jets – that originate from a PB or multiple z-bins – to make a trigger decision indicating whether an event should be read out or not. Section 9.3 discusses the efficiency with which the correct PB is selected using the above two methods. Trigger performance, i.e. *trigger rate* and *trigger efficiency* of TTT-jets, is presented in

---

[1] Note that the present day calorimeters are almost blind in pointing its objects to a particular z-vertex.

[2] Note that extra timing detector layers or calorimetry with precise timing can also be used to suppress pile-up. In this case, the precise timing information of the reconstructed vertex together with other kinematic parameters (of the associated objects) are used to identify the PV from pile-up collisions.

Section 9.4 following which is the comparison of their performance to the performance of the emulated calorimeter jets. The effect of pile-up on trigger rates and trigger efficiencies and as a result on the jet p_{T} thresholds is highlighted. It is shown that the TTT-jets can be used to improve the trigger performance by a substantial amount, i.e. a significant reduction in the trigger rate while maintaining a high signal efficiency is attained.

9.1 Reconstruction of Trigger Objects

The objects used for making trigger decisions in high energy physics experiments depend on the physics goals of that experiment. Generally, they include isolated tracks (of leptons and photons), jets, multi-tracks and multi-jets. The sum of the trigger rates of each of the trigger signatures must comply with the rate/bandwidth limitations of the detector. Since pile-up events dominate the total event rate of 40 MHz in a 25 ns BX, trigger rates are estimated using the minimum bias sample ($\langle\mu\rangle = 1\,\mathrm{k}$) alone. This chapter focuses on triggering of the multi-jet signatures in very high pile-up environment of the FCC-hh experiment and presents the possible pile-up rate reductions. The HH $\rightarrow b\bar{b}b\bar{b}$ sample with $\langle\mu\rangle = 1\,\mathrm{k}$ is used as an example to determine the trigger efficiency of multi-jet signatures. The emulation of a calorimeter and the reconstruction procedure of the corresponding emulated calo-jets – to estimate the calo-jet trigger rate of minimum bias events in $\langle\mu\rangle = 1\,\mathrm{k}$ – was presented in Section 5.4.1. The procedure adopted to cluster the reconstructed TTT tracks into TTT-jets for both signal (with pile-up) and pile-up is detailed below.

9.1.1 TTT-jets

At first, the entire luminous region ($\sim \pm 10\,\mathrm{cm}$) along the beam-axis (the z-axis) is divided into several overlapping z regions (z-bins). The precise z-vertex information of the TTT tracks – reconstructed using the algorithm described in Section 7.2 – is then exploited to group them into several z-bins. An overlap for each of the i^{th} bin with its immediate neighbouring bins is ensured. Figure 9.1 illustrates the grouping of TTT tracks into these z-bins. For simplicity, the bin overlaps are not displayed in the figure. The number of TTT tracks in each of the i^{th} bin is displayed along the y-axis. TTT-jets for a given event are then obtained by running jet clustering algorithms over the TTT tracks parallelly, in all z-bins. The anti-k_t jet clustering algorithm with a jet radius parameter $\Delta R_{\mathrm{jet}} = 0.4$ and minimum jet transverse momentum of $p_{\mathrm{jet}}^{\mathrm{min}} = 5\,\mathrm{GeV/c}$ is used [28]. TTT tracks are required to fulfil the final selection cuts of $p_{\mathrm{T}} > 2\,\mathrm{GeV/c}$, $|\eta| < 1.5$ and $|z_0| < 10\,\mathrm{cm}$, before being fed to the jet clustering algorithm.[3]

Note that before running the jet clustering algorithm, TTT tracks with $p_{\mathrm{T}} > 100\,\mathrm{GeV/c}$ are re-assigned a p_{T} value of $100\,\mathrm{GeV/c}$ (henceforth called as the *ceiling cut*). This is because a single very high p_{T} fake track from a pile-up collision has the potential to completely change the energy-momentum of the corresponding TTT-jet to a very high value. This very high

---

[3] The trigger performance for an extended rapidity region, i.e. $|\eta| \leq 2.5$ is presented in Appendix C, where the effects of having an unrealistic barrel geometry in the forward rapidity region on the trigger performance are highlighted.

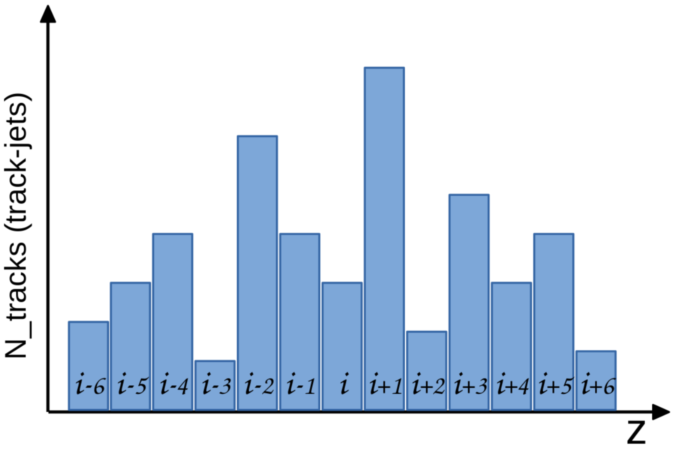

Figure 9.1: Grouping of TTT tracks into small z-bins by division of the luminous region along the beam-axis based on their reconstructed z-vertex.

p_T TTT-jet may then appear to have originated from the PV, resulting in misidentification of the hard interaction or PB.

9.2 Event Selection

The reconstructed TTT-jets can now be used to select events containing the hard interaction with multi-jet signatures. TTT-jets in each of the z-bins from an event are sorted in descending order of their transverse momentum. They are ranked based on their transverse momentum in each of the z-bins. Their p_T can be viewed as a matrix, as shown in Tables 9.1. For simplicity, these tables contain only integer values of TTT-jet p_T's.

Two different approaches of event selection, namely, the max-bin and the multi-bin method to trigger on TTT-jets coming from the hard interaction are presented in the sections below.

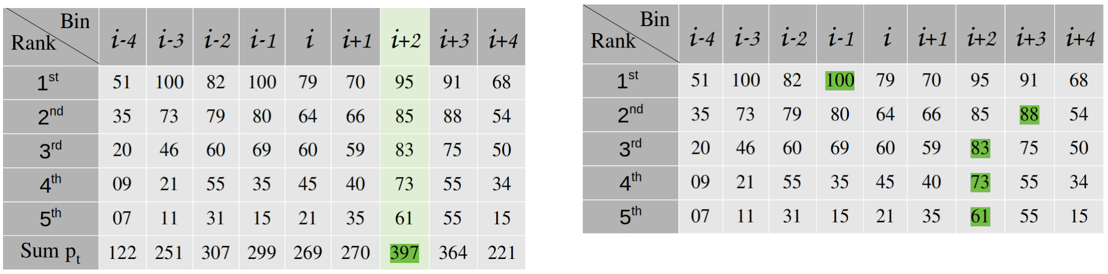

Bin / Rank	i-4	i-3	i-2	i-1	i	i+1	i+2	i+3	i+4
1st	51	100	82	100	79	70	95	91	68
2nd	35	73	79	80	64	66	85	88	54
3rd	20	46	60	69	60	59	83	75	50
4th	09	21	55	35	45	40	73	55	34
5th	07	11	31	15	21	35	61	55	15
Sum p_t	122	251	307	299	269	270	397	364	221

(a)

Bin / Rank	i-4	i-3	i-2	i-1	i	i+1	i+2	i+3	i+4
1st	51	100	82	100	79	70	95	91	68
2nd	35	73	79	80	64	66	85	88	54
3rd	20	46	60	69	60	59	83	75	50
4th	09	21	55	35	45	40	73	55	34
5th	07	11	31	15	21	35	61	55	15

(b)

Table 9.1: Illustration of selection of the first five leading jets in an event using max-bin (a) and multi-bin (b) approach.

9.2.1 Max-bin event selection

First, the sum of the p_{T} of the first few ($\sim$ 20) TTT-jets is determined for each of the bins in an event. For illustrative purpose, sum over only the first five leading p_{T} TTT-jets for each bin is shown in Table 9.1(a). The bin with the highest sum-p_{T} is chosen as the PB. Once the PB for a particular event is identified, e.g. the $(i+2)^{th}$ bin highlighted in green in Table 9.1(a), trigger decisions can be made on one or more of the first five leading p_{T} TTT-jets from the PB. Notice that this method heavily relies on the calculated sum of jet p_{T}'s per bin in an event. A single very high p_{T} fake track from a bin containing pile-up objects can completely ruin the PB selection. The ceiling cut mentioned before, suppresses this effect to a large extent.

9.2.2 Multi-bin event selection

In this method, the n^{th} leading p_{T} TTT-jet for an event is chosen by selecting the highest of the n^{th} ranked TTT-jets from all of the z-bins, where $n = 1, 2, 3, 4, 5$. For example, in Table 9.1(b), the leading p_{T} TTT-jet in an event is the maximum of all the leading p_{T} TTT-jets from all the bins, i.e. 100 GeV/c from the $(i-1)^{th}$ bin. Similarly, the maximum of all the 2^{nd} ranked TTT-jets from all the bins, i.e. 88 GeV/c from the $(i+3)^{th}$ bin (marked in green), is chosen as the sub-leading TTT-jet in this event. The $3^{rd}, 4^{th}$ & 5^{th} leading p_{T} TTT-jets are also chosen in the same way.

Very high p_{T} fake tracks from a pile-up event also affect this method of event selection. However, pile-up mostly consists of low p_{T} objects, while most of the jets from a hard interaction have a comparatively large p_{T}. Now imagine that there are some very high p_{T} fake tracks in few of the z-bins, for example, in the $(i-3)^{th}$ & the $(i-1)^{th}$ bin. As a result, the corresponding TTT-jets also have a very high p_{T}. Therefore, the chances that these high ranked pile-up TTT-jets fake a TTT-jet coming from the PB is very high, e.g. the leading jet is selected from the $(i-1)^{th}$ bin instead from the $(i+2)^{th}$ bin. Similarly, the sub-leading jet is selected from the $(i+3)^{th}$ bin instead from the $(i+2)^{th}$ bin. On the contrary, the chances of very high p_{T} fake tracks faking a low ranked pile-up TTT-jet as the one coming from the PB are much lower. Therefore, triggering on low ranked, viz. $3^{rd}, 4^{th}$ *or* 5^{th} leading p_{T} TTT-jets selected using this method is more promising in the identification of the hard interaction. This method is thus, more robust against triggering on a pile-up vertex.

9.2.3 Optimisation for Primary Bin finding

For selecting primary bin using the above two methods, a few different z-bin sizes (overlap included) i.e. ±7.5 mm, ±3.0 mm, ±1.5 mm and ±1.2 mm were used. Naively, one would think that finer the division along the z-axis better would be the primary bin selection. However, very small divisions along the z-axis would require large number of FPGA's running the jet clustering algorithms in parallel. Factors like cost and power consumption limit would then decide the z-bin size (or the number of FPGA's that would run in parallel). Furthermore, finite z_0 resolution of the reconstructed tracks will smear out the tracks from a given collision vertex over several neighbouring bins. Thus, very fine divisions along the

beam axis leads to division of the jet constituents of a PB jet amongst the neighbouring bins (even if overlap between the neighbouring bins is ensured), that would otherwise belong to a single jet.
In this section, the results are presented for a total of 200 bins in the luminous region of $z \in [-100\,\text{mm}, +100\,\text{mm}]$. This corresponds to a z-bin size of $\pm1.5\,\text{mm}$, with an overlap of $\pm0.5\,\text{mm}$ with the immediate neighbour bins included.

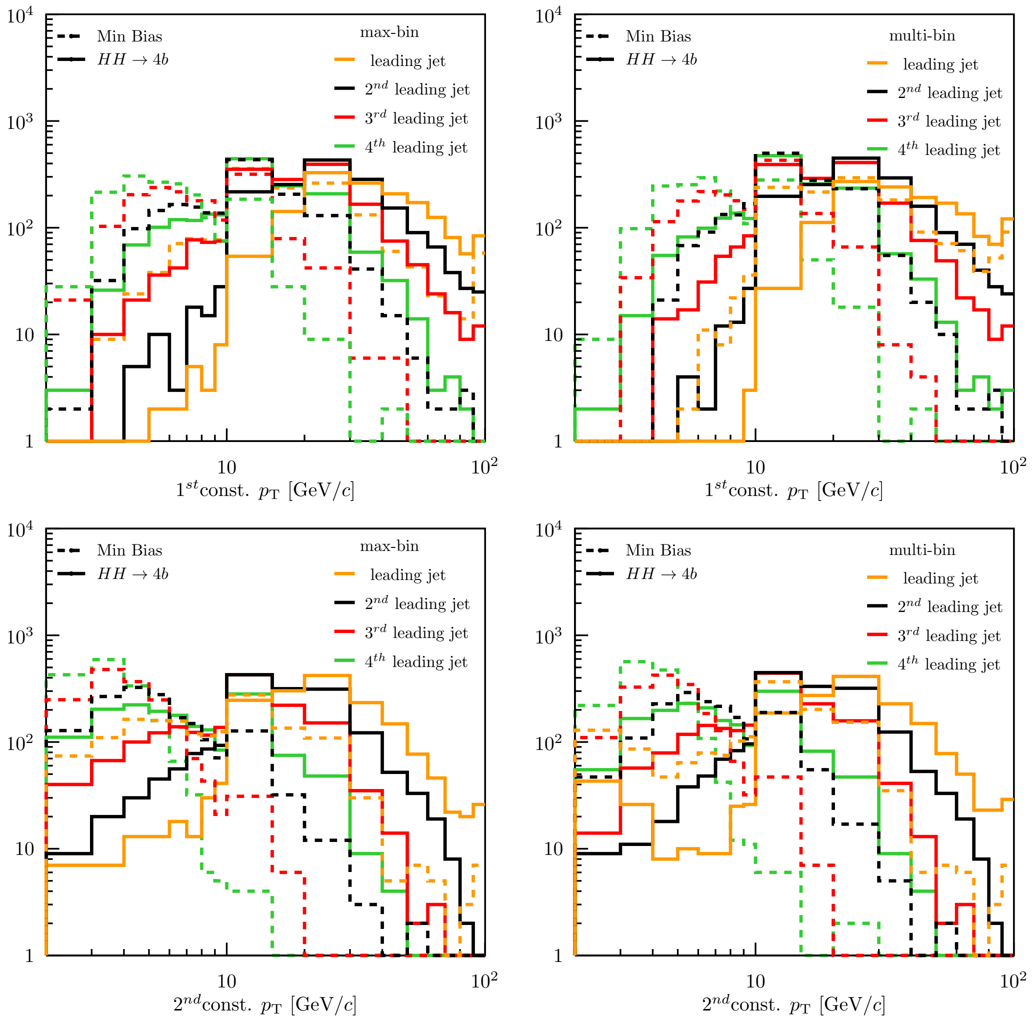

Figure 9.2: Constituent p_{T} per TTT-jet with max-bin selection (left) and multi-bin selection (right) for HH → $4b$ signal events with $\langle\mu\rangle = 1000$ (solid lines) and minimum bias events with $\langle\mu\rangle = 1000$ (dashed lines). Different colours are used to indicate the leading, sub-leading, 3^{rd} leading, and 4^{th} leading jets. A z-bin size of $\pm1.5\,\text{mm}$ together with the cuts specified in 2^{nd} and the 3^{rd} row of Table 9.2 were used for these plots.

In addition to choosing an optimum z-bin size, a constraint on the p_{T} of the first few constituents of the leading TTT-jets can be applied for pile-up rate reduction. Figure 9.2 shows the 1^{st} (top) and the 2^{nd} (bottom) highest constituents transverse momentum of the first four leading jets in signal, i.e. HH → $4b$ events with $\langle\mu\rangle = 1\,\text{k}$ (solid lines) and pile-up, i.e. minimum bias events with $\langle\mu\rangle = 1\,\text{k}$ (dashed lines), for the two methods.

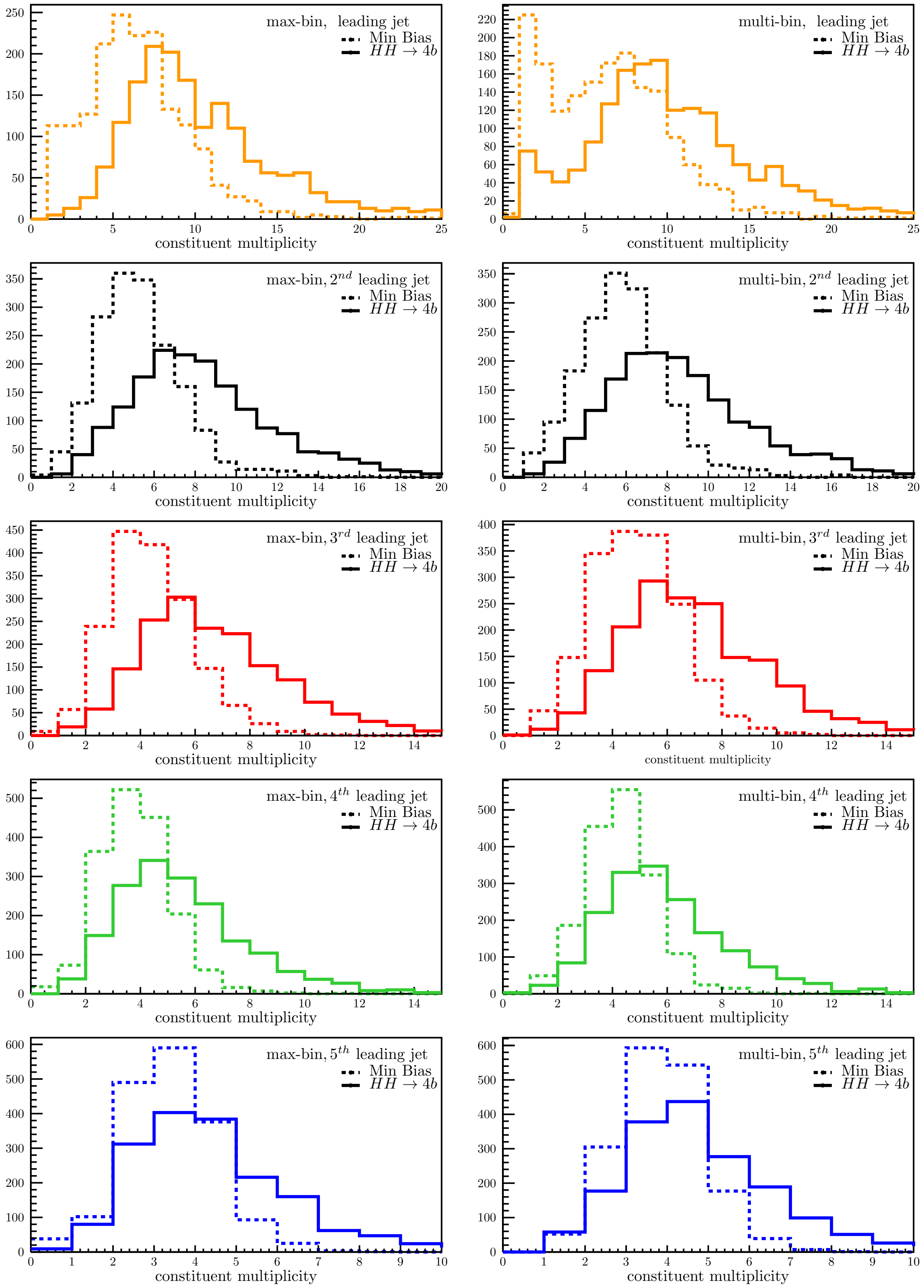

Figure 9.3: Constituent multiplicity per TTT-jet with max-bin selection (left) and multi-bin selection (right) for HH → $4b$ signal events with $\langle\mu\rangle = 1000$ (solid lines) and minimum bias events with $\langle\mu\rangle = 1000$ (dashed lines). Different colours are used to indicate the first five leading jets. A z-bin size of ±1.5 mm together with the cuts specified in 2^{nd} and the 3^{rd} row of Table 9.2 were used for these plots.

A large number of signal events from the selected bin have the highest constituent p_T larger than that of the pile-up events. This is because the pile-up jets have a softer p_T distribution unlike those originating from the PV. Hence, although the pile-up jets may comprise large track multiplicities per TTT-jet, they lack very high p_T tracks per TTT-jet. Therefore, a minimum p_T on the 1^{st} highest constituent of 9 GeV/c for leading jet, 7 GeV/c for 2^{nd} leading jet, 4 GeV/c for 3^{rd} leading jet and 3 GeV/c for the 4^{th} leading jet is required. By imposing these requirements, soft pile-up jets have smaller chances of being triggered.

Figure 9.3 shows the constituent multiplicities of the first five leading TTT-jets in signal (solid lines) and pile-up (dashed lines) for the max-bin (left) and the multi-bin (right) event selections. One can see that the first few leading jets from the selected PB have large constituent multiplicities in signal events compared to that in the pile-up events. As a result, a requirement of a certain minimum number of constituent tracks per TTT-jet reduces the rate of the TTT-jets with low constituent multiplicities (pile-up). A very tight requirement on the constituent multiplicities will, however, lead to a substantial loss of signal events. Therefore, at least 3 constituents per leading TTT-jet and at least 2 constituents per 2^{nd} and 3^{rd} leading TTT-jet are required. A summary of the selection requirements discussed above (which will be used in the results presented henceforth) is summarised in Table 9.2.

Table 9.2: Summary of the selection cuts used before jet clustering and after jet clustering in a z-bin size of $\pm 1.5\,\mathrm{mm}$ for $z_0 \in [-10\,\mathrm{cm}, +10\,\mathrm{cm}]$.

<table>
<tr><th colspan="6">Requirements before jet clustering</th></tr>
<tr><td colspan="6">$p_\mathrm{T} \geq 2\,\mathrm{GeV/c}$, $|\eta| < 1.5$, $|z_0| < 10\,\mathrm{cm}, p_\mathrm{T}^{ceiling} = 100\,\mathrm{GeV/c}$</td></tr>
<tr><td colspan="6">Requirements after jet clustering, $\Delta R_\mathrm{jet} = 0.4$, $p_\mathrm{T,jet}^\mathrm{min} = 5\,\mathrm{GeV/c}$</td></tr>
<tr><td>Jets</td><td>leading</td><td>sub-leading</td><td>3^{rd} leading</td><td>4^{th} leading</td><td>5^{th} leading</td></tr>
<tr><td>1^{st} const. $p_\mathrm{T}^\mathrm{min}$ [GeV/c]</td><td>9</td><td>7</td><td>4</td><td>3</td><td>2</td></tr>
<tr><td>min const. multiplicity</td><td>3</td><td>2</td><td>2</td><td>1</td><td>1</td></tr>
</table>

9.3 Primary Bin Selection Efficiency

Section 9.2.1 and Section 9.2.2 described the procedure for selecting a PB (for both signal with pile-up 1 k and pile-up 1 k events alone) using two different approaches. Some additional requirements to improve the PB selection using these two approaches were given in Section 9.2.3. In order to quantify how often the selected bin is the one corresponding to the PV ($\mathrm{PB}^\mathrm{truth}$), a primary bin selection efficiency is defined as the ratio of the number of events with the correctly selected primary bin to the total number of events within the acceptance of the detector:

$$\epsilon_\mathrm{PB} = \frac{\#\ \text{events with PB matched to PB}^\text{truth}\ \text{(sel. \&\& acc.)}}{\#\ \text{total events (sel. \&\& acc.)}} \tag{9.1}$$

The selection cuts listed in Table 9.2 are used for the for the reconstructed jets.[4] Selected PB's with the same z-bin as $\mathrm{PB}^{\mathrm{truth}}$ or its immediate neighbour bins are considered as matched events ($|\mathrm{PB} - \mathrm{PB}^{\mathrm{truth}}| \leq 1$).

Figure 9.4 shows the scatter plots for the selected PB as a function of $\mathrm{PB}^{\mathrm{truth}}$ for $\mathrm{HH} \rightarrow 4b$ with $\langle\mu\rangle$ =1 k events and z-bin size of ±1.5 mm in the pseudorapidity region $|\eta| < 1.5$. The y-axis indicates the method via which the PB was selected. For multi-bin event selection, since each of the leading jets can be chosen from a different z-bin, there are five different plots for the first five leading jets. One can see that the scatter plots are diagonal, i.e. majority of the PB's have been selected correctly, and a very high PB selection efficiency of 93.5 % is observed for the max-bin method. In the case of the multi-bin method, the PB selection efficiency is the best for the 2^{nd} leading jet (92.09 %) followed by the one for the 3^{rd} leading jet ($\sim$ 91 %). Although the leading jet consists of many high p_{T} (signal) tracks, a lower PB selection efficiency of $\sim$ 84 % is due to the presence of the high p_{T} fake tracks from pile-up events mimicking as leading jet from PB. This effect of fakes does not influence the low ranked jets so much. The slightly lower efficiency of $\sim$ 88 % and 79 % for the 4^{th} and the 5^{th} leading jet is due to the fact that these jets are rather soft even for signal events and hence more likely to have p_{T} less than the pile-up jets from another bin.

Scatter plots indicating the primary bin selection efficiency can similarly be plotted for the minimum bias events alone (with $\langle\mu\rangle = 1\,\mathrm{k}$). To do this, the same sample (as for the signal case) without the hard scattered objects was used for jet clustering. However the information of the PV or the hard scattered vertex was kept for identifying $\mathrm{PB}^{\mathrm{truth}}$. From Figure 9.5 one can see that in contrast to the signal (with pile-up) events, primary bins are now randomly selected (as expected) for minimum bias events ($\langle\mu\rangle = 1\,\mathrm{k}$) using both the methods.

The PB selection efficiencies for $\mathrm{HH} \rightarrow 4b$ sample in the presence of an enormous pile-up of $\langle\mu\rangle = 1\,\mathrm{k}$ using two different event selection procedures are summarized in Table 9.3.

Table 9.3: Primary bin selection efficiency in $\mathrm{HH} \rightarrow 4b$, $\langle\mu\rangle = 1\,\mathrm{k}$ for the TTT based on max-bin and multi-bin event selection. At least 3, 2, 2, 1, 1 constituent(s) per n^{th} leading jet with the leading track constituent having a minimum p_{T} of 9, 7, 4, 3, 2 GeV/c in each of the n^{th} leading jet were required, where n = 1 to 5. A minimum track p_{T} of 2 GeV/c and a maximum track p_{T} of 100 GeV/c were used for each of the TTT tracks before jet clustering.

max-bin	multi-bin				
	1L	2L	3L	4L	5L
93.54 %	84.12 %	92.09 %	90.98 %	87.73 %	79.17 %

Such an excellent primary bin selection efficiency even in such harsh pile-up environment results not only due to the reduction of the pile-up events per bin (because of fine z-binning), but also due to the large smearing of the reconstructed z_0 of low p_{T} tracks over several bins.[5]

---

[4] Results are also presented for a TTT barrel extending upto $|\eta| < 2.5$ in Appendix C.2

[5] The z_0 resolution at low p_{T} is slightly worse than at high p_{T} due to multiple Coulomb scattering; see Figure 8.7(j).

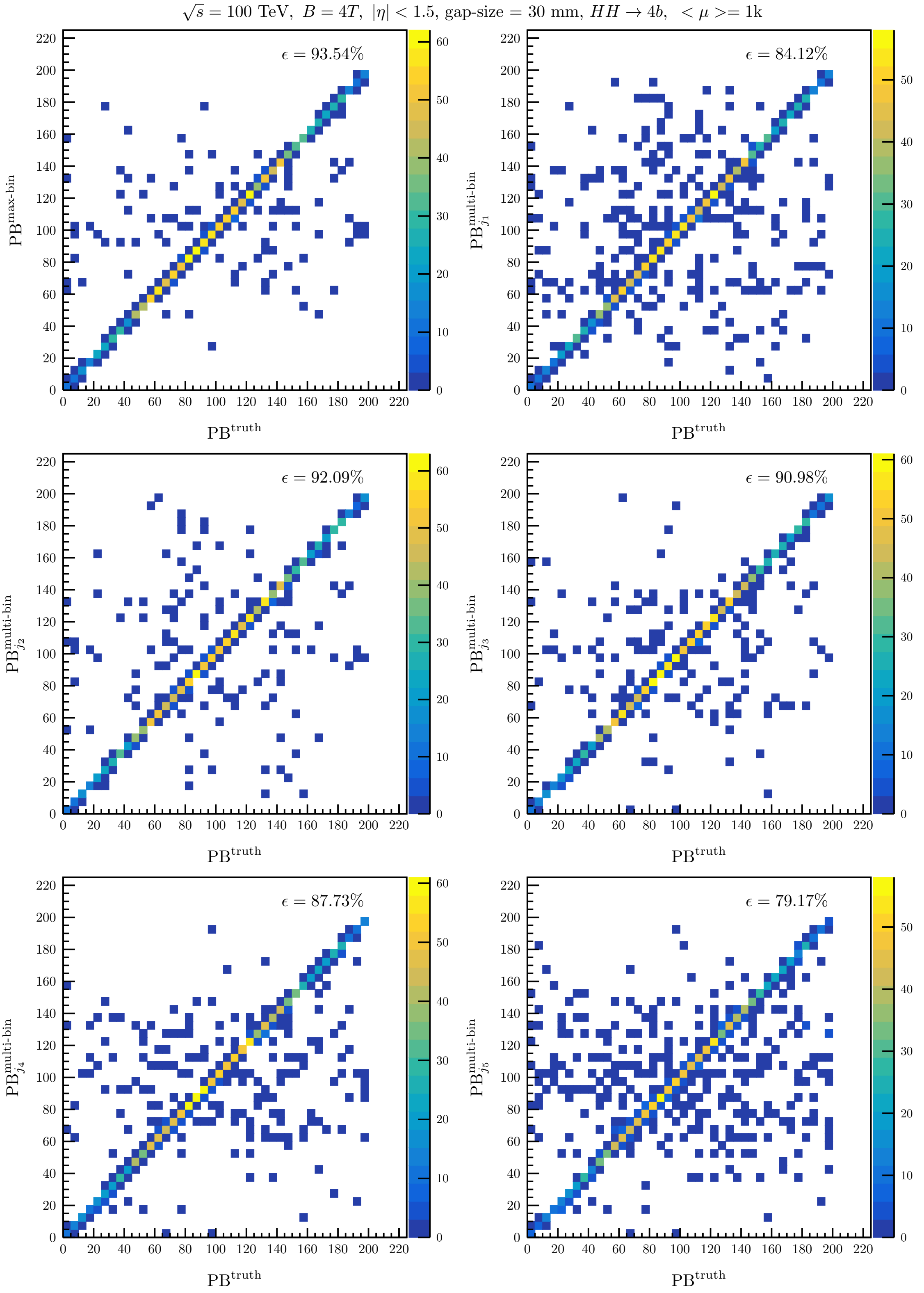

Figure 9.4: Scatter plot of the selected primary bin as a function of the truth primary bin for the max-bin method and – for the first five leading jets using – the multi-bin method in HH $\to 4b$, $\langle \mu \rangle = 1$ k events. z-bin size of ± 1.5 mm was used for parallel jet clustering of the reconstructed tracks. The PB selection efficiency is also quoted.

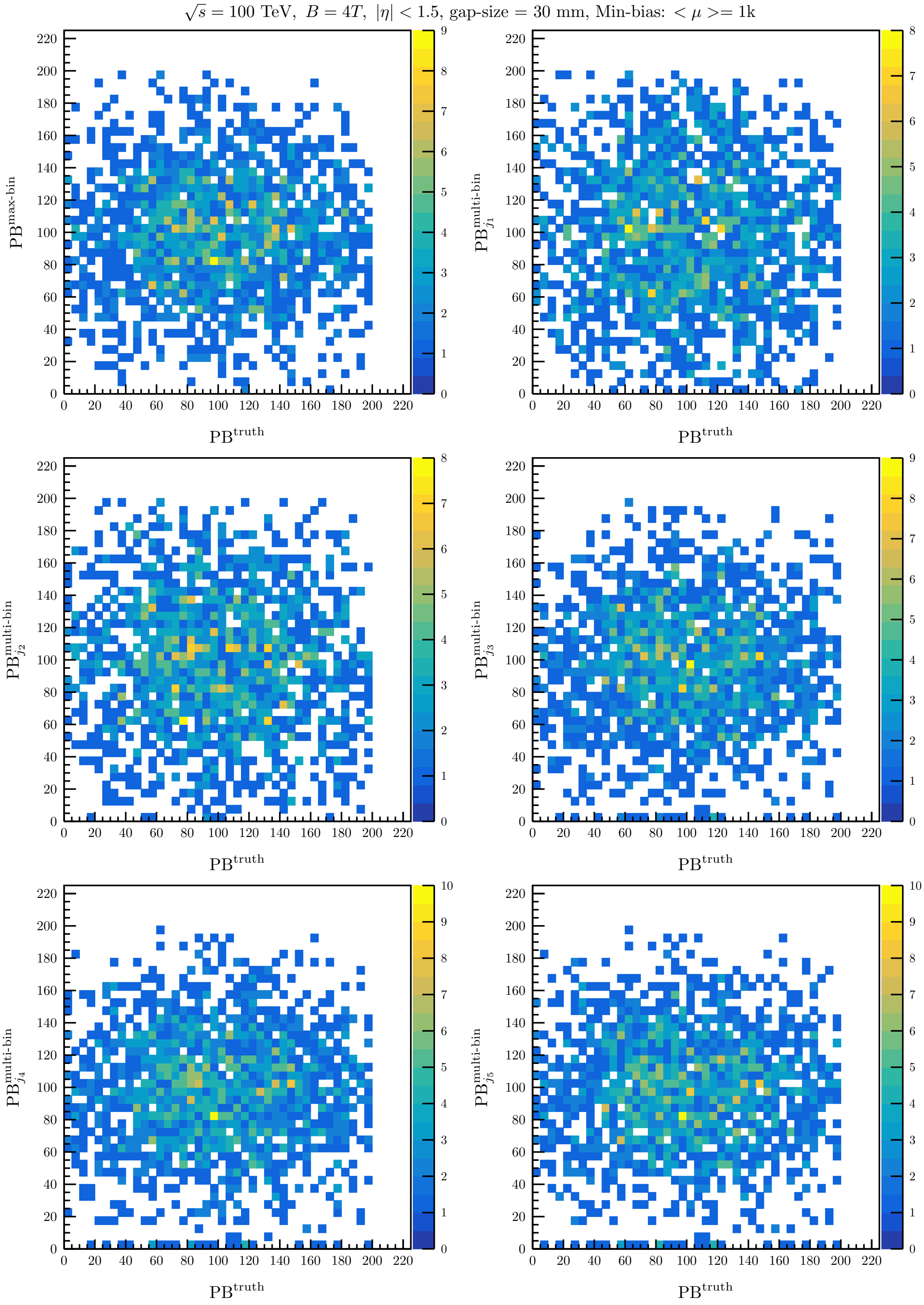

Figure 9.5: Scatter plot of the selected primary bin as a function of the truth primary bin for the max-bin method and – for the first five leading jets using – the multi-bin method using minimum bias events alone with $\langle\mu\rangle = 1\,\mathrm{k}$. z-bin size of $\pm 1.5\,\mathrm{mm}$ was used for parallel jet clustering of the reconstructed tracks.

9.4 Trigger Performance

Low rate of pile-up objects and high acceptance for signal objects will ensure excellent performance of a trigger system in experiments with harsh pile-up environment. In this section, the trigger performance based on the first five leading TTT-jets selected with z-binning (using the max-bin and the multi-bin event selection), without z-binning and emulated calo-jets are compared. For this, the relevant quantities, i.e. the trigger efficiency and trigger rate are first defined and the trigger performance is then presented in the form of ROC curves (trigger rate versus trigger efficiency).

9.4.1 Trigger Efficiency

Trigger efficiency is defined as the ratio of the number of signal events satisfying trigger selection cuts, e.g. events with $p_{\mathrm{T,j}} > p_{\mathrm{T,j}}^{\mathrm{threshold}}$ to the total number of signal events well within the acceptance of the detector. It can be mathematically formulated as:

$$\text{trigger efficiency} = \frac{\#\text{ signal events (trigger sel. \&\& acc.)}}{\#\text{ total signal events (acc.)}} \tag{9.2}$$

Here the denominator which is the total number of signal events within the acceptance includes a list of events with $\langle\mu\rangle = 1\,\mathrm{k}$ such that the objects (generator level jets) from the hard interaction in every event satisfy the offline selection cuts described in Section 3.1. The numerator is then the number of events from this total that contain five leading jets satisfying a given trigger threshold, $p_{\mathrm{T,j}} > p_{\mathrm{T,j}}^{\mathrm{threshold}}$. These leading jets can be either calo-jets, or TTT-jets obtained by either binning or not binning the luminous region (as explained in the previous sections).

9.4.2 Trigger Rate

Trigger rate is defined as the ratio of the number of pile-up events satisfying trigger selection criteria, e.g. events with $p_{\mathrm{T,j}} > p_{\mathrm{T,j}}^{\mathrm{threshold}}$ to the total number of events well within the acceptance of the detector. It can be mathematically formulated as:

$$\text{trigger rate} = \frac{\#\text{ pile-up events (trigger sel. \&\& acc.)}}{\#\text{ total pile-up events (acc.)}} \tag{9.3}$$

The denominator here corresponds to the same events that are used for trigger efficiency determination; however with the hard scattered objects removed, i.e. only minimum bias events with $\langle\mu\rangle = 1\,\mathrm{k}$. The numerator is the fraction of events from the denominator with leading jets (calo- or TTT-jets) satisfying the trigger criteria ($p_{\mathrm{T,j}} > p_{\mathrm{T,j}}^{\mathrm{threshold}}$). Since rate is generally quoted in Hz, the ratio above is normalised with the BX time of 25 ns, which corresponds to the total output rate of 40 MHz.

9.4.3 Performance Comparison of TTT-jets and Calorimeter-jets

The trigger performances (in the form of ROC curves) of the emulated calo-jets, TTT-jets reconstructed: without z-binning, with the multi-bin method and with the max-bin method are summarised in Figures 9.6(a)-(d) and 9.7(a)-(d) respectively. Performances with a coarse bin size ±7.5 mm and a fine bin size of ±1.5 mm are also compared. A curve of the form: trigger efficiency $= \sqrt{(\text{trigger rate}/\ 40\,\text{MHz})}$, in red has been added as a reference indicating signal selectivity. Points above the red line would imply no selectivity gain using the trigger. The farther the points are below the red line, the better is the signal selectivity gain, i.e. the best trigger performance corresponds to the lowest pile-up rate (or trigger rate) and highest signal efficiency (or trigger efficiency). In addition to trigger efficiency and trigger rate, the corresponding trigger thresholds are also shown with the help of the colour axis.

The following interesting observations can be made from these summary plots in Figures 9.6 and 9.7:

- For the 2^{nd} leading jets (see sub-figure(a)), the trigger performance of the emulated calo-jet is similar to that of the TTT-jets reconstructed without z-binning. The trigger thresholds required for rate reduction differ mostly due to the presence of the neutrals in the calo-jets. For reducing the pile-up rate from 40 MHz to let's say 1 MHz, trigger thresholds as high as 800 GeV/c on the 2^{nd} leading calo-jet would be needed resulting to a trigger efficiency of only $\sim$ 30 %.

- On the other hand, the trigger efficiency for the 2^{nd} leading TTT-jet using the multi-bin and the max-bin approach for a bin size of ±7.5 mm is $\sim$ 45 % at 1 MHz compared to around 33 % without z-binning. Notice the drop in trigger threshold from $\sim$ 250 GeV/c without z-binning to $\sim$ 100 GeV/c with ±7.5 mm bin size.

- A further improvement in the trigger efficiency of 55.3 % using the multi-bin method and 58.2 % using the max-bin method for the 2^{nd} leading jet is observed by going to even finer bin size of ±1.5 mm. The max-bin method performs slightly better than the multi-bin method in case of the 2^{nd} leading jet, because in case of the max-bin method the trigger performance of all the leading jets depends on the PB selected (which is quite high; see Table: 9.3). This is not the case for the 1^{st} and the 2^{nd} leading jets in the multi-bin method, where the chances of high p_{T} fake tracks from pile-up events faking as TTT-jets from a PB are quite high. This, however, does not affect the trigger performances of the 3^{rd}, 4^{th} and the 5^{th} leading TTT-jets. They show a similar improvement in trigger performance on using a finer z-bin size.

- The best trigger performance can be obtained by triggering on the 3^{rd} leading jet with a trigger efficiency of 60.1 % (84 %) at a trigger rate of 1 MHz (4 MHz) using the multi-bin TTT trigger approach with ±1.5 mm bin-size. The corresponding trigger threshold required is around 44 GeV/c (30 GeV/c).[6]

---

[6] Note that this trigger threshold is from the TTT track-jets which does not include the neutral tracks. Associating these track-jets with the energy deposits in the calorimeter for the neutral counterpart (also known as track-assisted jets) will correspond to a higher jet p_{T}. TTT-jets from the fine z-bins are also not completely pile-up free at this stage. Hence complex pile-up subtraction algorithms can be employed to suppress pile-up from the track assisted jets at HLT and offline, ensuring large acceptance

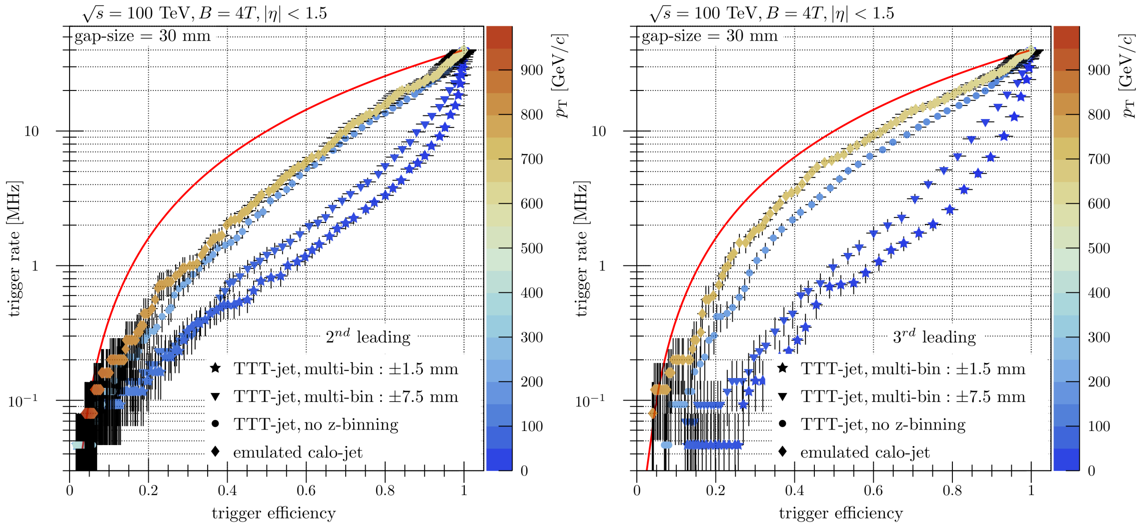

(a) 2^{nd} leading **(b)** 3^{rd} leading

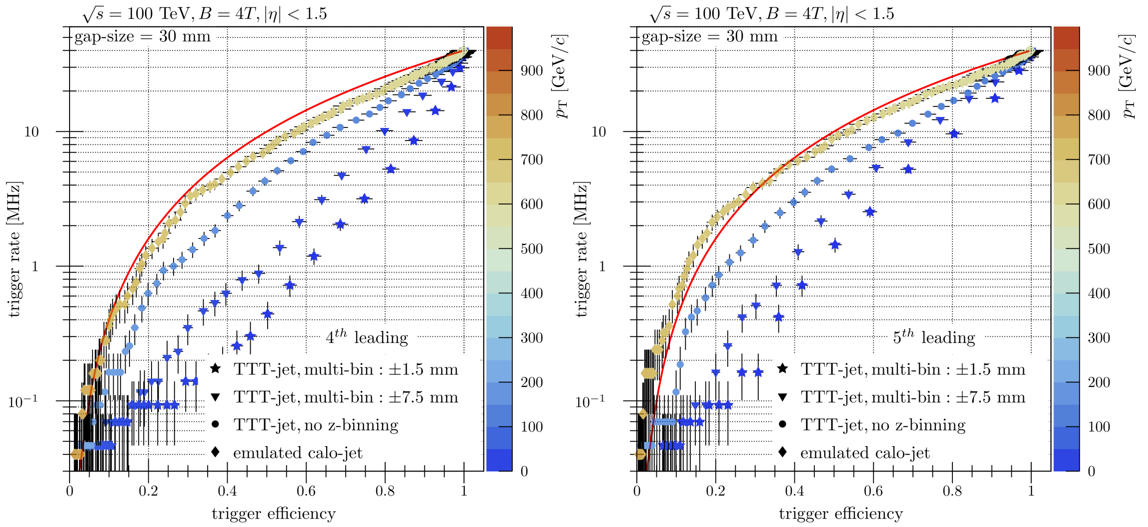

(c) 4^{th} leading **(d)** 5^{th} leading

Figure 9.6: Trigger rate as a function of trigger efficiency for emulated calo-jet (diamond), TTT-jet w/o binning along the z-axis (circle), TTT-jet reconstructed with multi-bin method for a bin size of ±7.5 mm (triangle) and ±1.5 mm (star). The color axis indicates the trigger thresholds on the transverse momentum of the jets needed for the corresponding trigger rates and trigger efficiencies. A pre-scaling curve (in red) in addition is indicated to show no selectivity of signal events.

- As mentioned before, fine z-binning not only reduces the pile-up contribution to the TTT-jets from the PB but also smears out the low p_T TTT tracks over several z-bins (much more than the high p_T TTT tracks due to different z_0 resolutions), thereby, enhancing the reduction in the pile-up contribution to TTT-jets from the PB.

---

for low p_T jets.

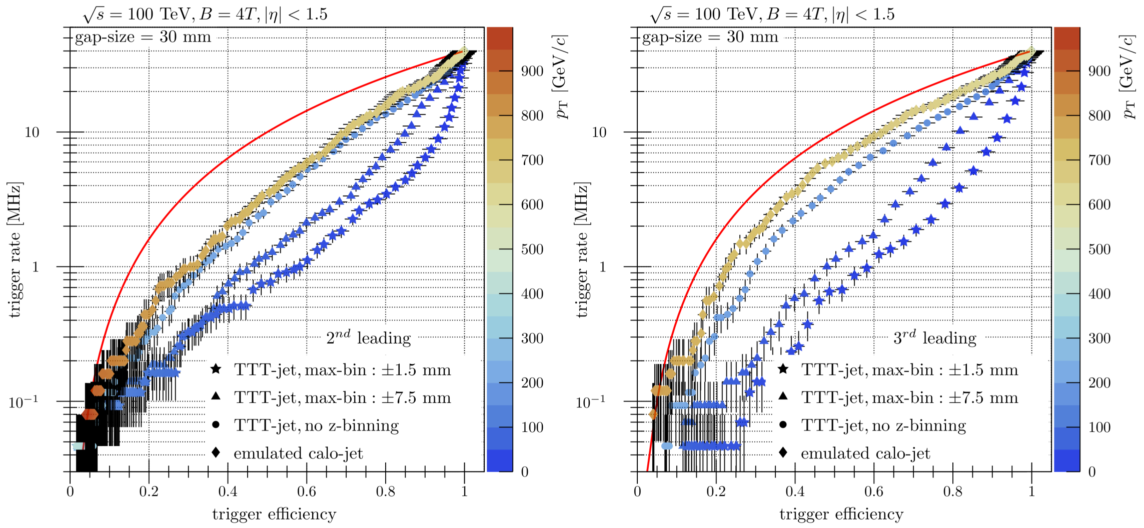

(a) 2^{nd} leading **(b)** 3^{rd} leading

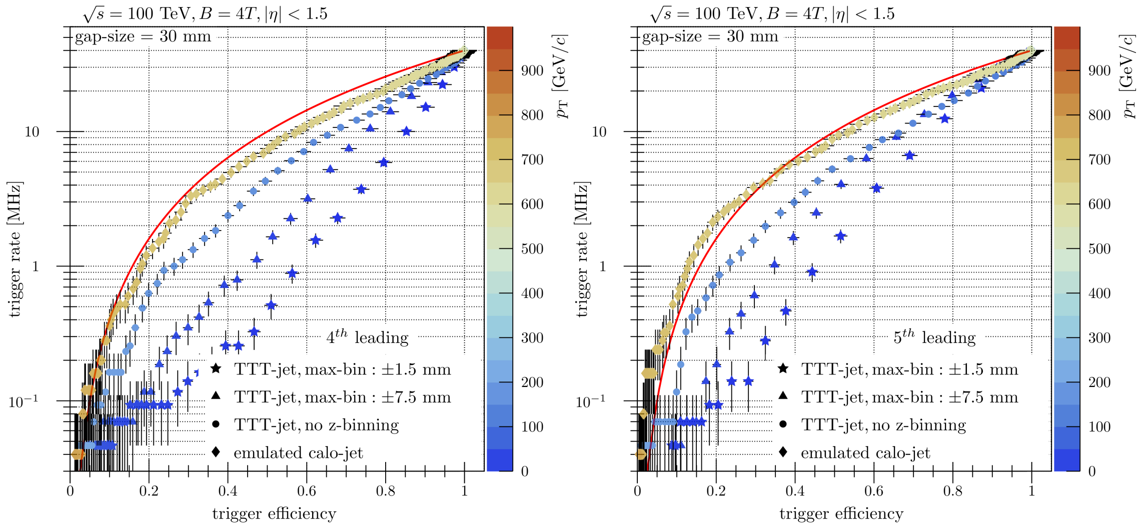

(c) 4^{th} leading **(d)** 5^{th} leading

Figure 9.7: Trigger rate as a function of trigger efficiency for emulated calo-jet (diamond), TTT-jet w/o binning along the z-axis (circle), TTT-jet reconstructed with max-bin method for a bin size of ±7.5 mm (triangle) and ±1.5 mm (star). The color axis indicates the trigger thresholds on the transverse momentum of the jets needed for the corresponding trigger rates and trigger efficiencies. A pre-scaling curve (in red) in addition is indicated to show no selectivity of signal events.

- Comparing diamonds and circles in sub-figures (a)-(d) of Figures 9.6 and 9.7, one sees that for the 2^{nd} leading jet, the calo-jet and the TTT trigger without z-binning perform very similar. With decreasing rank of the leading jets, TTT trigger outperforms the calo-jet trigger. Also, the higher the rank of the calo-jet, better is the corresponding trigger performance. The worst performance is observed for the 5^{th} leading calo-jet, where the calorimeter has almost no selectivity. This must be due to the degrading energy resolution of the calorimeter with decreasing energy.

- Similarly, the trigger performance for the 5^{th} leading TTT-jet (with and without z-binning) is comparatively worse than the performance of the first four, owing to the absence of more than four leading jets and softness of p_T distribution of the 5^{th} leading jet in the HH → $4b$ events.

- The ceiling constraint on the maximum track p_T of 100 GeV/c prevents the high p_T fake tracks from spoiling the sum of the jet transverse momenta and hence the trigger performance. This effect is negligible for very fine z-bin size as the number of fakes per bin is very small. Summary of trigger performances with (Figure C.2) and without (Figure C.1) the ceiling cut of 100 GeV/c are presented in Appendix C.1 for $|\eta| < 2.5$, where one can nicely visualise the impact of the ceiling cut on the trigger performance of TTT-jets. The trigger performance degrades without a ceiling cut, especially for coarse bin sizes. For fine bin size of ±1.5 mm the ceiling cut has no major influence. Note that for the pseudorapidity range $|\eta| < 2.5$, an unrealistic extension of the barrel geometry to large η results in larger number of fake tracks.

Table 9.4 summarises the trigger efficiencies and the corresponding trigger thresholds of the 2^d, 3^{rd}, 4^{th}, and 5^{th} leading jets (calo- and TTT-jets), required for a trigger rate reduction to 1 MHz (4 MHz) from 40 MHz. The trigger efficiency comparison between the different kinds of jets clearly shows that the a high signal efficiency is achievable by reducing the effect of pile-up through division of the luminous region. Besides, significantly lower trigger thresholds are required for substantial pile-up rate reduction using the TTT-jets selected with the multi-bin and the max-bin method. Another important point to note is the instability of the calorimeter trigger to pile-up fluctuations. Since the number of pile-up collisions is not a constant over several events and follows a Poisson distribution, fluctuations in the number of pile-up collisions will be reflected in the trigger rate. In the case of calo-jets, one can see that a small change in the trigger threshold of $\sim 5-6\,\%$, e.g. from 750 GeV/c to 796 GeV/c, causes a explosion of trigger rate from 1 MHz to 4 MHz. This indicates that the calorimeter trigger is highly unstable to pile-up fluctuations in FCC-hh like detector environment. On the contrary, the trigger rates are more robust

Table 9.4: Trigger efficiencies for HH → $4b, \langle\mu\rangle = 1\,\mathrm{k}$ and the corresponding trigger thresholds that will be required for a trigger rate of 1 MHz and 4 MHz for jets reconstructed through four different procedures.

Jet reconstruction procedure $\lvert\eta\rvert < 1.5$	Trigger Efficiency [%] at 1MHz (4MHz)				Trigger Threshold [GeV/c] at 1MHz (4MHz)			
	2L	3L	4L	5L	2L	3L	4L	5L
calo-emulation	31.3 (52.8)	23.1 (41.8)	18.0 (36.2)	12.8 (30.8)	796 (750)	756 (724)	734 (706)	720 (694)
no z-binning	33.3 (56.2)	29.6 (49.9)	26.3 (48.2)	22.6 (44.5)	252 (224)	222 (204)	204 (190)	194 (180)
multi-bin (±1.5 mm)	55.3 (82.8)	60.1 (83.9)	59.5 (77.4)	45.1 (64.3)	74 (50)	44 (30)	28 (22)	22 (18)
max-bin (±1.5 mm)	58.2 (82.9)	58.4 (82.1)	57.3 (74.5)	45.2 (61.3)	68 (46)	42 (28)	26 (20)	20 (16)

against pile-up fluctuations, when using the TTT trigger with z-binning; see the last two rows of Table 9.4 where trigger thresholds must change by more than $20 - 45\,\%$ for a rate increase from 1 MHz to 4 MHz.

9.5 Signal Significance for HH $\rightarrow b\bar{b}b\bar{b}$ using the TTT (Rough Estimate)

TTT track-jets of the HH $\rightarrow b\bar{b}b\bar{b}$ sample with $\langle\mu\rangle = 1\,\mathrm{k}$ can be triggered with a trigger efficiency of around 60 % (at 1 MHz trigger rate) and 80 % (at 4 MHz trigger rate) in the pseudorapidity range of $|\eta| \leq 1.5$ using the 3^{rd} leading jet; see the multi-bin row in Table 9.4. Assuming the same trigger efficiencies for the QCD ($pp \rightarrow b\bar{b}b\bar{b}$) background, a rough estimate on the signal significance of the HH $\rightarrow b\bar{b}b\bar{b}$ channel in FCC-hh like detector environment can be obtained. The first row of Table 9.5 lists the number of events qualifying the final invariant mass cut (see Table 3.2) of the parton level analysis presented in Section 3.1. It represents the trigger-less readout scenario (i.e. 100 % trigger efficiency) for the FCC-hh with the corresponding estimates of signal significances (without differential binning) in parenthesis for HH $\rightarrow b\bar{b}b\bar{b}$ physics channel. The second and the third row in Table 9.5 give the corresponding number of selected events (and signal significances) if the signal and QCD background could be triggered at 4 MHz and 1 MHz with an efficiency of 80 % and 60 %, respectively. One can see that the signal significance drops by a factor of $1/\sqrt{\text{trigger efficiency}}$, i.e. around 1.1 and 1.3 with a TTT at 4 MHz and 1 MHz respectively.

Table 9.5: The number of signal (HH $\rightarrow b\bar{b}b\bar{b}$) and background ($pp \rightarrow b\bar{b}b\bar{b}$) events after all analysis cuts presented in Section 3.1, assuming the same trigger efficiencies for signal and background samples. The event numbers are quoted for 1M background and 0.5M signal events for various trigger scenarios. The corresponding signal significances (for an integrated luminosity $\mathcal{L} = 30\,\mathrm{ab}^{-1}$) are also quoted in parenthesis.

Trigger Efficiency	$pp \rightarrow 4b$	k_λ values for HH $\rightarrow 4b$					
		1.0	0.0	-1.0	-2.0	2.0	3.0
100 %	3680	43789 (21.3)	41694 (38.9)	40684 (64.7)	39590 (97.3)	45587 (11.4)	40265 (8.8)
80 % at 4 MHz	2944	35031 (19.1)	33355 (34.8)	32547 (57.9)	31672 (87.0)	36469 (10.1)	32212 (7.9)
60 % at 1 MHz	2208	26273 (16.5)	25016 (30.2)	24410 (50.1)	23754 (75.3)	27352 (8.8)	24159 (6.9)
30 % Calo-trig at 1 MHz	1104	13137 (11.7)	12508 (21.3)	12205 (35.4)	11877 (53.3)	13676 (6.2)	12079 (4.8)

If the calorimeter trigger were to trigger the $4b$ events at 1 MHz using the 2^{nd} leading jet, the trigger efficiency would drop to around 30 %. This would correspond to a signal significance drop of roughly a factor of 2 compared to the trigger-less readout, in addition to the very high trigger thresholds compared to the TTT. In Section 3.2, we saw that the lower di-Higgs production cross-section at $k_\lambda = 1$ decreases the signal significance for the SM case. However, it allows one to more easily differentiate scenarios with a modified trilinear Higgs coupling, especially for $k_\lambda < 1$, where the cross-sections (and hence the signal significances) are greatly enhanced. In particular, systematic uncertainties and b-tagging efficiency would play a crucial role in the precision measurement of Higgs pair production in the $4b$ final state. Assuming negligible systematic uncertainties, the calorimeter trigger alone might manage to allow for discovery of Higgs pair production in the $4b$ final state at FCC-hh with a signal significance of around 11 for the SM case. However, trigger thresholds as high as $750 - 800\,\mathrm{GeV/c}$ due to vast pile-up would result in much larger systematic uncertainties (especially those related to background determination) as only the higher end of the p_T spectrum will be available for signal and background discrimination. This in turn would dramatically degrade the sensitivity (and hence the precision) to the measurement of trilinear Higgs self-coupling (as discussed in Chapters 2 and 3).

The Triplet Track Trigger, on the other hand, would record a signal significance of around 16 for the SM case with much lower trigger thresholds (due to a significant pile-up suppression attained by using the z_0 information).[7] Lower trigger thresholds would avail a wide range of the p_T spectrum for studying systematic uncertainties. Thus, leading to an increased sensitivity and hence precision with which λ can be determined using the TTT.

---

[7] Note that the signal significance can be improved further (almost by a factor of 2) by computing it in differential bins of a kinematic variable; see Section 3.2.

10

Summary and Outlook

In this thesis, a new track trigger concept (called the *Triplet Track Trigger (TTT)*) based on three closely spaced pixel detector layers (detector triplet) is proposed for future high-rate hadron collider experiments. The TTT is studied in the context of two future hadron collider experiments, namely, the ATLAS Phase-II experiment at the 14 TeV HL-LHC and the reference detector of the 100 TeV FCC-hh. The FCC-hh (HL-LHC) will collide *pp* beams with a luminosity of around 30 (5 – 7) times the design luminosity of the LHC ($10^{34}\,\mathrm{cm}^{-2}\mathrm{s}^{-1}$). One of the main challenges is the humongous amount of *pile-up* collisions per event. Pile-up affects almost all the reconstructed objects in particle physics experiments and together with the computational, electrical and storage limitations it forces trigger systems to increase the trigger thresholds for trigger objects manifold. High trigger thresholds will prevent measuring the full p_T spectrum of physics processes, thereby, making detection and systematic study of rare physics in this region more difficult. One of the primary motivations is, therefore, to acquire a substantial pile-up suppression at the earliest possible stage of a trigger system in experiments with vast pile-up. At the same time, the goal is to keep the trigger thresholds low enough such that the interesting physics signals from the lower end of the p_T spectrum are not filtered away.

In this context, the focus was laid on the measurement of *Higgs pair production*, which is one of the very rare processes – with a cross-section of $\sim 1220\,\mathrm{fb}$ ($40\,\mathrm{fb}$) at $\sqrt{s} = 100\,\mathrm{TeV}$ ($14\,\mathrm{TeV}$) – that will allow for direct detection of the *trilinear Higgs-self coupling* (λ). Its dominant production mode (gluon-gluon fusion) has contributions from a box and a triangle diagram at leading order, with the triangle diagram (dominant at low p_T) allowing for the measurement of λ. Probing and constraining λ is one of the crucial next steps to understanding the nature of the *Higgs potential.* Higgs pair production is associated with a rich set of final states of which there are four *golden* final states (channels) that are much more sensitive than the others, namely, the HH $\rightarrow b\bar{b}b\bar{b}$ ($4b$) channel, the HH $\rightarrow WWb\bar{b}$ channel, HH $\rightarrow b\bar{b}\tau^+\tau^-$ channel, and HH $\rightarrow b\bar{b}\gamma\gamma$ channel. As an example, a simple cut-based parton level analysis using the gluon-gluon fusion production mode for a pair of Higgs bosons in the $4b$ final state was presented. Although the HH $\rightarrow 4b$ channel is the most dominant production channel of all, it lacks the presence of prominent objects (e.g. photons or leptons) that are convenient to trigger on. Besides, the same final state can be profusely produced by the QCD interactions without any electro-weak contribution. Therefore, the HH $\rightarrow 4b$ process serves as showcase for the TTT and was used for the trigger studies in the context of this thesis. In a first step, the maximum achievable signal significance is determined for FCC-hh assuming full trigger efficiency and ignoring systematic uncertainties. For the SM HH $\rightarrow 4b$ process, a signal significance ($S/\sqrt{B}$) of ~ 21 was obtained using the simplest event count-based technique with a b-tagging efficiency of 80 % and negligible systematic uncertainties for an integrated luminosity of $\mathcal{L} = 30\,\mathrm{ab}^{-1}$ in accordance with previous studies [36]. Further improvements in signal significance – by around a factor of 2 – were attained by exploiting p_T dependence of the jet and quadratically summing the signal significances over all the bins. This allowed studying the effect of different 4^{th} jet p_T ($p_{\mathrm{T,j_4}}$) thresholds on the signal significance, with a higher gain in significance for lower 4^{th} jet p_T thresholds. The total or differential cross-section for di-Higgs production is sensitive to λ. A precision for λ_SM of $< 5\,\%$ with a threshold of $p_{\mathrm{T,j_4}} \geq 60\,\mathrm{GeV/c}$ was estimated at FCC-hh with $\mathcal{L} = 30\,\mathrm{ab}^{-1}$ and negligible systematic uncertainties. Estimates for other channels are given in Reference [36]. One of the most promising channels to measure λ at FCC-hh is HH $\rightarrow b\bar{b}\gamma\gamma$, as the γ's are easy to trigger and provide a narrow mass peak with a clean Higgs signal. With $\mathcal{L} = 30\,\mathrm{ab}^{-1}$ at FCC-hh using 75 % b-tagging efficiency and negligible systematic uncertainties, a precision of the order of 1.6 % can be obtained corresponding to a signal significance of 61 [36].

Limitations on the readout bandwidth together with the enormous amount of pile-up will restrict the efficiency with which the signal and background events can be triggered. Detailed Geant4 simulations were performed to understand the implications of limited trigger rate and trigger efficiency on the signal significance of HH $\rightarrow 4b$ process. The baseline tracker of the FCC-hh and the ATLAS ITk geometries were modified to include a barrel-shaped detector triplet at a radius of 857 mm in the simulations.

For the FCC-hh setup ($B = 4\,\mathrm{T}$), an optimum gap-size (between the layers of the detector triplet) of 30 mm was chosen, and the corresponding tracking performances for the TTT were presented in Chapter 8. The tracks were reconstructed with a very good relative p_T resolution of $< 1\,\%$ at $10\,\mathrm{GeV/c}$ and a z_0 resolution of $< 0.5\,\mathrm{mm}$ for $p_\mathrm{T} > 5\,\mathrm{GeV/c}$. A sub-mm z_0 resolution allows distinguishing between different collision vertices to a large extent. Using the HH $\rightarrow 4b$ sample with $\langle\mu\rangle = 1000$ in the FCC-hh environment an overall track reconstruction efficiency of $\sim 85\,\%$ (mainly due to pions, while close to 100 % for muons) was observed for $p_\mathrm{T} > 6\,\mathrm{GeV/c}$ and $|\eta| < 1.7$. The inefficiencies were mainly due to the inelastic nuclear interactions of the pions and bremsstrahlung emission of the electrons. Using the same MC sample, very high track purities $> 95\,\%$ were obtained for a wide range of p_T.

For the ATLAS setup ($B = 2\,\mathrm{T}$), a TTT gap-size of 20 mm was used. Implementation of the triplet track reconstruction algorithm within the official ATLAS track reconstruction framework (ATHENA) facilitated the comparison of the TTT tracking performance with the tracks reconstructed using the offline reconstruction algorithm in ATLAS. The TTT tracking performance obtained using the ATLAS setup is not very far from the offline ITk tracking performance, despite using only three tracking layers compared to nine in the ITk. An overall track reconstruction efficiency of $\sim 88\,\%$ and an excellent track purity of $> 98\,\%$ was observed using the HH $\rightarrow 4b$ sample without pile-up, for $\sqrt{s} = 14\,\mathrm{TeV}$ and $|\eta| < 1.5$.

In Chapter 9, the trigger performance of the TTT was evaluated for multi-jet signatures with an average pile-up of 1000 using the FCC-hh setup. Reconstructed TTT tracks (based on their z_0) were clustered into jets (TTT-jets) by running the anti-k_t jet clustering algorithm (over the TTT tracks). The performance is improved by constructing and analysing the vertices of the TTT-jets in parallel z-regions (z-bins). Two different methods, namely, the max-bin and the multi-bin method, were used to generate a trigger for the signal event by identification of the Primary Bin (PB) containing the hard scattered vertex. Both methods were able to correctly identify the PB of the hard scattered HH → $4b$ process from a pile-up of 1000 with very high efficiency of $> 92\,\%$ using a z-bin size of $\pm 1.5\,\mathrm{mm}$ in the pseudorapidity range of $|\eta| < 1.5$. With the help of the TTT, trigger efficiencies of $\sim 60\,\%$ and $\sim 80\,\%$ were observed for anticipated trigger (pile-up) rates of 1 MHz and 4 MHz in $\langle \mu \rangle = 1000$ conditions assuming a bunch crossing collision frequency of 40 MHz. The corresponding trigger thresholds were $\sim 45\,\mathrm{GeV/c}$ and $\sim 30\,\mathrm{GeV/c}$, respectively. On the contrary, calorimeter triggers are almost blind at pointing its objects to a specific z-vertex and suffer considerably due to the immense pile-up. An emulated calorimeter trigger based on the specifications of the FCC-hh reference detector could trigger signal events with an efficiency of less than 30 % at a trigger rate of 1 MHz for most of the highest five leading jets with trigger thresholds as high as 750 GeV/c. Besides, the calorimeter trigger was observed to be very sensitive to pile-up fluctuations as only a 5 % change in the jet trigger thresholds at 1 MHz caused an explosion of trigger rate to around 4 MHz. In other words, the calorimeter based trigger is highly unstable in very high pile-up environment like that of the FCC-hh.

Finally, an estimate on the signal significance after accounting for event losses due to trigger inefficiencies was given for the HH → $4b$ channel (assuming equal trigger efficiencies for signal and background samples). A reduction in the signal significance by a factor of 1.1 and 1.3 was estimated using a TTT that would trigger at a rate (efficiency) of 4 MHz (80 %) and 1 MHz (60 %) compared to a trigger-less readout scenario of 40 MHz (100 %) at FCC-hh. It corresponds to a signal significance of ~ 19 (at 4 MHz trigger rate) and ~ 16 (at 1 MHz trigger rate) with trigger thresholds low enough to cover a broad phase-space region (and hence making it easier to find the evidence and confidence for the HH → $4b$ channel). In contrast, the signal significance drops by almost a factor of 2 (corresponding to $S/\sqrt{B} \sim 11$) using the emulated calorimeter trigger compared to the trigger-less readout scenario, with a trigger efficiency of 30 % at 1 MHz. The very high trigger thresholds ($\geq 750\,\mathrm{GeV/c}$) expected at FCC-hh for a calorimeter trigger, however, would restrict the phase space region available for background determination, leading to much larger systematic uncertainties. Despite HH → $4b$ being one of the most challenging di-Higgs channels, it is possible to preserve almost full sensitivity with the TTT at the FCC-hh if all events could be triggered. A more accurate determination of signal significance for realistic trigger scenarios will require full simulation and reconstruction of all the relevant background processes, including a treatment of the systematic uncertainties. Besides, many other analyses (especially with multi-jet final states) will significantly profit from the very good pile-up suppression capabilities of the TTT at trigger level. Although, trigger performance studies weren't presented for the ATLAS phase-II setup, a TTT also works for the HL-LHC (ATLAS) and would be a useful tool for reducing pile-up already at the first trigger level (L0).

Part IV

Appendix

Pile-up 1k Merge Procedure

As explained in Section 1.4.3, pile-up refers to the additional soft *pp* collisions that take place together with the hard collisions during a Bunch Crossing (BX). At the FCC-hh, on an average about 1000 pile-up collisions are expected in a single 25 ns BX. One BX event therefore corresponds to one hard interaction mixed together with abound 1000 minimum bias events. The ideal way to perform a detector simulation for such a BX event would be to simulate MC samples that contain all the particles produced from both the hard interaction and the soft pile-up collisions simultaneously. This has to be preceded by merging (at particle level) of the particle information from the hard collision and about 1000 soft pile-up collisions per event. However, the CPU expense and the memory consumption would explode and one single $\langle\mu\rangle = 1\,\mathrm{k}$ event can take hours to complete.

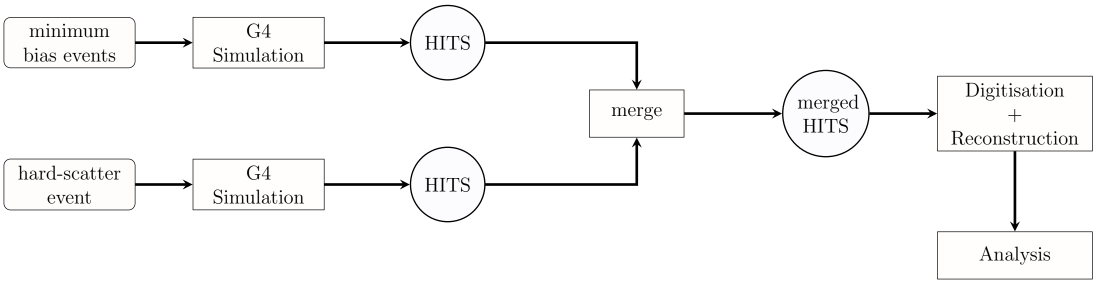

Figure A.1: Flowchart illustrating the entire chain of simulation and track reconstruction for a hard-scatter event together with a certain amount of pile-up.

Hence, in order to speed up the detector simulation step for HH → $b\bar{b}b\bar{b}$ with $\langle\mu\rangle = 1\,\mathrm{k}$ events, single *pp* interactions are simulated individually using the minimum bias events and the hard scatter event. The hits produced from the Geant4 simulations are then merged to form *merged events* each of which contains hits from one hard scattered simulated event and around 1000 minimum bias simulated events. The merged hits are then fed to the TTT reconstruction algorithm for determining the track parameters of all the particle trajectories. The entire chain of simulation and track reconstruction with a merge step in between is illustrated with the help of the flowchart in Figure A.1.

For pile-up a mixture of low-p_{T} and high-p_{T} minimum bias samples were used as in the case for ATLAS official simulations. Assuming pile-up collisions follow a Poisson distribution and the fraction of times the low (high) pile up events happen to be proportional to the low (high) minimum bias cross sections we have:

$$\begin{aligned}\langle\mu\rangle &= N_{\mathrm{low}}^{\mathrm{mean}} + N_{\mathrm{high}}^{\mathrm{mean}}, \text{ and} \\ \frac{N_{\mathrm{low}}^{\mathrm{mean}}}{N_{\mathrm{high}}^{\mathrm{mean}}} &= \frac{\mathrm{Xsec}_{\mathrm{low}}}{\mathrm{Xsec}_{\mathrm{high}}} = \mathrm{Xsec}_{\mathrm{ratio}},\end{aligned}$$

where $\mathrm{Xsec}_{\mathrm{low}} = 0.49140049 * 1.066 \times 10^2$ mb and $\mathrm{Xsec}_{\mathrm{high}} = 0.038762695 * 1.066 \times 10^2$ mb are obtained from the Pythia log file. Therefore, the mean number of high and low pile-up collisions in terms of the average pile-up $\langle\mu\rangle$ and $\mathrm{Xsec}_{\mathrm{ratio}}$ is:

$$\begin{aligned}N_{\mathrm{high}}^{\mathrm{mean}} &= \frac{\langle\mu\rangle}{(\mathrm{Xsec}_{\mathrm{ratio}} + 1)}, \\ N_{\mathrm{low}}^{\mathrm{mean}} &= \frac{\langle\mu\rangle\,\mathrm{Xsec}_{\mathrm{ratio}}}{(\mathrm{Xsec}_{\mathrm{ratio}} + 1)}.\end{aligned}$$

Now a merge sample can be created by selecting a random number from a Poisson distribution with mean $N_{\mathrm{high}}^{\mathrm{mean}}$ for high-p_{T} pile-up events and another from a Poisson distribution with mean $N_{\mathrm{low}}^{\mathrm{mean}}$ for low-p_{T} pile-up events and merging them together with one event from the hard-scatter sample.

B

Derivation of p_{T} resolution

A charged particle passing through three detector layers immersed in a uniform magnetic field perpendicular to the transverse plane is shown in Figure B.1. If the three layers are equally spaced with a distance L between the first and the third layer, then the sagita s of a trajectory with radius R is given by:

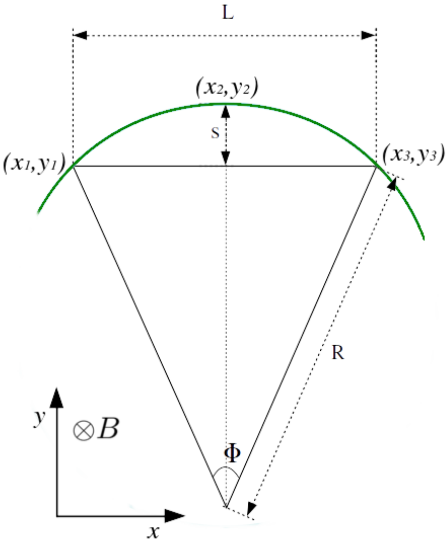

Figure B.1: A charged particles trajectory (green) passing through three detector layers in the transverse $(x - y)$ plane. It makes three hits indicated as (x_i, y_i), $i = 1, 2, 3$ when passing through a uniform magnetic field B perpendicular to the transverse plane.

$$\begin{aligned} s &= R - R\cos\left(\frac{\Phi}{2}\right) \\ &= R\left[1 - \cos\left(\frac{\Phi}{2}\right)\right] \\ &= R\left[2\sin^2\left(\frac{\Phi}{4}\right)\right] \\ &\approx R\frac{\Phi^2}{8}, \quad \text{for small } \Phi. \end{aligned} \tag{B.1}$$

Also,

$$\sin\left(\frac{\Phi}{2}\right) = \frac{L}{2\,R}$$
$$\implies \Phi \approx \frac{L}{R}, \quad \text{for small } \Phi. \tag{B.2}$$

From Equations B.1 and B.2, the sagita can be now written in terms of L and R as:

$$s \approx \frac{L^2}{8\,R}. \tag{B.3}$$

The transverse momentum (p_{T}) of this trajectory is determined by measurement of its curvature κ ($= 1/R$):

$$p_{\mathrm{T}}[\mathrm{GeV/c}] = 0.3\,B[\mathrm{T}]\,R[\mathrm{m}]. \tag{B.4}$$

From Equations B.3 and B.4:

$$s \approx \frac{0.3\,B\,L^2}{8\,p_{\mathrm{T}}}. \tag{B.5}$$

Also from the above equations:

$$\left(\frac{\sigma_{p_{\mathrm{T}}}}{p_{\mathrm{T}}}\right)^2 = \left(\frac{\sigma_R}{R}\right)^2 = \left(\frac{\sigma_\kappa}{\kappa}\right)^2. \tag{B.6}$$

The relative momentum resolution has contributions from a hit measurement term and a multiple scattering term:

$$\left(\frac{\sigma_{p_{\mathrm{T}}}}{p_{\mathrm{T}}}\right)^2 = \left(\frac{\sigma_{p_{\mathrm{T}}}}{p_{\mathrm{T}}}\right)^2_{\mathrm{Hit}} + \left(\frac{\sigma_{p_{\mathrm{T}}}}{p_{\mathrm{T}}}\right)^2_{\mathrm{MS}}. \tag{B.7}$$

The hit uncertainty term can be determined by determining the uncertainty on the sagita measurement:

$$\left(\frac{\sigma_{p_{\mathrm{T}}}}{p_{\mathrm{T}}}\right)^2_{\mathrm{Hit}} = \left(\frac{\sigma_s}{s}\right)^2. \tag{B.8}$$

For 3 detector layers, the sagita can be calculated using:

$$s = |\vec{\mathrm{r}}_2| - |(\vec{\mathrm{r}}_1 + \vec{\mathrm{r}}_3)|/2,$$

where $\vec{\mathrm{r}}_i = (x_i, y_i)$, for $i = 1, 2, 3$. The uncertainty on sagita measurement is then given by:

$$\sigma_s^2 = \sigma_{\mathrm{r}_2}^2 + \left(\frac{1}{2}\,\sigma_{\mathrm{r}_1}\right)^2 + \left(\frac{1}{2}\,\sigma_{\mathrm{r}_3}\right)^2.$$

With uncorrelated error in the transverse plane $\sigma_{\mathrm{r}_i} = \sigma_t$,

$$\sigma_s^2 = \sigma_t^2 + 2\,\frac{\sigma_t^2}{4} = \frac{3}{2}\,\sigma_t^2. \tag{B.9}$$

Thus for 3 measurement points, the hit uncertainty contribution to the relative momentum resolution (using Equations B.5, B.8, and B.9) is given by:

$$\left(\frac{\sigma_{p_\mathrm{T}}}{p_\mathrm{T}}\right)^2_\mathrm{Hit} = \left(\frac{\sigma_s}{s}\right)^2 = \left[\sqrt{\frac{3}{2}}\,\sigma_t \cdot \frac{8\,p_\mathrm{T}}{0.3\,B\,L^2}\right]^2 ,$$

which for equidistant spacing between the three layers with $L = 2\,d$ reduces to:

$$\left(\frac{\sigma_{p_\mathrm{T}}}{p_\mathrm{T}}\right)^2_\mathrm{Hit} = \left[\frac{\sqrt{6}\,\sigma_t}{0.3\,B\,d^2}\,p_\mathrm{T}\right]^2 ,$$

$$\Longrightarrow \left(\frac{\sigma_{p_\mathrm{T}}}{p_\mathrm{T}}\right)^2_\mathrm{Hit} = \left(\frac{\sigma_\kappa}{\kappa}\right)^2_\mathrm{Hit} = \left(\frac{\mathrm{K}_\mathrm{Hit}}{\kappa}\right)^2 , \tag{B.10}$$

where

$$\mathrm{K}^2_\mathrm{Hit} = \left(\frac{\sqrt{6}\,\sigma_t}{d^2}\right)^2 , \text{ and } \kappa = \frac{1}{R} = \frac{0.3\,B}{p_\mathrm{T}} \tag{B.11}$$

is a geometric constant. In the case of N equidistant layers, with $N \geq 10$, the hit uncertainty term can be determined by using the Gluckstern's formula [108]:

$$\sigma_s = \frac{\sigma_t}{8}\sqrt{\frac{720}{N+5}},$$

$$\Longrightarrow \left(\frac{\sigma_{p_\mathrm{T}}}{p_\mathrm{T}}\right)^2_\mathrm{Hit} = \left(\frac{\sigma_s}{s}\right)^2 = \left[\frac{\sigma_t\,p_\mathrm{T}}{0.3\,B\,L^2}\sqrt{\frac{720}{N+5}}\right]^2 . \tag{B.12}$$

If t is the thickness of the layers, then the expected multiple scattering uncertainty at a layer is given by the Highland Formula [109]:

$$\sigma_\Phi = \sigma_\mathrm{MS} \approx \frac{13.6\ \mathrm{MeV/c}}{\beta p}\sqrt{\frac{X}{X_0}} = \frac{13.6\,\mathrm{MeV/c}}{\beta p}\sqrt{\frac{t}{X_0\sin(\theta)}}, \tag{B.13}$$

where p is the momentum, $\beta \approx 1$ is the particle velocity, and t/X_0 is the material thickness given in units of radiation length. The contribution to the momentum error from multiple Coulomb scattering (using Equations B.2 and B.13) is given by:

$$\begin{aligned}\left(\frac{\sigma_{p_\mathrm{T}}}{p_\mathrm{T}}\right)^2_\mathrm{MS} &= \left(\frac{\sigma_\Phi}{\Phi}\right)^2_\mathrm{MS} \\ &= \left[\frac{13.6\,\mathrm{MeV/c}}{p}\sqrt{\frac{t}{X_0\sin(\theta)}} \cdot \frac{p}{0.3\,B\,L}\right]^2 \\ &= \left(\frac{\mathrm{K}_\mathrm{MS}}{\sqrt{\sin(\theta)}}\right)^2 ,\end{aligned} \tag{B.14}$$

where

$$\mathrm{K}^2_\mathrm{MS} = \left[\frac{13.6\,\mathrm{MeV/c}}{0.3\,B\,L}\sqrt{\frac{t}{X_0}}\right]^2 . \tag{B.15}$$

Thus, the combined total momentum error is:

$$\left(\sigma_{\delta p_T/p_T}\right)^2 \propto \left(\frac{\mathrm{K}\,\sigma_t}{\sqrt{N}BL^2}p_T\right)^2 + \left(\frac{\mathrm{K}_{\mathrm{MS}}}{\sqrt{\sin(\theta)}}\right)^2 . \qquad \text{(B.16)}$$

C

Trigger Performance Studies for extended TTT barrel

C.1 Performance Comparison of Triplet Track-jets and Calorimeter-jets

The trigger performance plots using the multi-bin method is presented for the extended TTT barrel (up to $|\eta| = 2.5$) in the FCC-hh setup, for the HH $\rightarrow b\bar{b}b\bar{b}$ sample with an average pile-up of 1000. Figures C.1 and C.2 allow to see the effect of fake tracks on the trigger performance of the 2^{nd}, 3^{rd}, 4^{th} and 5^{th} leading jets. In Figure C.1, the performance plots are shown without any ceiling cut on the TTT tracks (before jet clustering), while in Figure C.2, they are shown with the ceiling cut of 100 GeV/c on the TTT tracks. One can see that the large number of fake tracks (w/o the ceiling cut) degrade the trigger performance of the TTT-jets reconstructed in coarser z-bins, while the effect of fakes is negligible when one goes to finer z-bin size (e.g. ± 1.5 mm). Using the ceiling cut suppresses this degradation in coarser z-bin sizes. Besides, the degradation is more pronounced for the higher ranked jets compared to the lower ranked jets, as expected in the multi-bin method. Compared to the results for the pseudorapidity range of up to $|\eta| = 1.5$ the trigger performance for the extended barrel is worser because of the unrealistic geometry in the forward η region leading to large multiple scattering effects and hence wrong hit combinations (or fake tracks). Nevertheless, the TTT trigger performance is far better than the calo-trigger performance even with an unrealistic TTT geometry. A realistic geometry would further improve the TTT trigger performance.

C.2 Primary Bin Selection Efficiency

Figure C.3 shows the primary bin selection efficiencies using the max-bin and the multi-bin method with z-bin size of ± 1.5 mm for the extended TTT barrel in the FCC-hh setup for HH $\rightarrow 4b$, $\langle \mu \rangle = 1$ k events. The larger number of fake tracks for the extended barrel geometry also degrades the the primary bin selection efficiency compared to those for $|\eta| < 1.5$.

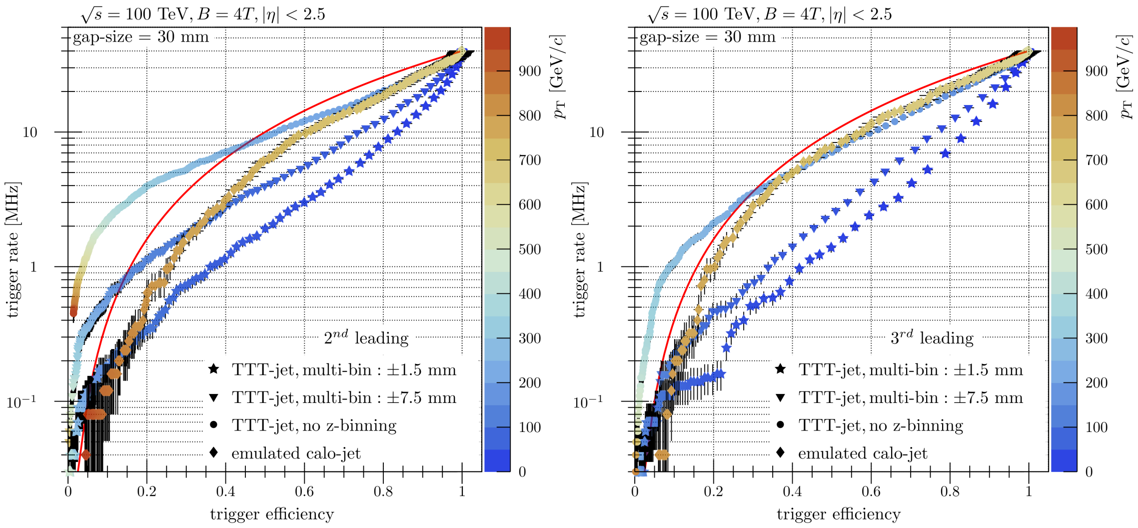

(a) 2^{nd} leading **(b)** 3^{rd} leading

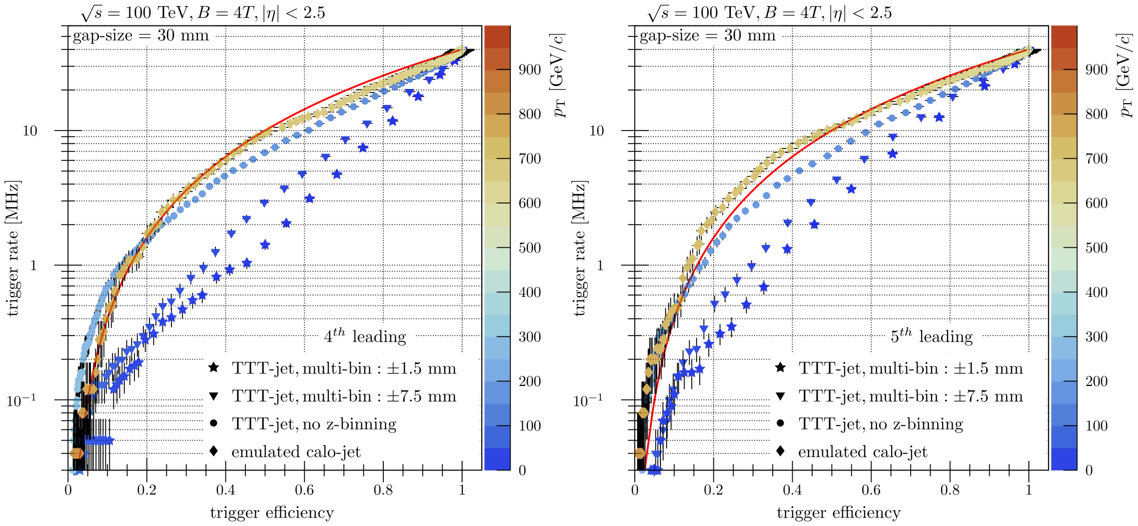

(c) 4^{th} leading **(d)** 5^{th} leading

Figure C.1: Trigger rate as a function of trigger efficiency w/o the ceiling cut of 100 GeV/c for emulated calo-jet (diamond), TTT-jet w/o binning along the z-axis (circle), TTT-jet reconstructed with multi-bin method for a bin size of ±7.5 mm (triangle) and ±1.5 mm (star) in the pseudorapidity range $|\eta| < 2.5$. The colour axis indicates the trigger thresholds on the transverse momentum of the jets needed for the corresponding trigger rates and trigger efficiencies. A pre-scaling curve (in red) in addition is indicated to show no selectivity of signal events.

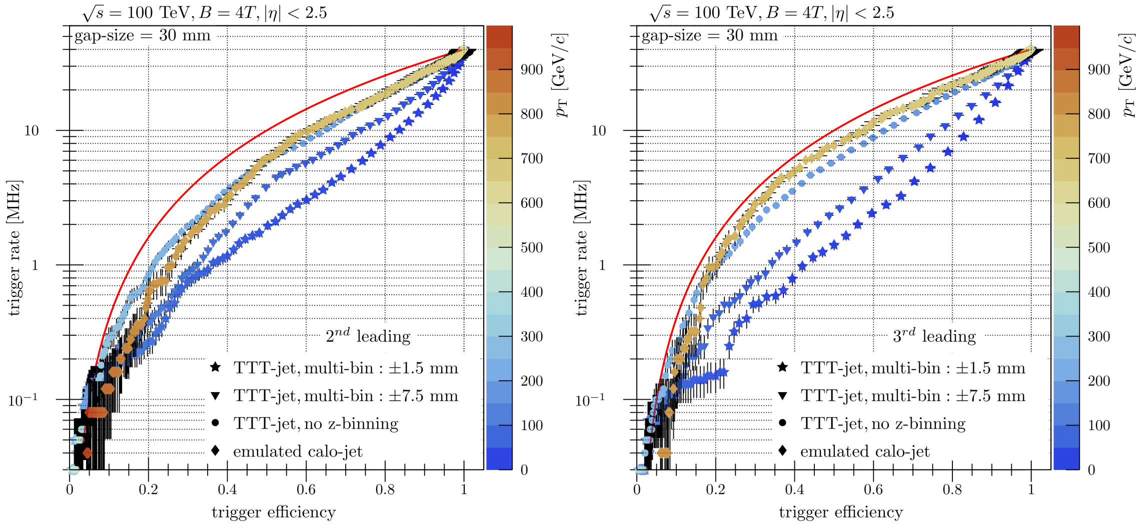

(a) 2^{nd} leading **(b)** 3^{rd} leading

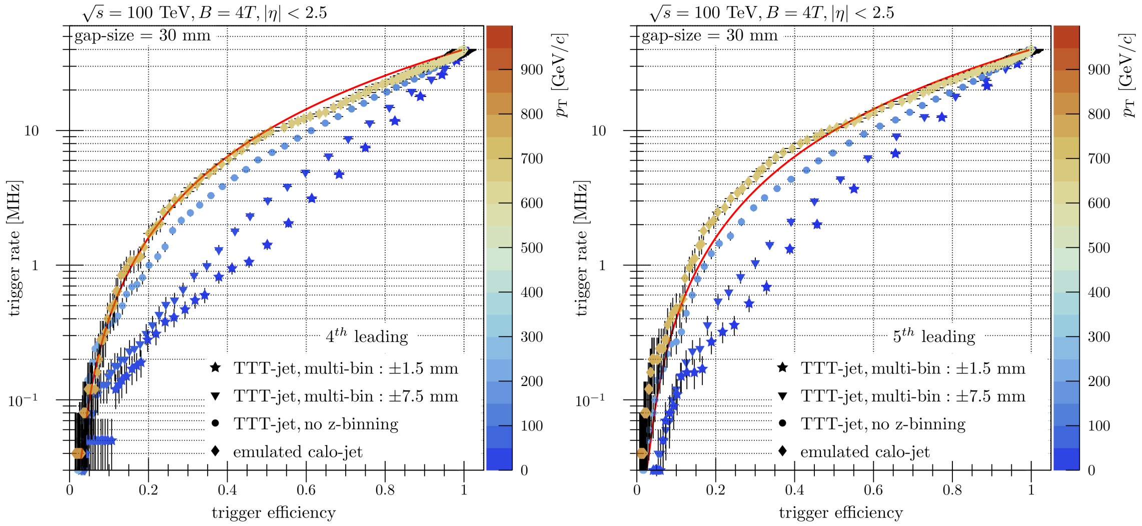

(c) 4^{th} leading **(d)** 5^{th} leading

Figure C.2: Trigger rate as a function of trigger efficiency with the ceiling cut of 100 GeV/c for emulated calo-jet (diamond), TTT-jet w/o binning along the z-axis (circle), TTT-jet reconstructed with multi-bin method for a bin size of ±7.5 mm (triangle) and ±1.5 mm (star) in the pseudorapidity range $|\eta| < 2.5$. The colour axis indicates the trigger thresholds on the transverse momentum of the jets needed for the corresponding trigger rates and trigger efficiencies. A pre-scaling curve (in red) in addition is indicated to show no selectivity of signal events.

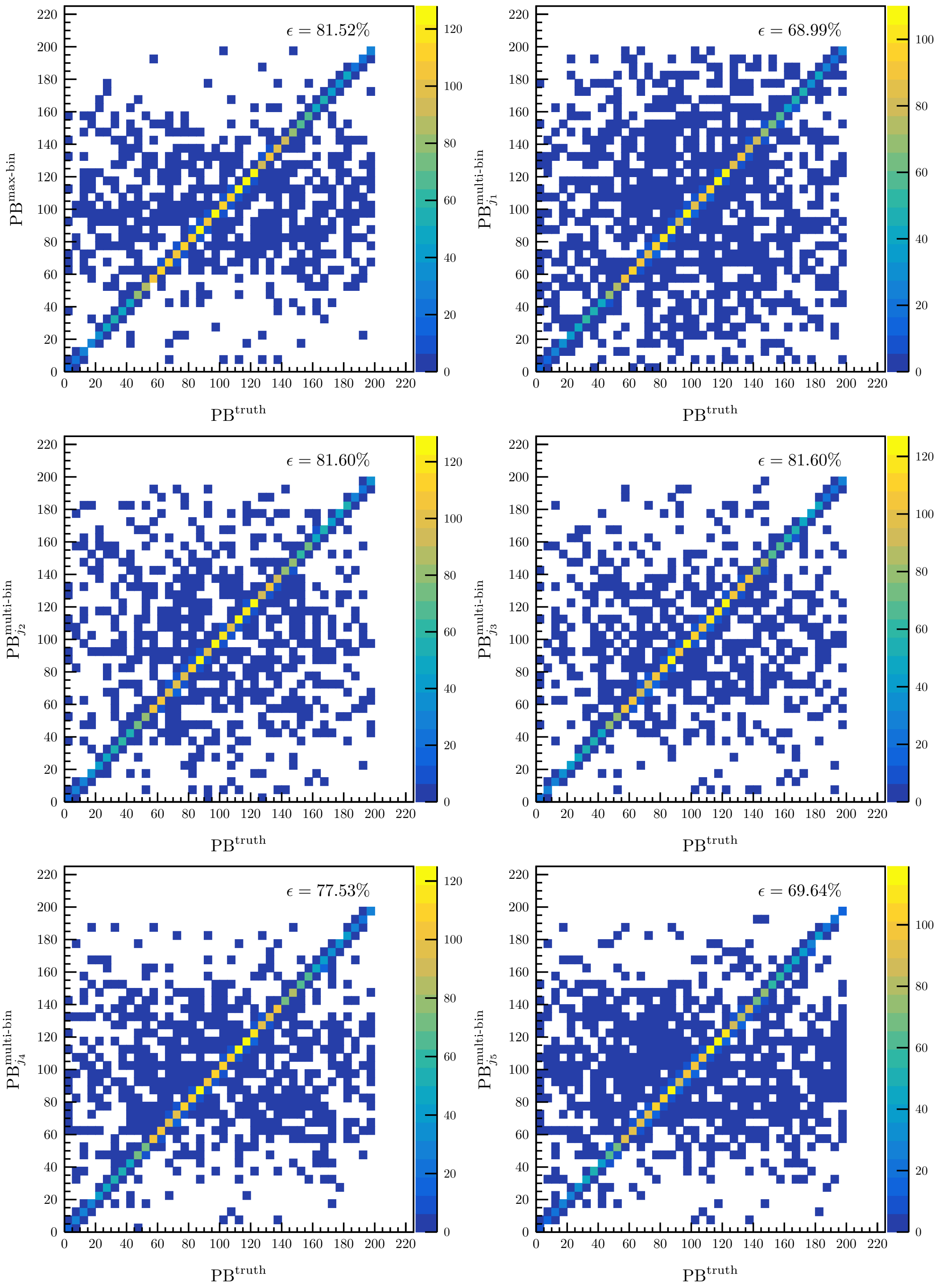

Figure C.3: Scatter plot of the selected primary bin as a function of the truth primary bin for the max-bin method and for the first five leading jets using multi-bin method in HH → $4b$, $\langle\mu\rangle = 1\,\mathrm{k}$ events in the pseudorapidity range $|\eta| < 2.5$. z-bin size of $\pm 1.5\,\mathrm{mm}$ was used for parallel jet clustering of the reconstructed tracks. The PB selection efficiency is also quoted.

Bibliography

[1] S.L. Glashow. “Partial Symmetries of Weak Interactions”. *Nucl. Phys.*, **22**:579–588, 1961. doi:10.1016/0029-5582(61)90469-2. 1, 7

[2] Steven Weinberg. “A Model of Leptons”. *Phys. Rev. Lett.*, **19**:1264–1266, Nov 1967. doi:10.1103/PhysRevLett.19.1264.

[3] N.F.V. Svartholm. *Elementary Particle Theory: Proceedings of the Eighth Nobel Symposium Held May 19-25, 1968 at Aspenäsgarden, Lerum, in the County of Älvsborg, Sweden. Edited by Nils Svartholm.* Almqvist & Wiksell, 1968.

[4] S. L. Glashow, J. Iliopoulos, and L. Maiani. “Weak Interactions with Lepton-Hadron Symmetry”. *Phys. Rev. D*, **2**:1285–1292, Oct 1970. doi:10.1103/PhysRevD.2.1285. 1, 7

[5] Lyndon R Evans and Philip Bryant. “LHC Machine”. *JINST*, **3**:S08001. 164 p, 2008. doi:10.1088/1748-0221/3/08/S08001. URL `https://cds.cern.ch/record/1129806`. This report is an abridged version of the LHC Design Report (CERN-2004-003). 1, 65

[6] ATLAS Collaboration. “The ATLAS Experiment at the CERN Large Hadron Collider”. *JINST*, **3**:S08003. 437 p, 2008. doi:10.1088/1748-0221/3/08/S08003. URL `https://cds.cern.ch/record/1129811`. Also published by CERN Geneva in 2010. 1, 65, 69

[7] CMS Collaboration. “The CMS experiment at the CERN LHC. The Compact Muon Solenoid experiment”. *JINST*, **3**:S08004. 361 p, 2008. doi:10.1088/1748-0221/3/08/S08004. URL `https://cds.cern.ch/record/1129810`. Also published by CERN Geneva in 2010. 1, 65

[8] ALICE Collaboration. “The ALICE experiment at the CERN LHC. A Large Ion Collider Experiment”. *JINST*, **3**:S08002. 259 p, 2008. doi:10.1088/1748-0221/3/08/S08002. URL `https://cds.cern.ch/record/1129812`. Also published by CERN Geneva in 2010. 1, 65

[9] LHCb Collaboration. “The LHCb Detector at the LHC”. *JINST*, **3** (LHCb-DP-2008-001. CERN-LHCb-DP-2008-001):S08005, 2008. doi:10.1088/1748-0221/3/08/S08005. URL `https://cds.cern.ch/record/1129809`. Also published by CERN Geneva in 2010. 1, 66

[10] ATLAS Collaboration. “Observation of a new particle in the search for the Standard Model Higgs boson with the ATLAS detector at

the LHC". *Physics Letters B*, **716**(1):1 – 29, 2012. ISSN 0370-2693. doi:https://doi.org/10.1016/j.physletb.2012.08.020. URL `http://www.sciencedirect.com/science/article/pii/S037026931200857X`. 1, 14

[11] CMS Collaboration. "Observation of a new boson at a mass of 125 GeV with the CMS experiment at the LHC". *Physics Letters B*, **716**(1):30 – 61, 2012. ISSN 0370-2693. doi:https://doi.org/10.1016/j.physletb.2012.08.021. URL `http://www.sciencedirect.com/science/article/pii/S0370269312008581`. 1, 14

[12] Apollinari G., Béjar Alonso I., Brüning O., Fessia P., Lamont M., Rossi L., and Tavian L. *"High-Luminosity Large Hadron Collider (HL-LHC): Technical Design Report V. 0.1"*. CERN Yellow Reports: Monographs. CERN, Geneva, 2017. doi:10.23731/CYRM-2017-004. URL `https://cds.cern.ch/record/2284929`. 2, 65, 68

[13] FCC Collaboration. "Homepage for the official Future Circular Collider (FCC) conceptual design reports (CDRs)", . URL `"https://fcc-cdr.web.cern.ch/"`. "visited on 01.07.2020". 2, 79

[14] Peter W. Higgs. "Broken Symmetries and the Masses of Gauge Bosons". *Phys. Rev. Lett.*, **13**:508–509, Oct 1964. doi:10.1103/PhysRevLett.13.508. 8

[15] F. Englert and R. Brout. "Broken Symmetry and the Mass of Gauge Vector Mesons". *Phys. Rev. Lett.*, **13**:321–323, Aug 1964. doi:10.1103/PhysRevLett.13.321.

[16] G. S. Guralnik, C. R. Hagen, and T. W. B. Kibble. "Global Conservation Laws and Massless Particles". *Phys. Rev. Lett.*, **13**:585–587, Nov 1964. doi:10.1103/PhysRevLett.13.585. 8

[17] Antonio Pich. "The Standard Model of Electroweak Interactions. The Standard model of electroweak interactions". (arXiv:0705.4264. IFIC-07-27. FTUV-07-0529): 1–49. 50 p, Jun 2007. doi:10.5170/CERN-2007-005.1. URL `http://cds.cern.ch/record/1041188`. 9, 10, 11

[18] Zyla P.A. and et al. "(Particle Data Group)". Mar 2020. URL `https://pdg.lbl.gov/2020/reviews/rpp2020-rev-standard-model.pdf`. to be published in Prog. Theor. Exp. Phys. 13, 14

[19] Christof Gattringer and Christian B. Lang. *Quantum chromodynamics on the lattice*, volume 788. Springer, Berlin, 2010. ISBN 978-3-642-01849-7, 978-3-642-01850-3. doi:10.1007/978-3-642-01850-3. 16

[20] Frank Siegert. *"Monte-Carlo event generation for the LHC"*. PhD thesis, Durham U., 2010. URL `https://cds.cern.ch/record/1600005`. 17

[21] Matthias Schott and Monica Dunford. "Review of single vector boson production in pp collisions at $\sqrt{s} = 7$ TeV.". *Eur. Phys. J. C*, **74**(arXiv:1405.1160):60 p, May 2014. doi:10.1140/epjc/s10052-014-2916-1. URL `https://cds.cern.ch/record/1699952`. 18

[22] Gerald C. Blazey et al. "Run II jet physics". In *"Physics at Run II: QCD and Weak Boson Physics Workshop: Final General Meeting"*, pages 47–77, 5 2000. 20

[23] John E. Huth et al. “Toward a standardization of jet definitions”. In *1990 DPF Summer Study on High-energy Physics: Research Directions for the Decade (Snowmass 90)*, pages 0134–136, 12 1990. 20

[24] Gavin P. Salam and Gregory Soyez. “A Practical Seedless Infrared-Safe Cone jet algorithm”. *JHEP*, **05**:086, 2007. doi:10.1088/1126-6708/2007/05/086. 20

[25] S Catani, Yu L Dokshitzer, Michael H Seymour, and Bryan R Webber. Longitudinally-invariant $k_\perp$-clustering algorithms for hadron-hadron collisions. *Nucl. Phys. B*, 406(CERN-TH-6775-93. LU-TP-93-2):187–224. 38 p, Feb 1993. doi:10.1016/0550-3213(93)90166-M. URL `http://cds.cern.ch/record/246812`. 21

[26] Yu.L Dokshitzer, G.D Leder, S Moretti, and B.R Webber. “Better jet clustering algorithms”. *Journal of High Energy Physics*, **1997**(08):001–001, Aug 1997. ISSN 1029-8479. doi:10.1088/1126-6708/1997/08/001. URL `http://dx.doi.org/10.1088/1126-6708/1997/08/001`. 21

[27] Matteo Cacciari, Gavin P. Salam, and Gregory Soyez. “The anti-k_t jet clustering algorithm”. *JHEP*, **04**:063, 2008. doi:10.1088/1126-6708/2008/04/063. 21

[28] G. P. Salam & G. Soyez M. Cacciari. “FastJet user manual”. *Eur.Phys.J. C*, **72**, 1896 (2012). doi:10.1140/epjc/s10052-012-1896-2. arXiv:1111.6097[hep-ph]. 21, 41, 148

[29] Nazar Bartosik. “B-tagging”. URL `https://commons.wikimedia.org/wiki/File:B-tagging_diagram.png`. "CC by 4.0, https://commons.wikimedia.org/w/index.php?curid=49738737 visited on 11.08.2020". 22

[30] Luca Scodellaro. “b tagging in ATLAS and CMS”. In *“5th Large Hadron Collider Physics Conference”*, 9 2017. 23

[31] Zyla P.A. and et al. “(Particle Data Group) Production and Decay of b-flavoured hadrons”. *Phys. rev. D*, April 2020. URL `https://pdg.lbl.gov/2020/reviews/rpp2020-rev-b-meson-prod-decay.pdf`. Revised April 2020 by P. Eerola (Helsinki U.), M. Kreps (Warwick U.) and Y. Kwon (Yonsei U.,Seoul). 23

[32] Estel Perez Codina and Philipp Gerhard Roloff. “Hit multiplicity approach to b-tagging in FCC-hh”. Technical Report CERN-ACC-2018-0023, CERN, Geneva, Jul 2018. URL `https://cds.cern.ch/record/2631478`. 23

[33] Grégory Soyez. “Pileup mitigation at the LHC: A theorist’s view”, 2018. 25, 26

[34] Morad Aaboud et al. “Identification and rejection of pile-up jets at high pseudorapidity with the ATLAS detector”. *Eur. Phys. J. C*, **77**(9):580, 2017. doi:10.1140/epjc/s10052-017-5081-5. 25

[35] D. de Florian et al. “Handbook of LHC Higgs cross sections:4. Deciphering the nature of the Higgs sector”. *Tech. report*, 2016. doi:10.23731/CYRM-2017-002. 26

[36] Michelangelo Mangano and Michelangelo Mangano. *Physics at the FCC-hh, a 100 TeV pp collider.* CERN Yellow Reports: Monographs. Oct 2017. doi:10.23731/CYRM-2017-003. URL `https://cds.cern.ch/record/2270978`. 27, 31, 166

[37] Zyla P.A. and et al. "(Particle Data Group) Status of Higgs Boson Physics". *Phys. rev. D*, August 2019. URL `https://pdg.lbl.gov/2020/reviews/rpp2020-rev-higgs-boson.pdf`. Revised by M. Carena (FNAL; Chicago U.; Chicago U., Kavli Inst.), C. Grojean(Theoriegruppe, DESY, Hamburg; Physik, Humboldt U.), M. Kado (Rome U. Sapienza; INFN,Rome; U. Paris-Saclay, IJCLab) and V. Sharma (UC San Diego). 27

[38] Mark Neubauer. "Higgs Boson Physics". URL `https://msneubauer.github.io/projects/4_project/`. "visited on 11.08.2020". 27

[39] The ATLAS Collaboration. "Standard Model Summary Plots Summer 2019". *ATL-PHYS-PUB-2019-024*, 2019. cds ID:2682186. 29

[40] John Campbell, Keith Ellis, Walter Giele, Tobias Neumann, and Ciaran Williams. "MCFM - Monte Carlo for FeMtobarn processes". URL `https://mcfm.fnal.gov/#examples`. visited on 23.07.2020. 30

[41] Michael Benedikt and et al. "FCC-hh: The Hadron Collider: Future Circular Collider Conceptual Design Report Volume 3. Future Circular Collider". Technical Report CERN-ACC-2018-0058, CERN, Geneva, Dec 2018. URL `https://cds.cern.ch/record/2651300`. 32, 80, 81, 82, 84, 85, 86, 88, 89, 91, 113, 114

[42] A. Abada, M. Abbrescia, S.S. AbdusSalam, and et al. "FCC Physics Opportunities". *Eur. Phys. J.*, C **79**:474, 2019. doi:10.1140/epjc/s10052-019-6904-3. 32, 33

[43] Koji Terashi, Ryu Sawada, Masahiko Saito, and Shoji Asai. "Search for WIMPs with disappearing track signatures at the FCC-hh". Technical Report CERN-ACC-2018-0044, CERN, Geneva, Oct 2018. cds ID:2642474. 32

[44] Philip Harris, Valentin V. Khoze, Michael Spannowsky, and Ciaran Williams. "Closing up on dark sectors at colliders: From 14 to 100 TeV". *Physical Review D*, **93** (5), Mar 2016. ISSN 2470-0029. doi:10.1103/physrevd.93.054030. arXiv:1509.02904 [hep-ph]. 33

[45] Tristan du Pree, Kristian Hahn, Philip B. Harris, and Christos Roskas. "Cosmological constraints on Dark Matter models for collider searches", 2016. arXiv:1603.08525 [hep-ph]. 33

[46] Clement Helsens and Michele Selvaggi. "Search for high-mass resonances at FCC-hh". Technical Report CERN-ACC-2019-0028, CERN, Geneva, Oct 2018. cds ID:2642473. 33

[47] B. Di Micco et al. "Higgs boson pair production at colliders: status and perspectives". *FERMILAB-CONF-19-468-E-T*, 2019. arXiv:1910.00012v1 [hep-ph]. 34, 35, 37, 40

[48] A. Djouadi et al. "Production of neutral Higgs-boson pairs at LHC". *Eur. Phys. J. C*, **10**:45–49, 1999. doi:10.1007/s100529900083. 34

[49] G. Degrassi et al. "Probing the Higgs Coupling via single Higgs production at the LHC". *JHEP*, **12**:080, 2016. arXiv:1607.04251v3 [hep-ph]. 35

[50] G. Degrassi et al. "Constraints on the trilinear Higgs self coupling from precision observables". *JHEP*, **04**:155, 2017. arXiv:1702.01737 [hep-ph].

[51] G. D. Kribs et al. "Electroweak oblique parametersas a probe of the trilinear Higgs boson self-interaction". *Phys. rev. D*, **95**, 2017. arXiv:1702.07678 [hep-ph]. 35

[52] The CMS Collaboration. "Combination of Searches for Higgs Boson Pair Production in Proton-Proton Collisions at $\sqrt{s} = 13$ TeV". *Phys. Rev. Lett.*, **122**, 2019. doi:10.1103/PhysRevLett.122.121803. 35

[53] The ATLAS Collaboration. "Combination of searches for Higgs boson pairs in pp collisions at $\sqrt{s} = 13$ TeV with the ATLAS detector". *Phys. Lett. B*, **800**, 2019. doi:10.1016/j.physletb.2019.135103. arXiv:1906.02025 [hep-ex]. 35

[54] The ATLAS Collaboration. "Constraints on the Higgs boson self-coupling from the combination of single-Higgs and double-Higgs production analyses performed with the ATLAS experiment". *ATLAS-CONF-2019-049*, 2019. cds ID:2693958. 35

[55] Maxime Gouzevitch and Alexandra Carvalho. "A review of Higgs boson pair production". *Reviews in Physics*, **5**:100039, 2020. ISSN 2405-4283. doi:https://doi.org/10.1016/j.revip.2020.100039. 35

[56] Javier Mazzitelli. "Precise QCD predictions for Higgs boson pair production". URL `https://indico.mpp.mpg.de/event/5508/attachments/9714/10823/seminar_hh_mazzitelli.pdf`. visited on 23.07.2020. 36

[57] Janna Katharina Behr, Daniela Bortoletto, James Frost, Nathan Hartland, Cigdem Issever, and Juan Rojo. "Boosting Higgs pair production in the $b\bar{b}b\bar{b}$ final state with multivariate techniques". *Eur. Phys. J. C*, **76**:1–31, 2015. doi:10.1140/epjc/s10052-016-4215-5. arXiv:1512.08928 [hep-ph]. 39, 53, 58, 59

[58] D. Wardrope et al. "Non-resonant Higgs pair production at the LHC in the $b\bar{b}b\bar{b}$ final state". *Eur.Phys.J. C*, **75**, 2015. doi:10.1140/epjc/s10052-015-3439-0. arXiv:1410.2794v3 [hep-ph]. 39

[59] D. E. Ferreira de Lima et al. "Standard Model Higgs boson pair production in the $(b\bar{b})(b\bar{b})$ final state". *JHEP*, 2014. doi:10.1007/JHEP08(2014)030. arXiv:1404.7139v2 [hep-ph]. 39

[60] J. Alwall et al. "The automated computation of tree-level and next-to-leading order differential cross sections, and their matching to parton shower simulations". *JHEP*, 2014. doi:10.1007/JHEP07(2014)079. arXiv:1405.0301v2 [hep-ph]. 39, 40

[61] Céline Degrande, Claude Duhr, Benjamin Fuks, David Grellscheid, Olivier Mattelaer, and Thomas Reiter. "UFO – the Universal FeynRules Output". *Comput. Phys. Commun.*, **183**, 08 2011. doi:10.1016/j.cpc.2012.01.022. arXiv:1108.2040 [hep-ph]. 39

[62] Richard D. Ball, Valerio Bertone, Stefano Carrazza, and et al. “Parton distributions with LHC data”. *Nuclear Physics B*, **867**(2):244–289, Feb 2013. doi:10.1016/j.nuclphysb.2012.10.003. arXiv:1207.1303 [hep-ph]. 40

[63] Andy Buckley, James Ferrando, Stephen Lloyd, Karl Nordström, Ben Page, Martin Ruefenacht, Marek Schoenherr, and Graeme Watt. “LHAPDF6: parton density access in the LHC precision era”. *Eur.Phys.J. C*, **75**:1–20, 2015. doi:10.1140/epjc/s10052-015-3318-8. arXiv:1412.7420 [hep-ph]. 40

[64] Torbjörn Sjöstrand et al. “An introduction to PYTHIA 8.2". *Comput. Phys. Commun.*, **191**:159–177, 2015. doi:10.1016/j.cpc.2015.01.024. 40

[65] J. Rojo P. Skands, S. Carrazza. “Tuning PYTHIA 8.1: the Monash 2013 tune". *Eur. Phys. J. C*, **74**:3024, 2014. doi:10.1140/epjc/s10052-014-3024-y. 40

[66] Helen Brooks and Peter Skands. “Average Event Properties from LHC to FCC-hh”. *Eur. Phys. J. C*, **78**(11):963, 2018. doi:10.1140/epjc/s10052-018-6460-2. 40

[67] Richard D. Ball, Valerio Bertone, Stefano Carrazza, Christopher Scott Deans, Luigi Del Debbio, Stefano Forte, Alberto Guffanti, Nathan Hartland, José Ignacio Latorre, Juan Rojo, Maria Ubiali, and The Nnpdf collaboration. “Parton distributions for the LHC run II”. *JHEP*, **2015**:1–148, 2015. doi:10.1007/JHEP04(2015)040. arXiv:1410.8849v4 [hep-ph]. 40

[68] Olaf Behnke, Kevin Kröninger, Thomas Schörner-Sadenius, and Gregory Schott, editors. *“Data analysis in high energy physics: A practical guide to statistical methods”*. Wiley-VCH, Weinheim, Germany, 2013. ISBN 978-3-527-41058-3, 978-3-527-65344-7, 978-3-527-65343-0. 44

[69] ATLAS Collaboration. “Technical Design Report for the Phase-II Upgrade of the ATLAS TDAQ System”. Technical Report CERN-LHCC-2017-020. ATLAS-TDR-029, CERN, Geneva, Sep 2017. cds ID:2285584. 46, 73, 74, 75

[70] Thomas Taylor and Daniel Treille. “The Large Electron Positron Collider (LEP): Probing the Standard Model”. *Adv. Ser. Direct. High Energy Phys.*, **27**:217–261. 45 p, 2017. doi:10.1142/9789814749145_0007. URL `https://cds.cern.ch/record/2312570`. 65

[71] CERN Document Server. “Overal View of the LHC”. URL `"https://cds.cern.ch/images/OPEN-PHO-CHART-2014-006-1/"`. "visited on 05.06.2020". 66

[72] Giuseppe Latino. “The TOTEM Experiment at LHC. cern”. *Frascati Phys. Ser.*, **47** (arXiv:0805.3968):631–646. 16 p, May 2008. URL `https://cds.cern.ch/record/1106304`. 66

[73] O Adriani and et al. “The LHCf detector at the CERN Large Hadron Collider”. *JINST*, **3**:S08006, 2008. doi:10.1088/1748-0221/3/08/S08006. URL `https://cds.cern.ch/record/1129808`. 66

[74] James Pinfold. “The MoEDAL experiment at the LHC”. *EPJ Web Conf.*, **145**:12002. 5 p, 2017. doi:10.1051/epjconf/201614512002. URL `https://cds.cern.ch/record/2288634`. 66

[75] Wikipedia. "CERN accelerator complex". URL https://commons.wikimedia.org/w/index.php?curid=15291088/. "visited on 05.06.2020". 66

[76] N Angert et al. *"CERN heavy-ion facility design report"*. CERN Yellow Reports: Monographs. CERN, Geneva, 1993. doi:10.5170/CERN-1993-001. cds ID:249000. 67

[77] "The Super Proton Synchrotron". Jan 2012. URL https://cds.cern.ch/record/1997188. 67

[78] Luigi Di Lella and Carlo Rubbia. "The Discovery of the W and Z Particles". *Adv. Ser. Dir. High Energy Phys.*, **23**:137–163, 2015. cds ID:2103277. 67

[79] Niels Doble, Lau Gatignon, Kurt Hübner, and Edmund Wilson. "The Super Proton Synchrotron (SPS): A Tale of Two Lives". *Adv. Ser. Direct. High Energy Phys.*, **27**: 135–177. 43 p, 2017. cds ID:2312568. 67

[80] CERN. "CERN's accelerator complex", . URL "https://home.cern/science/accelerators/accelerator-complex". "visited on 05.06.2020". 67

[81] CERN. "Ultimate HL-LHC Luminosity projection", . URL "https://lhc-commissioning.web.cern.ch/schedule/images/LHC-ultimate-lumi-projection.png". "visited on 09.06.2020". 68

[82] Iva Raynova and Iva Maksimova Raynova. First tests of crab cavities promise a luminous future. Mar 2017. URL https://cds.cern.ch/record/2257842. 68

[83] ATLAS Collaboration. "Luminosity Public Results", . URL "https://twiki.cern.ch/twiki/bin/view/AtlasPublic/LuminosityPublicResultsRun2". "visited on 05.06.2020". 69

[84] ATLAS Collaboration. "Event Displays from Upgrade Physics Simulated Data", . URL "https://twiki.cern.ch/twiki/bin/view/AtlasPublic/UpgradeEventDisplays". "visited on 05.06.2020". 69

[85] Joao Pequenao. Computer generated image of the whole ATLAS detector. Mar 2008. URL https://cds.cern.ch/record/1095924. 70

[86] *"ATLAS inner detector: Technical Design Report, 1"*. Technical Design Report ATLAS. CERN, Geneva, 1997. URL https://cds.cern.ch/record/331063. 70

[87] Peter Jenni, Markus Nordberg, Marzio Nessi, and Kerstin Jon-And. *"ATLAS Forward Detectors for Measurement of Elastic Scattering and Luminosity"*. Technical Design Report ATLAS. CERN, Geneva, 2008. URL https://cds.cern.ch/record/1095847. 70

[88] M Capeans, G Darbo, K Einsweiller, M Elsing, T Flick, M Garcia-Sciveres, C Gemme, H Pernegger, O Rohne, and R Vuillermet. "ATLAS Insertable B-Layer Technical Design Report". Technical Report CERN-LHCC-2010-013. ATLAS-TDR-19, Sep 2010. URL https://cds.cern.ch/record/1291633. 71

[89] T Kawamoto, S Vlachos, L Pontecorvo, J Dubbert, G Mikenberg, P Iengo, C Dallapiccola, C Amelung, L Levinson, R Richter, and D Lellouch. "New Small Wheel Technical Design Report". Technical Report CERN-LHCC-2013-006. ATLAS-TDR-020, Jun 2013. URL https://cds.cern.ch/record/1552862. 71

[90] ATLAS Collaboration. “LS2 Report: ATLAS upgrades are in full swing”, . URL "https://home.cern/news/news/experiments/ls2-report-atlas-upgrades-are-full-swing". "visited on 16.06.2020". 71

[91] “Expected Tracking Performance of the ATLAS Inner Tracker at the HL-LHC”. Technical Report ATL-PHYS-PUB-2019-014, CERN, Geneva, Mar 2019. URL https://cds.cern.ch/record/2669540. 72, 73

[92] Collaboration ATLAS. “Letter of Intent for the Phase-II Upgrade of the ATLAS Experiment”. Technical Report CERN-LHCC-2012-022. LHCC-I-023, CERN, Geneva, Dec 2012. URL http://cds.cern.ch/record/1502664. 71

[93] ATLAS Collaboration. “Technical Design Report for the ATLAS Inner Tracker Strip Detector”. Technical Report CERN-LHCC-2017-005. ATLAS-TDR-025, CERN, Geneva, Apr 2017. URL https://cds.cern.ch/record/2257755. 72, 73

[94] ATLAS Collaboration. “Technical Design Report for the ATLAS ITk Pixel Detector”. Technical Report ATL-COM-ITK-2018-019, CERN, Geneva, Mar 2018. URL https://cds.cern.ch/record/2310230. 71, 98

[95] Adrian Herkert. *“Characterization of a Monolithic Pixel Sensor Prototype in HV-CMOS Technology for the High-Luminosity LHC”*. PhD thesis, 01 2020. 72, 97

[96] R. E. Kalman. “A New Approach to Linear Filtering and Prediction Problems”. *Journal of Basic Engineering*, **82**(1):35–45, 03 1960. doi:10.1115/1.3662552. 73, 101, 142

[97] ATLAS Collaboration. “Technical Design Report for the Phase-I Upgrade of the ATLAS TDAQ System”. Technical Report CERN-LHCC-2013-018. ATLAS-TDR-023, Sep 2013. URL http://cds.cern.ch/record/1602235. 73

[98] Joao Pequenao. “Computer Generated image of the ATLAS calorimeter”. Mar 2008. URL https://cds.cern.ch/record/1095927. 75

[99] *“ATLAS liquid-argon calorimeter: Technical Design Report”*. Technical Design Report ATLAS. CERN, Geneva, 1996. URL https://cds.cern.ch/record/331061. 76

[100] *“ATLAS tile calorimeter: Technical Design Report”*. Technical Design Report ATLAS. CERN, Geneva, 1996. URL https://cds.cern.ch/record/331062. 76

[101] Joao Pequenao. “Computer generated image of the ATLAS Muons subsystem”. Mar 2008. URL https://cds.cern.ch/record/1095929. 78

[102] ATLAS Collaboration. “Technical Design Report for the Phase-II Upgrade of the ATLAS Muon Spectrometer”. Technical Report CERN-LHCC-2017-017. ATLAS-TDR-026, CERN, Geneva, Sep 2017. URL http://cds.cern.ch/record/2285580. 78

[103] ATLAS Collaboration. “Technical Proposal: A High-Granularity Timing Detector for the ATLAS Phase-II Upgrade”. Technical Report CERN-LHCC-2018-023. LHCC-P-012, CERN, Geneva, Jun 2018. URL http://cds.cern.ch/record/2623663. 78, 88

[104] "Future Circular Collider (FCC) home page". URL "https://fcc.web.cern.ch/Pages/default.aspx". "visited on 01.07.2020". 79

[105] CERN press release. "Particle physicists update strategy for the future of the field in Europe". URL "https://home.cern/news/press-release/physics/particle-physicists-update-strategy-future-field-europe". "visited on 01.07.2020". 79

[106] Michael Benedikt and et al. "FCC-ee: The Lepton Collider: Future Circular Collider Conceptual Design Report Volume 2.". Technical Report CERN-ACC-2018-0057.2, CERN, Geneva, Dec 2018. URL https://cds.cern.ch/record/2651299. 79

[107] B. Goddard and et al. "Physics Opportunities with the FCC-hh Injectors. Physics Opportunities with the FCC-hh Injectors". *CERN Yellow Report*, (arXiv:1706.07667.3):693–705. 13 p, Jun 2017. doi:10.23731/CYRM-2017-003.693. URL http://cds.cern.ch/record/2271775. 79

[108] R.L. Gluckstern. "Uncertainties in track momentum and direction, due to multiple scattering and measurement errors". *Nucl. Instrum. Meth.*, **24**:381–389, 1963. doi:10.1016/0029-554X(63)90347-1. 83, 175

[109] V. L. Highland. "Some practical remarks on multiple scattering". *Nucl. Inst. & Meth. A*, **129**:497–499, 1975. doi:10.1016/0029-554X(75)90743-0. 83, 111, 175

[110] C Neubüser. "Performance Studies and Requirements on the Calorimeters for a FCC-hh Experiment". *Springer Proc. Phys.*, **213**:37–43. 7 p, 2018. doi:10.1007/978-981-13-1316-5_7. URL https://link.springer.com/content/pdf/10.1007%2F978-981-13-1316-5_7.pdf. 85

[111] O. Kortner, S. Kortner, H. Kroha, S. Podkladkin, and R. Richter. "Design of the FCC-hh muon detector and trigger system". *Nucl. Instrum. Meth. A*, **936**:447–448, 2019. doi:10.1016/j.nima.2018.10.013. 86

[112] Matteo Cacciari and Gavin P. Salam. "Pileup subtraction using jet areas". *Phys. Lett. B*, 659:119–126, 2008. doi:10.1016/j.physletb.2007.09.077. 87

[113] Gregory Soyez, Gavin P. Salam, Jihun Kim, Souvik Dutta, and Matteo Cacciari. "Pileup subtraction for jet shapes". *Phys. Rev. Lett.*, 110(16):162001, 2013. doi:10.1103/PhysRevLett.110.162001.

[114] Jonathan M. Butterworth, Adam R. Davison, Mathieu Rubin, and Gavin P. Salam. "Jet substructure as a new Higgs search channel at the LHC". *Phys. Rev. Lett.*, 100:242001, 2008. doi:10.1103/PhysRevLett.100.242001.

[115] Stephen D. Ellis, Christopher K. Vermilion, and Jonathan R. Walsh. "Recombination Algorithms and Jet Substructure: Pruning as a Tool for Heavy Particle Searches". *Phys. Rev. D*, 81:094023, 2010. doi:10.1103/PhysRevD.81.094023.

[116] David Krohn, Jesse Thaler, and Lian-Tao Wang. "Jet Trimming". *JHEP*, 02:084, 2010. doi:10.1007/JHEP02(2010)084.

[117] Andrew J. Larkoski, Simone Marzani, Gregory Soyez, and Jesse Thaler. "Soft Drop". *JHEP*, 05:146, 2014. doi:10.1007/JHEP05(2014)146.

[118] Daniele Bertolini, Philip Harris, Matthew Low, and Nhan Tran. "Pileup Per Particle Identification". *JHEP*, 10(arXiv:1407.6013):59. 23 p, Jul 2014. doi:10.1007/JHEP10(2014)059. URL `https://cds.cern.ch/record/1745357`. 87, 88

[119] CMS Collaboration. "The Phase-2 Upgrade of the CMS Endcap Calorimeter". Technical Report CERN-LHCC-2017-023.CMS-TDR-019, CERN, Geneva, Nov 2017. URL `https://cds.cern.ch/record/2293646`. 87, 88

[120] Benjamin Kreis. "Particle Flow and PUPPI in the Level-1 Trigger at CMS for the HL-LHC", 2018. 88

[121] CMS Collaboration. "The Phase-2 Upgrade of the CMS Tracker". Technical Report CERN-LHCC-2017-009.CMS-TDR-014, CERN, Geneva, Jun 2017. URL `https://cds.cern.ch/record/2272264`. 88

[122] Roel Aaij, Johannes Albrecht, Ben Couturier, and et al. "Upgrade trigger: Biannual performance update". Technical Report LHCb-PUB-2017-005. CERN-LHCb-PUB-2017-005, CERN, Geneva, Feb 2017. URL `https://cds.cern.ch/record/2244312`. 91

[123] Andreas Salzburger. Track Simulation and Reconstruction in the ATLAS experiment, 2008. URL `http://cds.cern.ch/record/2224514`. 95, 103

[124] Philip Allport. "Applications of silicon strip and pixel-based particle tracking detectors". *Nature Reviews Physics*, 1, 08 2019. doi:10.1038/s42254-019-0081-z. 96

[125] Cinzia Da Via et al. "3D silicon sensors: Design, large area production and quality assurance for the ATLAS IBL pixel detector upgrade". *Nucl. Instrum. Meth. A*, **694**: 321–330, 2012. doi:10.1016/j.nima.2012.07.058. 97

[126] J. Lange, G. Giannini, S. Grinstein, M. Manna, G. Pellegrini, D. Quirion, S. Terzo, and D. Vázquez Furelos. "Radiation hardness of small-pitch 3D pixel sensors up to a fluence of 3×10^{16} $\mathrm{n_{eq}/cm^2}$". *JINST*, 13(arXiv:1805.10208. 09):P09009. 21 p, May 2018. doi:10.1088/1748-0221/13/09/P09009. URL `http://cds.cern.ch/record/2633861`. 21 pages. 98

[127] N. Savić. Development of Pixel Detectors for the Inner Tracker Upgrade of the ATLAS Experiment, 2017. 98

[128] Valentina Raskina and Filip Krizek. "Characterization of Highly Irradiated ALPIDE Silicon Sensors". *Universe*, **5**(4):91, 2019. doi:10.3390/universe5040091. 98

[129] Ivan Peric. "A novel monolithic pixelated particle detector implemented in high-voltage CMOS technology". *Nucl. Instrum. Meth. A*, **582**:876–885, 2007. doi:10.1016/j.nima.2007.07.115. 98

[130] W Snoeys, G Aglieri Rinella, H Hillemanns, T Kugathasan, M Mager, L Musa, P Riedler, F Reidt, J Van Hoorne, A Fenigstein, and T Leitner. "A process modification for CMOS monolithic active pixel sensors for enhanced depletion, timing performance and radiation tolerance". *Nucl. Instrum. Methods Phys. Res., A*, **871**:90–96. 7 p, 2017. doi:10.1016/j.nima.2017.07.046. URL `http://cds.cern.ch/record/2280552`. 99

[131] A. Blondel, A. Bravar, M. Pohl, S. Bachmann, N. Berger, M. Kiehn, A. Schöning, and et. al. "Research Proposal for an Experiment to Search for the Decay $\mu \rightarrow eee$.". Technical Report arXiv:1301.6113, Jan 2013. URL `http://cds.cern.ch/record/1510317`. 99

[132] A. Schöning et al. "MuPix and ATLASPix – Architectures and Results". *in Proceedings of the 28th International Workshop on Vertex Detectors (VERTEX 2019)*, 2019. arXiv:2002.07253[physics.ins-det]. 99, 113

[133] Heather M. Gray. "Track reconstruction algorithms in high pile up environment", 2017. URL `https://indico.cern.ch/event/567550/contributions/2656690/attachments/1510637/2355709/hgray_ACAT2017.pdf`. visited on 23.07.2020. 99

[134] The ATLAS collaboration. "A neural network clustering algorithm for the ATLAS silicon pixel detector". *Journal of Instrumentation*, **9**(09):P09009–P09009, sep 2014. doi:10.1088/1748-0221/9/09/p09009. 100

[135] Christian Gumpert, Andreas Salzburger, Moritz Kiehn, Julia Hrdinka, and Noemi Calace. "ACTS: from ATLAS software towards a common track reconstruction software". Technical Report ATL-SOFT-PROC-2017-030. 4, CERN, Geneva, Jan 2017. URL `https://cds.cern.ch/record/2243297`. 100

[136] Are Strandlie and Rudolf Frühwirth. "Track and vertex reconstruction: From classical to adaptive methods". *Rev. Mod. Phys.*, **82**:1419–1458, May 2010. doi:10.1103/RevModPhys.82.1419. 102

[137] Rainer Mankel. "Pattern recognition and event reconstruction in particle physics experiments". *Rept. Prog. Phys.*, **67**:553, 2004. doi:10.1088/0034-4885/67/4/R03. 103, 142

[138] Veikko Karimaki. "Effective circle fitting for particle trajectories". *Nucl. Instrum. Meth. A*, **305**:187–191, 1991. doi:10.1016/0168-9002(91)90533-V. 103

[139] V. Blobel. "A new fast track-fit algorithm based on broken lines". *Nuclear Instruments and Methods in Physics Research A*, **566**(1):14–17, October 2006. doi:10.1016/j.nima.2006.05.156. 103

[140] Claus Kleinwort. "General Broken Lines as advanced track fitting method". *Nucl. Instrum. Meth. A*, **673**:107–110, 2012. doi:10.1016/j.nima.2012.01.024. 103

[141] Niklaus Berger, Alexandr Kozlinskiy, Moritz Kiehn, and André Schöning. "A new three-dimensional track fit with multiple scattering". *Nucl. Instrum. Methods Phys. Res. A: Accelerators, Spectrometers, Detectors and Associated Equipment*, **844**:135 – 140, 2017. ISSN 0168-9002. doi:https://doi.org/10.1016/j.nima.2016.11.012. 103

[142] A. Schöning. "A New Track Reconstruction Algorithm suitable for Parallel Processing based on Hit Triplets and Broken Lines". *EPJ Web Conf*, **127**:00015, 2016. doi:10.1051/epjconf/201612700015. arXiv:1611.01671 [physics.ins-det]. 103, 111

[143] I. Abt, D. Emelyanov, I. Gorbunov, and I. Kisel. "Cellular automaton and Kalman filter based track search in the HERA-B pattern tracker". *Nucl. Instrum. Meth. A*, **490**:546–558, 2002. doi:10.1016/S0168-9002(02)01097-5. 104

[144] Paul C. Hough V. Method and means for recognizing complex patterns. (3069654), December 1962. URL `http://www.freepatentsonline.com/3069654.html`. 104

[145] Tamasi Kar, Danilo Lima, Andre Schöning, and Jike Wang. “Triplet Track Trigger for Future High Rate Experiments”. *in Proceedings of Connecting the Dots and Workshop on Intelligent Trackers*, 2019. arXiv:1910.06946[physics.ins-det]. 105

[146] A. Schöning. “Three-Dimensional Triplet Tracking for LHC and Future High Rate Experiments”. *JINST*, **9**:C10025, 2014. doi:10.1088/1748-0221/9/10/C10025. 105

[147] S Agostinelli and et al. “GEANT4–a simulation toolkikt. GEANT4. A Simulation toolkit”. *Nucl. Instrum. Methods Phys. Res., A*, 506(CERN-IT-2002-003. SLAC-PUB-9350. 3):250–303. 54 p, Jul 2002. doi:10.1016/S0168-9002(03)01368-8. URL `https://cds.cern.ch/record/602040`. 112, 115

[148] Nigel Hessy. “Summary of Performance Studies on BCL”. *ATLAS ITK Week*, 2018. Indico link:2018-02-02BCLFinal.pdf. 112

[149] P. Calafiura et al. “The Athena Control Framework in Production, New Developments and Lessons Learned”. *Computing in high energy physics and nuclear physics*, 2004. cds ID:865624p456.pdf. 123

[150] R. Aggleton and et al. “An FPGA based track finder for the L1 trigger of the CMS experiment at the High Luminosity LHC”. *Journal of Instrumentation*, **12** (12):P12019–P12019, dec 2017. doi:10.1088/1748-0221/12/12/p12019. 137

Acronyms

pp proton-proton.

ALFA Absolute Luminosity For ATLAS.
ALICE A Large Ion Collider Experiment.
ALPIDE ALICE pixel detector.
ASIC Application Specific Integrated Circuits.
ATLAS A Toroidal LHC ApparatuS.

BE back-end.
BEH Brout-Englert-Higgs.
BSM Beyond Standard Model.
BX Bunch Crossing.

CC Crab Cavity.
CCDs Charge-Coupled Devices.
CDR Conceptual Design Report.
CERN European Organization for Nuclear Research.
CLIC Compact Linear Collider.
CMOS Complementary Metal-Oxide-Semiconductor.
CMS Compact Muon Solenoid.
COMPASS Common Muon and Proton Apparatus for Structure and Spectroscopy.
CSC Cathode Strip Chambers.
CTP Central Trigger Processor.

DAQ Data Acquisition.
DM Dark Matter.

ECAL Electromagnetic Calorimeter.

EF Event Filter.
EM Electromagnetic.
EMB Electromagnetic Barrel.
EMEC Electromagnetic Endcap Calorimeter.
EMF Electromagnetic Forward.
ESPPU European Strategy for Particle Physics Update.
EWSB Electroweak Symmetry Breaking.

FCal LAr Forward Calorimeters.
FCC Future Circular Collider.
FCC-ee electron-positron Future Circular Collider.
FCC-eh electron-hadron Future Circular Collider.
FCC-hh hadron-hadron Future Circular Collider.
FE front-end.
FPGA Field-Programmable Gate Array.
FSR Final State Radiation.

GEM Gas Electron Multiplier.
ggF gluon-gluon fusion.

HCAL Hadronic Calorimeter.
HEB High Energy Booster.
HEC Hadronic Endcap Calorimeter.
HEP High Energy Physics.
HGCAL High Granularity Calorimeter.
HGTD High Granularity Timing Detector.
HL-LHC High Luminosity Large Hadron Collider.
HLT Higher Level Trigger.
HS hard scattering.
HTT Hardware Track Trigger.
HV-MAPS High Voltage Monolithic Active Pixel Sensors.

IBL Insertable B-layer.

ID Inner Detector.
IP Interaction Point.
IR infrared.
ISR Initial State Radiation.
ITk Inner Tracker.
ITS Inner Tracking System.

LAr Liquid Argon.
LEP Large Electron-Positron Collider.
LGAD Low Gain Avalanche Detector.
Lhapdf Les Houches Accord Parton Distribution Function.
LHC Large Hadron Collider.
LHCb Large Hadron Collider beauty.
LHCf Large Hadron Collider forward.
Linac 2 Linear Accelerator 2.
Linac 4 Linear Accelerator 4.
LO Leading Order.
LUCID Luminosity measurement using a Cherenkov Integrating Detector.

MAPS Monolithic Active Pixel Sensors.
MC Monte Carlo.
MDT Muon Drift Tubes.
MIP minimum ionising particle.
MoEDAL Monopole and Exotics Detector At the LHC.
MS Muon Spectrometer.
MVA Multivariate Analysis.

NA61/SHINE SPS Heavy Ion and Neutrino Experiment.
NIEL Non-Ionizing Energy Loss.
NLO Next-to Leading Order.
NNLO Next-to-Next-to Leading Order.
NNPDF Neural Network Parton Distribution Function.
NSW New Small Wheel.

PB Primary Bin.

Pb-Pb lead-lead.

PCB Printed Circuit Board.

PDF Parton Distribution Function.

PMTs photo-multiplier tubes.

PS Proton Synchrotron.

PSB Proton Synchrotron Booster.

PUPPI Pile-up Per Particle Identification.

PV Primary Vertex.

QCD Quantum Chromodynamics.

QED Quantum Electrodynamics.

QFT Quantum Field Theory.

RF Radio Frequency.

RHIC Relativistic Heavy Ion Collider.

RPC Resistive Plate Chambers.

SCT Semiconductor Tracker.

SiPMs silicon photo-multipliers.

SISCone Seedless Infrared-Safe Cone.

SM Standard Model.

sMDT small-diameter Muon Drift Tubes.

SPS Super Proton Synchrotron.

STAR Solenoid Tracker at RHIC.

SUSY Super Symmetry.

TDAQ Trigger and Data Acquisition.

TGC Thin Gas Chambers.

TID Total Ionizing Dose.

TileCal Tile Calorimeter.

TOTEM Total Elastic and diffractive cross-section Measurement.

TRT Transition Radiation Tracker.

TTT Triplet Track Trigger.

UFO Universal FeynRules Output.

VBF vector-boson fusion.

WIMP Weakly Interacting Massive Particles.

YETS Year End Technical Stop.

Acknowlegdements

This thesis would be incomplete without acknowledging some of the fantastic people that I have met during the adventurous journey of my PhD. My sincere gratitude to my primary advisor Prof. Dr André Schöning, for offering me this exciting project of Triplet Track Trigger. I am fortunate to have had a PhD supervisor like him and thank him for his patience, enthusiasm, motivation, immense knowledge, and support throughout this challenging ride. Those three encouraging words "*You will manage*", always did wonders! I am also very grateful to Prof. Dr Silvia Masciocchi for agreeing to be the second referee.

I have been extremely fortunate to have had the chance to work with one of the genius and the kindest person of all, Danilo Ferreira de Lima. His immense knowledge about almost each and every topic, his style of making his points, be it in the meetings or during the coffee-breaks are all very inspiring. He made our small ATLAS group more like a family and dealing with ATHENA without him would have been a nightmare. His guidance & support during the years I worked with him boosted my confidence to a large extent and have greatly helped me meet this challenge. A special thanks to some colleagues from the ATLAS collaboration, namely, Andi Salzburger, Noemi Calice, Nigel Hessy & Ben Smart for the skype and email exchanges w.r.t. the ATLAS software. I would also like to thank Louis Helary, for being a very helpful and friendly colleague. Many thanks to one of the nicest (and silent) person, Adrian Herkert, for bearing me as his officemate. Thank you, Adrian, for just listening to my queries at times & helping me embrace silence like never before! I thank Christof Sauer & Marta Czurylo for always being there to discuss problems and ideas, and support me when I would panic. Thank you, Marta, for pushing me to run an extra mile or two (during lockdown), & for all the laughter that we've had in the past few months (oh, and for that meme!). A big thanks to all my former and present colleagues, Frank, Ann-Kathrin, Maddalena, Sebastian D., Annie, Thomas, Luigi, Heiko, Anjali, Arthur, David, Lennart & Joachim for all the coffee-breaks and fun we had during *Boßeln*. Thanks to Thomas, for inviting me to the Christmas dinner; it made me less homesick while producing some results present in this thesis. And how can I not thank Claudia, for all the help in the administrative work and the big warm smiles & greetings.

I am very grateful to the HighRR training group, for funding my PhD and all the travels to some incredible conferences and workshops. A special thanks to the proof-readers: André, Christof, Marta, Sebastian, Neeraj Amin, from Germany, Archana Radhakrishnan and Rushabh Gala, from my friends in the US, and Deepesh Bhamre, from India.

Last but not least, I am extremely thankful to have had the most amazing bunch of friends and family members. Thank you, Mummy, for your trust and confidence in me, for your love, care and support, for making me the person I am today, and for being more than just a mother. I am thankful to my elder brother (Tapan), sister (Tapasi) and grandmother, for inspiring me with their strength and bravery with which they have overcome many hardships. Many thanks to Hem Sir and Lynette didi for being the mentors before I stepped into this journey. Thank you Radhika, Archana, Nilesh and Sudip for always being there to listen to me. I cherish the bond we have. Thanks to my friends from my bachelors and masters, for keeping in touch and always being ready to hear me out. Cheers to some of the amazing friends I have met in Heidelberg: Sarah, Flavia, Reena, Sonam, and my previous flatmate, Vikas, without whom this journey wouldn't be fun at all. Finally, thanks to the Indian community and ISKCON in Heidelberg, for helping me practice spirituality and stay connected to my roots. (More in this blog.)